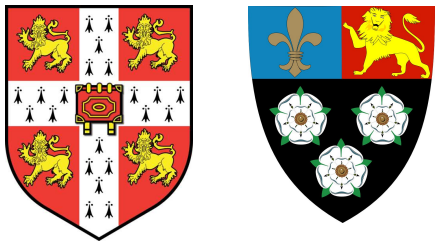

UNIVERSITY OF CAMBRIDGE

INSTITUTE OF ASTRONOMY

A DISSERTATION SUBMITTED TO THE
UNIVERSITY OF CAMBRIDGE FOR THE DEGREE
OF DOCTOR OF PHILOSOPHY

DISSECTING THE MILKY WAY WITH SPECTROSCOPIC STUDIES

KEITH AUSTIN HAWKINS

KINGS COLLEGE

Submitted to the Board of Graduate Studies
August 14, 2016

UNDER THE SUPERVISION OF
PROF. GERRY GILMORE & DR. PAULA JOFRÉ

"But in the heavens we discover by their light, and by their light alone, stars so distant from each other that no material thing can ever have passed from one to another; and yet this light, which is to us the sole evidence of the existence of these distant worlds, tells us also that each of them is built up of molecules of the same kinds as those which we find on earth."

– James Clerk Maxwell, *Molecules*, 1873

DECLARATION OF ORIGINALITY

I, Keith Austin Hawkins, declare that this Thesis entitled *'Dissecting the Milky Way with Spectroscopic Studies',* I confirm that this work was done wholly while in candidature for a research degree at this University, and that this thesis has not previously been submitted for a degree or any other qualification at this University or any other institution. This thesis is the result of my own research and contains nothing resulting from collaboration, except where explicitly noted. The length of this thesis does not exceed the stated limit of the Degree Committee of Physics and Chemistry of 60,000 words.The parts of this Thesis based on published work are as follows:

- **Chapter 2**
  "On the ages of the α-rich and α-poor populations in the Galactic halo'
  Hawkins, K., Jofré, P., Gilmore, G., Masseron, T, 2014, MNRAS, **445,** 2575

- **Chapter 3**
  'Characterizing the high-velocity stars of RAVE: the discovery of a metal-rich halo star born in the Galactic disc'
  Hawkins, K., Kordopatis, G., Gilmore, G., Masseron, T., Wyse, R. F. G., Ruchti, G., Bienaym, O., Bland-Hawthorn, J., Boeche, C., Freeman, K., Gibson, B. K., Grebel, E. K., Helmi, A., Kunder, A., Munari, U., Navarro, J. F., Parker, Q. A., Reid, W. A., Scholz, R. D., Seabroke, G., Siebert, A., Steinmetz, M., Watson, F., Zwitter, T., 2015a, MNRAS, **447,** 2046

- **Chapter 4**
  'Using Chemical Tagging to Redefine the Interface of the Galactic Halo and Disk'
  Hawkins, K., Jofré, P., Gilmore, G., Masseron, T, 2015b, MNRAS, **453,** 758

- **Chapter 5**
  'Gaia FGK benchmark stars: new candidates at low-metallicities'
  Hawkins, K., Jofré, P., Heiter, U, Soubiran, C., Blanco-Cuaresma, C., Casagrande, L., Gilmore, G., Lind, K., Magrini, L., Masseron, T., Pancino, E., Randich S., Worley, C. C., 2016a, A&A, 592, A70

- **Chapter 6**
  'An Accurate and Self-Consistent Chemical Abundance Catalogue for the APOGEE/Kepler Sample'
  Hawkins, K., Masseron, T., Jofré, P., Gilmore, G., Elsworth, Y., Hekker, S., 2016b, A&A, Accepted for publication

_____

Signed

_____

Date

ACKNOWLEDGEMENTS

There is an African proverb that says "it takes a village to raise a child." I think this also holds for a doctoral student; "it takes a village to raise a Ph.D." I have, from the time I was young, been surrounded by a village of amazing, supportive, and encouraging people that have made this Thesis possible. There is not enough space in this work to mention them all, but I will mention a few here. For those I do not mention fear not, because this Thesis is dedicated to all of my mentors, past and present.

First, and foremost, I must thank my supervisors Prof. Gerry Gilmore and Dr. Paula Jofré. If it were not for you two, I would not have been able to do this. Your words of encouragement, and advice have taught me so much! This Thesis would not have been nearly as productive or fun if it were not for the 'army' of support I received from the various postdoc members of the group including: Thomas Masseron, Georges Kordopatis, Andy Casey, Clare Worley, Anna Hourihane, and Jason Sanders and various collaborators including Rosie Wyse, Greg Ruchti, Gus Williams, and the Gaia-ESO, and RAVE survey teams. All of you fit me into your busy schedules, whenever I needed, to coach me through various aspects of astrophysics and for that I am forever grateful. Particular thanks to Thomas Masseron for not only the many long conversations that improved my understanding of the technical details, but also for the basic stellar parameter code, BACCHUS, that was heavily used in this work.

Like most things in life, I became passionate about astronomy because of a girl, Rachel Cuenot. Fifth grade me was enamored by her, in part, because she loved space at that time. She inspired me to become an astronomer before her family moved away. Thank you Rachel for the initial spark that emboldened me to peer into the telescope!

I would also like to acknowledge my partner Ashleigh Chalk, Sahar Mansoor, Luca Matrá, the Chalk-Newman family (Sally, Richard, Caz, and Joe), Hiren Joshi, Georgia Crick-Collins, Aimée Hall, Nicoletta Fala, Suzzie Wood, Shizuyo Ichikawa, and last but not least my fellow 2013(4,5) Marshall scholars, for the immense support, words of encouragement, nights out, and great experiences all around that have helped me settle in and find/make a home in Cambridge.

To my officemates in H27 (Luca, Aimée, Nimisha, Sebastián, Tom, and Christina), we had some really great times! From H27-big-chat, to Luca's tortoise noises. From backpacking the Alps with Luca and Co. to poker nights. You all have really made working at the IoA one of my most enjoyable experiences.

I would not have been able to take up the PhD offer in Cambridge without the generous support of the Marshall Aid Commemoration Commission and King's College Studentship. I particularly want to thank the Marshall Scholars program for many well-planned events that allowed me to learn a lot about the UK. Additionally, I would like to acknowledge Cary Frith, Beth Clodfelter, Profs. David Drabold, Markus Böttecher, Joe Shields, John Johnson, Simon Schuler, Adam Kruas, Katy Garmany, Caitlin Casey, and Jarita Holbrook for encouraging me and supporting my efforts to do astronomy and make it more a more diverse community throughout the years before, during, and beyond my time at Ohio University. If it were not for you all, I would not have been able to obtain the Marshall Scholarship to complete this work.

Finally, last but not least, this would not be a proper acknowledgment without thanking the role that my family has played in my life. I want to thank my mom, pops, my twin Kevin, Jasmyn, Tahnda, and Darrell for not only their support and encouragement over the last half-century but also dealing with me from start to finish!

Keith A. Hawkins, *Cambridge, 9th May, 2016*

DISSECTING THE MILKY WAY WITH SPECTROSCOPIC STUDIES

KEITH AUSTIN HAWKINS

SUMMARY

In the last decade, the study of Galactic stellar populations has been completely transformed by the existence of large spectroscopic surveys including the Gaia-ESO survey (GES), the Sloan Digital Sky Survey (SDSS), the RAdial VElocity Experiment (RAVE), the APO Galactic Evolution Experiment (APOGEE), and others. These surveys have produced kinematic and chemical information for upwards of 10^5 stars. The field of Galactic astronomy consists of exploring this information to understand the Milky Way and other systems like it.

As such, the collection of studies in this thesis are focused around examining several of these surveys to dissect the structure of the Milky Way with an emphasis on the Galactic halo. I begin with an introduction including the relevant prior knowledge of Galactic structure and, in particular, the 'accreted' and 'in situ' components of the Galactic halo (Chapter 1). In the following chapters, I dissect and explore the various components of the Milky Way in several phase-spaces including age, kinematics, and chemistry.

In Chapter 2, I focus on the addressing the question of whether there is an age difference between the 'accreted' and 'in situ' components of the Galactic halo. I also discuss the development of a technique to measure chemical abundances from low-resolution stellar spectra which was used to separate the 'accreted' and 'in situ' components.

In Chapter 3, I examine the chemical nature of high-velocity stars in the RAVE survey and address the role of disk heating in the formation of the Galactic halo. I also find evidence for a sample of metal-rich high velocity stars that are currently a part of the Galactic halo but likely born in the Galactic disk.

In Chapter 4, I search for both the 'accreted' halo component and metal-rich high-velocity stars in the APOGEE survey, which samples a large volume of the Galaxy by targeting giant stars. I present evidence for the accreted halo, and a metal-poor thin disk, as well as propose a chemical-only approach to decompose the Galaxy.

In working with the various surveys in the above chapters, particularly APOGEE, it became apparent that there are sometimes metallicity calibration issues which can plague the survey. I provide two possible solutions to this which I discuss in Chapters 5 and 6.

Specifically, in Chapter 5, I propose a new set of candidate metal-poor benchmark stars which can be used to help calibrate large spectroscopic surveys. These new candidates are critical because they fill a parameter space where there is a clear lack of usable calibrators.

In Chapter 6, I use a automated stellar parameter pipeline and a careful line selection to improve and include new chemical abundances within the APOGEE survey allowing for further study of the structure of the Galaxy.

Finally, in Chapter 7, I discuss the impact of the work carried out in this thesis and present a glimpse of future prospects.

Contents

List of Figures

List of Tables

1 Introduction

On a clear, moonless, night after the sun has set, it is possible to see many celestial objects in the sky. If it is dark enough, as the ancient Greeks and Romans found, you may even find a stream of white light situated in a band across the sky. The ancient Greeks believed this band to resemble a river of flowing milk and so they called it *Galaxias*, which is a derivative of the word milk in their language. The study of this milky system continued for many millennia. However, with rather basic technology and methods progress was slow. Significant advances in our understanding of the Milky Way system was not made until after the middle ages (ending in around the 15th century). In the early 1600s, Galileo Galilei pointed the newly perfected telescope to the Milky Way and realized that it was constructed of many individual stars. Over the course of the preceding two centuries and continuing to the present day, with more powerful telescopes being built, it was discovered that the Milky Way not only consists of billions of individual stars like our sun, but also has complex structure. Fast-forwarding to today, one of the primary objectives of modern astronomy is to understand the structure of galaxies like our own and the physical processes involved in their formation and evolution. That is the topic of this Thesis.

1.1 Motivation

This work has been motivated by the desire to uncover and constrain our understanding of galaxy formation using the Milky Way as a test case. What makes the Galaxy unique is that it is the easiest system where, with state-of-the-art astronomical tools, we can obtain detailed information of not only the positions and velocities of individual stars but also their chemical fingerprint. The Milky Way is also thought to be a representative spiral galaxy in the Universe. All of these points make it a perfect testing ground, in contrast to external galaxies, for our theories of galaxy formation and evolution.

Additionally, in the last few years, we have entered an era of large-scale spectroscopic surveys which has enabled systematic and homogenous studies of many stars in the Milky Way

that was just not possible before. Therefore, on the cusp of these advances, the work discussed in this Thesis makes use of large spectroscopic surveys to answer questions about Milky Way structure and formation. This work also comes on the heels of data from the recently launched Gaia mission (Perryman et al., 2001). Gaia aims to measure the distance, tangential (or proper) motion, radial velocities, and some chemical abundances for $\sim 10^9$ stars. It is widely believed that this data will completely revolutionize the field of astrophysics. Its first set of data is scheduled to be released in summer 2016. In this context, the work presented in this Thesis is an exploration of the groundwork for chemo-kinematic analyses that can be achieved with Gaia.

In the following sections, I review the spectroscopic toolbox that I have used (section 1.2) and the background theories on Galactic structure and formation (section 1.3) required for the Thesis.

1.2 The Toolbox of Stellar Spectroscopists

In this section, I will review the role of stellar spectroscopy as a toolbox for studying the Galaxy as well as how it is utilized in this Thesis.

1.2.1 Chemical Fingerprinting

Stars, similar to our Sun, are the among the basic constituents of the Milky Way. It is believed that there are $\sim$100 billion stars in our Galaxy alone. Each star is held up against gravitational collapse by nuclear fusion at its core which, for the most part, converts H into He. However, the gas at the star's surface is mostly unchanged from its original composition. Thus, most stars have a chemical fingerprint that is unique to the environment and time in which it was born. Additionally, a star's chemical fingerprint, for the most part, does not change over its lifetime. Therefore, the chemical abundance pattern of these stars offer crucial information that can be used to inform our understanding of the formation and evolution of the Milky Way. The evolution of the chemical composition of stars in the Milky Way comes from the fact that the cores of these stars make elements heavier than Li and enrich the local environment upon their death. We can explore the chemical abundance pattern of stars across a variety of ages to probe how the Galaxy is evolving over time. However, this requires the use of many stars. This why the onset of several large spectroscopic surveys has brought stellar spectroscopy to the forefront of astrophysics.

One of the primary advantages in obtaining the spectra of individual stars is that one can measure their stellar parameters including the temperature ($T_{\rm eff}$), surface gravity (log g), and iron content ([Fe/H]) as well as the abundances of specific chemical elements. In stellar astrophysics, the measurement of chemical abundances within the atmosphere of a star is usually displayed as a logarithmic ratio of element X to element Y relative to the sun, [X/Y], such that

$$[\mathrm{X/Y}] = \log\left(\frac{N_X}{N_Y}\right)_{star} - \log\left(\frac{N_X}{N_Y}\right)_{sun}, \tag{1.1}$$

where N_X and N_Y is the number of element X and element Y per unit volume respectively. The overall stellar metallicity, denoted as [M/H][1], is related to the iron abundance, [Fe/H], and is

[1] We remind the reader that all elements except for H and He are considered 'metals' in astronomy.

always displayed relative to H. In this way, the metallicity of a star is approximated by [Fe/H][2]. The nomenclature is such that the unit volume is that which is required to encompass 10^{12} H atoms. For example, the sun has [Fe/H] = 0.00 by definition and $\log(N_{Fe})$ = 7.45 dex (Asplund, Grevesse & Sauval, 2005). Therefore, for every 10^{12} H atoms there are $10^{7.45}$ Fe atoms in the atmosphere of the sun.

The spectrum of a star's atmosphere can be used to determine its chemical fingerprint because it contains absorption lines corresponding to photons of different energies being absorbed by atoms of different elements. The prerequisite material for measuring chemical abundances in the atmosphere of stars includes: (1) a line list, which includes the collected information for the atomic transitions of elements that have absorption features in the spectrum, (2) a model atmosphere grid which defines the atmospheric temperature-pressure profile of the star, and (3) a radiative transfer code, which predicts how photons pass through the atmosphere of a star by numerically solving the radiative transfer equation. After these prerequisites are acquired, the chemical abundances of stars can be derived in following several steps:

- STEP 1: Take a spectrum of a star's atmosphere using a spectrograph. Each spectrograph will have several parameters of interest but most importantly is its wavelength coverage and resolving power, which is defined as R = $\lambda/\Delta\lambda$. In this case, $\Delta\lambda$ is the minimum separation between resolved wavelengths. In this work, I will refer to spectrographs with R $\sim$1000 – 6000, R $\sim$7000 – 18000, R $>$ 20000 as low-resolution, moderate-resolution, and high-resolution, respectively.

- STEP 2: Reduce and extract the spectrum from the raw CCD image from the telescope to its wavelength versus flux from where absorption features can be modeled and analyzed.

- STEP 3: Flux normalize the spectrum, usually by a fitting low-order polynomial and line-of-sight (or radial) velocity correct the spectrum (see section 1.2.2).

- STEP 4: Derive the stellar parameters ($T_{\rm eff}$, log g, [Fe/H]), usually done with the standard Fe-ionization-excitation balance technique or with fitting a synthetic spectrum to the data.

- STEP 5: Derive the chemical abundance of a specific element using a selection of its absorption lines. Features which are clean, strong, and unblended are often preferred.

High-resolution spectra give more precise estimates of the chemical abundances and stellar parameters because the light is more finely dispersed and thus the lines can be resolved with more detail. However, this requires significantly longer integration time at the telescope to achieve a comparable signal-to-noise ratio (SNR). This makes obtaining high-resolution spectra more expensive and difficult compared to the low-resolution regime. This is, in part, why older surveys used low-resolution spectrographs to obtain larger samples of stars in a cheaper way. Newer surveys have begun using both high- and low-resolution spectrographs. The exact implementation of Steps 4 and 5 is strongly dependent on the resolution of the spectra. For example, deriving chemical abundances from low-resolution spectra usually involves fitting or empirically calibrating (e.g. the method developed in Chapter 2) large wavelength segments while in the high-resolution case, fitting individual absorption features is more common. Finally, large spectroscopic surveys often have to make trade-offs between SNR, resolution, and sample size depending on their science goals.

[2]For historical reasons, [Fe/H] is used interchangeably with [M/H] even though they are not explicitly the equivalent.

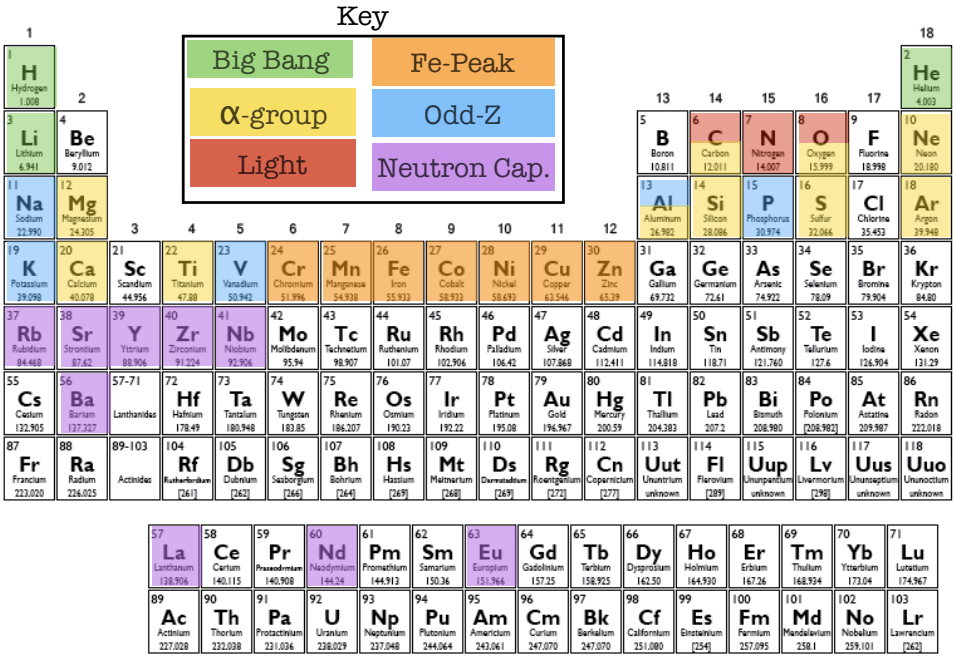

Figure 1.1 – The periodic table of elements for the stellar spectroscopic. The elements discussed in this (or relevant) work(s) are color-coded by the main elemental 'family' of the primary isotope. The production sites of these elements can be found in Table 19 of Woosley & Weaver (1995).

Once the chemical fingerprint for many stars have been derived, they can be used to study the nature of the Galaxy by exploring the chemical distributions of the Milky Way, which is part of the goal of this work. However, it is worth mentioning that measuring chemical abundances can be a very time expensive endeavor and that not all elements can be derived, in part because some elements only have very weak lines or no clean lines in the typical wavelength coverage of spectrographs. But this begs the question, which elements can we measure and which are most important?

There are 92 elements which are formed naturally and organized on a periodic table. The first three H, He, and Li, are primarily formed in the Big Bang. All of the other elements on the periodic table are formed inside, or a result of supernovae explosions, of stars. Figure 1.1 shows the periodic table of elements from the perspective of a stellar spectroscopist. The relevant elements in this work are color-coded by their 'chemical family', which is connected to the main production of the primary isotope of the element. These chemical 'families' include the:

- *Light-elements group (C, N, O):* Carbon and oxygen are made in hydrostatic burning inside high mass stars via helium nuclei, α-particle capture (e.g. Nomoto, 1984; Woosley & Weaver, 1995; Nomoto et al., 1997; Iwamoto et al., 1999). However, carbon is also made in low mass stars. Both are distributed into the interstellar medium via type II core-collapse supernovae, or winds of AGB stars but are not synthesized significantly in type Ia supernovae. On the other hand, nitrogen is created in H burning via the CNO cycle reaction ^{12}C(p, γ)^{14}N. After which nitrogen captures a proton yielding oxygen in the reaction ^{14}N(p, γ)^{15}O. This latter reaction occurs at a longer time scale than the other

reactions in the chain having the effect of depleting ^{12}C while enhancing ^{14}N. In this way, unlike carbon, the production of nitrogen is metallicity dependent.

While most elements do not change their surface abundance over the lifetime of the star, this is not the case for light elements such as CNO, which are affected by the dredge up process (e.g. Iben, 1965). In this process, the convective envelope of a star extends deep into its interior, which mixes up some of the nuclear processed material from the the core to its surface. In stars where the CNO cycle is active, the total amount of C+N+O remains constant over the lifetime of the star but their relative amounts change.

- *α-elements group (Mg, Ca, Si, Ti, S, O):* These elements are mainly produced by α-particle capture during various stages of C, He, and Ne burning inside of massive stars. These elements are then scattered into the interstellar medium predominantly by type II, core-collapse, supernovae (e.g. Woosley & Weaver, 1995; Matteucci & Recchi, 2001). While carbon is technically an α-element because it is formed from α-particle capture, its surface abundance changes due to dredge up effects (Iben, 1965), therefore it is usually classified as a light element.

- *Fe-peak (Mn, Ni, Co, Cr, Zn):* These elements are close in proximity in the periodic table to Fe, which is an element that requires energy input for (rather than yielding energy from) fusion because it has the largest average binding energy per nucleon compared to all other elements. Elements which are near the 'Fe-peak' also have high average binding energy per nucleon and thus are produced in a similar way to iron (i.e., in various stages of explosive and regular burning) and dispersed into the interstellar medium primarily via type Ia supernovae.

- *Odd-Z elements (Na, Al, K, V, P, Cu):* These elements are produced in both regular and explosive C, O, and Ne burning. Many of them can also be produced in both Type Ia and Type II supernovae. Thus, this group of elements tend to have a variety of behaviors with respect to Fe. For example, Na and Al are largely created and dispersed in Type II supernovae and thus display trends with metallicity similar to the α-elements[3]. On the other hand, Cu shows a relatively flat trend with metallicity (e.g. Reddy et al., 2003; Reddy, Lambert & Allende Prieto, 2006). Where required in this Thesis, a more detailed discussion of the production of these elements is presented.

- *Neutron capture (Sr, Y, Zr, Ba, La, Eu, Nd):* This last group of elements is produced by neutron capture and decay processes. This group is usually split into two subgroups based on the neutron flux required for the production of a given element. There is the slow neutron capture (s-process) elements (low neutron flux) and rapid neutron capture (r-process) elements (extremely high neutron flux). The s-process is thought to take place in asymptotic giant branch (AGB) stars, while the r-process is thought to take place in supernovae ejection although this is still an open question (e.g. McWilliam, 1997). Traditionally, s-process elements include Sr, Y, Zr, Ba, La, and Rb, while the r-process elements include Eu and Nd among others.

For a detailed discussion on the several production sites of the individual isotopes, which is beyond the scope of this Thesis, we refer the reader to the seminal work of Woosley &

[3]In fact, because Na and Al are thought to be created in large amount by type II supernovae, they are sometimes referred to as "mild" α-elements (e.g. McWilliam, 1997).

Weaver (1995), Samland (1998), and the annual reviews from McWilliam (1997) and Nomoto, Kobayashi & Tominaga (2013) and references therein.

1.2.2 Line-of-Sight Velocities

The spectra of stars not only provide us with the information necessary to quantify their chemical makeup but also one dimension of their velocity vector along the line-of-sight. Due to the doppler effect, spectral lines are shifted towards longer wavelengths (redshift) when a star is moving away from an observer and shifter towards shorter wavelengths (blueshift) when it is moving toward an observer. This relative change in the location of the spectral features is caused by the radial, or line-of-sight, velocity. To obtain the full 3-dimensions of the velocity vector, the radial velocity must be combined with the transverse velocity which is computed using the star's proper motion (in right ascension and declination) and distance. The transverse velocity and/or the radial velocity, to some extent, can be used to constrain the orbit of the star. Combining this information with the chemistry enables us to study Galactic structure in many dimensions.

1.2.3 The Role of Large Spectroscopic Surveys

The spectroscopic studies of the Galaxy during the late 20th and early 21st century have used the radial velocities and chemistry of up to 10 or so elements for small-to-moderate samples of stars ($\sim$100–1000 stars) to pin down Galactic structure (e.g. Norris, 1986; Edvardsson et al., 1993; Nissen & Schuster, 1997; Fuhrmann, 1998; Chen et al., 2000; Fulbright, 2000; Reddy et al., 2003; Reddy, Lambert & Allende Prieto, 2006; Venn et al., 2004; Nissen & Schuster, 2010). These studies have only contained a relatively local sample of stars and mostly probe the Galactic disk. Although, some studies were biased specifically to study the halo. It was realized that to progress our knowledge further, we would need to obtain chemical and velocity of information outside of the local bubble and increase the sample size of observed stars from $\sim 10^2$ to $\sim 10^5$.

Large spectroscopic surveys such as the Sloan Digital Sky Survey (SDSS, York et al., 2000), RAdial Velocity Experiment (RAVE, Steinmetz et al., 2006), the Apache Point Galactic Evolution Experiment public spectroscopic survey (APOGEE, Eisenstein et al., 2011; Majewski et al., 2015), and the Gaia-ESO Survey (GES, Gilmore et al., 2012; Randich, Gilmore & Gaia-ESO Consortium, 2013) have completely revolutionized the study of our Galaxy by making way for homogeneously analyzed stellar spectra for upwards of 10^5 stars. These surveys have allowed us to study the Galaxy in statistical ways (e.g. deriving the main-sequence turnoff age of the Galactic halo, Jofré & Weiss, 2011; Hawkins et al., 2014), and have enabled discovering rare objects (e.g. hypervelocity stars, Palladino et al., 2014; Hawkins et al., 2015b) among other things. This Thesis is a collection of original research projects which utilize data from each one of these surveys.

1.3 The Formation and Structure of Milky Way

In this section, I review some of the key theories of Galactic formation and structure. I note here that this review neglects the bulge of the Milky Way as it is only discussed very briefly in this work.

1.3.1 Galactic Formation Scenerios

The formation of the Milky Way is a problem that has been the subject of great interest throughout the twentieth century. In the 1950's it began to be understood that the kinematics, chemistry (only crude metallicities at that time) and ages could be combined to construct a more complete picture of Galactic formation (e.g. Roman, 1954). This combined framework led the way for a seminal paper by Eggen in 1962 (henceforth the ELS model, Eggen, Lynden-Bell & Sandage, 1962) in which it was shown that there were correlations between a star's ultraviolet (UV) excess, that is sensitive to the metal content of the star due to metal-line blanketing, and its orbital eccentricity, angular momentum and vertical velocity, usually denoted as W (see their figure 4-6). These correlations, they posited, indicated that the Galaxy was formed in a rapid ($\sim$220 Myr) collapse of a protogalactic gas cloud which formed a spherical halo first and spun up into a centrifugally supported disk due to conservation of angular momentum at later times. While many of the details of this top-down theory have been updated or changed over the years to better fit observational data, it still forms the basis for modern discussions on the formation of the Milky Way.

About a decade after classic ELS model was proposed, there were criticisms that the collapse timescale was too short (e.g Isobe, 1974). This and other criticisms of the model led to 'modified' ELS scenarios, which better accounted for the data at the time. For example, the idea of 'rapid' collapse was changed to an extended collapse period which was required due to the slow dissipation rate of turbulent gas clouds as a result of supernovae feedback and metal-line cooling (e.g. Yoshii & Saio, 1979; Wyse & Gilmore, 1988). These papers suggested a 2-3 Gyr collapse timeframe instead of the Myr timescales suggested by ELS.

Around the same time as new 'add-ons' to the ELS model were being thought up, a completely different idea of Galactic formation was being developed. It was observationally shown by Searle & Zinn (1978), or SZ for short, that globular clusters located in the halo of the Milky Way have a wide dispersion in mean metallicity and there seems to be little to no gradient in their metallicity as a function of distance from the Galactic center. This, they argued, suggested that the Galactic halo may have formed from many relatively small independent systems which merged together. Therefore, the metallicity of these small systems would be dependent on their star formation histories, which is independent of one another. In this way, a wide metallicity range and no significant radial metallicity gradient would be expected. This idea was in contrast to the ELS model in that instead of constructing the Galaxy from a large protogalactic gas cloud, it would have formed through the coalescing of the smaller systems.

Since these seminal works, there have been several models of Galactic formation which come in two forms: (1) top-down models (similar to ELS) and (2) bottom-up models (similar to SZ). The top-down models of Galaxy formation tend to form galaxies, like the Milky Way, from large structures which collapse into several components. On the other hand, bottom-up formation models of Galactic formation generally all have one common feature, little sub galactic systems are the basic building block for the Milky Way.

With the rise of numerical simulations in the context of galaxy formation, it has been possible to make more sophisticated models with predictions that can be observationally tested with large samples of Milky Way stars. The most comprehensive numerically simulated model to date is the bottom-up Dark-Energy-Cold-Dark-Matter (ΛCDM) model. The ΛCDM model has the significant advantage that it is a physically motivated cosmological framework which encompasses information about the Universe's initial conditions (e.g. baryonic, dark matter,

and dark energy densities). Under this model, galaxies like the Milky Way, are formed in a hierarchical way. That is to say that small dark matter halos form first and merge via dissipationless gravitational processes after which baryonic systems (e.g. stars and galaxies) form inside (White & Rees, 1978). The first numerical simulation under the ΛCDM paradigm was done in the mid 1980s (Davis et al., 1985). Over the years these simulations have become more sophisticated and include more input physics.

Modern ΛCDM simulations (e.g. Cooper et al., 2010; Vogelsberger et al., 2014) have made several successful predictions in regards to Galactic formation. For example, the simulations tend to build galaxies through hierarchical merging events and thus they predict that if the Milky Way were created in this way that there should be significant substructure in the Galactic halo that is a result of the debris from these events. This debris has been observed in the form of tidal streams (Ibata, Gilmore & Irwin, 1994; Belokurov et al., 2006, 2007). Despite all of the successes of ΛCDM it still has its problems. For example, it predicts hundreds to thousands of dwarf galaxies around the Milky Way system but observations have only detected ∼40–50 or so satellites (Klypin et al., 1999). This discrepancy which was pointed out in the late 1990s is often referred to as the 'missing satellite problem' and is still unresolved. However, there have been a significant advances towards solving this problem through the detection of new ultra-faint dwarf galaxy systems in recent years (e.g. Koposov et al., 2015). Additionally, many of the details of Galactic formation in this model, such as the importance of internal processes (e.g. radial migration, which acts to move stars from one orbital radius to another) or external processes (major and/or minor merging events) are still open questions. Other open questions from this model include: whether the Milky Way is made of many low-mass systems or a few larger mass systems, the global star formation rate within the Galaxy, and the extent of substructure beyond the gross components of the Galaxy, among many others.

Often both top-down and bottom-up models are used in order to fully describe the structure that we see in the Galaxy today.

1.3.2 Galactic Structure

From an observational standpoint, the classical picture of the Milky Way reveals a rather complex galaxy, with four primary "internal" components – the bulge, the thin disk, the thick disk and the halo, and one "external" component – the accreted material. Nowadays, these components form the basis of any attempt to model, to simulate and to understand the formation and evolution of our Galaxy (see e.g. the reviews of Majewski, 1993; Freeman & Bland-Hawthorn, 2002; Ivezić, Beers & Jurić, 2012, and references therein). They are displayed in a cartoon diagram of our Galaxy in figure 1.2. These components are usually defined by the phase spaces in which we observe them (spatially, kinematically, and chemically). However, there is an ongoing debate as to whether these components are truly distinct objects or a part of a continuous sequence of an evolving galaxy (e.g. Bovy, Rix & Hogg, 2012; Rix & Bovy, 2013). In the following subsections, I review each component independently except for the Galactic bulge since it is not covered significantly in this work.

The Thin Disk

Classically, the Galactic disk is often split into a thin disk and thick disk component (e.g. Gilmore & Reid, 1983; Freeman & Bland-Hawthorn, 2002; Rix & Bovy, 2013). The formation

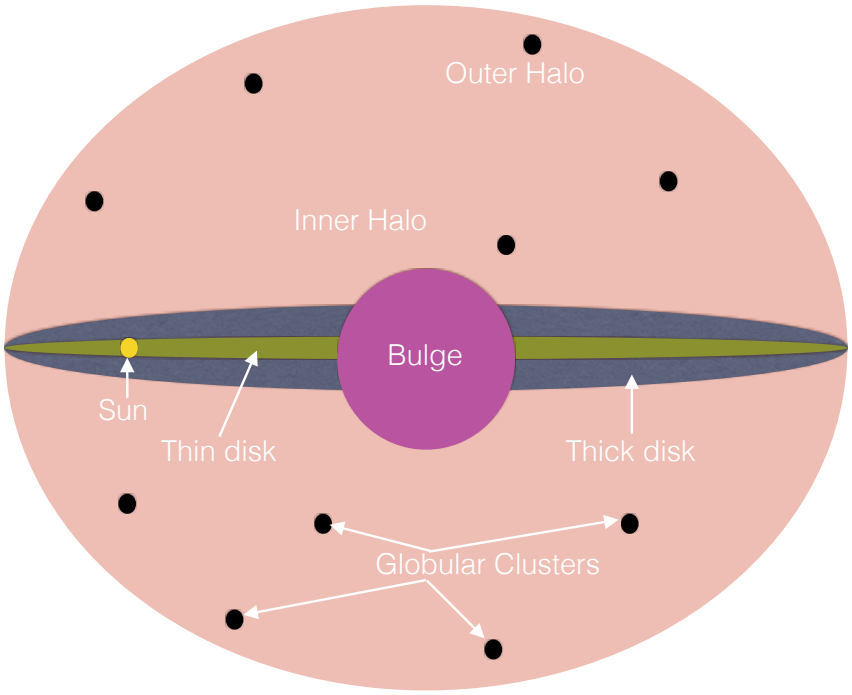

Figure 1.2 – A cartoon of Galactic structure including the thin disk, thick disk, bulge, and halo(s). Note this is not drawn to scale but is used as a basic representation of Galactic components.

of the thin disk is thought to be the final stage of dissipative collapse. Additionally, the gas, which would, at later times, create the thin disk, may have been smoothly accreted from satellite systems that collided with the Galaxy $\sim$10 Gyr ago. The same (set of) satellite system(s) may also be responsible for formation of the thick disk (e.g. Walker, Mihos & Hernquist, 1996; Binney & Merrifield, 1998; Wyse, 2008).

It is defined spatially by an exponential power law with a small (0.30 kpc) vertical scale height and large (3.4 kpc) radial scale length (e.g. Bensby et al., 2011; Cheng et al., 2012; Bovy et al., 2012; Haywood et al., 2013). Kinematically the thin disk stars follow near circular, co-rotational orbits with a low velocity dispersion (e.g. Edvardsson et al., 1993; Reddy et al., 2003; Kordopatis et al., 2013b; Rix & Bovy, 2013). Chemically, the thin disk is thought to extend over a metallicity range of +0.1 $<$ [Fe/H] $<$ –0.70 dex and is near solar values in the α-elements (e.g. Bensby, Feltzing & Oey, 2014). While, the thin disk is thought to contain stars across all ages, it is dominated by relatively young (8 Gyr) stars (e.g. Haywood et al., 2013).

The Thick Disk

The thick disk was initially found to be separate from the thin disk on the basis of the spatial distribution of its stars (e.g. Yoshii, 1982; Gilmore & Reid, 1983). It is thought to form potentially through a variety of processes including: satellite heating, accretion, or merging induced star formation, secular disk heating, radial migration, and others (for a review of these mechanism we refer the reader to the review of Freeman & Bland-Hawthorn, 2002; Rix & Bovy, 2013, and references therein). However the importance of each of these mechanisms in the

formation and assembly of the thick disk is still poorly understood. In fact, there are at least eight separate models of thick disk formation which range from accretion of thick disk material directly, violent thin disk heating by satellites, and to rapid dissipation. The details of the formation of the thick disk are still an active area of research today (e.g. Wyse, 2008).

The thick disk is defined spatially by an exponential power law with a larger vertical scale height (0.9 kpc) and smaller radial scale length (1.8 kpc) compared to the thin disk (e.g. Bensby et al., 2011; Cheng et al., 2012; Bovy et al., 2012; Haywood et al., 2013). Kinematically, thick disk stars co-rotate with the disk, albeit with a smaller rotational velocity and overall have hotter orbits than their thin disk counterparts (e.g. Edvardsson et al., 1993; Reddy et al., 2003; Bensby et al., 2005; Haywood et al., 2013; Kordopatis et al., 2013b). Chemically, it is thought to be distinct from the thin disk component in the [α/Fe]-metallicity plane with a high [α/Fe] signature (e.g. Bensby, Feltzing & Oey, 2014; Nidever et al., 2014; Recio-Blanco et al., 2014). The thick disk has a metallicity that extends significantly lower than the thin disk, and can extend down to well below [Fe/H] $<$ –1.0 dex (e.g. Beers et al., 2002). The thick disk is also thought to be older than the thin disk (e.g. Haywood et al., 2013; Masseron & Gilmore, 2015).

The Halo

The Galactic halo is thought to naturally form very early on from a mixture of dissipative collapse and accretion (ELS, SZ, Ibata, Gilmore & Irwin, 1994). As such most of its stars are very old (Jofré & Weiss, 2011; Hawkins et al., 2014). In this way, the halo formation is a combined ELS and SZ formation model.

It is spatially defined by a power-law with an index of approximately –3.5 (e.g. Helmi, 2008). As noted in Fig. 1.2, the Galactic halo may have an 'inner' component (dominated by stars that have galactocentric radii less than 15 kpc) which is more metal-rich and an 'outer' component (e.g. Carollo et al., 2007, 2010). However, this dual-halo model is still debated in the literature (e.g. Schönrich, Asplund & Casagrande, 2011, 2014). This Thesis will mostly focus on the inner halo.

Kinematically, the (inner) Galactic halo is thought to be pressure supported, have a small net prograde rotation (e.g. Carollo et al., 2010), and contain the highest velocity stars (e.g. Hawkins et al., 2015b). Chemically, the Galactic halo is predominantly metal-poor (e.g. Schlesinger et al., 2012) and enriched in the α-elements (e.g. Ishigaki, Chiba & Aoki, 2012). The (inner) Galactic halo has been shown to split into two chemically distinct components. Several recent studies have reported the presence of α-poor stars in halo samples (Nissen & Schuster, 2010, 2011; Schuster et al., 2012; Ramírez, Meléndez & Chanamé, 2012; Sheffield et al., 2012; Bensby, Feltzing & Oey, 2014; Jackson-Jones et al., 2014; Hawkins et al., 2014, 2015a). These studies have shown that the α-poor sequence is distinct in kinematics, ages, and other chemical elements such as C, Na, and Ni compared to the α-rich sequence. It is thought that the α-poor sequence is assembled through the accretion of satellite galaxies. Whether this material is a result of selection effect, whether it may come from one or many systems, and its age distribution are all still open questions.

A summary of properties of these Galactic components in several phase-spaces, including age, density profile, velocity, and chemistry, discussed above can be found in Table 1.1.

Table 1.1 – Properties of Galactic Components.

Property	Thin Disk	Thick Disk	Halo
Density Law	Exponential[a]	Exponential[a]	Power law[b]
Scale Length[b] (kpc)	3.4	1.8	...
Scale Height[c] (kpc)	0.3	0.9	...
Power Law Index[a]	...	...	-3.5 ± 0.5
(V_r,V_θ,V_Z)[d]/ (km s^{-1})	(–2, +215, 0)	(+2,+180,–4)	(7, 15,–7)
Velocity Dispersion[d]/(km s^{-1})	(30, 20, 18)	(61, 45, 44)	(160, 119, 110)
(Mean [Fe/H], σ[Fe/H])[d]	(–0.10, 0.18)	(–0.45, 0.26)	(–1.25, 0.56)
Age (Gyr)	0–8[e]	8–12[d]	> 10[a]

NOTES: ([a]) denotes values taken from Jurić et al. (2008), ([b]) denotes parameters that have been taken from Cheng et al. (2012), ([c]) denotes parameters that have been taken from Helmi (2008), ([d]) denotes values taken from Table 1 of Kordopatis et al. (2013b). ([e]) denotes values taken from Haywood et al. (2013).

1.3.3 Decomposition of Galactic Components Using the Toolbox

Decomposing these components chemo-kinematically, particularly in the region of metallicity space where they overlap (–1.2 < [Fe/H] < –0.60 dex) is a significant challenge yet critical to understand the formation and assembly of the Galaxy. The problem arises with the fact that the original dynamical and spatial distributions of stars are perturbed over time, potentially erasing the memory of the original sites. Kinematical heating and spatial disruption can be produced via several processes, such as bar resonances and radial mixing, clumpiness in the gas, and minor mergers, to name a few (e.g. Minchev et al., 2012; Rix & Bovy, 2013; Haywood et al., 2013; Sanders & Binney, 2013, 2015). Furthermore, dynamical and spatial distributions depend heavily on the distance of the stars, which is subject to large uncertainties for the majority of them (e.g. Binney, 2013, and references therein). Thus, matching models and simulations to observational data continues to be one of the fundamental challenges in Galactic astronomy today.

Despite this, the current mode through which Galactic components are decomposed is through kinematics via the Toomre diagram with aid of the [α/Fe]-[Fe/H] plane. The left panel of Figure 1.3 shows an illustration of the Toomre diagram which plots the quadrature sum of the vertical (denoted by W) and radial (U) velocities as a function of the velocity along Galactic rotation (V). These velocities are relative to the local standard of rest (LSR). This diagram or a similar probabilistic kinematic Galactic component decomposition techniques are widely used in the literature (e.g. Bensby, Feltzing & Lundström, 2003; Venn et al., 2004; Nissen & Schuster, 2010; Schuster et al., 2012; Ishigaki, Chiba & Aoki, 2012; Bensby, Feltzing & Oey, 2014; Hawkins et al., 2015b). The power of the Toomre diagram lies in the fact that the canonical thin disk, thick disk, and halo have increasingly hotter kinematics (i.e., each component lies in an increasingly larger constant velocity circle on the Toomre diagram) and thus are further elevated in the diagram. The fundamental drawback to this diagram is the need for accurate proper motion and distances to fully resolve the 3D velocity vector. This may be possible in the post-Gaia era, but for now, we can only constraint the 3D velocity vector for very few stars.

The [α/Fe]-metallicity plane (a cartoon version of this is shown in the right panel of Figure 1.3) is another approach to decompose the Galactic components. Under this scheme, a given

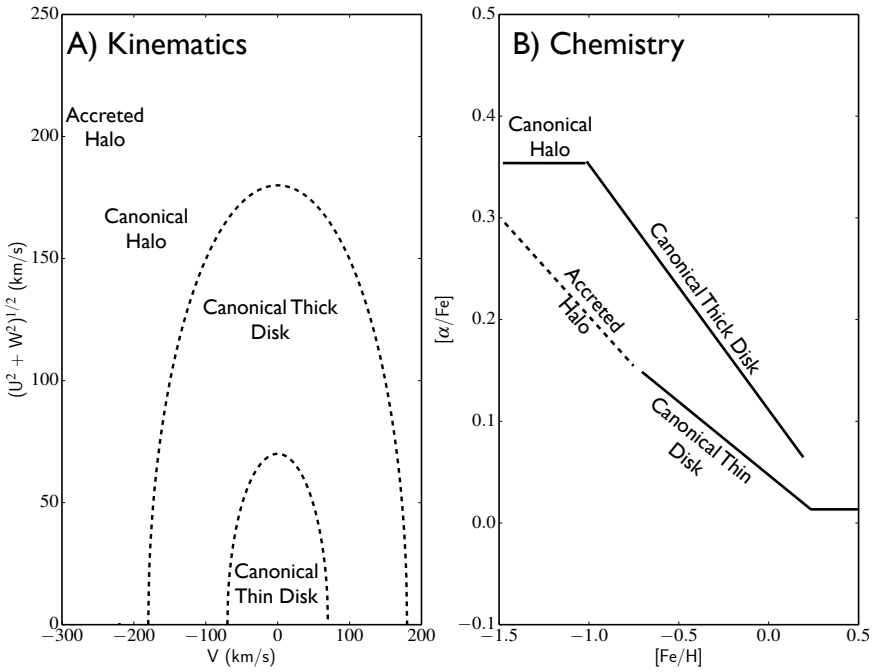

Figure 1.3 – A) A cartoon illustration of the decomposition of the Galactic components along the Toomre diagram which plots the quadrature of the radial (U) and vertical (W) velocities as a function of the velocity along rotation (V). All velocities in the Toomre diagram are relative to the LSR. (B) A cartoon illustration of the decomposition of the Galactic components along the [α/Fe]-metallicity plane. Taken from Hawkins et al. (2015a).

stellar population is marked by the chemical distribution of the medium from which the stars formed. This distribution is principally defined by the initial mass function of the previous generation of stars that enriched the gas, the star formation rate, and the different yields from the nuclear reactions.

1.3.4 Outstanding Problems with Galactic Structure and Formation

Despite a steady effort in the last fifty years to develop a complete working theory of Galactic structure and formation, there are still several outstanding problems which arise from new discoveries of substructure and an incomplete understandings of the physical processes involved in both stellar structure and galaxy formation which have been alluded to in the previous sections. Some of the open questions (OQs) which have motivated or are addressed in this work are:

1. What is the age-metallicity relationship of the 'in situ' and 'accreted' Galactic halo components suggested in Nissen & Schuster (2010)? Are they the same or different?

2. Is the 'accreted' halo of Nissen & Schuster (2010) due to selection effects?

3. Is there significant disk debris in the stellar halo?

4. To what extent are the components (thin disk, thick disk, bulge, 'in situ' halo, and accreted halo) chemically distinct?

5. What are the best ways to decompose the Galactic components?

1.4 This Thesis

This Thesis is a collection of projects which are centered on the theme of dissecting different parts of Galactic structure using large spectroscopic surveys. In particular, the Thesis will explore some of the OQs discussed in section 1.3.4.

- It begins in **Chapter 2**, by addressing the question of whether there is an age difference between the 'accreted' and 'in situ' components of the Galactic halo. It also presents the development of a technique to measure chemical abundances from low-resolution stellar spectra. This chapter addresses OQ1.
- In **Chapter 3**, I examine the chemical nature of high-velocity stars in the RAVE survey as a means to search for disk debris in the stellar halo. This chapter begins to address processes that may 'blur' boundaries between the Galactic disk(s) and halo(s). This chapter addresses OQ3.
- In **Chapter 4**, I search for both the 'accreted' halo component and metal-rich high-velocity stars in the APOGEE survey, which samples a large volume of the Galaxy by targeting giant stars. I present evidence for the accreted halo, and a metal-poor thin disk, as well as propose a chemical-only approach to decompose the Galaxy. In this chapter, it was realized that APOGEE, and likely other large surveys, are plagued by metallicity calibration problems. This chapter addresses OQ2, OQ4, and OQ5. This chapter also raises new questions regarding how to improve metallicity calibration of future surveys.
- As a result of the metallicity calibrations problems described in chapter 4, in **Chapter 5**, I propose a new set of candidate metal-poor benchmark stars which can be used to help calibrate large spectroscopic surveys. These new candidates are critical because they fill a parameter space where there is a clear lack of usable calibrators. This chapter addresses questions raised in Chapter 4.
- In **Chapter 6**, I use an automated stellar parameter pipeline and a careful line selection to improve and include new chemical abundances within the APOGEE survey allowing for further study of the structure of the Galaxy. This chapter also addresses questions raised in Chapter 4.
- Finally, in chapter **Chapter 7**, I collect and summarize the achievements of this Thesis and discuss its recommendations together with a small discussion on future projects.

2

On the Relative Ages of the α-rich and α-poor Halo Populations

This chapter reproduces the paper: *"On the ages of the α-rich and α-poor populations in the Galactic halo',* **Hawkins, K.**, Jofré, P., Gilmore, G., Masseron, T, 2014, MNRAS, **445,** 2575.

The author's contribution to the chapter includes: selection of sample, design and technical development of the spectral index approach used in this work to derive [α/Fe] abundance ratios, execution of the several validation tests, analysis of all results including measurement of turnoff $T_{\rm eff}$ from two isochrone sets and ages for the α-rich and α-poor samples, and production of the original manuscript.

Abstract

In this chapter, I study the ages of α-rich and α-poor stars in the halo using a sample of F- and G-dwarfs from the Sloan Digital Sky Survey (SDSS). To separate stars based on [α/Fe], we have developed a new semi-empirical spectral-index based method and applied it to the low-resolution, moderate signal-to-noise SDSS spectra. The method can be used to estimate the [α/Fe] directly providing a new and widely applicable way to estimate [α/Fe] from low-resolution spectra. We measured the main-sequence turnoff temperature and combined it with the metallicities and a set of isochrones to estimate the age of the α-rich and α-poor populations in our sample. We found all stars appear to be older than 8 Gyr confirming the idea that the Galactic halo was formed very early on. A bifurcation appears in the age-metallicity relation such that in the low metallicity regime the α-rich and α-poor populations are coeval while in the high metallicity regime the α-rich population is older than the α-poor population. Our results indicate the α-rich halo population, which has shallow age-metallicity relation, was formed in a rapid event with high star formation, while the α-poor stars were formed in an environment with a slower chemical evolution timescale.

2.1 Introduction

Interestingly, inner halo stars seem to have two chemical patterns: a classical one with [α/Fe] $\sim$ +0.40 which is related to the product of star formation in the large initial collapsing proto-galactic gas cloud (often thought of as the *in-situ* population); and another one with [α/Fe] $\sim$ +0.20, which is related to the formation of stars in an environment of lower star formation rate, typically in smaller gas regions (e.g. Nissen & Schuster, 2010, hereafter N10). The latter are attributed to have extra-galactic origins that were accreted onto the Milky Way after the formation of the main population (i.e. *accreted* stars). These two populations are commonly referred to as "α-rich" and "α-poor" (Nissen & Schuster, 2010), which have been subject of interest among other studies (Ramírez, Meléndez & Chanamé, 2012; Sheffield et al., 2012). These two populations have been extensively studied in a series of papers by Schuster & Nissen. They have used a sample of high resolution and high signal-to-noise ratio (SNR) spectra of halo stars to show that these two populations are distinct in kinematics and abundances of α-elements (N10), but indistinguishable from other chemical abundances such as Li and Mn (Nissen & Schuster, 2011, 2012). One interesting question arises with the findings of N10: do the α-poor and α-rich populations have the same age and/or is there correlation between age and metallicity? Determining the age differences between these two populations will help distinguish between the formation and assembly timescales of the Galactic halo.

Schuster et al. (2012) attempted to answer this question by finding that the α-poor stars in their sample are $\sim$ 2-3 Gyr younger than the α-rich population. This is in favor of the models of Zolotov et al. (2009, 2010). Yet, the recent simulations of Font et al. (2011) found that in situ stars can be as much as 3-4 Gyr younger than the accreted population. Schuster et al. (2012) argued that their α-rich and α-poor populations can be explained by a scenario where an initial disk/bulge formed in a monolithic collapse producing the α-rich population. At later times, the α-rich stars in the primeval disk were scattered into the halo via merging events that subsequently populated the α-poor component of the halo. However, the conclusions of Schuster et al. (2012) were drawn from only 9 stars lying in the metallicity range of -0.4 $<$ [Fe/H] $<$ -1.40 dex. This made us wonder whether a difference in age between α-poor and α-rich can also be found using the data from the Sloan Digital Sky Survey (SDSS, York et al., 2000), which contains thousands of halo stars extending the metallicity domain towards much lower metallicities compared to Schuster et al. (2012). Although the spectra from SDSS have much lower resolution, it is still possible to rank the metal-poor stars in α-abundance space.

Most of the current methods developed for measuring α-abundances with low-resolution spectra attempt synthetic spectral matching (e.g Lee et al., 2011). In these methods, a grid of synthetic spectra is constructed with relatively fine spacing in [α/Fe] and degraded to low-resolution. Other methods (e.g. Franchini et al., 2010, 2011), use a set of Lick indices to measure the [α/Fe]. Franchini et al. (2011) determined the [α/Fe] of a sample of F, G, and K stars observed with SDSS within $\pm$ 0.04 dex (accounting for the internal errors only). These methods heavily rely on having a good representation of real spectra through a synthetic grid of spectra and fairly well determined stellar parameters. The primary disadvantage to those methods, is that the estimated [α/Fe] is strongly affected by the stellar parameter uncertainties because of the degeneracies that exist between the stellar parameters and the [α/Fe]. These factors make estimating [α/Fe] at low metallicity extremely difficult. We developed a new method which moves beyond the grid matching techniques, of current methods by defining an index, with the aid of a synthetic grid of spectra, which is computed using only the observed

spectra. In this way our method is a semi-empirical way to estimate [α/Fe]. Using this method, we can rank our sample based on their α-abundance in a more model-independent way than the current methods. With this method, we aim to measure the age-metallicity relation of α-rich and α-poor halo field stars, separately.

Due to poor distance estimates, we did not attempt to determine ages with the standard isochrone fitting technique (for a discussion on the method consult, Soderblom, 2010) which was also employed by Schuster et al. (2012). The large number of stars in our sample allows us to group stars in metallicity and determine the age of that population precisely, provided that there is a single coeval dominant population (Unavane, Wyse & Gilmore, 1996; Schuster et al., 2006; Jofré & Weiss, 2011). This way of determining ages relies on using the colour (or temperature) of the main sequence turn-off of the population, which presents a sharp edge in the temperature distribution. By comparing the turn-off temperature of an α-rich population at a certain metallicity and an α-poor population of that metallicity, we can quantify the age difference between those populations. That age difference (if any), using a much larger sample of stars and a larger metallicity coverage, provides clues as to when the accreted stars of the inner halo formed relative to the in-situ ones. That information is valuable for constraining theoretical models of the Milky Way formation.

This chapter is organized in the following way: In section 2.2, we define the sample of SDSS halo stars for which we estimated the α-abundances and ages. In section 2.3, we describe our new method to categorize low-resolution spectra based on their α-abundances in the regime of the Galactic halo. In section 2.4, we validate our method. In section 2.5, we employ the method to split our sample into a α-rich and α-poor population for which we determine the ages, and their errors in each population. In section 2.6, we discuss the results and their implications for the formation of the Galactic halo. Finally, we summarize our findings in section 2.7.

2.2 Data

This study made use of the SDSS/DR9 (Ahn et al., 2012) and the SEGUE database (Yanny et al., 2009). SEGUE/SDSS provides approximately half a million low-resolution (R $\sim$ 2000) spectra which have stellar parameters estimates from the SEGUE stellar parameter pipeline (SSPP, Lee et al., 2008a). The spectra have wavelength coverage of 3900 – 9000 Å. We are interested in halo F- and G-type dwarfs, which allows us to determine the location of the turnoff. We selected these dwarf stars via a colour cut requiring the de-reddened $g - r$ colours to be in the range: $0.1 < (g - r)_0 < 0.4$ mag. We further required the SNR achieved to be at least 40 (see section 2.3.6). To maximize the number of halo stars while deselecting other Galactic components we focused on the metallicity below –0.80 dex and further required the absolute Galactic latitude, |b|, to be larger than 30 degrees. While we expect some contamination from the thick disk in the most metal-rich bin, given the metallicity distribution function of Kordopatis et al. (2013b), it is likely that our sample is dominated by halo stars. However, accurate distances and proper motions would be needed to fully resolve the space motion of the stars to study the contamination fraction.

We made additional cuts on the adopted SSPP parameters such that they are within the stellar parameter range defined in section 2.3.4. Finally, we co-added any duplicated spectra to increase the SNR. Our final sample contains 14757 unique objects. A colour-colour diagram of

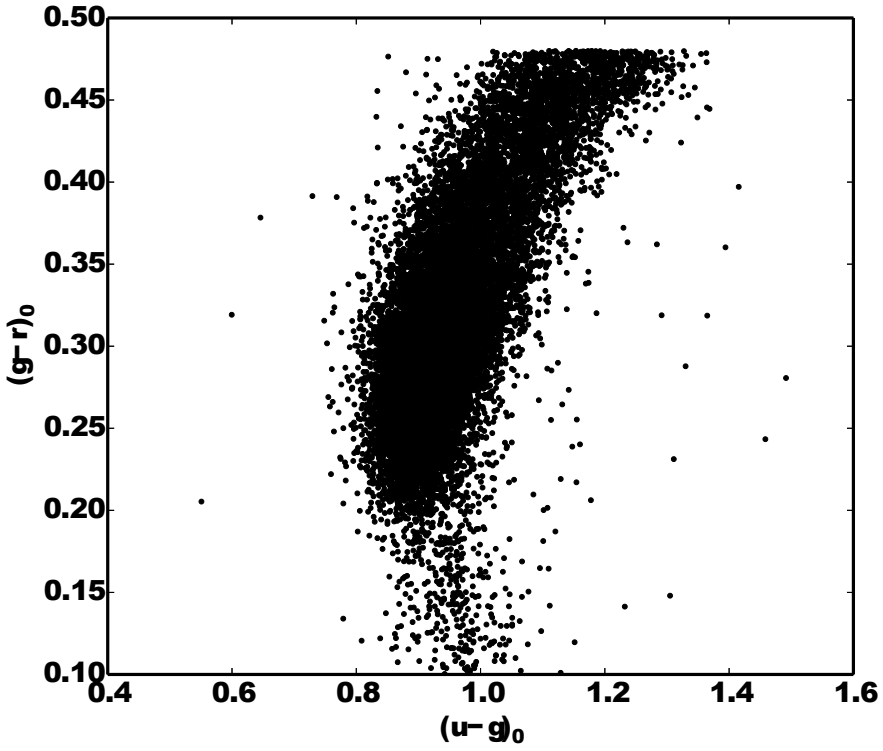

Figure 2.1 – The de-reddened colour-colour diagram of our F-, G-type dwarf sample from SDSS.

the sample can be found in Figure 2.1. The $(g-r)_0$ colour is directly related to the temperature of the star. Thus, Figure 2.1 illustrates the main-sequence F- and G-dwarf stars of our sample are plentiful until $(g-r)_0 \sim 0.2$ mag, which is the approximate location of the turnoff. Above this temperature, i.e. smaller $(g-r)_0$ colours, are likely blue stragglers. Given the SNR cut and the fact that we select dwarfs; our sample is limited to stars near the sun and thus the inner halo.

2.3 A Method to Estimate α-Abundances

2.3.1 Grid of Synthetic Spectra

We used a grid of synthetic spectra to develop and test our spectral-index method. In the grid, α-enhancement is achieved by increasing (or decreasing) in lockstep the individual α-elements (Ca, Ti, Si, Mg, O) from their solar-scaled values. The synthetic spectra make use of the 1D LTE MARCS model atmospheres of Gustafsson et al. (2008a) which have a variety of α-abundances. The synthetic grid was created using the Turbospectrum synthesis code (Alvarez & Plez, 1998; Plez, 2012) which uses the line broadening treatment described by Barklem & O'Mara (1998). Solar abundances were taken from Asplund, Grevesse & Sauval (2005). Atomic lines used by Turbospectrum are sourced from VALD, Kupka & Ryabchikova (1999), Hill et al. (2002), and Masseron (2006). Line-lists for the molecular species are provided for

CH (T. Masseron et al. 2014, in press), and CN, NH, OH, MgH and C2 (T. Masseron, in prep); the lines of SiH molecules are adopted from the Kurucz linelists and those from TiO, ZrO, FeH, CaH from B. Plez (private communication). Microturbulence velocity for each spectrum were estimated using a polynomial relationship (Bergemann et al., in preparation) between microturbulence velocity and surface gravity developed for the Gaia-ESO Survey (Gilmore et al., 2012). The final grid covers 3000 K $\leq T_{\rm eff} \leq$ 8000 K in steps of 200 K, 0.0 $\leq$ log g $\leq$ 5.0 in steps of 0.2 dex, and -3.0 $\leq$ [Fe/H] $\leq$ +1.0 in steps of 0.1 dex and -0.1 $\leq$ [α/Fe] $\leq$ +0.4 dex in steps of 0.1 dex. The synthetic grid has only been used to provide a starting point to inform our placement of spectral bands which are sensitive to [α/Fe].

2.3.2 Spectral-Index Method (SIM)

Our aim is to classify stars as α-rich or α-poor on the basis of an index that is relatively insensitive to stellar parameters. Following similar methods, often employed when studying stellar populations in other galaxies (e.g. Thomas, Maraston & Bender, 2003), we used a spectral index which was designed to be very sensitive to the enhancement in the [α/Fe]. This allowed us to use a simplistic approach to find the α-abundances using low-resolution SDSS spectra. The index was built with a combination of (1) spectral bands that are sensitive to α-abundances and (2) control bands whose response to the stellar parameters mimic the response function of the α-sensitive bands. All spectral bands must be large enough as to not be dominated by noise, yet not too large to be dominated by broad structures in the spectrum. Since we are interested primarily in [α/Fe], we only choose bands which are sensitive to α-abundances to be the main driver of our index diagnostic. We employed a semi-automatic method to explore the synthetic spectral grid to find moderate-size (15 Å$<$ band width $<$ 80 Å) spectral bands. We found five bands that are sensitive to the α-abundances (listed in the top part of Table 2.1). We combined these bands in a linear way to obtain an index sensitive to [α/Fe].

The control bands, on the other hand, were found via an iterative process by systematically scanning a grid of possible control bands. A good control band is one that minimizes the scatter in the index over a range of stellar parameters while maximizing the mean difference between the index at [α/Fe] = 0.0 dex and [α/Fe] = +0.4 dex. We found three control bands, whose wavelength ranges are listed at the bottom of Table 2.1. Figure 2.2 shows two synthetic spectra, one with solar-scaled α-abundances (black solid line) and the other α-enhanced (green dotted line). The spectral regions are designated with red dashed lines corresponding to control bands and blue solid lines for α-sensitive bands.

With the set of spectral bands defined in Table 2.1, we define our α index diagnostic by:

$$\text{Index} = \frac{\text{5Mgb+4KTi+3KSi+KCa+K1}}{\text{CB1+CB2+CB3}}. \tag{2.1}$$

The weights in the equation are motivated by the line-strengths of the α-sensitive bands, and were determined after trying several combinations. The proposed method differs from current methods which rely on a synthetic grid to model out the effects of the stellar parameters (e.g. Thomas, Maraston & Bender, 2003; Franchini et al., 2010, 2011). The advantage of our method is that we can use the spectrum alone to estimate the [α/Fe] with relatively little effect from the uncertainties in the stellar parameters provided they are within the stellar parameter range defined in section 2.3.4 below.

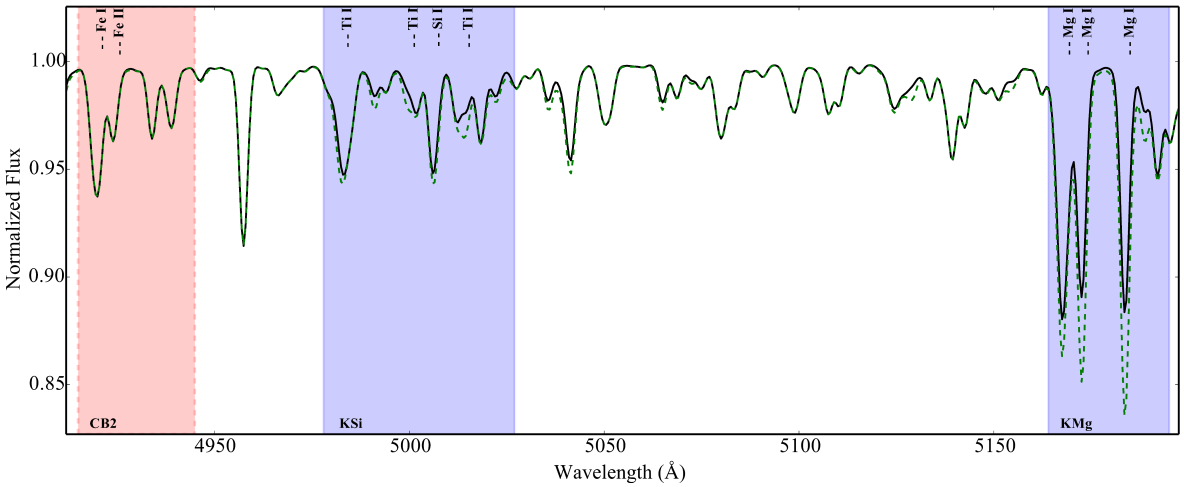

Figure 2.2 – Illustration of the KSi and Mgb (blue shaded regions), CB1 (red shaded region) spectral bands for an α-rich (green dotted) and α-poor (black solid) spectra with T_{eff} = 6200 K, log g = 4.4 dex, and [M/H] = -1.50 dex.

Table 2.1 – Spectral Bands defined in the Index.

Band	λ_i (Å)	λ_f (Å)
KTi	4510	4591
KSi	4978	5027
Mgb	5164	5195
KCa	5258	5274
K1	6148	6172
CB1	4915	4945
CB2	5225	5275
CB3	5390	5430

From a physical point of view, the numerator of the index is defined by spectral bands that are centred near the spectral features of the α-elements. Therefore, an increase in the α-abundance causes an increase in the strength of the α-sensitive spectral bands. An example of this can be seen in the KSi spectral band in Figure 2.2 which is centred on the a series of Ti and Si features. The control bands (e.g. CB1) in the denominator are centred near Fe-peak elements (mostly Fe spectral features) yet have very similar transition properties (e.g. oscillator strength and excitation potential) as the α-sensitive bands. As a result of this, the index tracks α-abundances divided by Fe-peak abundances while simultaneously controlling for the stellar parameters. We note that the CB2 and KCa bands overlap. While the Fe and Cr lines in the CB2 band overlap in wavelength space with the KCa band, the response of the CB2 band to the stellar parameters is different from the α-sensitive lines in the KCa band. Tests have shown that excluding the overlapping KCa band region from the CB2 band increases the scatter in the index at high α-abundance by a factor of 1.4 leading to a less precise estimate.

2.3.3 Processing Spectra

Synthetic and object spectra were preprocessed before searching for and measuring spectral features. All spectra were preprocessed in the same way so that it is possible to compare them directly. We applied this method to the SDSS spectra and as such their spectral parameters (e.g. resolution, etc.) defined the preprocessing parameters. We started by converting the wavelength scale of all spectra to an air-based system. Synthetic, and validation spectra were degraded to a resolution of 2,000 using a Gaussian kernel. All spectra were resampled to 0.5 Å pixels over a wavelength range of 4000 – 7000 Å.

We defined the local continuum via a boosted-median pseudo-continuum (BMC, Rogers et al., 2010). This method is defined by taking a window around any particular wavelength and setting the continuum to be at a prescribed percentile of the fluxes within the window. The BMC method is based on two parameters: (1) the width of the window around a given wavelength and (2) the percentile of the flux which defines the pseudo-continuum. We started by assuming the parameters used in Rogers et al. (2010), a window of 100 Å with a percentile of 90% . The effect of the choice of these parameters is analyzed in detail in section 2.3.7.

2.3.4 Performance of the Index on Synthetic Spectra

We are interested primarily in F-, G-, and K-dwarf stars and thus we restricted the stellar parameters to:

- 5000 K $\leq$ T_{eff} $\leq$ 7000 K
- log g $\geq$ 3.5 dex
- -2.0 dex $\leq$ [M/H] $\leq$ 0.0 dex

Selecting warm stars means that we avoided significant molecular features that would require a more careful calibration in the index. Therefore, we required that the effective temperature must be at least 5000 K. However, if the temperature is too high, the lines we need for our diagnostic will be weaker and thus we set an upper limit in temperature at 7000 K, potentially excluding any very young metal-poor stars. We required the metallicities to be above -2.0 dex because below that limit it can be difficult, especially at high temperatures, to estimate the α-abundance given the lack of strong lines (for more discussion see section 2.3.5). The log g cut is to ensure we have selected dwarf stars. It is interesting to note that this simple method is used to search for spectral peculiarities, in our case stars with strong features around the α-elements. However, the method could, in theory, be re-calibrated to search for other scientifically exciting targets such as s-process or r-process enriched stars or others. This method could also be adapted to determine the abundance of other chemical species using low-resolution spectra.

In Figure 2.3 we plot the value of the index for a sample of 200 synthetic stars (selected from the parameter space and synthetic grid above), where the y-axis labels the index value and the x-axis is the synthetic value for [α/Fe]. The colour code represents the temperature, metallicity, and surface gravity in the top, middle, and lower panels, respectively. We see a tight, linear correlation between the index value and the [α/Fe], such that high index values indicate high α-abundances. There does not appear to be any major systematic variations as a result of the stellar parameters. Figure 2.3 shows that it is possible to distinguish between an α-rich and α-poor population as the mean index of stars with [α/Fe] $\leq$ +0.25 dex is smaller than

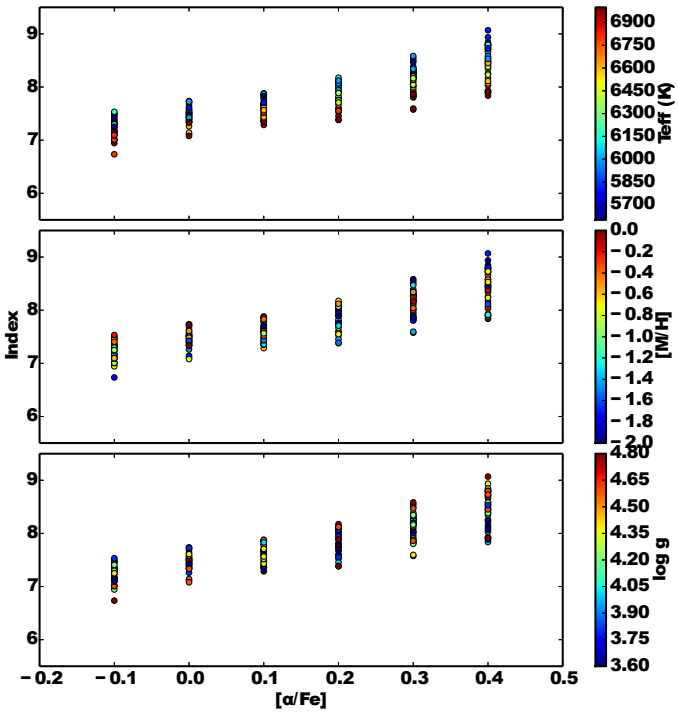

Figure 2.3 – The index value as a function of [α/Fe] colour coded by T_{eff} (top panel), [Fe/H] (middle panel), log g (bottom panel) for a sample of 200 synthetic spectra.

the mean index of stars with [α/Fe] $>$ +0.25 dex. A star with an index below approximately 7.4 can be interpreted as α-poor while a star with an index about 7.6 α-rich. Figure 2.3 also suggests that it may be possible to calibrate the index in a linear way to estimate the [α/Fe] directly (which we explore in section 2.4.4).

2.3.5 Effects of Stellar Parameters

In this section, we study the effect of the stellar parameters on the index. The index is a linear combination of α-sensitive spectral bands divided by a set of control spectral bands. Ideally, the index should be constant with a given [α/Fe] regardless of the stellar parameters. In practice, the stellar parameters have a small effect on the index. To study this effect, we computed the index over a broad range of stellar parameters (outlined in section 2.3.4) at a constant [α/Fe]. Figure 2.4 shows the value of the index (colour) as a function of both temperature and metallicity. The plot illustrates that the index is stable and only varies on the order of 1-2% at effective temperatures below $\sim$6500 K. However, the index seems to vary significantly at the very metal-poor and high temperature end (bottom right corner of Figure 2.4). This is expected as the metal-poor hot stars will likely have significantly weaker lines. From this figure, we can see that the method does not perform nearly as well for the hot (particularly at temperatures above 7000 K), metal-poor stars.

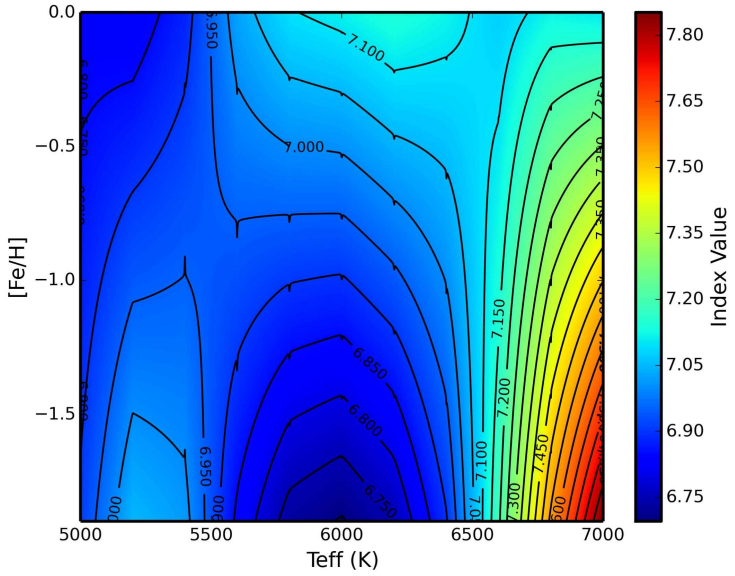

Figure 2.4 – The value of the index (colour) as a function of both the effective temperature and the metallicity for all dwarfs in the synthetic grid at [α/Fe] = 0.00 dex.

2.3.6 Effects of Signal-to-Noise

To study the effect of both the signal-to-noise ratio (SNR) and the stellar parameters on the stability of the index, we have completed noise-injection experiments. We used the synthetic grid of spectra described in section 2.3.1. Once these spectra were preprocessed, we added Gaussian white noise to simulate spectra at SNR between 20 and 100 typical for SDSS data. We then performed a BMC continuum normalization. Finally, we calculated the index and plotted the variation in the index as a result of the stellar parameters at each SNR for [α/Fe] = 0.00 dex and [α/Fe] = +0.40 dex. Both the SNR and stellar parameters cause a variation in the index at a constant [α/Fe].

Figure 2.5 shows that it is possible to separate [α/Fe] = 0.00 and [α/Fe] = +0.40 dex at SNR larger than 40. We find, at a SNR = 40, the total 1σ internal error on the index, which is defined as its mean variation, is found to be 0.60. Figure 2.4 illustrates that this value can be decreased significantly by further restricting the parameter space below 6500 K. For example, by restricting the the parameter space to metal-poor halo turnoff stars ($6000 < T_{\rm eff} < 6500$ K, log g > 3.5 dex, and -2.0 $<$ [Fe/H] $<$ - 0.80 dex), the total internal error is 0.20 instead of 0.60.

2.3.7 Effect of Pseudo-Continuum Placement

We used the BMC method to determine the local continuum for our spectra. It that has the benefit of better control the continuum in the local region of our bands. It also has the advantage of reducing the uncertainty in the total flux of our measured spectral bands (Rogers et al., 2010). The BMC method is sensitive to two parameters and a balancing act must be played with both. These parameters are:

- The width of window around any spectral band - The width must be large in order to avoid small scale fluctuations and noise in the spectra but not too large as to encode

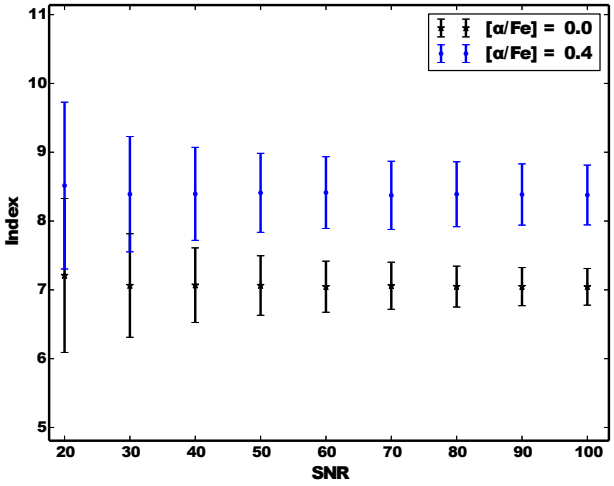

Figure 2.5 – The mean and 1σ dispersion in the index over the full range in stellar parameters as a function of SNR.

large-scale structure (e.g. G band at $\sim$ 4300 Å).

- The percentile of flux within the window which is defined as the continuum - The percentile must be high enough to 'see' the true continuum but cannot be so high that it becomes only sensitive to noise.

Therefore, it is useful to study the sensitivity of our index to these two parameters that define the placement of the continuum. To do this, we took a single random synthetic spectrum and plotted the contours of the measured index for that spectrum as a function of both the width and percentile. The index should be insensitive to our choice of BMC parameters and thus we searched for regions where the derivative of the index to the BMC parameters is minimized. Remembering that the density of contours is proportional to the derivative of the index as a function of the BMC parameters, we selected a region where the index is very stable over a range of BMC parameters. The choice of BMC parameters adopted from Rogers et al. (2010), which is the 'X' in Figure 2.6, worked very well because the index does not seem to depend strongly on the choice of BMC parameters. This experiment has shown that as long as the percentile is between 89 and 95% and the width is between 45 and 115 Å the index varies by less than 1%. These results are independent of our choice of test spectra. We therefore define the pseudo-continuum at any wavelength as the 90th percentile flux in 100 Å window around that wavelength.

2.4 Validation

To achieve a good validation we needed several validation sets. These validation datasets were employed to allow us to study the performance of our method in different regimes of stellar parameter space, across large datasets, and with low-resolution SDSS data. In this section, we describe the validation sets and the reason they were chosen separately below.

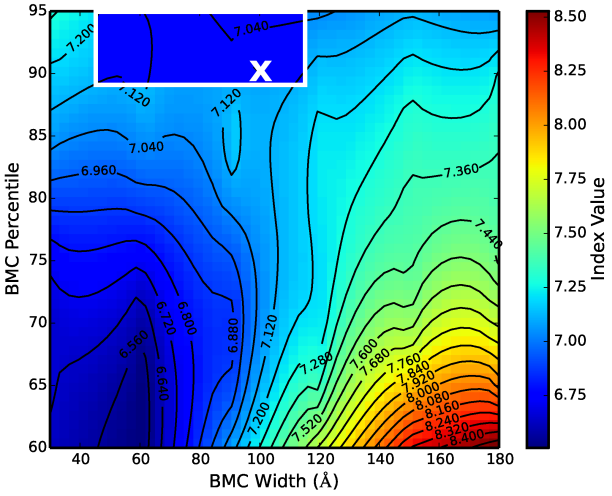

Figure 2.6 – Stability of index as a function of BMC parameters. 'X' is the location suggested by Rogers et al. (2010). The shaded region represents the region where the index varies on an order of less than 1% .

2.4.1 Comparison with the ELODIE Library

The ELODIE library is a publicly available library of about 2,000 spectra of 1,388 stars observed with the ELODIE spectrograph on the Observatoire de Haute-Provence 1.93-m telescope. ELODIE3.1 (Prugniel & Soubiran, 2001; Moultaka et al., 2004) contains high-resolution spectra (R = 42,000), high SNR ($>$ 100) observations of stars with 3700 $<$ $T_{\rm eff}$ $<$ 13600 K, 0.03 $<$ log g$<$ 5.86 dex and –2.8 $<$ [Fe/H] $<$ +0.17 dex. Lee et al. (2011) used a sample of 425 ELODIE spectra that have well known stellar parameters and their [α/Fe] from the literature. It is important to note that because the [α/Fe] values are taken from the literature there may be some scatter that exists in this validation set (Lee et al., 2011).

We processed the ELODIE spectra in the same way as the rest of the spectra: degraded the resolution to R = 2,000 using a Gaussian kernel, resampled the spectra to 0.5 Å pixels, and applied a BMC normalization. We calculated the index for all stars that fall in our parameter range and studied the index as a function of [α/Fe] (Figure 2.7). The colour scheme is the same as Figure 2.3.

We see a tight correlation between the index and the α-abundance over the full range of stellar parameters indicating that it is possible to estimate the [α/Fe] directly from the index. This result illustrates that we can rank stars from low to high [α/Fe] using the index only. A star with an index below approximately 7.2 would be considered α-poor while a star with an index about 7.4, α-rich. These index values are consistent with the synthetic spectra in section 2.3.4. Although a large number of stars exist in the ELODIE library, they are mostly metal-rich compared to the halo stars we are interested in. As such, this validation set is not completely suitable for our purposes. Thus we must explore other validation sets.

2.4.2 Comparison with Nissen & Schuster Data

Nissen & Schuster (2010) measured the Mg, Ti, Si, Ca, and Fe-peak elemental abundance abundances of 78 halo stars and 16 disk stars using spectra from the Very Large Telescope's (VLT)

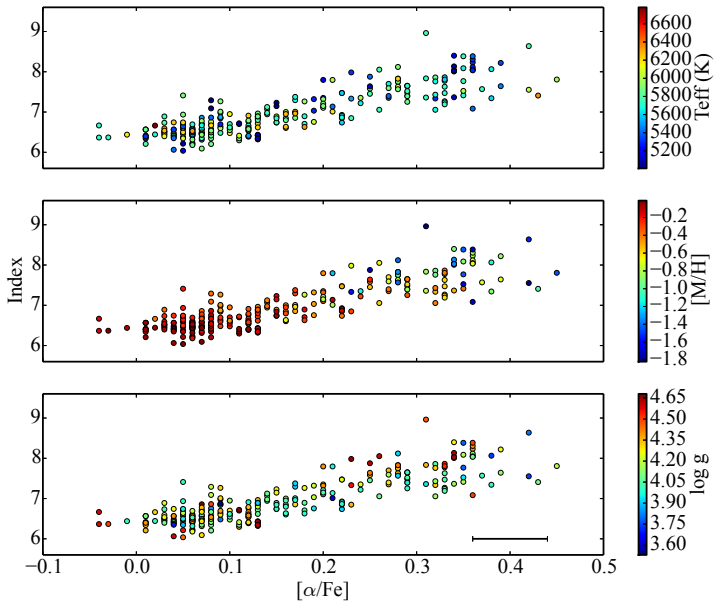

Figure 2.7 – The index value as a function of [α/Fe] colour-coded by T_{eff} (top panel), [Fe/H] (middle panel), log g (bottom panel) for metal-poor F-, G-, and K-dwarf ELODIE stars that are within our parameter range. The error bar represents the typical errors on the [α/Fe] from the ELODIE high-resolution validation set.

Ultraviolet and Visual Echelle Spectrograph (UVES) spectra and the Fiber fed Echelle Spectrograph (FIES) on the Nordic Optical Telescope (NOT). These spectra were kindly provided to us by P. Nissen. The wavelength coverage of VLT/UVES sample extends only to $\sim$ 4700 Å. Since the index includes a Ti I feature at $\sim$ 4500 Å, the VLT/UVES data from N10 could not be used for validation. The NOT/FIES spectra have a wavelength coverage that allows us to use this Ti I feature. In total, there are 47 stars from the N10 dataset that meet our criteria in wavelength coverage and stellar parameters space. N10 represents the parameters space we are most interested in, and is also internally consistent. This dataset is rather small and thus this set alone does not allow detailed analysis of the performance of the index but compliments the ELODIE validation set. Figure 2.8 shows the performance of the index as a function of [α/Fe] for the N10 data. The colour coding represents the stellar parameters as in Figure 2.3.

We found again a tight correlation between the index and the α-abundance over the full range of stellar parameters. Figure 2.8 makes it clear that we can use the index alone to categorize the high-α' and 'low-α' stars from N10. Stars with an index below 7.2 would be considered α-poor while a star with an index of 7.4 is α-rich. These values are the same as for the synthetic grid and the ELODIE validation sets. The tightness of the linear correlation between the index and the [α/Fe] is further proof that we may be able to estimate the α-abundance directly from the index.

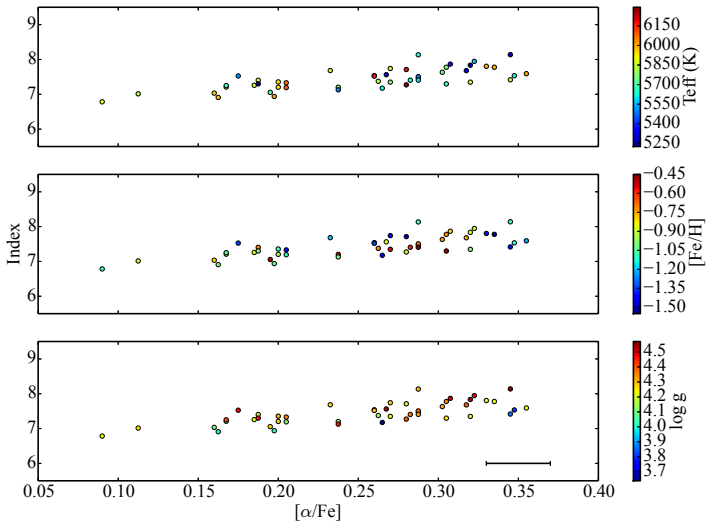

Figure 2.8 – The index value as a function of [α/Fe] colour coded by T_{eff} (top panel), [Fe/H] (middle panel), log g (bottom panel) for the NOT/FIES subset of the N10 data. The error bar represents the typical errors on the [α/Fe] from the N10 high-resolution validation set.

2.4.3 Comparison with SDSS Calibration targets

Finally, we used a sample of SDSS spectra with accurate stellar parameters and [α/Fe] determined from high-resolution spectra. This sample was used in Lee et al. (2011) and was originally constructed to validate the SSPP pipeline (for more details consult Allende Prieto et al., 2008; Smolinski et al., 2011). We used a subset, totaling 73 stars, from the SDSS calibration targets discussed in Lee et al. (2011) that exist inside our stellar parameter range.

We studied the index as a function of [α/Fe] and the stellar parameters in Figure 2.9. The colour scheme and axes are the same as Figure 2.3. We see again that it is possible to separate stars based on their α-abundances using the index alone as long as the star exists inside our parameter range. The index value needed to separate stars into α-rich and α-poor populations is consistent with the tests on the synthetic grid as well as the ELODIE and N10 validation sets.

2.4.4 Converting the Index to an Estimate of [α/Fe]

We have shown, for all of our tests with synthetic and real spectra, that there is a linear relationship between our index and [α/Fe]. We used a linear regression model to approximate the index as a function of [α/Fe], to estimate the [α/Fe] directly from the index. The ELODIE validation set was used as a calibration set because it is the largest one. A linear regression model for the ELODIE dataset yields:

$$\text{Index} = [\alpha/\text{Fe}] \times 4.32 + 6.28 \tag{2.2}$$

The regression model achieved a correlation coefficient of 0.86 and is statistically significant with relatively low scatter (5% in index space). The equation to convert our index into a direct estimate of [α/Fe] was tested on the remaining validation sets (N10, and SDSS high-resolution targets). We also added an additional validation set using globular clusters and open

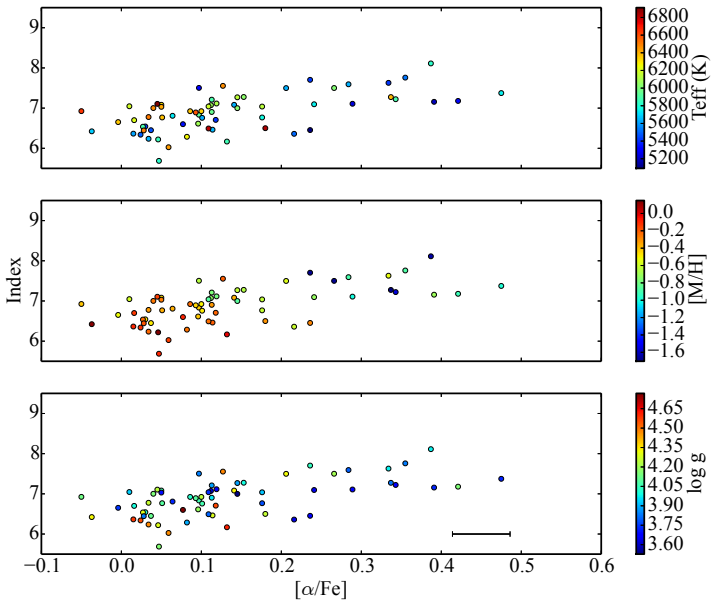

Figure 2.9 – The index value as a function of [α/Fe] broken down by T_{eff} (top panel), [Fe/H] (middle panel), log g (bottom panel) for 73 SDSS stars with parameters obtained by high resolution spectra that exist in our parameter range. The error bar represents the typical errors on the [α/Fe] from the SDSS high-resolution validation set.

clusters to compare the estimated [α/Fe] with the high-resolution average measured in the literature.

For the case of N10, we used the ELODIE dataset as a calibration set to convert our index in the [α/Fe] through Equation 2.2. We found the estimated [α/Fe] and those from N10 are in good agreement with a mean offset of 0.01 dex and an external error of $\pm$0.05 dex (Figure 2.10). We also found no significant offsets or correlations between the residuals in [α/Fe] and the stellar parameters (Figure 2.11). Finally, we repeated the analysis for the SDSS calibration targets and found a very good agreement between our estimated α-abundances and the high-resolution estimates with an offset in [α/Fe] = 0.00 dex and an external error of $\pm$0.10 dex.

2.4.5 Comparison with SDSS Clusters

We used a sample of two globular clusters and one open cluster observed with the SDSS to validate our estimated [α/Fe] values. Clusters are a good test bed to further validate our method, as each cluster should have an average [α/Fe] with a relatively small spread. While clusters have small star-to-star variations in their abundances of light elements (C, N, Al, Na) we expect these to not strongly affect the α-elements and thus the [α/Fe] measurement. In order to achieve a large enough sample of stars in the clusters, we had to decrease the log g constraint to log g $>$ 3.0 dex. Further, we require the SNR to be larger than 40 (see section 2.3.6) to only select out stars for which we can obtain suitable values of [α/Fe].

The literature values for [α/Fe] were compiled by averaging the mean cluster abundances of the individual α-elements for each cluster. The standard deviation was also computed and

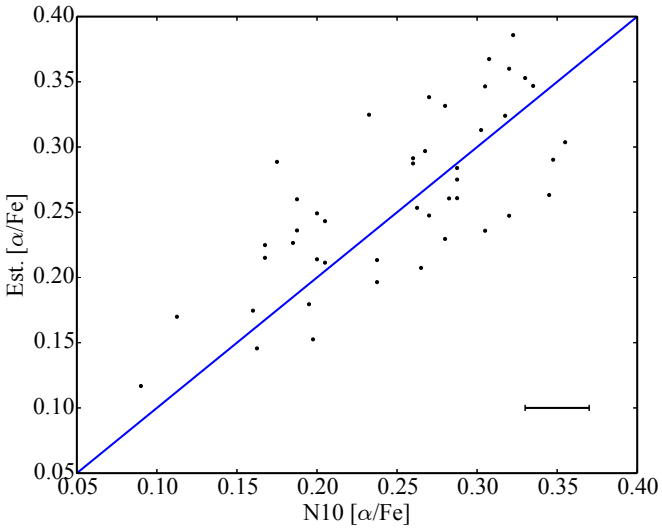

Figure 2.10 – The estimated [α/Fe] as a function of the high-resolution [α/Fe] measurement from N10. The blue line represents a 1:1 relation. The error bar represents the typical errors on the [α/Fe] from the N10 validation set.

Table 2.2 – Globular/Open Cluster data.

Cluster	$<$[Fe/H]$>_{lit}$ (dex)	$<$ [α/Fe]$>_{lit}$ (dex)	$<$[α/Fe]$>_{est.}$ (dex)	N_{mem}
M13	-1.58 $\pm$ 0.04	0.20 $\pm$ 0.04	0.19 $\pm$ 0.18	57
M71	-0.80 $\pm$ 0.02	0.23 $\pm$ 0.10	0.13 $\pm$ 0.05	5
NGC 2420	-0.05 $\pm$ 0.02	0.03 $\pm$ 0.09	0.08 $\pm$ 0.08	72

NOTES: The data for each of the clusters were compiled from the following sources: M13: Sneden et al. (2004), Cohen & Meléndez (2005); M71: Boesgaard et al. (2005); NGC2420: Pancino et al. (2010). N_{mem} is the total number of stars in the SDSS that were used to compute the average abundances.

is displayed in Table 2.2. We estimated the [α/Fe] for likely cluster members[1] from M71 and M15, and the open cluster NGC 2420 using our spectral index method. The other clusters of Lee et al. (2011), M13, M67, NGC 6791, are outside our metallicity range. For the three clusters that are in our parameter range, we estimated the mean and standard deviation in [α/Fe]. Both the literature and estimated values for the mean [α/Fe] can be found in Table 2.2. Our estimated mean [α/Fe] for each cluster is in very good agreement with the literature values providing further proof that our method can produce meaningful values for [α/Fe].

2.4.6 Computation of Internal and External Error on the Index

The total internal error on the index at any SNR can be estimated by completing noise injection experiments on both the SDSS data and synthetic spectra. We do the latter in section 2.3.6 and find the internal error can be as high as 0.60 ($\sim$ 10%) at SNR = 40. Propagating this to

[1]For more information regarding the selection of likely cluster members in the clusters consult Lee et al. (2008b); Smolinski et al. (2011)

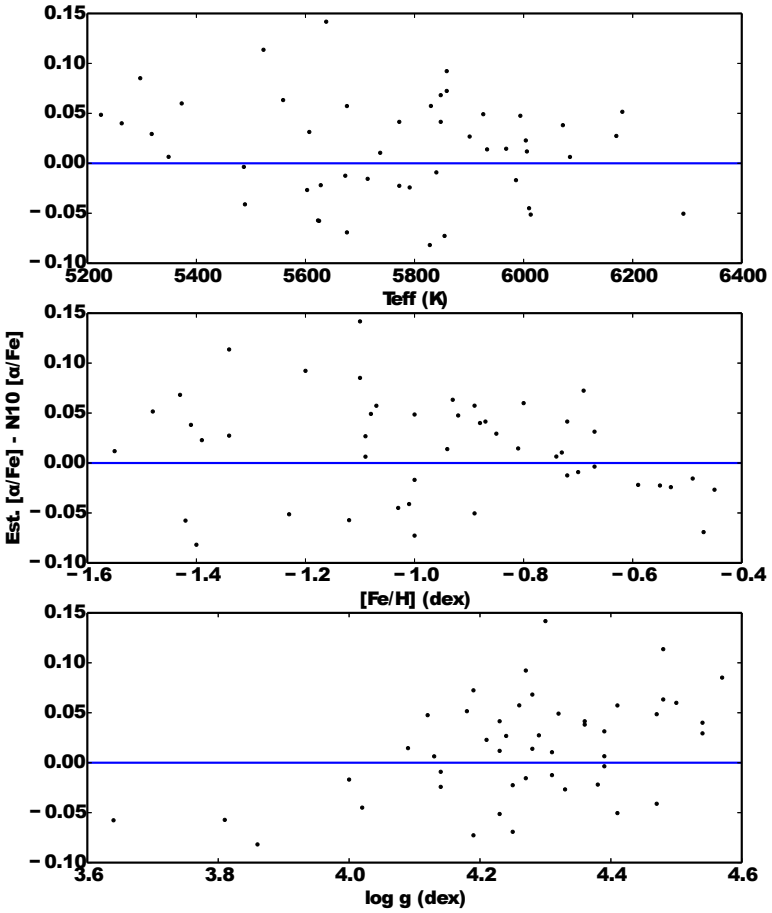

Figure 2.11 – The residual between the estimated and true [α/Fe] broken down by $T_{\rm eff}$ (top panel), log g (middle panel), [Fe/H] (bottom panel) for the NOT/FIES subset of the N10 data.

estimate the uncertainty in [α/Fe] via Equation 2.2 yields $\sigma_{internal} = \pm$ 0.13 dex. The external uncertainty in the [α/Fe] is estimated by using the validation sets is shown to be as high as $\sigma_{external} = \pm$ 0.1 dex. Thus a conservative estimate of the total uncertainty in [α/Fe] is the internal and external errors added in quadrature and is $\sigma_{[\alpha/\mathrm{Fe}]} = \pm$ 0.16 dex at a SNR = 40. The external and internal errors are comparable but the internal error can be greatly decreased by carefully selecting the range of stellar parameters. For example, when we constrained the temperature between 6000 and 6500 K and the metallicity between -0.8 and -2.0 dex, i.e. the expected turnoff region in our sample, we found that the index varies on the order of 0.20. This implies we can estimate [α/Fe] with an internal error of $\pm$ 0.05 dex by constraining the stellar parameter to focus on the turnoff region only.

Our method improves on the current methods of Lee et al. (2011) and Franchini et al. (2011) by decreasing the dependence on models and uncertainties in the stellar parameters. We have shown that with our empirical spectral index method we can estimate [α/Fe] to within $\sim \pm$ 0.1 dex when accounting for the full parameter space described in section 2.3.4, which has a temperature span of 2000 K, log g span of 1.5 dex and a metallicity coverage of 2.0 dex. In context, the spectral matching technique of Lee et al. (2011) has an internal error of $\sim \pm$ 0.1 dex in [α/Fe] for a temperature uncertainty of only $\pm$ 300 K.

2.5 Results

2.5.1 Distribution of α-elements in the Inner Halo

The effective temperature and metallicity for each of our targets are sourced from the adopted values from the SDSS SSPP. We computed the [α/Fe] for our targets using the spectral index method. The estimated [α/Fe] distribution and metallicity-[α/Fe] diagram are shown in Figure 2.12(a) and Figure 2.12(b), respectively. The peak of the [α/Fe] in Figure 2.12(a) is +0.30 dex which confirms that halo stars are, on average, α-enhanced with a large sample from SDSS (Helmi, 2008; Feltzing & Chiba, 2013, and references therein). The dash-dotted line in Figure 2.12(a) shows the Gaussian fit to the [α/Fe] distribution function. It is interesting to point out that the fit over predicts the amount of low-α stars near [α/Fe] = 0.20 dex. We plan to explore this and the relative ratio of these two populations as a function of Galactic parameters further in the next work of this series. Constraining the sample to just the turnoff region, i.e. 6000 $<$ T_{eff} $<$ 6500 K, log g $>$ 3.5 dex, -0.8 $<$ [Fe/H] $<$ -2.0 dex, produced a standard deviation of the distribution in [α/Fe] of 0.15 dex. This dispersion is larger than the estimated uncertainty in the constrained parameter space indicating we can resolve the α-rich and α-poor populations.

Motivated by the conversion described in section 2.4.4 and N10, α-poor stars are defined as any stars which have an index less than 6.93, corresponding to an [α/Fe] $<$ +0.15 dex and α-rich stars as any stars which have an index larger than 7.79, corresponding to an [α/Fe] $>$ +0.35 dex. These criteria are designed to account for the boundary of α-rich and α-poor stars at $\sim$ [α/Fe] = +0.25 dex (N10) and the uncertainty in the estimated [α/Fe]. The criteria are used to select, in a statistical way, stars which are have a high probability of being either α-rich or α-poor based on the 1-σ uncertainties in the estimated [α/Fe]. A gaussian-mixture model, whereby the global [α/Fe] distribution is fitted by a two-gaussian model could be used as an alternative to select α-rich or α-poor stars.

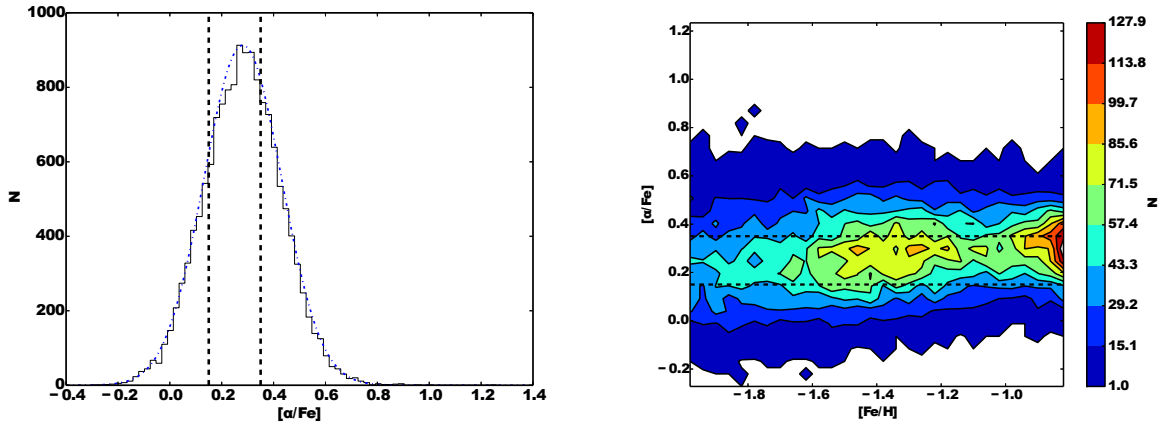

(a) (b)

Figure 2.12 – (a) The [α/Fe] distribution of our sample of 14757 SDSS F and G stars. (b) The [α/Fe] as a function of [Fe/H] for our sample. The [α/Fe] was determined by converting the index via Equation 2.2. The dotted lines in both panels represent the cut in [α/Fe] to obtain the α-rich and α-poor subsamples. The blue dash-dotted line in panel (a) represents a single Gaussian fit to the distribution.

2.5.2 Turnoff Detection and its Uncertainties

The turnoff temperature can be used to determine the age of the youngest stellar population (for further discussion on this method consult Soderblom, 2010). We used a Sobel-Kernel edge detector algorithm to determine the temperature of the main sequence turnoff (for more details consult Jofré & Weiss, 2011). The method assumes the temperature distribution of a stellar population will display a very sharp decline (i.e. edge) near the turnoff as the more massive, hotter stars in the population have evolved off the main sequence (see top panel of Figure 2.13). The edge, or turnoff temperature in our case, was determined by constructing a temperature distribution function for a range of metallicity bins and computing maximum of its derivative. An example of this method applied to the metallicity range –1.40 $<$ [Fe/H] $<$ –1.70 dex of the sample considered in this chapter can be found in Figure 2.13. This algorithm is sensitive to the sampling and in order to determine the uncertainty in the turnoff temperature we used a bootstrap method (Jofré & Weiss, 2011; Tabur, Kiss & Bedding, 2009). In the bootstrap, we randomly re-sampled 80% of our effective temperature distribution and recomputed the turnoff temperature via the Sobel-Kernel edge detector. We computed 500 iterations to find the variation in the turnoff temperature as a result of the sampling. Typical 3-σ uncertainties in the turnoff temperature from the bootstrap are on the order of 60 K.

The number of stars sampled near the turnoff primarily affects the bootstrapping error. The more stars near the turnoff, the better sampled it is and the lower the overall bootstrapping error becomes. This can be accomplished by increasing the metallicity bin. However, since the turnoff temperature depends on metallicity, increasing the metallicity bin size can cause a noisier turnoff. Jofré & Weiss (2011) used a Monte Carlo approach and showed that the errors on the metallicity measurement will also induce a significant effect on the turnoff detection error because this method relies on binning in both temperature and metallicity space. We adopted this approach computing 500 realizations including the errors on the metallicity. The results of

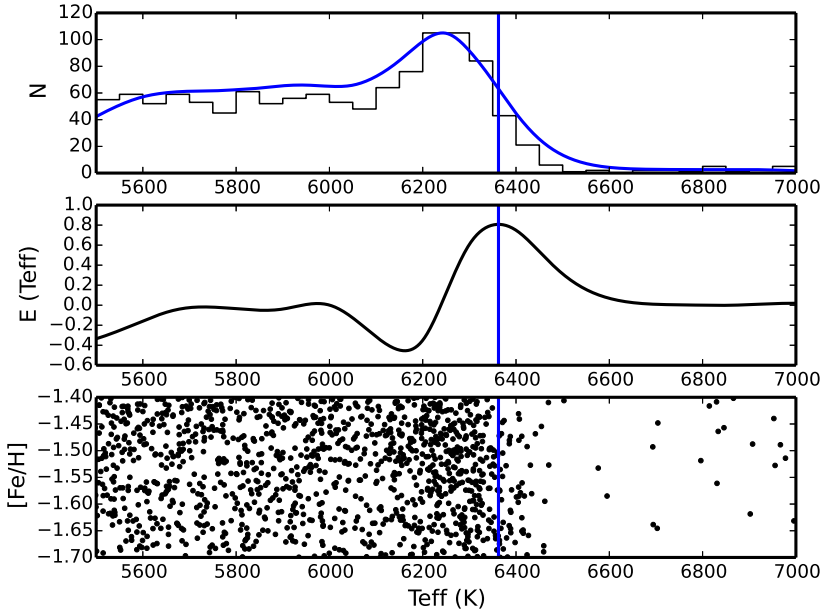

Figure 2.13 – The T_{eff} distribution (top panel), and the Sobel-Kernel edge detector algorithm (middle panel), and metallicity (bottom panel) as a function of $T_{eff}$for the α-rich sample with –1.40 < [Fe/H] < –1.70 dex . The peak of the Sobel-Kernel (middle panel) is selected as the turnoff temperature, above which there are very few (blue straggler) stars.

this simulation confirm that if the bin size is smaller than $\sim 2\sigma_{[Fe/H]}$ then an individual star in our sample can jump between different metallicity bins and thus change the detected turnoff temperature significantly (Jofré & Weiss, 2011). On the other hand, excessively large bin sizes can lead to a less precise turnoff temperature because the turnoff temperature is metallicity-dependent. Typical uncertainties in [Fe/H] at these higher SNR are on the order of 0.15-0.2 dex. Our simulations showed that the uncertainty in the turnoff temperature due to the metallicity becomes small relative to the bootstrapping error as the metallicity bin size becomes larger than $\sim$ 0.3 dex. Therefore, the uncertainty in the turnoff temperature is defined as the 3σ error as a result of the bootstrapping with a bin size in metallicity of 0.3 dex.

2.5.3 Metallicity - Temperature Diagram

In the left panel of Figure 2.14, we plot the turnoff temperature as a function of metallicity of our SDSS sample over plotted with the α-rich and α-poor Dartmouth (Dotter et al., 2008) isochrones. The right panel of Figure 2.14 shows the turnoff temperature as a function of metallicity for our sample over plotted with the Yonsei-Yale (Y^2, Demarque et al., 2004) isochrones. The first thing to note is that the turnoff temperature as a function of metallicity does not follow along an isochrone of a constant age indicating there is a correlation between age and metallicity. These plots also show that the turnoff temperature of the α-rich and α-poor stars in our sample are, within the errors, equal at low-metallicity. As the metallicity increases, upwards of $\sim$ -1.4 dex the α-rich stars have a significantly lower turnoff temperature indicating they are older than the α-poor stars. All of our stars are older than 8 Gyr with both isochrones. The

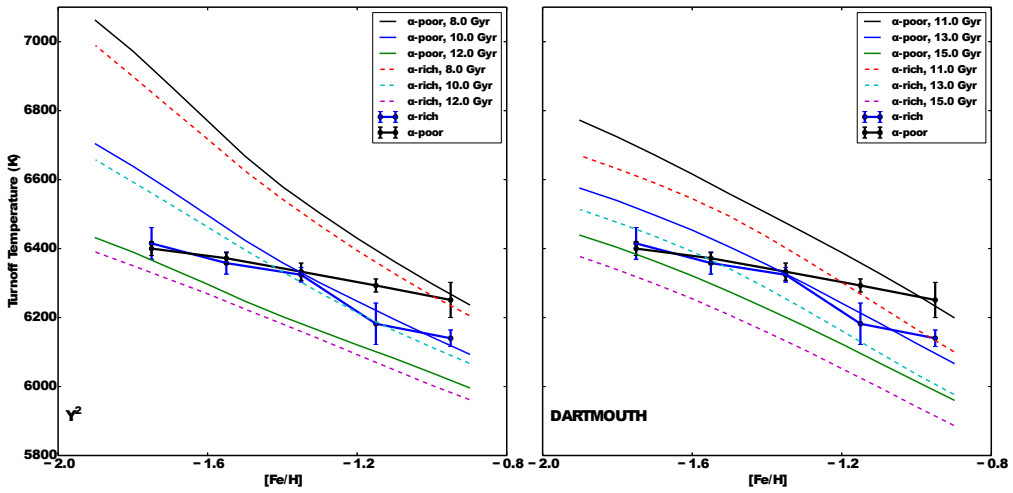

Figure 2.14 – Metallicity as a function of turnoff temperature withY^2 isochrones (left panel) and Dartmouth isochrones over plotted (right panel).

Dartmouth isochrones produce larger ages compared to the Y^2 isochrones and in some cases have ages larger than the accepted age of the universe (13.8 Gyr, Planck Collaboration et al., 2013). This is likely a result of the prescription of atomic diffusion (Jofré & Weiss, 2011).

Qualitatively, the turnoff temperature of the α-rich component as a function of metallicity is not significantly different with the results of Jofré & Weiss (2011). This is expected as the bulk of the stars in the sample are α-rich. Another interesting finding we observe from the over plotted isochrones is that the Dartmouth isochrones have larger differences in the turnoff temperature between α-rich and α-poor stars at the same age. This indicates that the two isochrones have different responses to α-enhancement. The different isochrone sets also use different helium mixtures, which can also affect the isochrones.

2.5.4 Isochrone Analysis: Ages and their Errors

With the turnoff temperatures, metallicities and a set of isochrones in hand, we can determine the age of our α-rich and α-poor populations. For this we used the Y^2 isochrones (Demarque et al., 2004) which were interpolated to determine the theoretical turnoff temperature as a function of age, metallicity, and [α/Fe]. The Y^2 isochrones include atomic diffusion (Demarque et al., 2004) while the Dartmouth isochrones only include moderate atomic diffusion (Dotter et al., 2008). As a result, the Dartmouth isochrones produce larger ages compared to the Y^2 isochrones. To avoid dependencies in the isochrones used, we have considered the relative ages between the α-rich and α-poor populations.

The effect of increasing [α/Fe] in an isochrone model, while keeping [Fe/H] fixed, is to effectively increase the total metal abundance. Dartmouth and Y^2 isochrones show that increasing the α-abundance will cause the turnoff temperature to decrease at a constant age. Physically, this can be attributed to the increase in the importance of the CNO cycle in energy generation causing an earlier hydrogen exhaustion for α-enhanced stars (Kim et al., 2002).

The metallicity of the isochrones used was equal to the metallicity of the bin centre. The [α/Fe] was set to +0.40 dex and +0.20 dex for the α-rich and α-poor subsamples, respectively.

Table 2.3 – Turnoff Temperature and Ages for our SDSS F- and G-dwarf sample using Y^2 models.

[Fe/H] (dex)	$T_{\rm eff,TO}$ (K)	$\sigma_{\rm T_{eff,TO}}$ (K)	Age (Gyr)	$\sigma_{\rm Age}$ (Gyr)	Normalized Age
		α-rich			
-0.95	6140	24	9.18	0.27	0.91
-1.15	6182	60	10.09	0.64	1.00
-1.35	6324	21	9.73	0.15	0.96
-1.55	6358	32	10.71	0.27	1.06
-1.75	6415	46	11.20	0.25	1.11
		α-poor			
-0.95	6251	51	8.23	0.32	0.82
-1.15	6293	19	9.04	0.13	0.90
-1.35	6333	25	9.98	0.20	0.99
-1.55	6372	16	10.89	0.12	1.08
-1.75	6400	20	11.67	0.11	1.16

The uncertainty in the age was determined by propagating the uncertainty in the turnoff temperature. In this case, the uncertainty in the turnoff temperature was determined by the bootstrap and Monte Carlo analysis in metallicity. We also considered the uncertainty in age due to metallicity by adding in quadrature the uncertainty in turnoff temperature as a result of metallicity errors. The final turnoff temperature, error in the turnoff temperature, ages, and uncertainty in the ages for our α-rich and α-poor subsamples are shown in Table 2.3. For our analysis, we used normalized ages, which we define as the absolute age divided by the mean age of all of the stars (10.07 Gyr), because of the large theoretical uncertainties in the ages determined from the turnoff temperature. Our goal is to quantify the age difference so using normalized ages is appropriate. It is important to point out that the error on the age we quote is only the internal error.

2.6 Discussion

2.6.1 Age-Metallicity Relation

We have, for the first time, measured the age-metallicity relation of an α-rich and α-poor population in the Galactic halo at metallicities between -0.80 dex and -2.0 dex (Figure 2.15). We note that: (1) at high metallicities ([Fe/H] $>$ -1.4 dex), the α-rich population is older than the α-poor population, and (2) at low metallicities ([Fe/H] $<$ -1.4 dex), the two populations are coeval within the errors. We have found that the shape of the age-metallicity relation differs for both α-populations. The α-poor stars tend to have a steeper correlation between age and metallicity compared to the α-rich stars. This is consistent with the idea that the α-poor stars were formed in areas with slower chemical evolution compared to their α-rich counterparts. The very shallow slope on the age-metallicity correlation for α-rich stars seems to infer they were formed in a quick event with high star formation rates which were able to produce a broad range in metallicities in a short time (less than $\sim 10^9$ years) to keep the α-abundance enhanced.

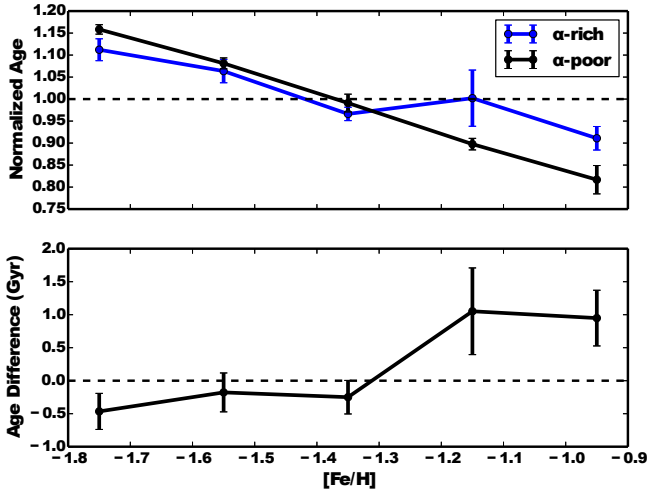

Figure 2.15 – Top panel: normalized Y^2 isochrone ages as a function of metallicity for α-rich (blue) and α-poor (black) populations. Bottom Panel: age difference between the α-rich and α-poor populations as a function of metallicity.

By testing multiple isochrone sets, we have found that our age sequence at low metallicities, namely that the α-rich population is coeval with the α-poor population, within the errors, is robust. Our age difference between the α-rich and α-poor populations in the most metal-rich bin is affected by as much as 1 Gyr. However, this difference does not affect the interpretation of our results.

It is also worth commenting that the age-metallicity relation that we observe in Figure 2.15, is similar to the 'Y'-like bifurcation seen in the globular clusters of Marín-Franch et al. (2009) and Leaman, VandenBerg & Mendel (2013). Marín-Franch et al. (2009) found two well defined tracks in the age-metallicity diagram for globular clusters: a 'young' track which can be associated with dwarf galaxies and an 'older' track with a small age dispersion which can be associated with an in situ population that may have formed from a protogalactic gas cloud. We found a similar bifurcation in our halo field star sample which supports a scenario of common origin for the GC and halo field stars (e.g. Martell & Grebel, 2010).

2.6.2 Implications for the Formation of the Galactic Halo

One unambiguous result from our study is that all of the stars in our sample, regardless of which isochrone set is used, are older than $\sim$ 8 Gyr. This confirms the notion that the Galactic halo was formed and assembled very early on as suggested by both theory (Robertson et al., 2005; Font et al., 2006; Zolotov et al., 2009, 2010; Font et al., 2011) and observations (e.g. Schuster et al., 2012).

The theoretical work of Robertson et al. (2005) and Font et al. (2006) lays out what Schuster et al. (2012) refer to as a 'dual-accretion' scenario. In this scenario, the halo is built from the bottom-up via hierarchical merging. The dual-accretion models produces a Galactic halo by merging smaller sub-units of stars together rapidly at early times fully destroying the sub-units in the process. The proto-halo systems form massive stars rapidly and are enriched primarily by Type II supernova producing an α-rich population. Since the sub-units are broken up quickly,

there is little iron enrichment via Type Ia supernova leaving behind a set of low metallicity, α-rich stars. These would correspond to the α-rich stars in our sample. Longer-lived dwarf galaxies, on the other hand, are polluted via both types of supernova leading to a population of stars that have a wide-range in metallicities and are α-poor. These stars are accreted onto the Milky Way at later times and could represent the α-poor stars in our sample.

Interestingly, the age-metallicity diagram from the theoretical work of Font et al. (2006) appears to have two tracks, one that has a steeper slope in age-metallicity space than the other which is the case in our sample (Figure 2.15). This bifurcation in the age-metallicity relation can be interpreted as evidence that the Galactic halo was built in two phases. One quick phase that produced the α-rich stars over broad metallicity ranges, leading to a shallow age-metallicity relation. Followed by a second phase of accretion of stars that evolved in environments of slower chemical evolution, leading to a more pronounced age-metallicity relation.

The more recent hydrodynamic simulations by Font et al. (2011) have predicted that the accreted stars are, on average, 3-4 Gyr older than the in situ population. If we make the assumption that the in situ population are tracked by our α-rich stars (an assumption often made in the literature, e.g. Schuster et al., 2012) than our relative age sequence would indicate that the accreted stars are $\sim$ 1 Gyr *younger* than the in situ population. This result does not agree with the results of Font et al. (2011) and is only about half of the 2-3 Gyr age difference observed by Schuster et al. (2012). However, this discrepancy could be remedied if we do not make the assumption that α-rich stars are the in situ population and the α-poor stars are the accreted population or if the feedback in their simulations were less efficient in low-mass halos (Font et al., 2011). The unavoidable (larger) errors on [α/Fe] with low-resolution spectra can lead to a slight mixing of the two populations which could also explain the diminished age difference compared to the results of Schuster et al. (2012).

Contrary to Robertson et al. (2005) and Font et al. (2006, 2011), the models of Zolotov et al. (2009, 2010) predicted that the in situ population within the Galactic halo is likely formed within the inner 4 kpc of the galaxy's centre and is formed via cold, in-falling gas. The in-falling gas creates a primeval bulge or disk. After which those stars in the primeval disk are kinematically heated into the halo via early accretion and merging events which at the same time populate the accreted component of the halo via tidal stripping (Purcell, Bullock & Kazantzidis, 2010). These in situ stars can be interpreted as our α-rich stars (just as in Schuster et al., 2012). The stars formed in dwarf galaxies, which merged at later times with the primeval disk/bulge, can be attributed to our α-poor stars. Zolotov et al. (2010) found, in all but one of their model halos, the in situ population was formed early on and the accreted population was formed, on average, at later times and then subsequently accreted onto the halo. However, it is not clear whether this is true at all metallicities or just higher metallicities. Our relative age sequence at high metallicities, namely α-rich stars being older than α-poor stars on average, favors the models of Zolotov et al. (2009, 2010) and at high metallicities confirms the observational results of Schuster et al. (2012) with a larger, statistical sample. Further the bifurcation we observed should still be present in these models. The results of this study can be used to help construct more realistic models and better constrain the basic physics, in particular feedback mechanisms, which can replicate the observations.

2.7 Conclusion

Motivated by the results of both Schuster et al. (2012) and Jofré & Weiss (2011), we addressed the intriguing problem of the relative ages of the α-rich and α-poor stars in the Galactic halo with a large sample of stars from SDSS. To that end, we developed a new spectral index-based method to estimate the [α/Fe] abundances using low-resolution (R $\sim$ 2000), moderate SNR ($>$ 40) SDSS spectra. We studied the ages of a sample of main sequence turnoff halo field stars selected using a cuts in colour and Galactic latitude. With our method (described in section 2.3), we could split the halo field star population statistically into an α-rich and α-poor subsample. We used a Sobel-Kernel edge detection method to determine the turnoff temperature, and thus ages of the two stellar subsamples. Our results can be summarized in the following points:

1. A spectral-index based method (see section 2.3 for more details) was constructed to rank stars based on [α/Fe]. We have estimated the uncertainties of the [α/Fe] to be on the order of $\sim \pm$ 0.15 dex. This method can be used on a range of stellar parameters and is a semi-empirical method to estimate [α/Fe] that automatically accounts for the stellar parameters. The uncertainty in [α/Fe] from our method is comparable to the other methods (e.g. Lee et al., 2011). Using this method, we found that the halo is comprised of an α-rich and α-poor population which may peak near [α/Fe] $\sim$ +0.40 dex and +0.20 dex respectively (see Figure 2.12). It may be possible to extend this basic method to find stars with spectral peculiarities (e.g. s-process enriched star, etc.) which is something we plan to explore in future. Finally, this method can be expanded to other elemental species and spectral-types.

2. Given the large absolute age, based on the Y^2 isochrones, which included α-enrichment and atomic diffusion, the Galactic halo must have been formed very early on. It is also likely that the Galaxy is a relatively quiet place not having undergone a major merging event in the last 8 Gyr. This is consistent with other observations and theoretical studies (e.g. Schuster et al., 2012; Robertson et al., 2005; Font et al., 2006; Zolotov et al., 2009, 2010).

3. We have made a first measure of the age-metallicity relation of halo field stars separated by α-abundances at low metallicities. There appears to be a difference, on the order of 1 Gyr, in the ages of the α-rich and α-poor subsamples (see section 2.5). Using the Y^2 isochrones we found the α-rich subsample is older than the α-poor subsample in the high-metallicity case ([Fe/H] $\gtrsim$ -1.4 dex) which confirms the observational results of Schuster et al. (2012) and the theoretical results of Zolotov et al. (2009, 2010). However, we extended the results of Schuster et al. (2012) to lower metallicities and found there is a break around [Fe/H] $\sim$ -1.4 dex, and the α-rich subsample becomes coeval with the α-poor subsample. Interestingly, this bifurcation in the age-metallicity diagram is also seen in globular clusters. This hints that the α-rich population, with a shallow age-metallicity relation, was formed in a rapid event with high star formation (e.g. collapse of a protogalactic gas cloud), while the α-poor stars were formed in an environment with a slower chemical evolution timescale. Our results also confirm the idea that the α-rich subsample may be a population formed in situ while the α-poor subsample may have formed in satellite galaxies and accreted into the Milky Way halo.

The relative age sequence we found support the models of Zolotov et al. (2009, 2010). These models point out that we can use the fraction of in situ and accreted stars to disentangle the importance of accretion events in the assembly of the Galactic halo. With this new spectral-index based method to estimate [α/Fe] from low-resolution spectra, we are in a good position to study the relative fraction of α-rich and α-poor stars in the Galactic halo. In fact, I co-supervised a masters student who completed a study on the fraction of α-rich and α-poor stars in the Galactic halo using the Gaia-ESO survey (Gilmore et al., 2012) and found that $\sim$20% of the metal-poor stars were α-poor (Jackson-Jones et al., 2014).

With upcoming large-scale surveys such as Gaia (Perryman et al., 2001), Gaia-ESO (Gilmore et al., 2012), 4MOST (de Jong et al., 2012), and GALAH (Anguiano et al., 2014), it will be possible to resolve large samples of stars in position, velocity, distance and chemical phase-spaces. The next generation of data will undoubtedly open new windows into studying the ages of individual halo field stars as a function of chemical abundances providing detailed insights of the early stages of our home galaxy.

Acknowledgements

We would like to thank P. Nissen for helpful comments and for the validation dataset he graciously provided us. This work was partly supported by the European Union FP7 programme through ERC grant number 320360. This study was made possible by the Sloan Digital Sky Survey.

3

Characterizing the High-Velocity Stars of RAVE: Discovering Metal-Rich High-Velocity Stars

This chapter reproduces the paper: '*Characterizing the high-velocity stars of RAVE: the discovery of a metal-rich halo star born in the Galactic disc',* **Hawkins, K.**, Kordopatis, G., Gilmore, G., Masseron, T., Wyse, R. F. G., Ruchti, G., Bienaym, O., Bland-Hawthorn, J., Boeche, C., Freeman, K., Gibson, B. K., Grebel, E. K., Helmi, A., Kunder, A., Munari, U., Navarro, J. F., Parker, Q. A., Reid, W. A., Scholz, R. D., Seabroke, G., Siebert, A., Steinmetz, M., Watson, F., Zwitter, T., 2015a, MNRAS, **447,** 2046.
The author's contribution to the chapter includes: selection of the sample, all orbital integrations, analysis of two high-resolution stellar spectra required for the project, and the production of the manuscript.

Abstract

In this chapter, I aim to characterize high-velocity (HiVel) stars in the solar vicinity both chemically and kinematically using the fourth data release of the RAdial Velocity Experiment (RAVE). We used a sample of 57 HiVel stars with Galactic rest-frame velocities larger than 275 km s^{-1}. With 6D position and velocity information, we integrated the orbits of the HiVel stars and found that, on average, they reach out to 13 kpc from the Galactic plane and have relatively eccentric orbits consistent with the Galactic halo. Using the stellar parameters and [α/Fe] estimates from RAVE, we found the metallicity distribution of the HiVel stars peak at [M/H] = –1.2 dex and is chemically consistent with the inner halo. There are a few notable exceptions that include a hypervelocity star (HVS) candidate, an extremely high-velocity bound halo star, and one star that is kinematically consistent with the halo but chemically consistent with the disk. High-resolution spectra were obtained for the metal-rich HiVel star candidate

and the second highest velocity star in the sample. Using these high-resolution data, we report the discovery of a metal-rich halo star that has likely been dynamically ejected into the halo from the Galactic thick disk. This discovery could aid in explaining the assembly of the most metal-rich component of the Galactic halo.

3.1 Introduction

The increase in the number of large spectroscopic surveys in the last decade has opened a new field of investigation: high-velocity (HiVel) stars. These stars are rare objects, defined by having velocities well above the typical speed of the stars one might expect (e.g. $>$80 km s^{-1} relative to the Sun, Schuster & Nissen, 1988), but below the Galactic escape speed. HiVel stars are intriguing in part because they can provide insight to the mechanism that produce their velocities. The origin of these HiVel stars can also provide useful information about the environments from which they are produced. While recent studies have used only the kinematics of high-velocity stars to obtain an estimate of the Galaxy's mass (e.g. Smith et al., 2007; Piffl et al., 2014), there have been only a few studies aimed at combining their chemical and kinematic information to get a picture of where these stars are produced and what caused them to achieve such high-velocities. Therefore, we aim to fill this gap by combining both the kinematics and chemistry of these HiVel stars using the RAdial Velocity Experiment (Steinmetz et al., 2006, RAVE) to discern if they are consistent with any particular component of the Milky Way and what may have produced them.

Ryan & Smith (2003) studied a sample of 10 intermediate-metallicity HiVel stars and found that most of them resemble the thick disk yet the HiVel stars of other studies (e.g. Schuster et al., 2006) suggested that HiVel stars are metal poor. This raises the question what is the chemical distribution (in [Fe/H] and [α/Fe][1] spaces) of HiVel stars in the solar neighbourhood? The answers to this question will ultimately aid in constraining where HiVel stars are born and thus help constrain models for how they are produced. In turn, this will help develop a better understanding for the assembly of the Galactic halo for which many of these HiVel stars are thought to currently reside. For example, if the metallicity distribution of HiVel stars is significantly more metal-rich compared to the halo, and if the [α/Fe] distribution is comparable to the disk, it may support the suggestion of Bromley et al. (2009) that the metal-rich tail of the Galactic halo may have come from kinematically heated, stars which formed in the disk.

These 'runaway' disk stars described above are a subclass of HiVel stars and were first identified by Humason & Zwicky (1947). Runaway disk stars can provide an invaluable connection between star formation in the Galactic disk and halo. These stars are rare and described by peculiar velocities up to 200 km s^{-1} and are thought to have formed in the disk and ejected into the halo. Theoretically, runaway stars can be produced through a number of different mechanisms including: (1) binary supernova ejection (e.g. Blaauw, 1961; Portegies Zwart, 2000) and (2) dynamical ejection due to 3- and 4-body encounters (e.g. Poveda, Ruiz & Allen, 1967; Bromley et al., 2009). It is thought that these above mechanisms can produce both low-mass and high-mass runaway stars. Yet most of the literature regarding runaway stars focuses on high-mass O and B type stars. This is likely because observationally O and B type runaway stars are bluer compared to normal, low-mass halo stars among where they were found (e.g.

[1]The α-elements include those which have atomic numbers as a multiple of 4, such as Mg, Ti, Si, and Ca. [α/Fe] in this paper is defined as the mean abundance of these α-elements.

Poveda, Allen & Hernández-Alcántara, 2005). Characterizing HiVel stars, particularly in a data set with evolved low-mass stars, will allow us to search for these elusive stars.

Another intriguing subclass of HiVel stars is hypervelocity stars (HVSs), which are racing through space at above the escape speed of the Milky Way. These stars are thought to be produced via three-body interactions between a binary star system and the super massive black hole at the Galactic Centre (Hills, 1988). However, other production mechanisms have been proposed to explain stars which do not seem to originate in the Galactic Centre (e.g. Yu & Tremaine, 2003; Przybilla et al., 2008; Heber et al., 2008; Tillich et al., 2009). HVSs and HiVel stars can be used to infer many aspects about the Milky Way such as Galactic escape speed, and Galactic mass (Smith et al., 2007; Piffl et al., 2014), and HVS, in particular, offer a window into the mass function and dynamics of the environment near the massive black hole at the Galactic center (Portegies Zwart et al., 2006; Löckmann, Baumgardt & Kroupa, 2008; Löckmann & Baumgardt, 2008; Lu, Yu & Lin, 2007; Brown, Geller & Kenyon, 2012). The benefit of finding and characterizing these HiVel stars and HVS can be translated into better understanding the structure, dynamics and evolution of the Milky Way. Most of the confirmed HVSs are early-type O and B type stars due to the selection bias of current HVS surveys. In recent years, there have been a few HVS candidates that are more evolved, later-type stars (Brown, Geller & Kenyon, 2012, 2014; Palladino et al., 2014). RAVE mostly targets late-type dwarfs and giants, and thus any HVS candidates will add to a now growing list of late-type HVSs candidates. Many studies have been devoted solely to search for HVS through dedicated surveys (e.g. Brown, Geller & Kenyon, 2012, 2014) as well as large surveys such as the Sloan Digital Sky Survey (Kollmeier et al., 2010; Palladino et al., 2014; Zhong et al., 2014, SDSS). However, HVS have not been searched for in the RAVE data set. In this paper, we can naturally explore this by searching for HiVel stars.

While the main purpose of our study is to characterize, kinematically and chemically, HiVel stars, we will also investigate the runaway and hypervelocity candidates, for which we also have high-resolution spectra. In this paper, we start by searching for these rare HiVel stars using the RAVE data set and a series of selection criteria (described in section 3.2). We then move on to discuss the kinematic, chemical distribution of our HiVel sample in section 3.3. Using these distributions, we search for and suggest the origins of HVS and runaway star candidates. We summarize our key findings, put our findings into context with other studies and conclude in section 3.4.

3.2 A Sample of High-Velocity Stars

3.2.1 RAVE Survey Data Release 4

One of the easiest ways to search for HiVels is to use large astronomical surveys with high quality kinematic measurements, such as radial velocity (RV) and proper motions, etc. To this end, we make use of the fourth data release of RAVE (Kordopatis et al., 2013a, RAVE DR4). RAVE has obtained data using the multi-object spectrograph on the 1.2-m Australian Astronomical Observatory's UK Schmidt Telescope in Australia. The RAVE DR4 catalogue has reduced spectra and radial velocities (RVs) for nearly a half-million stars and represents one of the largest available catalogues to date. RAVE spectra are moderate resolution (R = $\lambda/\Delta\lambda \sim 7000$) around the Ca II triplet covering the wavelength range of 8410 – 8795 Å. For more information regarding RAVE, we refer the reader to the data release papers: Steinmetz

et al. (2006); Zwitter et al. (2008); Siebert et al. (2011); Kordopatis et al. (2013a) and the review of Kordopatis (2014). In addition to the accurate RV estimates, with errors on the order of 2 km s^{-1}, DR4 contains stellar parameters and distances with errors of about 10-20 percent. RAVE also has an associated chemical abundance catalogue, which provides estimates of 6 elements including Fe and several α-elements (described in Boeche et al., 2011). The chemical pipeline used a hybrid approach of inferring abundance using the curves-of-growth for different elements as well as a penalizing χ^2 technique of synthetic grid matching. Boeche et al. (2011) was able to determine the abundances of [α/Fe] and iron with a mean error of $\sim \pm$ 0.2 dex. This work will refer to [M/H] as metallicity and the traditional [Fe/H] as the iron abundance. [M/H] $\sim$ [Fe/H] under the assumption that the star follows the standard α-enrichment scheme observationally seen in the Milky Way:

1. $[\alpha/Fe]$ = 0.00 dex for [Fe/H] $\geq$ 0.00 dex
2. $[\alpha/Fe]$= -0.40 $\times$ [Fe/H] dex for -1 $\leq$ [Fe/H] $<$ 0.00 dex
3. $[\alpha/Fe]$ = 0.40 dex for [Fe/H] $<$ -1.00 dex

If these criteria do not hold, the global RAVE metallicity, [M/H], does not equal [Fe/H]. However, this only happens for a small percentage of the stars. The trend for RAVE stars is such that [M/H] $>$ [Fe/H] for low metallicity (Kordopatis et al., 2013a, Figure 28).

3.2.2 High-Resolution Data

A few targets, namely several interesting HiVel and HVS candidates were followed up at high-resolution to enable detailed elemental abundance analysis. The high-resolution (R $\sim$ 31500) spectra were obtained using the ARC Echelle Spectrograph (ARCES) on the Apache Point Observatory (APO) 3.5-m telescope. The spectra were reduced in the standard way: bias subtraction, extraction, flat field division and stacking using the echelle package of IRAF[2]. The final high-resolution spectra have a typical SNR $\sim$ 90-200 $pixel^{-1}$ in the wavelength region of 4500 – 9000 Å.

Stellar parameters (T_{eff}, log g, microturbulent velocity, ξ, and [Fe/H]) have been derived spectroscopically using the Brussels Automatic Code for Characterizing High accUracy Spectra (BACCHUS, Masseron et al., in preparation) code. The current version uses a grid of MARCS model atmospheres (Gustafsson et al., 2008a), a specific procedure for interpolating the model atmosphere thermodynamical structure within the grid (Masseron, 2006) and the radiative transfer code TURBOSPECTRUM (Alvarez & Plez, 1998; Plez, 2012). Atomic lines are sourced from VALD, Kupka & Ryabchikova (1999), Hill et al. (2002), and Masseron (2006). Linelists for the molecular species are provided for CH (T. Masseron et al. 2014, in press), and CN, NH, OH, MgH and C2 (T. Masseron, in prep); the lines of SiH molecules are adopted from the Kurucz linelists and those from TiO, ZrO, FeH, CaH from B. Plez (private communication).

The stellar parameters determination relies on a list of selected Fe lines. The first step consists in determining accurate abundances for the selected lines using the abundance module for a given set of $T_{eff}$and log g. The abundance determination module proceeds in the following way: (i) a spectrum synthesis, using the full set of (atomic and molecular) lines, is used for local

[2]Distributed by NOAO, operated by AURA under cooperative agreement with the NSF.

continuum level finding; (ii) cosmic and telluric rejections are performed; (iii) local signal-to-noise is estimated; (iv) a series of flux points contributing to a given absorption line is selected. Abundances are then derived by comparing the observed spectrum with a set of convolved synthetic spectra characterized by different abundances. Four different diagnostics are used: χ^2 fitting, core line intensity comparison, global goodness-of-fit estimate, and equivalent width comparison. A decision tree then rejects the line, or accepts it keeping the best matching abundance.

The second step consists in deducing the equivalent widths of Fe lines using the stellar parameter module. The last step of the procedure consists in injecting the derived equivalent widths in TURBOSPECTRUM to derive abundances for a grid of 27 neighboring model atmospheres (including three $T_{\rm eff}$, three log g and three microturbulence velocities, covering the parameter space of interest). For each model, the slopes of abundances against excitation potential and against equivalent widths, as well as Fe I and Fe II lines abundances are computed. The final parameters are determined by forcing that the ionization equilibrium is fulfilled, and that simultaneously null slopes for abundances against excitation potential and against equivalent widths are encountered. The whole procedure is iterated twice per star, a first guess using the RAVE stellar parameters as a starting point and then again with a different starting point. This was done to obtain an independent set of stellar parameters compared to RAVE. We adopted the parameters from the second iteration for each star, however both iterations produce parameters that are in very good agreement. Individual elemental abundances in each of the absorption features were determined using a χ^2 minimization technique to synthesized spectra. We visually inspected all fits in order to ensure the abundances were determined accurately. We take the mean and dispersion of the individual line abundances as the abundance and internal error respectively.

3.2.3 Distances and Proper Motions

Proper motions were sourced from the fourth US Naval Observatory CCD Astrograph Catalogue (UCAC4), which contains proper motions for over 100 million objects. We choose UCAC4 because the error in proper motion is generally smaller compared to other catalogues (see Binney et al., 2014b, for discussion). UCAC4 reaches a limiting magnitude of R = 16, with a peak in the formal uncertainty on the order of 4 mas/year (Zacharias et al., 2013). The small uncertainties in proper motion make them ideal for estimating the total velocity vector accurately. Following the suggestion of Zacharias et al. (2013), we discard any star with an uncertainty in proper motion larger than 10 mas/year to avoid stars which have been labeled as 'problematic' by the UCAC4. For most stars, the UCAC4 proper motions are, within the uncertainty, in good agreement with other proper motion catalogues. Stars with no proper motions were discarded because the full kinematics cannot be explored without estimated proper motions. All stars that had a double star flag not equal to zero (it was either identified as a component of a double star system or it could not be ruled out as a double star) were excluded. Distances were determined from the estimated spectrophotometric parallax for each star using a method described by Binney et al. (2014a). We selected only stars that have estimated parallaxes because we need the distance to study the full kinematics of the stars. We expect typical uncertainties in parallax for our sample are on the order of 25% (see Binney et al., 2014a, for more details).

3.2.4 Selection of High-Velocity Stars

To obtain robust data, we employed the quality control cuts laid out by Kordopatis et al. (2013a) as well as some additional cuts described here.

1. The signal-to-noise ratio (SNR) must be larger than 20 pixel^{-1}. This cut was chosen to ensure that we are selecting out spectra that have well known uncertainties in the stellar parameters, and chemical abundances. Where there is more than one entry in the database we accept the entry with the highest SNR.

2. The errors in the heliocentric RV (HRV) must be lower than 10 km s^{-1}. This is to obtain precise RV measurements in order to constrain the full space motion. This cut is also necessary for accurate parameter estimation (Kordopatis et al., 2013a).

3. The estimated log g must be larger than 0.5 dex. Stars with log g less than 0.5 dex are much more likely to be treated in a problematic way during the stellar parameter estimation (Kordopatis et al., 2013a).

4. Calibrated metallicity [M/H] must be larger than -5 dex (measured by the stellar parameter pipeline). Stars below this were discarded stars because the stellar parameter estimation (Kordopatis et al., 2013a) pipeline was not designed to perform for these stars.

5. Calibrated $T_{\rm eff}$ must be between 4000 K and 7000 K. This was based on the range bounded by the synthetic library with which the RAVE chemical pipeline used.

6. The estimated stellar rotation velocity of the star, $V_{\rm rot} < 50$ km s^{-1}. This cut allowed us to discard stars that the stellar parameter and chemical pipelines would be likely to not produce reliable results.

7. All spectroscopic morphological flags defined by Matijevič et al. (2012) must be 'normal'. This criterion minimized the chance of binary star contamination or highly uncertain stellar parameters and distances (Kordopatis et al., 2013a; Binney et al., 2014a; Boeche et al., 2011).

8. The DR4 algorithm convergence parameter (algo_conv) must not equal 1. We used this cut to ensure the stellar parameter pipeline converged (Kordopatis et al., 2013a)

9. The value frac (i.e. the fraction of the spectrum that matches the model in a satisfactory way) associated with the chemical pipeline must be greater than 0.7.

10. The χ^2 associated to the chemical pipeline must be lower than 2000. This cut along with the value frac cut was used to confirm that the spectra were adequately fit with no glaring errors in the continuum (Boeche et al., 2011).

11. The Tonry-Davis correlation coefficient, which is a measure of the quality of the template fit for each stellar spectra during the RV measurement, must be larger than 10 (Piffl et al., 2014; Steinmetz et al., 2006; Kordopatis et al., 2013a).

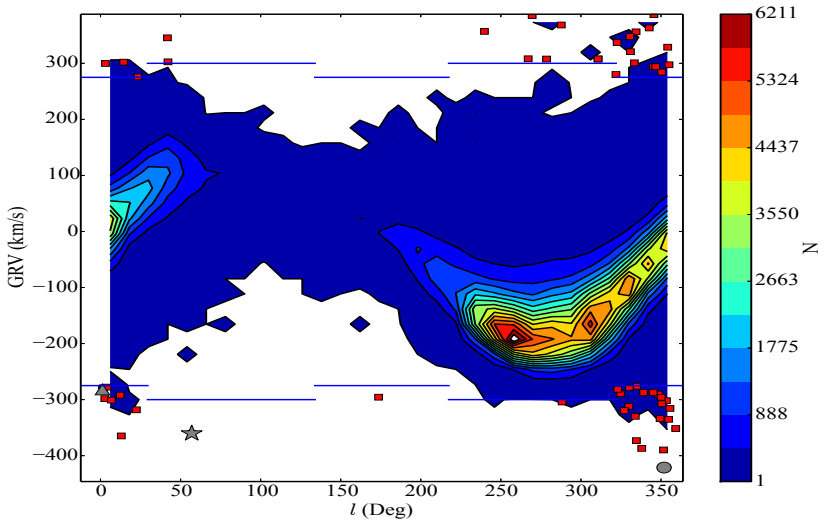

Figure 3.1 – The selected HiVel targets (red squares) in l-Galactic relative radial velocity (GRV) space. The blue lines indicate the selection criteria where the $|\mathrm{GRV}|>$ 300 km s^{-1} near galactic latitudes pointed in the direction of disk rotation ($l = 90 \pm 50°$ and $270 \pm 50°$) and $|\mathrm{GRV}| >$ 275 km s^{-1} elsewhere. The contours show the full RAVE DR4 sample from which the HiVel targets were selected. The colour in all 2D density diagrams, like this one, represents the number of stars in each density contour for the full RAVE dataset. The gray circle, star and triangle refers to three interesting targets, namely J1544, J2217, and J1610 respectively, that we discuss in the further detail in later sections.

A total of 274 481 objects passed the 11 quality cuts described above. We corrected the HRVs for solar and local standard of rest (LSR) motion to obtain a RV relative to the Galactic rest-frame (GRV) using the following formula:

$$\mathrm{GRV} = \mathrm{HRV} + (U_\odot \cos l + (V_\odot + V_{\mathrm{LSR}}) \sin l) \cos b + W_\odot \sin b, \tag{3.1}$$

where $U_\odot, V_\odot, W_\odot, V_{\mathrm{LSR}}, l, b$ are the 3-dimensional solar velocity, the velocity of the local standard of rest (assumed to be 220 km s^{-1}), the Galactic longitude and latitude, respectively. For reference, the velocity convention adopted by this work is: U is positive if directed toward the Galactic Centre (l = 0°, b = 0°), V is positive along the direction of rotation (l = 90°, b = 0°) and W is positive if pointed toward the North Galactic Pole (b = 90°). In this convention, the Sun's orbital velocity vector $\vec{v}_\odot = [U_\odot, V_\odot, W_\odot] = [14.0, 12.24, 7.25]$ km s^{-1}, $\mathrm{V_{LSR}}$ = 220 km s^{-1} and its position is at [X, Y, Z] = [8.28, 0, 0] kpc (Schönrich, 2012).

We initially selected objects with a $|\mathrm{GRV}| >$ 300 km s^{-1} in regions where most of the disk velocity is along the line-of-sight (at l = 90 ±50° and 270 ±50°) and $|\mathrm{GRV}| >$ 275 km s^{-1} elsewhere. This requirement was designed to cut out most of the disk contamination that would otherwise occur owing to the geometry. These boundaries are selected to be just above the speed one would expect when considering disk rotation and velocity dispersion. Lowering the cut on GRV would cause larger contamination from ordinary disk stars while increasing the threshold decreases the total sample size. The selection of our sample can be found in Figure 3.1. The open circle, star and triangle refers to three interesting targets including J154401.1-162451, J221759.1-051149, and J161055.6-112009 (henceforth J1544, J2217, and J1610) respectively, that we discuss in the further detail in later sections. The signal of the disk can be seen as the

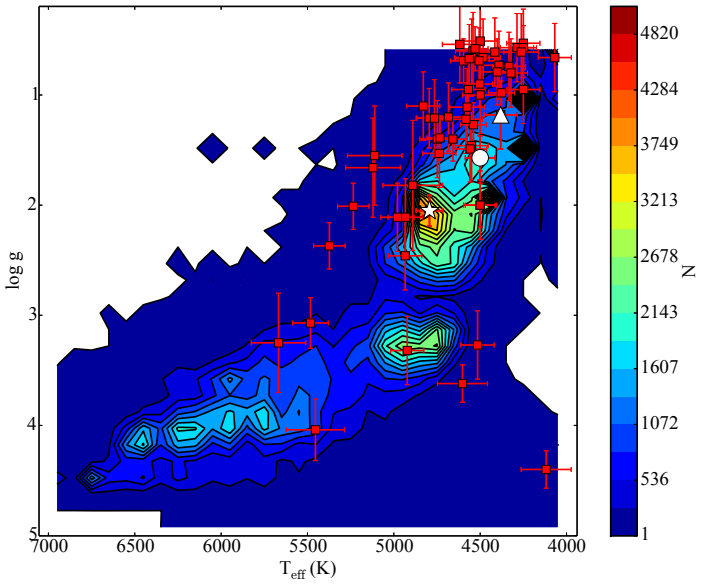

Figure 3.2 – Contours of the T_{eff}- log g for stars in the RAVE sample with the HiVel stars (red squares) shown as being primarily giant stars. The open circle, star and triangle are the same as in Figure 3.1.

sinusoidal-like high-density path seen in Figure 3.1. This is a geometric effect caused by the fact that disk stars move along rotation and thus when we observe at angles directed towards or away from rotation, most of the disk star velocity will be in the line-of-sight direction. The high density around $l = 270°$ with GRV $\sim$ –220 km s^{-1} represents the disk because at that Galactic longitude, the total velocity vector is primarily in the line-of-sight direction.

We further required the distances, proper motions (with uncertainties less than 5 mas/yr) and metallicities to be known. There are 57 stars in our final sample that passed all of the 11 quality control cuts and the kinematic cut described above. Piffl et al. (2014) used a sample of 76 HiVel stars in RAVE to determine the mass of the Milky Way halo. Our sample has fewer HiVel stars than Piffl et al. (2014) which is a result of the fact that they use a much lower GRV cut (200 km s^{-1}) than we do by selecting for a counter-rotating population assumed to be the halo population. Our kinematic selection criteria in l-GRV space can be seen in Figure 3.1. It is important to note that we choose to select our HiVel stars on the GRV rather than the full space motion because of the smaller error in GRV, on the order of a few km s^{-1}, compared to the error on the full space motion (few tens of km s^{-1}). Most of the HiVel stars in our sample are giant stars (Figure 3.2) and located within 5 kpc of the Sun (Figure 3.3). RAVE is run out of the Southern Hemisphere and as a result the spatial distribution of the selected HiVel stars is not symmetric around the Sun.

3.2.5 Full Space Velocity and Stellar Orbits

We fully resolve the space velocity and position vectors in order to study the orbital parameters of our sample. The right ascension (α), declination (δ), and distances for each source yield a full 3D position vector relative to the Galaxy. These vectors are related by the Sun's Galactocentric position ($\vec{r}_\odot = [8.28, 0, 0]$ kpc) such that $\vec{r} = \vec{r}_* + \vec{r}_\odot$ (Schönrich, 2012). Furthermore, the

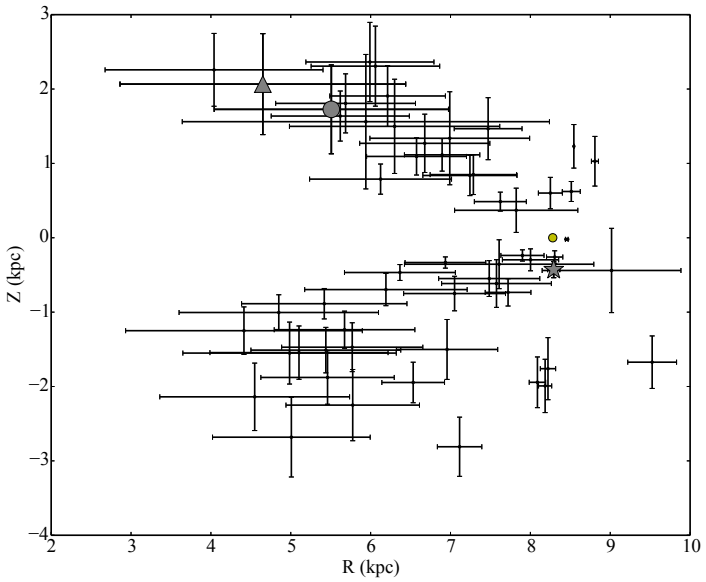

Figure 3.3 – The position of our HiVel stars relative to the Galaxy. For reference the Sun (yellow circle) is at (R, Z) = (8.28, 0) kpc. The gray circle, star and triangle are the same as in Figure 3.1.

proper motions give two dimensions of velocity within the plane of the sky, $\vec{\mu}$. We use the estimated proper motion, distance, and RV to construct a current velocity vector (relative to the Galactic-rest frame) via Johnson & Soderblom (1987). Uncertainties in the current position and velocity vector were determined using a Monte Carlo approach with a thousand realizations, randomly varying the uncertainties of all of the observables and recalculating the position and velocity vectors and studying the final distribution, similar to the approach used by Gratton et al. (2003) and Boeche et al. (2013). We excluded two stars with uncertainties in the total space velocity larger than 200 km s^{-1} as it would be difficult to constrain their total space motions.

To obtain the orbital parameters for our HiVel sample, we integrated the orbit of a test particle through an assumed Galactic potential (Φ) which is a sum of the potential of a logarithmic halo ($\Phi_{halo}(r)$), Miyamoto-Nagai disk ($\Phi_{disk}(R, z)$), and a Hernquist bulge ($\Phi_{Bulge}(r)$). We made use of the same parameter choices as Johnston, Spergel & Hernquist (1995).

$$\Phi_{halo}(r) = \frac{v_0^2}{2} \ln (r^2 + d^2), \tag{3.2}$$

where v_0 is a characteristic velocity of 186 km s^{-1} with a scale length, d, of 12.0 kpc.

$$\Phi_{disk}(R, z) = -\frac{GM_{disk}}{\sqrt{R^2 + \left(a + \sqrt{z^2 + b^2}\right)^2}}, \tag{3.3}$$

where the M_{disk} is the mass of the disk assumed to be 10^{11} M$_\odot$), a and b are scale lengths set to 6.5 kpc, and 0.26 kpc, respectively.

$$\Phi_{Bulge}(r) = -\frac{GM_{Bulge}}{r + c}, \tag{3.4}$$

where M_{Bulge} is the mass of the bulge and is set to $3.4 \times 10^{10} M_{\odot}$ and c is a scale-length set to 0.7 kpc. In the above definitions $r = \sqrt{x^2 + y^2 + z^2}$ and $R = \sqrt{x^2 + y^2}$. Using this potential, we confirmed the circular speed, $v_{\rm circ}$, at the solar radius of 8.28 kpc to be $v_{\rm circ}$ = 224 km s^{-1} and an orbital period for the local standard of rest (LSR) at this radius of 220 Myr consistent with Schönrich (2012). We also verified that energy and angular momentum is conserved in all orbital integrations to at least one part in a million or better.

To better understand the kinematics of our stars, we estimated the maximum distance above the Galactic plane (denoted Z_{max}) and the eccentricity from the orbital integration. We define the eccentricity as a function of the apogalactic distance, r_{ap}, and the perigalactic distance, r_{per}, such that $e = (r_{ap} - r_{per})/(r_{ap} + r_{per})$. Uncertainties in the orbital integrations were estimated in a similar Monte Carlo approach as above (the initial conditions were varied to within their uncertainties) with 100 orbital integrations. The uncertainty in the eccentricity is less than 0.15.

3.3 Results: Metal-Poor High-Velocity Stars, Ejected Disk Stars and Hypervelocity Stars

In this section we discuss the kinematic (section 3.3.1) and chemical (section 3.3.2) distributions of our HiVel star sample. By combining the results of these two sections we discuss the discovery of a metal-rich halo star that likely originated in the Galactic disk and put forward a HVS candidate.

3.3.1 Kinematics of High-Velocity Stars

We first studied the kinematics of our HiVel sample using a Toomre diagram (Figure 3.4), which quantifies different Galactic components using the velocity vector. It is important to note that the velocities in the Toomre diagram are relative to the LSR and thus the HVS boundary (green line, Figure 3.4), which must be converted to a non-rotating reference frame, was shifted by V = –220 km s^{-1}. From inspection, there are two stars which sit at or above the HVS boundary (green line, Figure 3.4). We note that the HVS boundary is position dependent. For simplicity, we choose the escape speed at the solar circle as an illustrative HVS boundary on the Toomre diagram. However, a true HVS candidate must have a velocity higher than the escape speed at its position. There is also one star that has disk-like kinematics and is likely with the high-velocity tail of the thin disk or disk-like contaminants. Using the rough boundaries that kinematically separate the thin-disk, thick disk and halo of Venn et al. (2004) for example, we found that most of our HiVel stars exist in the halo-region of the Toomre diagram which means these stars are likely be on highly elliptical orbits reaching out to a maximum distances from the Galactic plane, Z_{max}, larger than 10 kpc with eccentricities of $e \gtrsim 0.5$. Adopting larger boundaries in the Toomre diagram that kinematically separate the thin-disk, thick disk and halo would result in a slight contamination by the thick disk.

We further studied the kinematics of our sample by comparing the e and Z_{max} (Figure 3.5). The power of the e-Z_{max} plane is the ability to sort out stars of similar orbits, because e describes the shape of the orbit and Z_{max} describes the amplitude of the vertical oscillations (e.g. Boeche et al., 2013). The e-Z_{max} plane combined with metallicity allows us to characterize the orbits of our HiVel stars while also considering the chemical distribution. Our HiVel sample has median e of 0.73 and median Z_{max} of 13 kpc, which is kinematically consistent with the halo

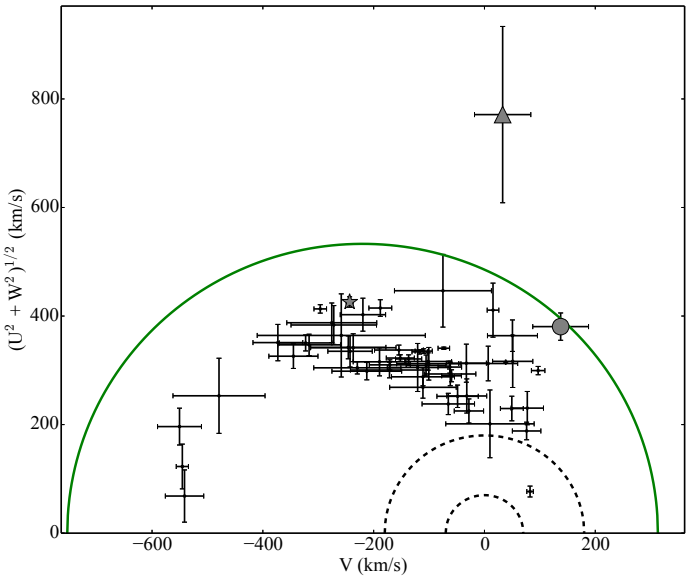

Figure 3.4 – Toomre diagram for the HiVel sample. All velocities are relative to the LSR. The 2 black dashed rings show roughly the boundaries of the thin disk and thick disk at a constant velocity of 70 km s^{-1}, 180 km s^{-1} respectively (Venn et al., 2004). We can see that most of our HiVel stars belong to the halo kinematically. The green solid line represents a constant galactic-rest frame velocity of 533 km s^{-1}, and is thus shifted relative to the other velocities. A star above this boundary may be a HVS candidate pending its position. We find one HVS candidate with a total Galactic rest frame velocity larger than 800 km s^{-1} (more than 1-σ above the escape speed). There are two stars, namely J1610 and J154401.1-16245, which have velocities above the HVS limit. The gray circle, star and triangle are the same as in Figure 3.1.

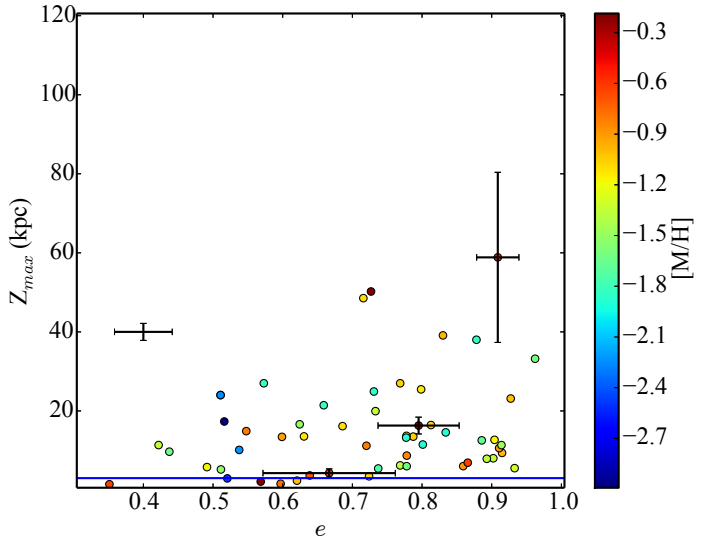

Figure 3.5 – Eccentricity, e, as a function of the maximum Galactic plane height obtained by our HiVel stars during a 1 Gyr orbital integration. The colour of each star represents it metallicity, [M/H]. The solid horizontal line represents the edge Z_{max} of the thick disk, Z = 3 kpc (Carollo et al., 2010). The error bar to the left represents the median uncertainty in both parameters. The other three error bars in e and Z_{max} are shown for the stars with the largest errors on distances. This plot excludes HVS candidates. The high Z_{max} and e for most of the HiVel stars indicate they are consistent with the Galactic halo.

population. This result confirms the assumptions of older works (e.g. Schuster & Nissen, 1988; Ryan & Smith, 2003; Schuster et al., 2006) that HiVel stars in the solar vicinity mostly belong to the halo. We note that while our specified Galactic potential is thought to be an adequate assumption locally, the potential at large distances from the Sun can be relatively uncertain. Since HiVel stars can probe these distant regimes the uncertainties in the orbital parameters, namely the Z_{max}, r_{ap} and r_{per}, are probably underestimated as we only quote the uncertainties by propagating the errors on the observables. There are a few stars with $Z_{max} \lesssim 3$ kpc and eccentricities below 0.6. These stars could be interpreted as thick-disk contaminants especially given their relatively high ($>$ –0.90 dex) metallicities (Boeche et al., 2013; Kordopatis et al., 2013b,c).

3.3.2 Chemical Distribution of High-Velocity Stars

The kinematics of our HiVel sample (Section 3.3.1) indicate that these stars are drawn from the halo population and thus they should also have a chemical fingerprint that is consistent with the halo. In Figure 3.6 we compare the normalized metallicity distribution of the RAVE and HiVel samples. It is clear that the mean metallicity of the RAVE sample ($\overline{[M/H]}_{\rm RAVE}$ = –0.22 dex) is significantly higher than mean metallicity of the HiVel sample ($\overline{[M/H]}_{\rm HiVel} \sim$ –1.2 dex). The mean metallicity of our HiVel sample is slightly higher but consistent within the errors with the inner Galactic halo, which is thought to have a mean metallicity around –1.60 dex (Carollo et al., 2007, 2010). The inner Galactic halo is also thought to have measurable α-enhancement (Nissen & Schuster, 2010; Haywood et al., 2013; Boeche et al., 2013).

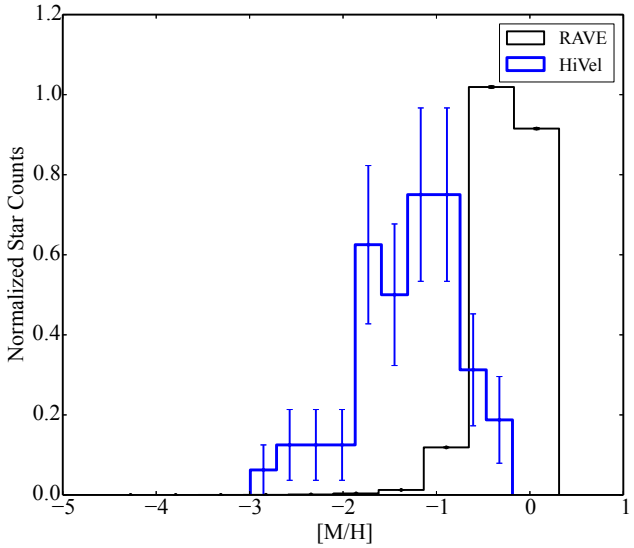

Figure 3.6 – [M/H] distribution for the RAVE catalogue (black) and the HiVel sample (blue). The HiVel stars in our sample are significantly more metal-poor compared to the RAVE mother sample. The peak of the metallicity distribution of HiVel stars is –1.18 dex and is consistent with the Galactic halo. The error bars are computed assuming Poisson noise.

The distribution in [α/Fe] space will provide information on the birthplace of the stars. Many recent surveys have shown that the different components of the Galaxy can be partially separated in [α/Fe] - metallicity space (Nissen & Schuster, 1997; Fulbright, 2002; Stephens & Boesgaard, 2002; Nissen & Schuster, 2010; Ruchti et al., 2010; Nissen & Schuster, 2012; Haywood et al., 2013; Feltzing & Chiba, 2013). These studies show a relationship between the metallicity and [α/Fe] that is described in section 3.2.1.

For comparison, we plot our HiVel stars in this space relative to the full RAVE sample along with the expected Galactic trend (see Figure 3.7). The expected uncertainty in both [M/H] and [α/Fe] is $\sim \pm$ 0.2 dex (Kordopatis et al., 2013a). Further, we can see from Figure 3.8 that our HiVel star sample is slightly α-enriched, with a mean α-abundance of $\overline{[\alpha/Fe]}_{HiVel}$ = +0.24 dex, compared to the RAVE mother sample, with a mean α-abundance of $\overline{[\alpha/Fe]}_{RAVE}$ = +0.14 dex. This result is, within the errors, chemically consistent with the halo population. The large dispersion (on the order of 0.25 dex) in the [α/Fe] is likely a result of the uncertainty of the individual [α/Fe] estimates, but may also represent an α-poor and α-enriched population in our HiVel sample. The large uncertainty in the [α/Fe] estimates, particularly at low metallicity, is a result of insufficient spectral information on the abundance of α-elements in the part of the spectrum covered by RAVE (Kordopatis et al., 2013a).

Combining the kinematic and chemical properties, we plot the 2-dimensional density of the GRV as a function of metallicity for the RAVE sample and our HiVel stars (red squares) in Figure 3.9. Viewing the results in this space allows us to identify clearly one star, J2217 that has an extremely high GRV ($\sim$ –360 km s^{-1}), but paradoxically is metal-rich ([M/H] = – 0.18 $\pm$ 0.08 dex). This star is an outlier compared to the rest of the metal-poor HiVel stars of our sample. If we make a simplistic assumption that the (inner) Galactic stellar halo metallicity distribution function can be modeled as a Gaussian with a mean of [M/H] = –1.50 dex and

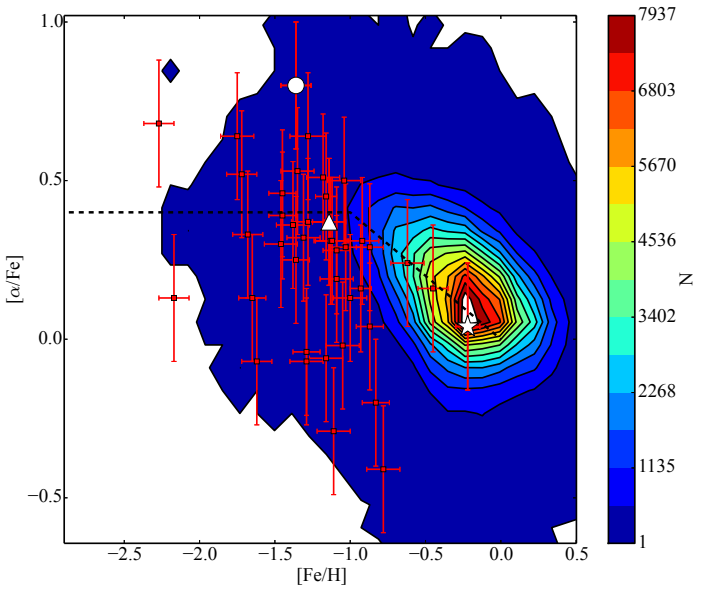

Figure 3.7 – Contour plot showing the [α/Fe] - [Fe/H] for RAVE including where the HiVel stars (red squares) fall in this space. The dotted black line represents the standard Galactic trend in this space. Most of our HiVel stars are, within the errors consistent with the halo population with [Fe/H] less than -1.0 dex and noticeable α-enrichment. The open circle, star and triangle are the same as in Figure 3.1.

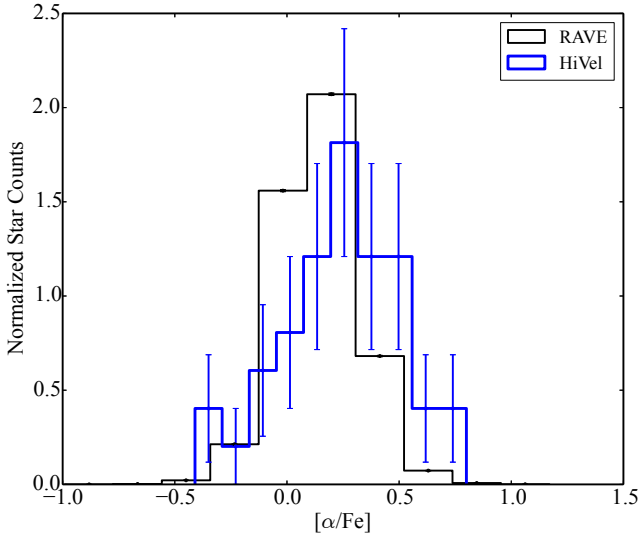

Figure 3.8 – [α/Fe] distribution for the RAVE catalogue (black) and the HiVel sample (blue). The HiVel sample is slightly more α-enriched compared to the RAVE mother sample but the dispersions are comparable.

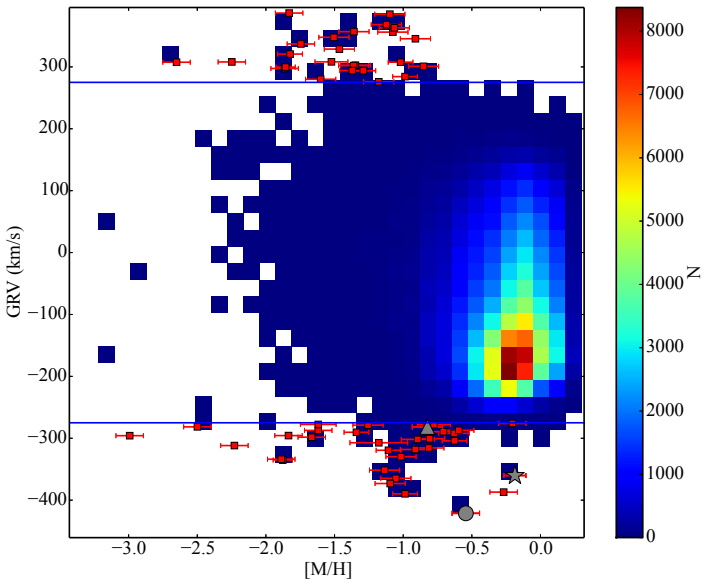

Figure 3.9 – 2D density plot of the GRV and [M/H] for the RAVE sample. The horizontal lines indicate the adopted kinematic minimum kinematic GRV needed to be classified as a HiVel candidate (i.e. $|\mathrm{GRV}| > 275$ km s^{-1}). It is interesting to note that there are three HiVel stars with relatively high metallicities ([M/H] larger than -0.5 dex). The gray circle, star and triangle are the same as in Figure 3.1.

$\sigma_{[M/H]}$ = 0.50 (Chiba & Beers, 2000), the probability of drawing a star of that metallicity is 0.4% (2.64σ). Assuming higher mean and dispersion values, (-1.20, 0.54, see Kordopatis et al., 2013b) the probability of drawing a star of that metallicity is 2.9% (1.89σ). In either case, the probability of drawing a star of this metallicity from the Galactic halo population is small ($<$ 4% Carollo et al., 2007, 2010; Kordopatis et al., 2013b; An et al., 2013). This star provides us with a unique opportunity to explore metal-rich halo stars. As such, the next section is devoted to exploring this object in more detail.

It is worth mentioning there are two additional stars that have [M/H] larger than –0.50 dex which are classified as HiVel stars. J152905.9-365544 is a giant star which has a GRV = – 276 $\pm$ 1.5 km s^{-1} with a metallicity of [M/H] = –0.21 $\pm$ 0.1 dex and [α/Fe] $\sim$ +0.16 $\pm$ 0.2 dex. On the Toomre diagram (Figure 3.4), this star sits just above the thick disk region. An orbital integration of this star was performed and showed that this star has an $e \sim 0.5$ with $Z_{max} \sim$ 3 $\pm$ 1 kpc. Using the same probabilistic kinematic classification from Bensby, Feltzing & Lundström (2003) this star would be categorized as a thick disk star. Given the kinematic and chemical properties of this star, we expect it is a thick disk contaminate. The second star, J193647.0-590741, has an estimated metallicity of [M/H] = –0.27 $\pm$ 0.1 dex, yet kinematically it has a GRV = –387 $\pm$ 1.7 km s^{-1}. Orbital integration for this star indicates it has an $e \sim$ 0.82 with $Z_{max} \sim 16 \pm 5$ kpc which resembles halo-like properties. While the stellar parameter pipeline is able to estimate its $T_{\rm eff}$, log g and [M/H], the chemical pipeline fails to provide an estimate of the [Fe/H] and [α/Fe]. This could be due to the low SNR ($\sim$ 20) and thus high-resolution, high SNR follow-up will be necessary to confirm the chemical signature of this star.

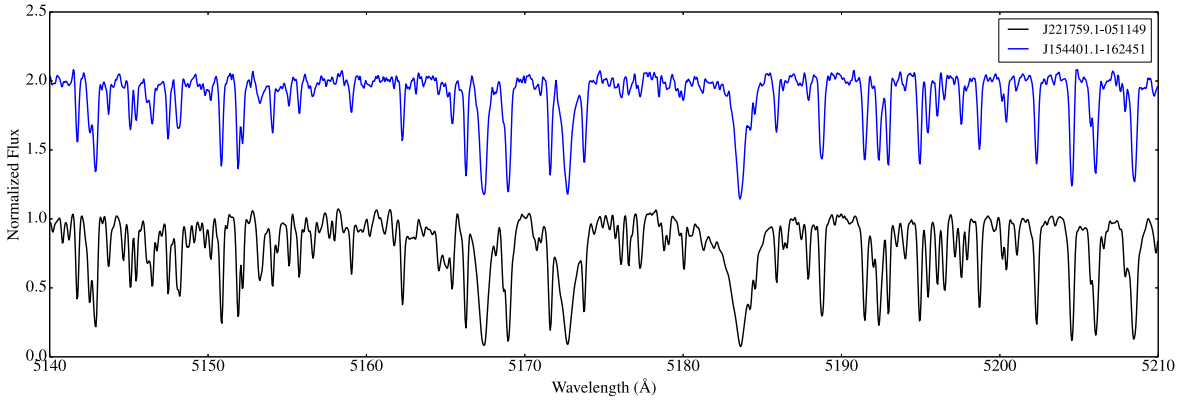

Figure 3.10 – The observed high-resolution ACRES spectrum of the giant star J2217 (black line) and J1544 (blue line) in the Mg I triplet region. In both cases, these spectra were used to determine the chemical abundances which are shown in Table 3.1 and Table 3.2.

3.3.3 Captured Star or High-Velocity Ejected Disk Star?: The Case of J2217

The giant star J2217 represents an unusually fast-moving object with a metallicity significantly above –1.0 dex. The RAVE stellar parameter pipeline has estimated it to have a T_{eff}= 4790 $\pm$ 80 K and log g = 2.05 $\pm$ 0.15 dex. It has a metallicity of –0.18 $\pm$ 0.1 dex (at a SNR = 71.0) and an [α/Fe] = +0.04 $\pm$ 0.2 dex. The chemistry of this star, particularly its high metallicity and low levels of α-enhancement, is consistent with the disk or possibly a star captured from an external source but not the Galactic halo like most of the other HiVel stars. We have no reason to believe this star is a member of a binary star based on the 'normal' spectral morphological classification of Matijevič et al. (2012). Additionally, it is also classified as a single normal star in the UCAC4 catalogue (Zacharias et al., 2013).

Kinematically, the star is in the extreme halo region residing below the HVS boundary on the Toomre Diagram (Figure 3.4). The total Galactic rest frame velocity of this star is 426 $\pm$ 10 km s^{-1}. The Tonry-Davis correlation coefficient estimated by RAVE is 65 indicating the template for cross-correlation was a good fit and the uncertainty in the measured RV approximately 1 km s^{-1}. This puts it $\sim$ 100 km s^{-1} below the Galactic escape speed of Piffl et al. (2014) at its Galactocentric distance of r = 8.01 $\pm$ 0.13 kpc. To better understand the kinematics of this object we integrated its orbit over 1 Gyr (Figure 3.13) to get an idea of the shape of the orbit without being dominated by errors due to the observables. We found that J2217 reaches a Z_{max} = 31 $\pm$ 5 kpc and has an overall eccentricity of e = 0.72 $\pm$ 0.02 . This star kinematically resembles a halo star given its Z_{max} (e.g. Coşkunoğlu et al., 2012) and eccentricity yet its chemistry suggests it may belong to the Galactic disk or a dwarf galaxy (e.g. Sheffield et al., 2012).

The orbital integration described above was used to estimate the time-of-flight (TOF) for this star assuming it was produced in the Galactic disk and ejected into the halo (Figure 3.13). The star is passing through the disk and the TOF required to get the star near the galactic disk again ($|z| < 3$ kpc) is $\sim$ 600 Myr well within the lifetime of a low-mass star. Bromley et al. (2009) argued that the metal-rich tail of the (inner) halo metallicity distribution may come from stars born in the disk and kinematically heated (by binary supernova ejection) into the halo as ejected disk stars. In terms of the time-scale, kinematics, and chemistry it is perfectly

reasonable this object was born in the Galactic disk and was kinematically heated, maybe as a result of binary ejection or tidal interactions with satellite galaxies as in Purcell, Bullock & Kazantzidis (2010) or other gravitational means, causing it to be now observed as a part of the Galactic halo. Alternatively, this star could be a captured star from a dwarf spheroidal galaxy. Reaching out to a vertical distance of 35 kpc is within the distance of a couple massive dwarf galaxies (e.g. Sagittarius dwarf galaxy). Chemically, massive dwarf galaxies like the Sagittarius dwarf spheroidal galaxy may contain some stars as metal-rich as [M/H] = -0.20 dex with a depletion in [α/Fe] $\sim$ -0.20 dex (Sbordone et al., 2007). J2217 is metal-rich with no noticeable enhancement in [α/Fe] (i.e. an [α/Fe] = –0.20 dex is at the edge of the $\pm$ 0.2 dex error budget for the [α/Fe]) estimate. However, given that the 3 dimensional velocity vector of this star indicates that it is currently on its way out of the Galaxy and chemically resembles the Galactic disk, it is more likely this star is an ejected disk star.

We observed J2217 in high-resolution (black line in Figure 3.10) using the APO to try determining whether the star is captured or ejected. The analysis of the high-resolution spectra (described in Section 3.2.2) yielded stellar parameters (T_{eff}= 4635 $\pm$ 77 K, log g = 2.06 $\pm$ 0.20 dex, and [Fe/H] = -0.21$\pm$ 0.13 dex, HRV = –490.8 $\pm$ 0.8 km s^{-1}) that are in very good agreement with those found in RAVE DR4. The confirmation of the impressively high metallicity for this HiVel star indicates that it is unlikely to have come from a dwarf galaxy that, on average, have significantly lower metallicities. The results of the abundance pattern in the α-elements (Figure 3.11(a)) and neutron-capture elements (Figure 3.11(b)), of J2217 can be found in Figure 3.11 and correspondingly in Table 3.1. We also explored the Na-Ni abundances of J2217 in Figure 3.12. Studies as early as Nissen & Schuster (1997) indicated that [Na/Fe] and [Ni/Fe] may distinguish stars that were accreted from other field population stars. Exploring this relationship between Ni-Na will allow us to determine if J2217 is consistent with having being accreted. We found that the abundance pattern of J2217 namely the α-elements, neutron-capture elements, and the abundance ratios of [O/Fe], [Ni/Fe], [Al/Fe], and [Na/Fe], most resembles the Galactic (thick) disk. It is worth mentioning that we found a relatively high enhancement in Barium, [Ba/Fe] = +0.35 dex, for J2217 however it is still within the range of the thick disk. Furthermore, the abundances in Table 3.1, namely Fe, Na, and O, were compared with known globular clusters (e.g. Carretta et al., 2009) to determine if this star is consistent with a metal-rich globular cluster. This test indicated that J2217 is not consistent with any known globular clusters.
When we couple the abundance analysis with that of the orbital integration we favor a scenario in which this star was kicked out of the Galactic (thick) disk. The mechanism by which this star was ejected from the disk, namely dwarf galaxy heating (Purcell, Bullock & Kazantzidis, 2010), binary supernova ejection (Bromley et al., 2009) or other gravitational mechanisms, is unclear. Regardless, this provides observational support for the idea that the most metal-rich stars in the Galactic halo may have been assembled by kicking out Galactic disk stars (Bromley et al., 2009).

3.3.4 Hypervelocity Star Candidates

HVSs are rare fast-moving stars which have velocities that exceed the Galactic escape speed ($\sim$ 533 km s^{-1} at the solar circle, Piffl et al., 2014). Recent studies have used HVSs to better understand conditions and dynamics of the hidden Galactic Centre as well as the Galactic halo

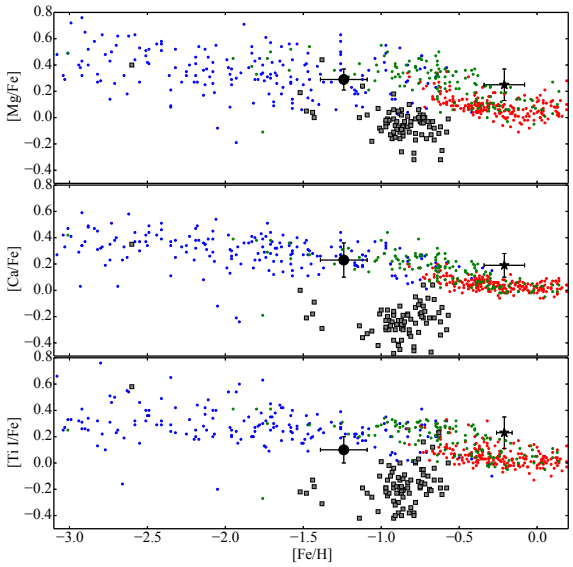

(a)

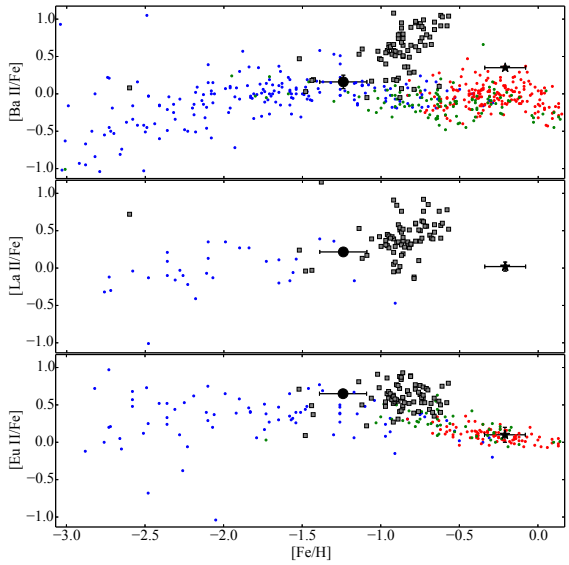

(b)

Figure 3.11 – (a) The abundance patterns of the α-elements as a function of metallicity including [Mg/Fe], [Ca/Fe] and [Ti/Fe] from top to bottom, respectively for J2217 (black star) and J1544 (black circle). (b) The abundance patterns of neutron-capture elements as a function of metallicity including [Ba II/Fe], [La II/Fe], and [Eu/Fe] from top to bottom respectively. The small coloured circles represent abundances of thin disk (red), thick disk (green) and halo (blue) stars from Venn et al. (2004). For comparison, the grey squares show an example of a dwarf galaxy (Fornax) from Letarte et al. (2010). J2217 is chemically consistent in the α-elements and most neutron-capture elements with the Galactic thick disk. On the other hand J1544 is chemically consistent with the halo field population or dwarf galaxies. The error bars on the side represent the mean error of the abundances from the literature.

Table 3.1 – ARCES Elemental Abundances for J2217

Species	N	log ϵ (X)	σ	[X/Fe]
Mg	8	7.56	0.14	+0.25
Ca	6	6.32	0.04	+0.23
Ti I	4	4.91	0.04	+0.23
Ti II	5	4.75	0.13	+0.07
Si	8	7.42	0.10	+0.13
C I	5	8.33	0.05	+0.16
O	1	8.69	0.10	+0.25
Fe I	60	7.23	0.13	...
Fe II	8	7.22	0.08	...
Al	3	6.43	0.03	+0.28
Na	5	617	0.09	+0.22
Ni	5	6.15	0.09	+0.14
Ba II	3	2.30	0.04	+0.35
La II	6	0.93	0.06	+0.02
Zr II	3	2.19	0.07	–0.18
Sr I	1	2.73	0.10	+0.03
Eu II	2	0.40	0.02	+0.08
Cu I	3	3.78	0.10	–0.21

NOTES: The chemical abundances of each species (column 1) are shown. Column 2 is the number of lines used to determine the abundance of each species. Column 3 is the log of the absolute abundance and the line-to-line dispersion is listed in column 4. Where there is only one line we quote a conservative error bar of $\pm$ 0.10 dex. Finally, column 5 is the solar relative [X/Fe] abundance ratios.

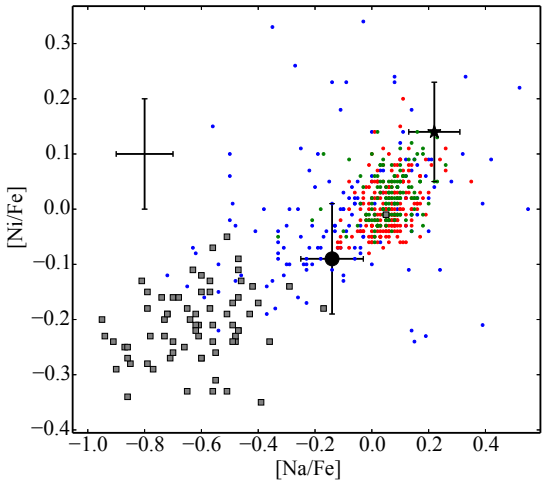

Figure 3.12 – The observed high-resolution abundances of Ni as a function of Na for J2217 (black star) and J1544 (black circle). The symbols are the same as Figure 3.11. We find that J2217 is chemically consistent with the disk and not a dwarf galaxy (such as the Fornax). However it is possible that J1544, within the errors, may be consistent with a massive dwarf galaxy. The error bars on the side represent the mean error of the abundances from the literature.

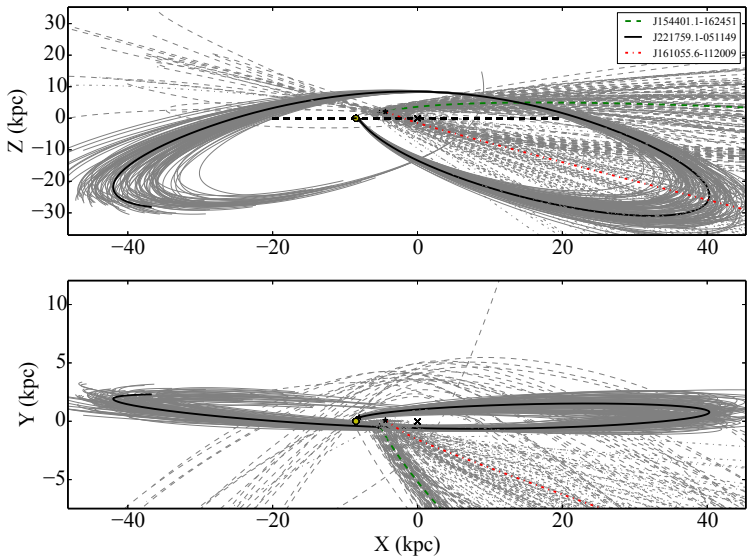

Figure 3.13 – A 1 Gyr orbital integration for J2217 (black solid line), J1544 (green dotted line), and J1610 (red dash-dotted line). The yellow circle represents the Sun, the black 'x' represents the Galactic center and the black asterisk represents the current position of J2217 and J1544. The thin grey lines are 100 draws of the orbital integration to illustrate the uncertainty. We find that both stars are currently passing through the disk.

(Kollmeier et al., 2010; Brown, Geller & Kenyon, 2009).

We have identified one HVS candidate whose galactic rest-frame velocity is more than 1-σ above the escape speed and three stars whose velocities, within the uncertainties, are above 500 km s^{-1} that are worth additional scrutiny. Their basic observational and kinematical properties can be found in Table 3.3 and Table 3.4, respectively. J1610 has a metallicity of –0.86 dex and is at a Galactocentric radius of approximately 5 kpc and has a V_{GRF} of 807 $\pm$ 154 km s^{-1}. Assuming the escape speed of Piffl et al. (2014) at this radius ($\sim$ 600 km s^{-1}), this candidate has a velocity at least 1-σ above the escape speed and is among the first HVS candidates from RAVE. If the escape speed were significantly higher, above 650 km s^{-1} , this candidate would have a velocity less than 1-σ escape speed but still impressively high. It is important to note that there is relatively bright star close to this star and thus the uncertainties in the proper motion may be underestimated. More accurate distance and proper motion estimates will help decrease the error in order to confirm the total space velocity of this target.

To date, the tens of known HVSs are massive (3-4 $M_{\odot}$) early-type main sequence stars, including hot O, B, and A type stars (Brown, Geller & Kenyon, 2009, 2012, 2014). Li et al. (2012) and Palladino et al. (2014) have recently identified potential later-type HVS candidates which still need confirmation. The HVS candidate J1610 is among the few that are not early-type stars. Orbital integration of this HVS candidate indicates that it does not originate in the Galactic Centre. If confirmed, this would add to an increasing list of candidate HVS that do not seem to originate in the Galactic Centre (e.g. Palladino et al., 2014) and thus need an alternative production mechanism (e.g. Yu & Tremaine, 2003; Abadi, Navarro & Steinmetz, 2009; Heber et al., 2008; Przybilla et al., 2008).

The second star, J1544, has a V_{GRF} of 523 $\pm$ 40km s^{-1}. This star has a velocity that is just below the escape speed at it position (which is expected to be $\sim$ 570 km s^{-1}). We have followed up J1544 with high-resolution echelle spectra from the ARCES instrument in order obtain detailed abundances in part because its high global metallicity ([M/H] = –0.54 dex). The spectrum of J1544 in the Mg I triplet region can be found in Figure 3.10. The stellar parameters of the star was determined using the high-resolution spectra and indicate that J1544 has a $T_{\rm eff}$= 4458 $\pm$ 120 K; log g = 1.44 $\pm$ 0.2 dex; [Fe/H] = -1.24 $\pm$ 0.15 dex; $\xi = 1.77 \pm 0.06$ km s^{-1} which is consistent with the RAVE parameters. Furthermore, we have confirmed the very high heliocentric RV (–406.7 $\pm$ 0.80 km s^{-1}) observed by RAVE for this star. Using the stellar parameters, we have determined the abundance of several α and neutron-capture elements. Table 3.2 contains the high-resolution abundance analysis for J1544 including the species, number of lines used, log of the absolute abundance, the uncertainty (which was estimated as the standard deviation of the abundance determined from each individual line), and the solar-scaled abundance ratio. The [α/Fe] for this star was determined by computing the mean abundance of the four α-elements including Mg, Ca, Ti, and Si.

The high-resolution abundances for the α-elements (Figure 3.11(a)) indicates that this star has a small enhancement with an [α/Fe] = +0.21 $\pm$ 0.07 dex. At this metallicity, the star would be classified as one of the 'low-α' stars of Nissen & Schuster (2010) which they interpret as an 'accreted' population. The neutron-capture elemental abundances of J1544 is consistent with both the field population and a dwarf galaxy like the Fornax (Figure 3.11(b)). The Al and Mg ratios, [Al/Fe] = +0.20 $\pm$ 0.05 and [Mg/Fe] = +0.29 $\pm$ 0.08 dex respectively, are consistent with the field population (Fulbright, 2002). The abundance of [Na/Fe] and [Ni/Fe] are both depleted (Figure 3.12). Within the errors, the Na-Ni of this star is consistent with both the field star population of Venn et al. (2004) and Nissen & Schuster (2011) and massive dwarf galax-

Table 3.2 – ARCES Elemental Abundances for J1544

Species	N	log ϵ (X)	σ	[X/Fe]
Mg	5	6.58	0.08	+0.29
Ca	8	5.30	0.13	+0.23
Ti I	5	3.76	0.09	+0.10
Ti II	1	3.74	0.10	+0.08
Si	7	6.50	0.06	+0.23
Al I	3	5.33	0.05	+0.20
Na I	5	4.79	0.11	–0.14
Ni I	5	4.90	0.10	–0.09
Fe I	95	6.21	0.15	...
Fe II	16	6.23	0.16	...
Ba II	3	1.11	0.09	+0.16
La II	5	0.13	0.04	+0.22
Eu II	2	-0.05	0.04	+0.65

NOTES: The format is the same as in Table 3.1.

ies. The chemical information from the high-resolution analysis indicates that this star is not consistent with the Galactic thin disk, because its metallicity is too low. The star also does not likely originate in the Galactic thick disk as one would expect a higher α-abundance. We also compared the abundances of this star to known globular clusters with similar iron abundances (e.g. Carretta et al., 2009). The depletion in Na and Ni combined with the abundances of Al and Mg do not seem consistent with globular clusters. Its chemistry suggests that this star may have a halo or dwarf galaxy formation site.

It is also worth mentioning that in addition to the HVS candidate there are two other extremely high velocity bound stars whose total velocity vectors are at or near 500 km s^{-1}. Namely, J142103.5-374549 has a $v_{GRF} = 460 \pm 70$ km s^{-1} and J155304.7-060620 has a $v_{GRF} = 474 \pm 43$ km s^{-1}. Orbital integration shows J142103.5-374549 is on a highly elliptical orbit (e = 0.91) getting as close as 3.72 kpc to the Galactic Centre. We note that J142103.5-374549 was excluded from Piffl et al. (2014) because of its unusual place on the Hertzsprung-Russell diagram. Further, both J142103.5-374549 and J155304.7-060620 have conflicting distance, and proper motions when comparing UCAC4 and distances from Binney et al. (2014a) with those of Bilir et al. (2012) and Francis (2013).

3.4 Discussion and Conclusion

We have aimed to characterize a set of HiVel stars in RAVE DR4. To do this, we applied a series of quality cuts on the initial RAVE DR4 ensuring the data have quality spectra and measurements needed to estimate the 6D position and velocity vector as well as estimates of metallicity. In order to maximize the HiVel stars in our sample, we selected stars which have absolute galactic-rest frame RVs (corrected for solar motion) > 275 km s^{-1}. This led to some contamination from disk stars near l = 90° and 270° where the primary component of the disk stars velocity is along the line-of-sight. To deselect these stars, we made a stricter cut in GRV within $\pm$ 50° of the above Galactic latitudes. We sourced the distances from the estimated spectrophotometric parallaxes from Binney et al. (2014a) and proper motions

Table 3.3 – Observational Properties of HVS and Metal-Rich HiVel Star Candidates

RAVEID	α (°)	δ (°)	$\mu_\alpha cos(\delta)$ (mas/yr)	$\sigma\mu_\alpha cos(\delta)$ (mas/yr)	μ_δ (mas/yr)	$\sigma\mu_\delta$ (mas/yr)	$d_\odot$ (pc)	$\sigma d_\odot$ (pc)	[M/H] (dex)	[α/Fe] (dex)
J155304.7-060620	238.26967	-6.10550	-28.0	1.3	26.9	1.3	1480	463	-1.67	0.33
J142103.5-374549	215.26442	-37.76361	8.7	1.4	3.1	1.4	3963	2541	-1.60	0.50
J154401.1-162451	236.00438	-16.41428	2.6	2.2	3.8	2.6	3544	1222	-0.54	0.80
J161055.6-112009	242.73183	-11.33589	-25.6	2.2	22.9	2.4	4369	1451	-0.82	0.37
J152905.9-365544	232.27450	-36.92883	-4.8	2.0	3.4	2.0	2863	738	-0.21	0.16
J193647.0-590741	294.19575	-59.12814	3.5	1.1	-8.4	2.2	618	301	-0.27	...
J221759.1-051149	334.49604	-5.19700	-20.4	1.1	5.0	1.1	580	147	-0.18	0.04

Table 3.4 – Kinematic Properties of HVS and Metal-Rich HiVel Star Candidates

RAVEID	HRV (km s^{-1})	σHRV (km s^{-1})	U (km s^{-1})	σU (km s^{-1})	V (km s^{-1})	σV (km s^{-1})	W (km s^{-1})	σW (km s^{-1})	V_{GRF} (km s^{-1})	σV_{GRF} (km s^{-1})
J155304.7-060620	-317.9	0.9	-408	46	235	10	47	66	473	47
J142103.5-374549	405.2	1.1	413	76	136	96	151	29	460	73
J154401.1-162451	-403.2	1.7	-335	21	358	48	-179	37	522	29
J161055.6-112009	-296.8	1.0	-589	112	249	50	492	209	807	159
J152905.9-365544	-189.8	1.5	-186	15	296	24	26	33	351	17
J193647.0-590741	-314.0	1.8	-261	8	317	12	146	6	436	8
J221759.1-051149	-491.0	0.9	-133	10	-23	6	404	9	426	8

from the UCAC4 catalogue (Zacharias et al., 2013) and combined it with the information from RAVE DR4 to obtain the full 6D position and velocity vectors. We also implemented an orbital integration code to determine orbital parameters, particularly Z_{max} and eccentricity, to study the kinematics. I note here that the orbital integration code that I wrote for this project was used in Kunder et al. (2015) to show that some metal-poor bulge stars may be halo contamination. We also studied the metallicity and [α/Fe] abundances that compliment the kinematical study of our sample by attempting to measure the chemical distribution of our HiVel stars.

Our results can be summarized in the following way:

1. Kinematically, HiVel stars are mostly consistent with the Galactic halo (Figure 3.4) and are characterized by eccentric orbits that can extend, on average, 14 kpc out of the Galactic plane. Chemically, HiVel stars in RAVE are metal-poor (peaking at [M/H] = –1.2 dex) compared to the rest of RAVE (peaking [M/H] = –0.22 dex), which is consistent with the (inner) halo (Kordopatis et al., 2013b; Carollo et al., 2007, 2010; Piffl et al., 2014). While the metal-weak thick disk overlaps the metallicity region of the HiVel stars, the rather hot kinematics that describe the HiVel stars (Figure 3.5) favours the Galactic halo as a current location. It is interesting to point out that the mean iron abundance of the inner Galactic halo from Carollo et al. (2007) is slightly more metal-poor compared to the mean *global metallicity* of our HiVel stars.

2. The HiVel stars in our sample are, on average, α-enhanced compared to the rest of the RAVE sample (Figure 3.8). The [α/Fe] distribution of the HiVel stars is consistent, within the 1-σ error, to the α-enhancement ([α/Fe] $\sim$ +0.4) expected of inner halo stars (Haywood et al., 2013; Nissen & Schuster, 2012, 2010; Ruchti et al., 2010; Adibekyan et al., 2012; Sheffield et al., 2012). The inner halo is thought to be formed of two components: an α-rich component maybe formed in situ and an α-poor component possibly accreted by dwarf galaxies (Nissen & Schuster, 2010; Schuster et al., 2012; Hawkins et al., 2014). The large spread in α-enrichment of both the RAVE ($\sim$ 0.18 dex) and HiVel stars ($\sim$ 0.25 dex) in our sample could be suggestive of an α-rich and α-poor population in both samples. However, it is more likely that this is blurred by the uncertainty in the [α/Fe] estimates from the chemical pipeline of the RAVE DR4 (Boeche et al., 2011; Kordopatis et al., 2013a).

3. While most of the HiVel stars are metal-poor, there are several stars that have metallicity above –1.0 dex. These stars, while having kinematics that resemble halo stars, have disk like metallicity and thus do not conform to the rest of HiVel stars. One of these stars, J2217 has a particular high metallicity ([M/H] = –0.18). Depending on how one defines the metallicity distribution function in the halo this star is a $\sim$ 1.9-4σ outlier (An et al., 2013; Carollo et al., 2007, 2010; Kordopatis et al., 2013b; Chiba & Beers, 2000). Conversely, we can assess the probability that this star is kinematically connected to the thin disk, thick disk, or halo. This star is described by an orbit with a Z_{max} = 35 $\pm$ 10 kpc, overall eccentricity of e = 0.72 $\pm$ 0.03, and a Galactic rest frame velocity of 426 $\pm$ 10 km s^{-1} (consistent with the Galactic halo). Using the population classification from the full space motion described in Bensby, Feltzing & Lundström (2003), we found this particular giant star is classified as a 'high-probability' halo star. Ivezić et al. (2008) found that while the metallicity distribution of the inner halo peaks at -1.2 dex, the tail of the distribution extends up to approximately solar metallicities. Theoretically, Bromley

et al. (2009) discusses the possibility of runaway disk stars being a contributor to the high-metallicity tail of the inner stellar halo. Could this star be observational evidence of this conjecture?

To help answer this, we obtained high-resolution spectrum J2217 (Figure 3.10) to do detailed chemical abundance analysis. We confirmed the stellar parameters of RAVE and measured the abundances of light elements, α-elements and neutron-capture elements, which can be found in Table 3.1. The abundances (see Figure 3.11 and Figure 3.12) and the orbital integration (see Figure 3.13) of J2217 confirm that this star was likely born in the Galactic thick disk. The abundances of Fe, Na, and O are not consistent with known globular clusters (e.g. Carretta et al., 2009). Given the lack of s-process enhancement, or other chemical peculiarities, it is likely this star was kicked into the Galactic halo via gravitation mechanisms. Alternatively, given that nearly half of solar-type stars are in binary systems (Duchêne & Kraus, 2013), this star could also have been launched into the halo by a binary disruption event. The lack of neutron-capture and carbon enhancement however could point to the former scenario. The discovery of this runaway disk star indicates that while almost all HiVel stars currently reside in the Galactic halo, they were not necessarily *born* in the halo.

4. We have found a HVS candidate using RAVE whose total Galactic rest frame velocity is larger the expected escape velocity (above the 1-σ level). The HVS candidate is an evolved giant which is different than the known B-type HVS that are currently discussed in the literature (e.g. Brown, Geller & Kenyon, 2014, 2009).

5. We also followed up the star with the second highest velocity (with V_{GRF} larger than 500 km s^{-1}) in our sample (J1544). We confirmed the stellar parameters determined by RAVE of this star as well as measured abundance of several α-elements, neutron-capture elements. The chemical abundances, found in Table 3.2, are consistent with either the halo field star origin or (massive) dwarf galaxy origin (see Figure 3.11 and Figure 3.12). The high speed, total Galactic rest frame velocity of 526 $\pm$ 40 km s^{-1} , is near but not above the Milky Way escape speed at its position and is unusually fast for a halo field star. Furthermore, the orbital integration indicates this object is currently passing through the disk (Figure 3.13). While it may be possible for this star to be born in the halo and achieve such a high velocity it is also possible that the star has been accreted from a dwarf galaxy (e.g. Abadi, Navarro & Steinmetz, 2009; Piffl, Williams & Steinmetz, 2011) and may explain its velocity near the escape speed. The chemodynamics of this particular star is consistent with either scenario leaving its origins unknown.

It is interesting to study the chemistry and kinematics together of the HVS and HiVel star candidates as they give us invaluable information about the formation environment of these populations. Our analysis has shown that HVS that are near the Galactic escape speed should have complimenting chemical information to better constrain its formation environment. Palladino et al. (2014) has found a set of 20 metal-poor HVS candidates with SDSS of those 6 have velocities within 100 km s^{-1} of the escape speed assuming a spherical potential. Could these be captured stars as well? Complementary chemical abundance analysis may help decipher where these stars originate from and thus shed light on potential formation mechanisms for HVS. With the upcoming Gaia mission, we will better be able to constrain the distances,

proper motions and thus the total velocity vector for all of our stars but more specifically the HVS candidates.

4

Using Chemical Tagging to Redefine the Interface of the Galactic Disk and Halo

This chapter reproduces the paper: *'Using chemical tagging to redefine the interface of the Galactic disk and halo'*, **Hawkins, K.**, Jofré, P., Gilmore, G., Masseron, T, 2015b, MNRAS, **453,** 758
The author's contribution to the chapter includes: selection of the sample from the SDSS-III/APOGEE catalogue via SQL, separation of various components, exploration of all chemical abundances within the APOGEE catalogue for the sample, all code needed for the project, and the production of the manuscript.

Abstract

In this chapter, I present a chemical abundance distribution study in 14 α, odd-Z, even-Z, light, and Fe-peak elements of approximately 3200 intermediate metallicity giant stars from the APOGEE survey. The main aim of our analysis is to explore the Galactic disk-halo transition region between –1.20 <[Fe/H] < –0.55 as a means to study chemical difference (and similarities) between these components. In this paper, we show that there is an α-poor and α-rich sequence within both the metal-poor and intermediate metallicity regions. Using the Galactic rest-frame radial velocity (RV) and spatial positions, we further separate our sample into the canonical Galactic components. We then studied the abundances ratios, of Mg, Ti, Si, Ca, O, S, Al, C+N, Na, Ni, Mn, V, and K for each of the components and found the following: (1) the α-poor halo subgroup is chemically distinct in the α-elements (particularly O, Mg, and S), Al, C+N, and Ni from the α-rich halo, consistent with the literature confirming the existence of an α-poor accreted halo population; (2) the canonical thick disk and halo are not chemically distinct in all elements indicating a smooth transition between the thick disk and halo; (3) a subsample of the α-poor stars at metallicities as low as [Fe/H] $\sim$ –0.85 dex are chemically and dynamically consistent with the thin disk indicating that the thin disk may extend to lower

metallicities than previously thought, and (4) that the location of the most metal-poor thin disk stars are consistent with a negative radial metallicity gradient. Finally, we used our analysis to suggest a new set of chemical abundance planes ([α/Fe], [C+N/Fe], [Al/Fe], and [Mg/Mn]) that may be able to chemically label the Galactic components in a clean and efficient way independent of kinematics.

4.1 Introduction

The stars in the Milky Way change their properties over time in almost every aspect. On one hand, their atmospheric parameters change as they age, producing significant changes in their colours and luminosities, with complete generations of stars enriching the interstellar medium with chemical elements as they die and new generations forming from this enriched material. On the other hand, their positions and kinematics change as they move with orbits governed mostly by gravitation. The disentanglement of their spatial and dynamical properties, complemented with their ages and chemical compositions (when possible), are the tools that have been used for decades to classify the stars into different stellar populations building up a picture of the structure of the Milky Way we have today (e.g. Gilmore, Wyse & Kuijken, 1989; Freeman & Bland-Hawthorn, 2002; Helmi, 2008; Rix & Bovy, 2013, and references therein).

Among the phase spaces to 'separate' the Galactic components, the method of using chemical abundance ratios as a means to probe the Galactic components has been performed and advanced significantly in the past decade by using relatively large samples of high-resolution spectra (e.g. Edvardsson et al., 1993; Fuhrmann, 1998; Venn et al., 2004; Nissen & Schuster, 2010; Sheffield et al., 2012; Ramírez, Meléndez & Chanamé, 2012; Feltzing & Chiba, 2013; Bensby, Feltzing & Oey, 2014; Mikolaitis et al., 2014). In particular, the ratio of the mean of the α-elements relative to iron has been shown to be very powerful to disentangle the various Milky Way components. Active research has been dedicated in order to explain the two sequences found in the abundances of the α-elements respect to the abundances of iron. On one hand, at low metallicities ([Fe/H] ~ -1.2 dex), the low–α sequence is attributed to stars that were chemically enriched in an environment separate from that of the bulk of the halo and later accreted on to the Galactic halo. At higher metallicities ([Fe/H] ~ -0.5 dex), the α-poor stars are interpreted as the thin disk. On the other hand, at low metallicities the high-α sequence is attributed to the halo and at high metallicities the high-α sequence is attributed to the thick disk although there is likely significant overlap between the two. For a more detailed discussion on each component and how it separates in chemo-kinematic space, refer to section 1.3.

As a part of the Thesis, we have studied the stars at the Galactic disk(s)-halo interface by taking advantage of the APOGEE public spectroscopic survey (Eisenstein et al., 2011), which contains not only thousands of stars at this interface, but its very high-resolution spectra allow us to go far beyond the study of only α-elements. Specifically we are interested to know if the Galactic components must be defined in chemo-kinematic-spatial spaces or if they can be defined purely by chemistry.

In this chapter, we present a detailed chemical abundance evolution analysis of 14 different elements available in the APOGEE survey (including α, odd-even, light, and Fe-peak elements) with the aim to discuss how the thin disk, the thick disk, the halo and the accreted halo stars are linked. In particular, we are interested in the α-elements, carbon, nickel (and other Fe-peak elements), and other odd-even elements as they can be used to distinguish the accreted halo

from the canonical halo, and canonical thin disk from the canonical thick disk (e.g. Bensby, Feltzing & Oey, 2014). In section 4.2 we describe APOGEE data selection criteria and the subsample definitions. In section 4.3, we compare and contrast, element-by-element, the various Galactic components in order to better understand how they are linked. We then use the element-by-element analysis in order to discuss our results compared to the current literature on the halo-disk transition regions in section 4.4. In section 4.5 we use the abundance ratio trends to propose a new powerful chemical labeling technique that uses only chemistry to efficiently separate the various Galactic components. Finally, we summarize our findings in section 4.6.

4.2 Data and Subsamples

4.2.1 Data: The APOGEE Survey

To study the interface of the Galactic disks and halo, we employed the first two years of data from the SDSS-III/APOGEE survey (described in Eisenstein et al., 2011). APOGEE used H band spectroscopy to determine the stellar parameters, chemical abundances, and radial velocities for a large sample of stars. The most current data release (SDSS DR12) contains nearly 100 000 stars with stellar parameters, chemical abundance determinations and spectra (Holtzman et al., 2015). The typical uncertainties in the parameters are $\pm$100 K, $\pm$0.1 dex, $\pm$0.04 dex, and $\pm$0.04 dex in $T_{\rm eff}$, log g, [Fe/H], and [α/Fe], respectively. While there may be some systematics biases (potentially up to +0.20 dex, see Masseron & Gilmore, 2015), the precision of APOGEE chemical abundances are expected to be relatively high (with typical internal uncertainties of less than 0.10 dex). To minimize the potential uncertainties in the accuracy in the abundance scales, in this chapter we have done a relative abundance analysis of the various Galactic components.

We selected a sample of giant stars, beginning with the full APOGEE sample and using the following cuts:

- The signal-to-noise ratio (SNR) had to be larger than 100. We used this cut to ensure that the selected stars have quality estimates of the stellar parameters and [α/Fe].

- $T_{\rm eff} >$ 4000 K. This cut was chosen because as noted by Holtzman et al. (2015), stars with $T_{\rm eff} <$ 4000 K will likely have larger uncertainties in stellar parameters and chemical abundance.

- The ASPCAP, metallicity, and [α/Fe] flags must be set to 0. This cut ensured that there were no major flagged issues (e.g. low SNR, poor synthetic spectral fit, stellar parameters near grid boundaries, etc.).

- 1.0 $<$ log g $<$ 3.5 dex. This cut was used to deselect any dwarf stars for which the stellar parameters and chemical abundances would likely have large uncertainties (e.g. Nidever et al., 2014; Holtzman et al., 2015).

- The stars had to be located at $|b| < 60$ degrees. This was needed to separate disk-like from non-disk like kinematics in l-Galactic rest frame radial velocity (GRV) space as we discuss in section 4.2.2.

The initial sample contained about 69000 stars. The sample was then restricted to the metallicity regions –1.20 < [Fe/H] < –0.55 dex, which encompasses the transition between the Galactic disks and halo. This reduced the sample to about 3200 stars. We note that we used the uncalibrated [Fe/H] for metallicity rather than the calibrated global metallicity, [M/H], for the purposes of comparing [X/Fe] abundance ratios to literature. Holtzman et al. (2015) noted that the APOGEE uncalibrated [Fe/H] tends to be overestimated at low metallicities. However, applying the calibration to [Fe/H] would cause the [X/Fe] ratios to be inflated compared to literature values. In this chapter, we focus on a relative abundance analysis within subgroups, and as such, the use of [Fe/H] as opposed to [M/H] only changes the absolute abundance scale but does not change the relative analysis leaving our conclusions robust (see section 4.4.3 for more details). In the following section we use the chemistry and kinematics to decompose the sample into the various canonical Galactic components (similar to the scheme outlined in Figure 1.3).

4.2.2 Chemokinematic decomposition of canonical Galactic components

Since we are primarily interested in the disks-halo interface, our focus in this chapter is on the intermediate metallicity (–1.20 < [Fe/H] < –0.55 dex) region. In Figure 4.2 we plot the standard [α/Fe]-metallicity for the intermediate metallicity stars. With our initial sample we recovered the two disk sequences discussed in section 1.3.3 and seen in other APOGEE studies (e.g Nidever et al., 2014; Masseron & Gilmore, 2015). In the low-metallicity regime (–1.20 < [Fe/H] < –0.70 dex), we found the two sequences: an α-poor sequence (left magenta selection box) and an α-rich sequence (the left orange selection box) similar to Nissen & Schuster (2010). We determined the boundary between these two sequences by identifying the trough in the [α/Fe] distribution in three metallicity bins and performing a linear fit in the [α/Fe]-metallicity plane of these three metallicity bins similar to Recio-Blanco et al. (2014). In Figure 4.1, we show the [α/Fe] distribution in each of the metallicity bins used to determine the separation between the α-poor and α-rich sequences. The bins were chosen to ensure at least 50 stars were in each bin. We note that the bimodality is most clear when all halo stars (i.e. those stars assigned only to canonical and accreted halos not including stars from the disks and undetermined groups) are used without binning in metallicity space.

With the lack distances and proper motions we do not employ the Toomre diagram as a means to assign the stars to a component because we cannot estimate their full 3D velocity. However, we made use of the RVs, which have typical uncertainties on the order of 0.1 km s^{-1} . We used a method that combines the l and GRV in order to disentangle the halo from disk stars similar to Sheffield et al. (2012). We computed the GRV by correcting the radial velocity for solar motion (see Equation 1 of Hawkins et al., 2015b). For this, we assumed $\vec{v}_{\odot} = [U_{\odot}, V_{\odot}, W_{\odot}] = [14.0, 12.24, 7.25]$ km s^{-1}, $V_{\rm LSR}$ = 220 km s^{-1} (Schönrich, 2012). In Figure 4.3 we show the GRV/cos(b) as a function of l for the full APOGEE sample that pass our quality cuts (black contours). As noted by Majewski et al. (2012) and Sheffield et al. (2012), dividing by the GRV by the cos(b) accentuates the difference between the disk and non-disk components provided the data is restricted to $|b|< 60$ degrees allowing us to separate out halo stars more efficiently. This cut, while potentially eliminating some halo stars, still leaves enough to study the chemical abundance trends. We have also tested several $|b|$ cuts between 40 – 60 deg with little to no affect on the chemical abundance trends and overall conclusions of this work. As $|b|$ approaches larger values, the cos(b) becomes too small relative to the GRV

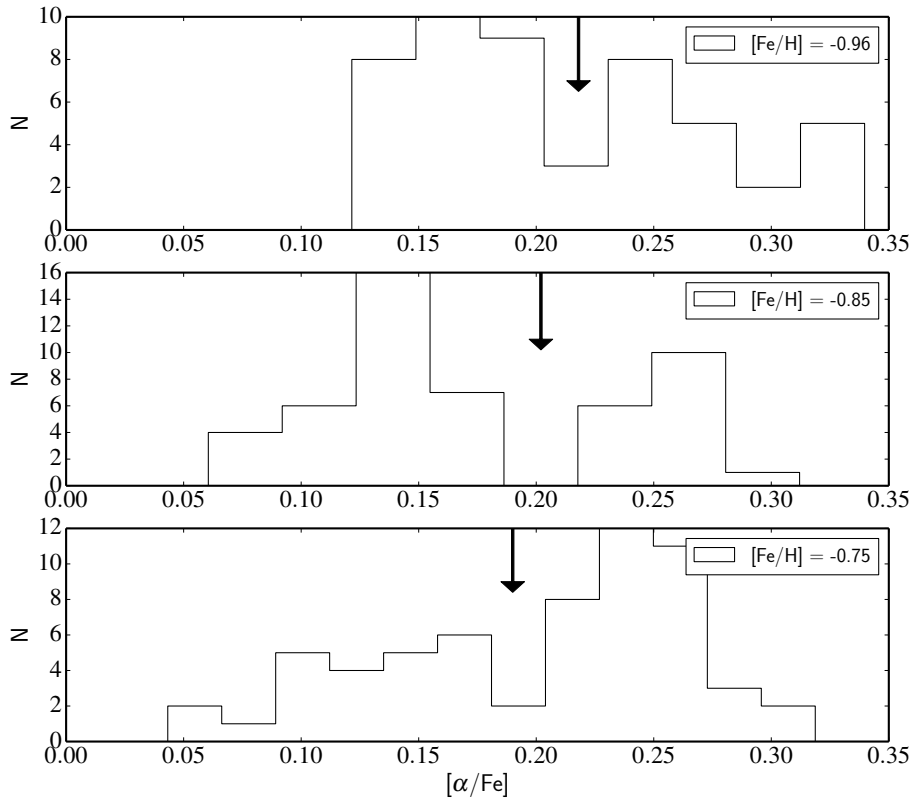

Figure 4.1 – The distribution of [α/Fe] in three metallicity bins, with bin centers at [Fe/H] = $-0.96, -0.85, -0.75$ dex, respectively. In each metallicity bin there appears to be a bimodal distribution in [α/Fe] the trough between the α-poor and α-rich components are marked by a black arrow.

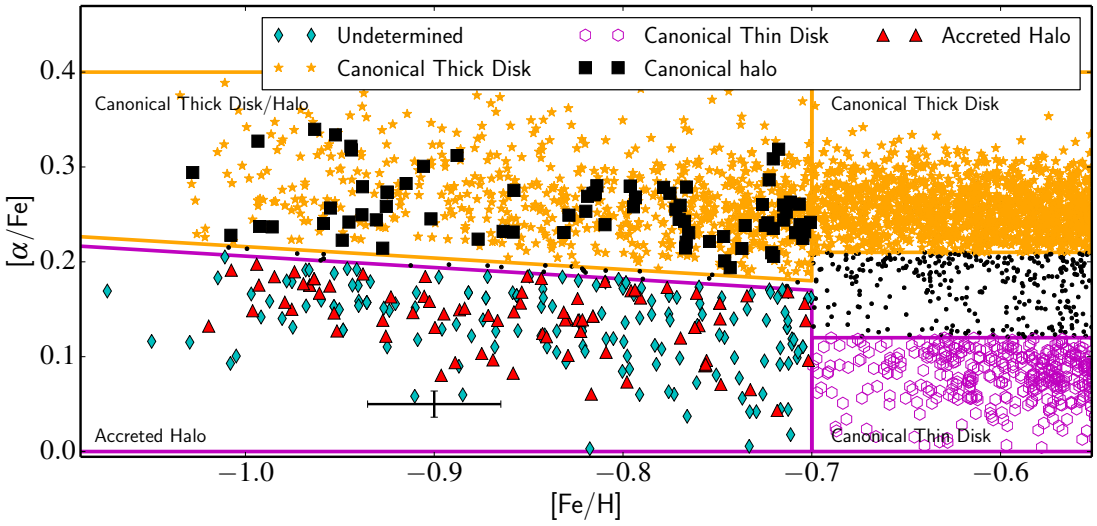

Figure 4.2 – The [α/Fe] as a function of metallicity for the intermediate metallicity APOGEE sample. We chemically seperated the various Galactic components based on where they sit in [α/Fe]-metallicity space. A cut is placed at [Fe/H] = –0.70 dex as this where the thin disk is thought to end (e.g. Bensby, Feltzing & Oey, 2014). The error bar represents the median uncertainty in [α/Fe] and metallicity. The black points are the stars that were deselected because it is difficult to classify those stars on the basis of their chemistry.

to be useful.

In l-GRV space (Figure 4.3), the Galactic disk makes a sinusoidal pattern with an amplitude approximately equal to the rotational velocity of the Galaxy and a dispersion that is correlated to the velocity dispersion of the disk. In the same space the Galactic halo has a more-or-less random distribution (e.g. Johnston et al., 2012). To characterize the disk in this space, we selected a subsample of APOGEE stars with metallicities between –0.50 and 0.00 dex (i.e. the metallicity range where the disk dominates) and binned in l space (20 degrees bins). The dotted blue lines in the top panel of Figure 4.3 are equal to 2.5 times the GRV dispersion in each l bin which represents stars with disk-like kinematics. Stars that have an absolute GRV/cos(b) that is at least 2.5σ or larger than the Galactic disk within a given l bin are considered to have non-disk like kinematics and are assigned to the halo. We note that there are a handful of stars which are assigned to the Galactic halo which appear to sit below GRV dispersion cut in Figure 4.3. These stars are on the l bin edges and assigning them to the halo or disk does not impact the results given the large sample size. While there still may be some disk contamination in the halo sample, this is likely to be small. Similarly, there may be halo stars with disk-like kinematics that this study also rejected. Full 3D space motions could aid in recovering these lost halo stars while further rejecting thick disk stars. We varied the GRV dispersion cut from 1 – 4 σ to asses the impact of the kinematic classification. We discuss the impact of the kinematic selection in section 4.4, however we note here it does not affect our conclusions.

As we are interested in studying the bulk properties of the thin-thick disk-halo transition, we must use the chemodynamical information to define our sample into the canonical Galactic components discussed in sections 1.3 and 1.3.3. Our selection is inspired by the literature described in section 1.3, however it is important to keep in mind that our definitions may not be the same as other studies thus comparisons should be done with care. We define the Galactic

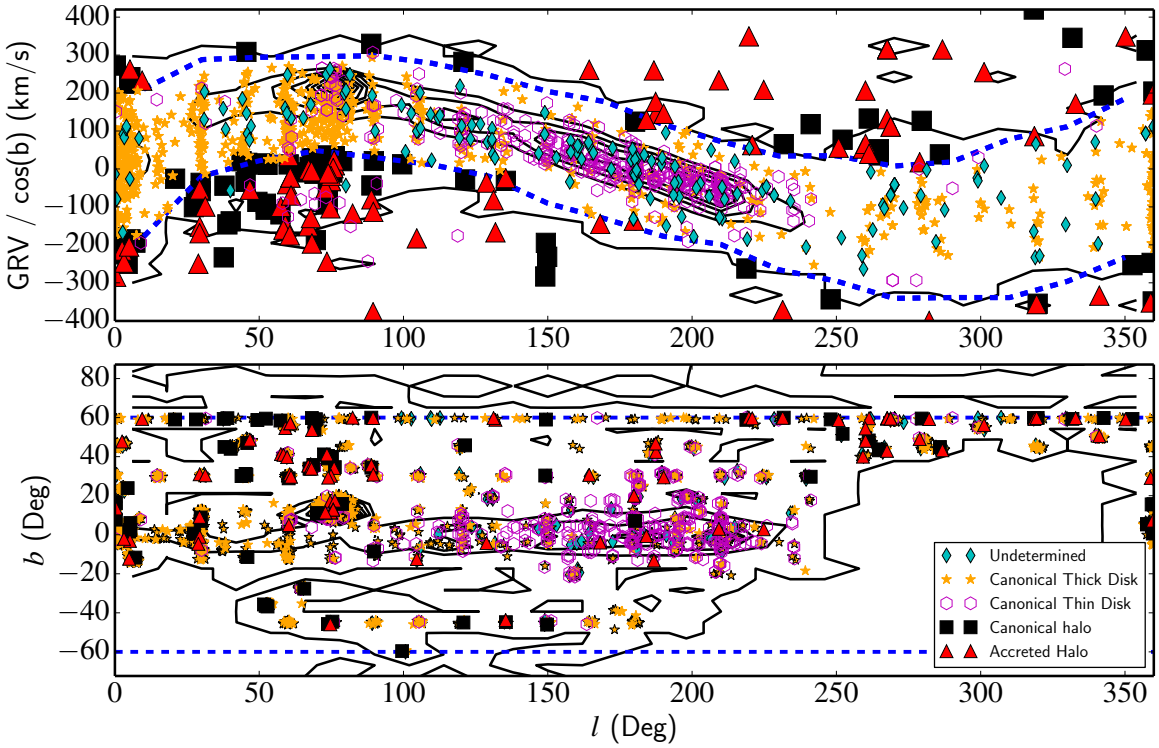

Figure 4.3 – The GRV as a function of l for the full APOGEE sample that pass our quality cuts (contours). The dotted blue lines represents 2.5 $\times$ disk GRV dispersion in each l bin. It is clear from this diagram that the disk signature is a sinusoidal pattern in l-GRV space. Therefore we select stars that have absolute GRVs larger than dotted blue line as our non-disk subsamples (i.e. these stars have, on average less than a 1.24 % chance of being kinematically a part of the disk), which are marked as black squares and red triangle for the α-poor and α-rich, respectively. While the orange stars and cyan diamonds are the α-rich and α-poor stars that have disk-like kinematics (i.e. they are inside of the blue dotted line) and thus are consistent with disk-like kinematics. Stars with metallicities larger than –0.70 dex that are α-poor are considered canonical thin disk stars (open magenta hexagons) Lower Panel: the l, b Galactic coordinates of the full APOGEE sample that pass our quality cuts (contours), following the same symbols as the top panel.

components in our sample in the following way:

- **Canonical Thin Disk (open magenta hexagon)** – These are stars (shown as the right magenta selection box in Figure 4.2) that have low [α/Fe] ratios ([α/Fe] $<$ +0.10 dex, e.g. Adibekyan et al., 2012; Haywood et al., 2013; Recio-Blanco et al., 2014) and have metallicities $>$ –0.70 dex (e.g. Bensby, Feltzing & Oey, 2014). The cut in [α/Fe] was designed to conservatively select out the Galactic thin disk. Kinematically, these stars have spatial-kinematic coherence (falling inside of the blue dotted line in Figure 4.3). Selecting metal-poor stars connected with the negative radial metallicity gradient found in the disk (e.g. Cheng et al., 2012) biases the thin disk stars in our sample to be preferentially found in the outer Galaxy.

- **Canonical Thick Disk (orange stars)** – These stars (orange selection boxes in Figure 4.2) have high [α/Fe] ratios ([α/Fe] larger than +0.22 dex at [Fe/H] $>$ –0.70 dex, e.g. Adibekyan et al., 2012; Haywood et al., 2013; Recio-Blanco et al., 2014). Kinematically these stars have spatial-kinematic coherence (falling inside of the blue dotted line in Figure 4.3).

- **Canonical Halo (black squares)** – These stars are defined as α-rich, metal-poor stars (left orange selection box in Figure 4.2). The [α/Fe] cut was determined by a linear fit to the trough in the [α/Fe] distribution in three metallicity bins below –0.70 dex, where the halo and thick disk will dominate. Kinematically they were selected to have high velocities (e.g. Nissen & Schuster, 2010; Schuster et al., 2012; Hawkins et al., 2015b) and not have significant spatial-kinematic coherence (falling outside of the blue dotted line in Figure 4.3). Additionally, there may be some contamination of this component from the accreted halo caused by the 'hard' cut used to separate the two. However, less than a fifth of the canonical halo stars fall within 1-σ of the [α/Fe] boundary.

- **Accreted Halo (red triangles)**– These stars are α-poor and metal-poor (left magenta selection box in Figure 4.2). They were selected kinematically to have high velocities (e.g. Nissen & Schuster, 2010; Schuster et al., 2012) and not have significant spatial-kinematic coherence (falling outside of the blue dotted line in Figure 4.3). Our choice to use a 'hard' boundary to separate the α-poor accreted halo and the α-rich canonical halo (as done in other literature, e.g. Nissen & Schuster, 2010, 2011; Schuster et al., 2012; Bensby, Feltzing & Oey, 2014) may result in some contamination of the accreted halo subsample from the α-rich canonical halo (or thick disk in some cases) or vice-versa. Accreted halo stars within $\sim$ 0.02 dex of the boundary, the typical 1-σ uncertainties in [α/Fe], could potentially be true canonical halo stars. This only accounts for less than a quarter of the total accreted halo sample. Thus the canonical halo is not likely to be a large contaminating source in the accreted halo.

- **Undetermined (cyan diamonds)**– These stars are α-poor (right magenta selection box in Figure 4.2) with metallicities less than –0.70 dex but may have spatial-kinematic coherence (falling inside the blue dotted line in Figure 4.3). In this way, these stars have the chemistry of what would be the accreted halo but kinematics that cannot rule out disk-like motion. The lowest metallicity thin disk stars have been found to have [Fe/H] = –0.70 dex (e.g. Bensby, Feltzing & Oey, 2014), thus these undetermined stars could be a part of the accreted halo or misidentified thick disk stars with lower [α/Fe]. Additionally,

the undetermined stars within ~ 0.02 dex of the boundary separating α-rich and α-poor stars may be canonical halo stars however, the lower the [α/Fe] of the undetermined stars the less likely that this is the case.

The halo is thought random in l-GRV space (e.g. Johnston et al., 2012) and thus with a lack of full 3D space motions there is a degeneracy that could result in some contamination of halo stars in all canonical disk subgroups. However, even though the halo is thought to extend to metallicities as large as –0.50 dex (e.g. Nissen & Schuster, 2011), the Galactic disk populations will dominate at metallicities above –0.80 dex (e.g. Schlesinger et al., 2012) particularly if they follow the sinusoidal disk-like pattern in Figure 4.3. A rough estimate of the upper limit of the contamination of the disk components on the halo components as a result of using the l-GRV diagram to decompose the Galaxy can be determined using the procedure outlined in section 5 of Sheffield et al. (2012). Assuming that all 3200 stars in our sample are disk stars, and that the stars in a given l bin are distributed in a Gaussian way around the underlying sinusoidal 'disk-like' feature, ~ 40 of those stars (i.e. 1.2 % or 2.5 σ) would be identified as 'halo' stars. However, we found nearly 160 potential halo stars of which we estimate at most 40 of these could be true disk members. This would yield a contamination rate of 25 %. Additionally, we used the Galaxia Galactic model (Sharma et al., 2011) to further study the expected contamination rate. The models have been set to have a metallicity distribution for each component described in section 3.1 of Kordopatis et al. (2013b). We used the same magnitude and color cuts of APOGEE. We applied the same selection routine as above. Results indicate that the contamination rate of the (thick) disk on the Galactic halo samples can range between 20–60 percent depending on the maximum distance surveyed. Larger sampling distances yield lower contamination rates. We also note that adopting a 3-σ cut, instead of 2.5-σ, reduces this contamination to in most cases below 15 %. As such, we varied the GRV dispersion cut to as high as 4-σ (changing the amount of contamination in the disk and halo subgroups) and found that the chemical abundance trend and the overall conclusions are not significantly affected.

Our final sample contains a total of approximately 150 undetermined stars (cyan diamonds) in the low-α, low-metallicity region with disk-like kinematics that could be thin disk stars or accreted stars. There are also approximately 160 halo-like stars split in almost equal parts between the accreted halo (red triangles) and the canonical halo components (black squares). The accreted halo seem to be distributed over all l, b space that has been sampled. Unsurprisingly there are more halo stars at high Galactic latitudes. Accurate distance and proper motions could help compare the total space motions and orbital parameters of the various components, which is beyond the scope of this chapter. There are approximately 370 canonical thin disk stars (open magenta hexagons), and 1400 canonical thick disk stars (orange stars).

4.3 Analysis of Chemical Abundances of the Canonical Galactic Components

In this section, we discuss the individual abundance ratios and trends as a function of metallicity of the five identified subsamples (i.e. canonical thin disk, canonical thick disk, halo and accreted halo and undetermined) defined in section 4.2.2. Although one may be concerned by the systematic errors of the absolute abundances in the APOGEE data, our study mainly relies on relative comparison between the different populations. Therefore, our discussion and

conclusions should not be affected by these systematic errors; in our case only the relative abundance precision matters.

4.3.1 The α-elements: O, Mg, Si, S, Ca, and Ti

We study the α-elements as a way to infer the properties of the size and star formation rate of the cloud that formed the different stellar populations. The α-elements are those elements that are, by definition, made by capturing α-particles. This implies that those elements have an atomic mass number that is a multiple of 4, thus $^{16}\mathrm{O}$,$^{24}\,\mathrm{Mg}$,$^{28}\,\mathrm{Si}$,$^{32}\,\mathrm{S}$,$^{40}\,\mathrm{Ca}$, and $^{44}\mathrm{Ti}$. While other isotopes of those elements exist, they cannot currently be distinguished in the APOGEE dataset, as such we will assume that the listed isotopes are the dominant contributor to the elemental abundances of the APOGEE data.

Those elements are made in the cores of stars by α-capture during post-main sequence burning and dispersed in the interstellar medium via type II supernovae (SNII), while relatively less is expected to be produced by type Ia supernovae (SNIa). Thus the ratio of [α/Fe] is thought to be sensitive to the environment enrichment history of the gas from which the star formed. Unlike the α-poor stars, the α-rich stars are thought to be formed in regions where SNII were numerous, thus in a significantly higher star formation region than the α-poor stars (e.g. Gilmore & Wyse, 1998).

In Figure 4.2 we see that indeed APOGEE data shows evidence of an α-poor and α-rich sequence at both the intermediate and low metallicity regimes, indicating a distinct formation history for each sequence (Nidever et al., 2011). In Figure 4.4 we plot the abundance of each α-element relative to iron as a function of metallicity in a different panel, ordered by atomic number. The different symbols represent the populations defined in section 4.2.2. The abrupt change of symbols at [Fe/H] = –0.70 dex is due to the definition of the populations only.

Unlike several Galactic studies in the literature (e.g. Reddy et al., 2003; Venn et al., 2004; Haywood et al., 2013; Bensby, Feltzing & Oey, 2014), our sample contains the α-element sulphur. Not surprisingly, it behaves in a similar way to the other α-elements (e.g. Nissen et al., 2007; Spite et al., 2011; Jönsson et al., 2011; Takada-Hidai & Takeda, 2012; Matrozis, Ryde & Dupree, 2013; Skuladottir et al., 2015) yet not used in the standard [α/Fe] definition. Since we used this the global [α/Fe] criteria to define our populations, we obviously find that our populations separate in each of the individual α-elements.

From Figure 4.4 we also note that in the –0.90 $<$ [Fe/H] $<$ –0.70 dex metallicity regime, O and Mg drive the largest distinction between the α-rich and α-poor sequences. The rest of the α element abundances appear to be very mixed, making it difficult to disentangle a clear α-poor sequence from an α-rich one. This could be a result of O and Mg SNII yields being mass-dependent (e.g. Nomoto, Kobayashi & Tominaga, 2013).

4.3.2 The Fe-peak elements: Mn, Ni

In contrast to the α-elements, Fe-peak elements, such as Mn and Ni, are thought to be formed primarily via SNIa (e.g. Iwamoto et al., 1999). Therefore they are expected to track Fe in such a way that [Mn/Fe] has been shown to be sub solar in low metallicity stars and increase as with [Fe/H] (e.g. Adibekyan et al., 2012; Battistini & Bensby, 2015). We plot in Figure 4.5 the abundances of the only Fe-peak elements in APOGEE, namely Mn and Ni, for the intermediate

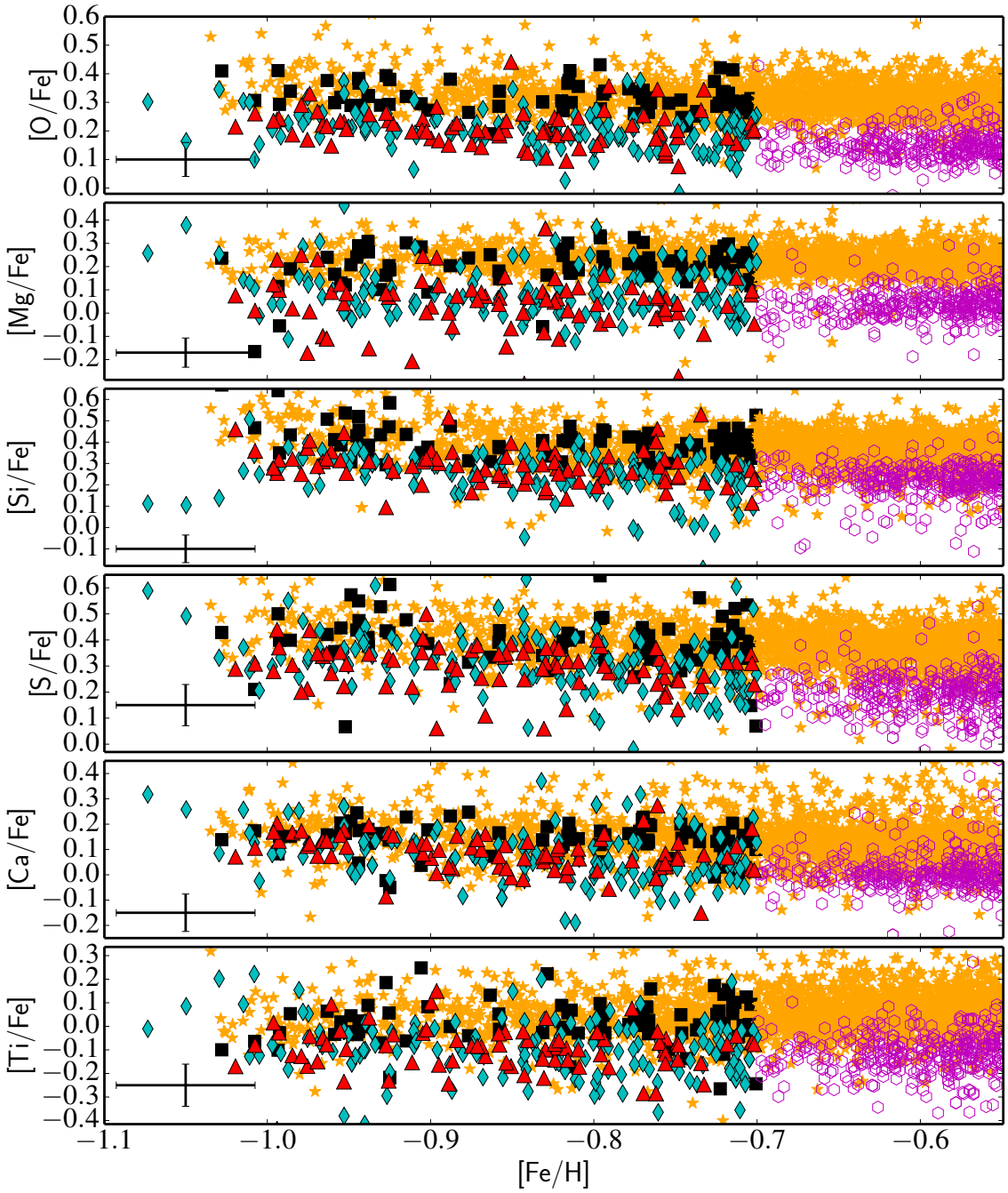

Figure 4.4 – The [O/Fe], [Mg/Fe], [Si/Fe], [S/Fe], [Ca/Fe], [Ti/Fe] from top to bottom respectively as a function of metallicity for the accreted halo (red triangles), canonical halo (black squares), canonical thick disk (orange stars) and undetermined (cyan diamonds), and canonical thin disk (magenta open hexagons) subgroups. It is clear that the distinction between the α-rich and α-poor sequence at low metallicity is likely driven by the [Mg/Fe] and [O/Fe] abundance ratios.

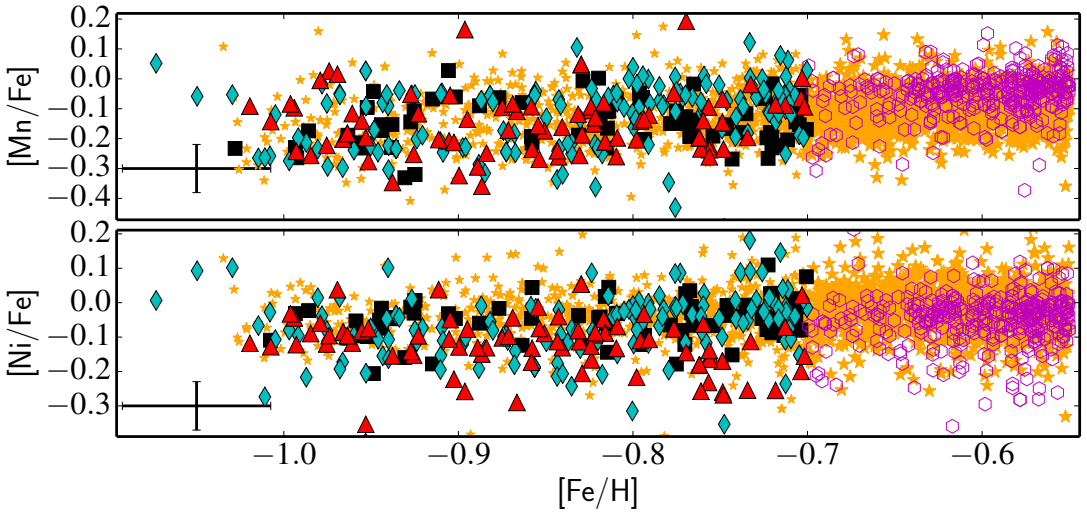

Figure 4.5 – The [Mn/Fe], [Ni/Fe] from top to bottom, respectively as a function of metallicity for the five groups with the same symbols as Figure 4.4.

metallicity stars as a function of [Fe/H]. As in Figure 4.4, the different symbols represent our definition of populations (see Sect. 4.2.2).

It is interesting to note that Mn has a different behaviour for thin and thick disk stars (orange and magenta colour, respectively) at comparable metallicities. While thin disk stars have Mn enhanced respect to iron, thick disk stars have it at the same level than iron. Since Mn is produced at a higher fraction compared to Fe during SNIa (e.g. Gratton, 1989; Iwamoto et al., 1999; Kobayashi et al., 2006) one may expect that at a given metallicity, α-poor stars – which have been polluted by more SNIa – will have higher [Mn/Fe] ratios compared to their α-rich counterparts. This offers an explanation as to why the canonical thin disk stars seem to have overall higher [Mn/Fe] ratios compared to the canonical thick disk. Kobayashi & Nakasato (2011) demonstrate from models that O and Mn should be anti correlated in the Galaxy, because O is produced mainly by SNII while Mn is produced predominantly by SNIa. We observe in Figure 4.4 that the canonical thin disk has lower [O/Fe] than its thick disk counterpart. Thus, given the results of Kobayashi & Nakasato (2011), one would expect the thin disk to have a higher [Mn/Fe] ratio than the thick disk.

The same authors also predict Ni to behave similarly to Mn. However, in Figure 4.5 the [Ni/Fe] remains constant between thin and thick disk stars. More puzzling is the fact that [Ni/Fe] behaves the opposite at low metallicities, in which the Ni abundances of the α-poor accreted population are lower than the those of the α-rich halo at same metallicities. This agrees with the results of Nissen & Schuster (2010), but there is currently no explanation for this unexpected tendency.

We note in Figure 4.5 the very tight dispersion of stars within each population (i.e. stars which have the same symbols). This confirms that despite APOGEE data requiring some further calibrations of the absolute values of the elemental abundances, they provide good precision for Mn and Ni, demonstrating that this dataset is excellent for chemical tagging purposes. Therefore they are very good candidates to allow accurate distinctions between our populations, besides the fact that the comparison of the absolute abundances of [Mn/Fe] and [Ni/Fe] with external studies might be non trivial.

4.3.3 The Odd-Z, Even-Z, and Light Elements

C+N

APOGEE stars are giants, and as such their surface C and N abundances have been partially affected during their evolution as a result of dredge up processes (e.g. Iben, 1965). However, because a large majority of the stars of this survey are expected to be low-mass stars ($\approx 1\mathrm{M}_{\odot}$), where CN cycling processes occurred, the initial C+N ratios are conserved throughout the evolution of those stars (see Masseron & Gilmore, 2015). Therefore, we can use C+N to discuss and compare the evolution of C in our defined populations. In Figure 4.6 we display in top panel [C+N/Fe] as a function of metallicity for our defined populations with the same symbols as previously.
Carbon is mostly made by He burning and its main contributors in the enrichment of the Galaxy are SNII at very low metallicity as well as AGB stars at around –1.50 dex in metallicity. Hence, C+N is expected to globally increase with metallicity, but decrease as soon as SNIa kicks in because it does not produce C. This is why in Figure 4.6, we can observe some enhancement of [C+N/Fe] for the lowest metallicity stars, but then there is an overall decrease, in particular in the thin disk which is the population most enriched by SNIa. Because of this unique interplay among other elements between different progenitors, and thanks to the good precision of C+N in the APOGEE data, the [C+N/Fe] ratios offer an opportunity to disentangle Galactic populations.

Odd-Z elements: Na, Al

The second and third panels of Figure 4.6 show the trends of [Na/Fe] and [Al/Fe] with metallicity, with the symbols representing the populations described in Sect. 4.2.2. While Na abundances are relatively scattered at low metallicities, Al tends to separate. It is expected the Na and Al are produced in SNII. However, according to Kobayashi et al. (2006), the production of those elements are strongly dependent on the initial C and N in the gas cloud that forms the stars. Therefore, it is expected that Na and Al are correlated with C+N. Besides the SNII production site, Na and Al are also expected to be partially produced by AGB stars at the metallicity we focus on in this chapter, as shown by Nomoto, Kobayashi & Tominaga (2013) at the metallicities we focus on in this chapter. This explains why in Figure 4.6 [Al/Fe] is rather enhanced in the lowest metallicity part of the thick disk population, because [C+N/Fe] is also enhanced. Moreover, since SNIa do not produce Al and Na as efficiently as Fe, the [Al/Fe] and [Na/Fe] tend to decrease towards higher metallicities. Nissen & Schuster (2010) demonstrate the effective ability of Na to characterize the α-poor populations. Unfortunately, at these metallicities APOGEE has difficulty measuring Na (see Figure 14 of Holtzman et al., 2015). Typical [Na/Fe] abundance uncertainties in this metallicity range approach $\sim \pm$ 0.20 dex. In contrast, the precision of Al abundances in the APOGEE data is effectively very high, and thus offers an alternative to Na.

K and V

The last bottom panels of Figure 4.6 display the trends of potassium and vanadium as a function of metallicity for our different defined populations with different symbols. The abundance V shows a very large dispersion and remains rather constant among all populations, thus tracking

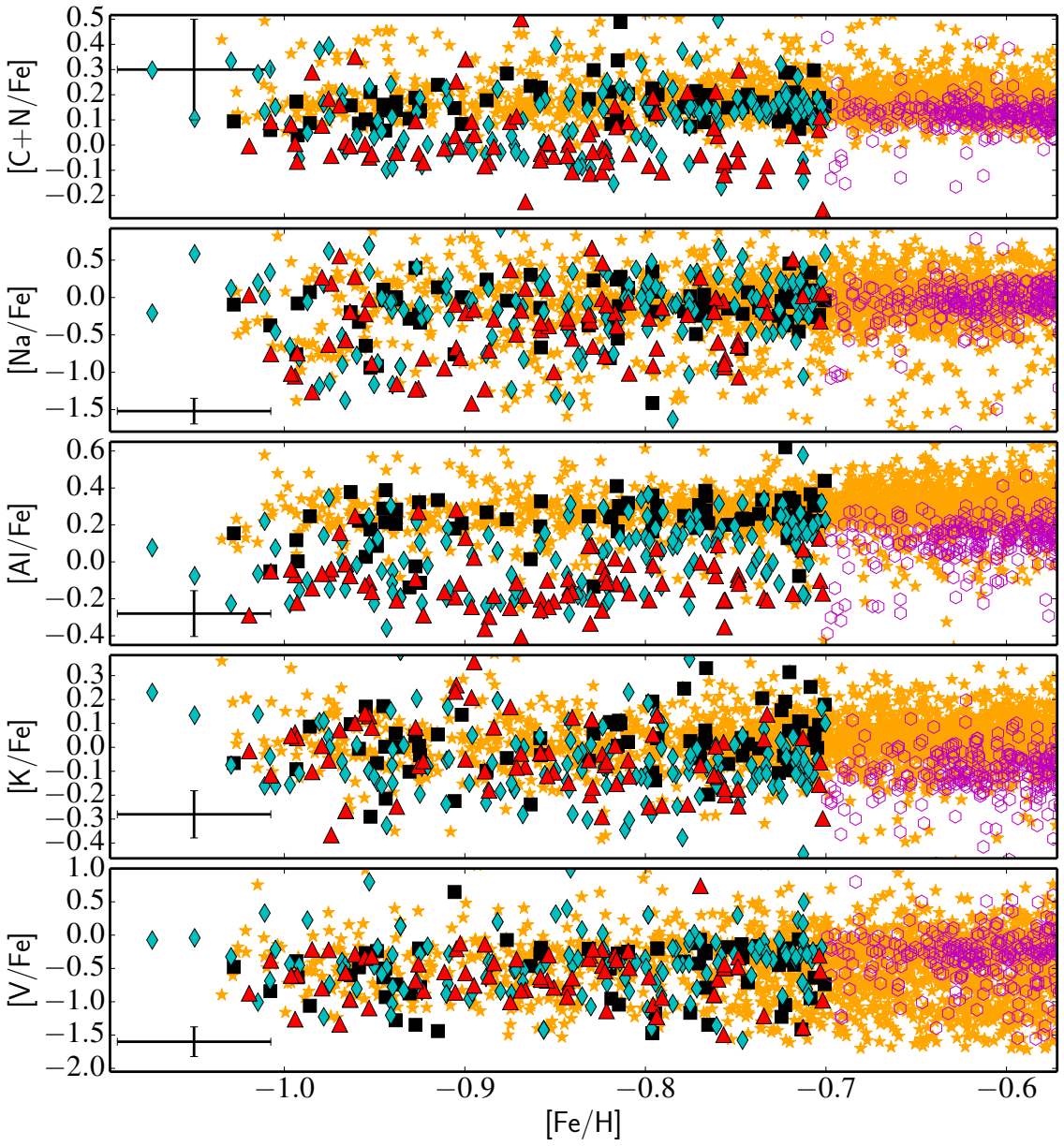

Figure 4.6 – The [C+N/Fe], [Na/Fe], [Al/Fe], [K/Fe], and [V/Fe] as a function of metallicity for the five subgroups are shown with same symbols as Figure 4.4.

Fe. This is similar to what is seen in the literature for V (e.g. Bodaghee et al., 2003; Battistini & Bensby, 2015). Concerning K, the abundances of this element seem to decrease towards higher metallicity consistent with literature (e.g. Shimansky et al., 2003). One can also notice a decrease in some of the accreted population stars, but this trend is rather shallow. Although we note that the nucleosynthesis channel is rather misunderstood for K and V, and the supernovae yields lead to largely underestimated values compared to their observed Galactic abundances (e.g. Nomoto, Kobayashi & Tominaga, 2013). As such, these elements do not give strong constrain to distinguish our defined populations.

With the element-by-element discussion above, in the next section we focus on using the abundance ratio trends to inform our understanding of the transition between the Galactic disks and halo.

4.4 Implications of chemical abundance trends

In the previous section, we have demonstrated that among α-elements, O and Mg bear distinction of the star formation activity, particularly at low metallicities. It also indicates that Mn and Ni are potential alternatives to disentangle the signatures of SNIa. Regarding the accreted population versus thin disk, Al and C+N represents a good diagnostic as they contain signatures of AGB nucleosynthesis. The observations of those elemental abundances provide insight about their origin, but this requires some further modeling taking into account stellar yields as well as a thoughtful discussion of the observational bias that is beyond the scope of this chapter. Nevertheless, we will rather use their relative abundance ratios in this section to discuss the connection and the transition phases of the different canonical components of the Milky Way.

4.4.1 Thick disk-halo transition

One of the primary goals of this work is to use the chemistry of a large sample of stars to study the disk-halo transition in the metallicity region where they are thought to overlap ($-1.20 <$ [Fe/H] < -0.70 dex) based on literature (see section 1.3.3 for more details). In each element studied, the canonical halo (black squares) and canonical thick disk (orange stars) components are completely indistinguishable (see Figures 4.4, 4.5, 4.6). This result was tested using different GRV dispersion cuts between $1 - 4\sigma$ (i.e. varying the amount of contamination between the two groups) and in all cases the canonical thick disk and halo overlap in every element. Another illustration of this can be seen in Figure 4.7 for the key elements we have previously highlighted. In each panel of that figure the canonical thick disk (shown in orange) and the canonical halo (shown in black) *not only overlap but have comparable dispersions* suggesting that the two formed in a similar high star formation environment with well-mixed turbulent gas making them indistinguishable in chemistry leaving only the kinematics and spatial distributions to separate the two.

Ishigaki, Chiba & Aoki (2012) found, using a sample of 97 stars, evidence that [Mg/Fe], [Si/Fe] in the thick disk are higher, on average, than halo stars. Their follow-up study (Ishigaki, Aoki & Chiba, 2013) found that [Na/Fe] and [Ni/Fe] were lower in the halo compared to the thick disk. It is important to note that we select our halo samples in different ways making it difficult to compare these two studies. The halo sample in Ishigaki, Chiba & Aoki (2012) was

selected kinematically on the basis of the Toomre diagram and is split into an 'inner halo' and 'outer halo' component. It is likely that both of their inner and outer halo components contain stars that we would classify as α-rich and α-poor. In our study, we selected the halo sample kinematically (using the l-GRV diagram) and found a bimodal distribution in [α/Fe]. As a result of this we called the α-rich components the 'canonical halo' and the α-poor component the 'accreted halo' (based on studies such as Nissen & Schuster, 2010). Since both halo samples in Ishigaki, Chiba & Aoki (2012) likely contain α-rich and α-poor stars, the mean [α/Fe] could be driven to lower values which may explain why the [Mg/Fe] and [Si/Fe] may have been found to be on average lower in the halo(s) than the thick disk.

The only chemical distinction between thick disk and canonical halo is solely in the mean and dispersion of the metallicity distribution function for the two components. This result could be biased by the fact that we choose the canonical halo to be α-rich, similar to the thick disk. It is interesting to point out that while we selected the canonical halo and thick disk to be α-rich, they are, in fact, similar in all other elements including elements that have different production channels to [α/Fe] (e.g. odd, even, and light elements) that we do not use for selection. If we had not initially separated the halo sample into α-rich and α-poor subsamples, we would conclude that in key elemental abundance spaces the halo is bimodal (see Figure 4.7) and the α-rich component of that bimodal distribution is chemically similar to the thick disk despite having a different metallicity distribution function while the α-poor component is chemically different. It is also interesting to note that the canonical halo has some evidence of spatial-kinematic coherence (black squares in Figure 4.3), indicating it may have net rotation in line with other studies (e.g. Carollo et al., 2007, 2010). This may suggest that the thick disk-halo transition is smooth kinematically and would be worth examining with full 3D space motions to confirm. As the thick disk is thought to form from well-mixed turbulent gas (e.g. Haywood et al., 2013), we interpret this smooth chemical transition between the canonical thick disk and halo components as evidence that the gas of the inner in situ Galactic halo may have been the precursor to the thick disk. We note that subject to careful modeling of selection functions, most of the inner halo (i.e. the α-rich stars) chemically resembles a single homogeneous self-enriching population, in which the major transition between the halo and thick disk is pressure support to angular momentum support in kinematic space.

4.4.2 The accreted halo

In section 4.2.2 we showed that there is a sequence of α-poor metal-poor halo giant stars in APOGEE (which we designated as 'accreted halo') that resembles the α-poor sequence of Nissen & Schuster (2010), Ramírez, Meléndez & Chanamé (2012), Bensby, Feltzing & Oey (2014), Hawkins et al. (2014), and others. What makes this result interesting is that APOGEE has a very different selection function and surveys a larger volume than past studies (e.g. Nissen & Schuster, 2010) which primarily rely on chemical analysis of relatively local dwarf stars. The discovery of the α-poor sequence in a large sample of giant stars from APOGEE with a different selection function and larger survey volume strengthens the argument that the α-poor halo sequence is real.

We used the APOGEE survey to study the chemistry of these α-poor stars (red triangles) in section 4.3 by comparing their abundances in 14 elements, including α (Figure 4.4), Fe-peak elements (Figure 4.5), odd, even, and light elements (Figure 4.6) to the canonical halo sequence (black squares). We found that the accreted halo is primarily distinguishable in the α-elements

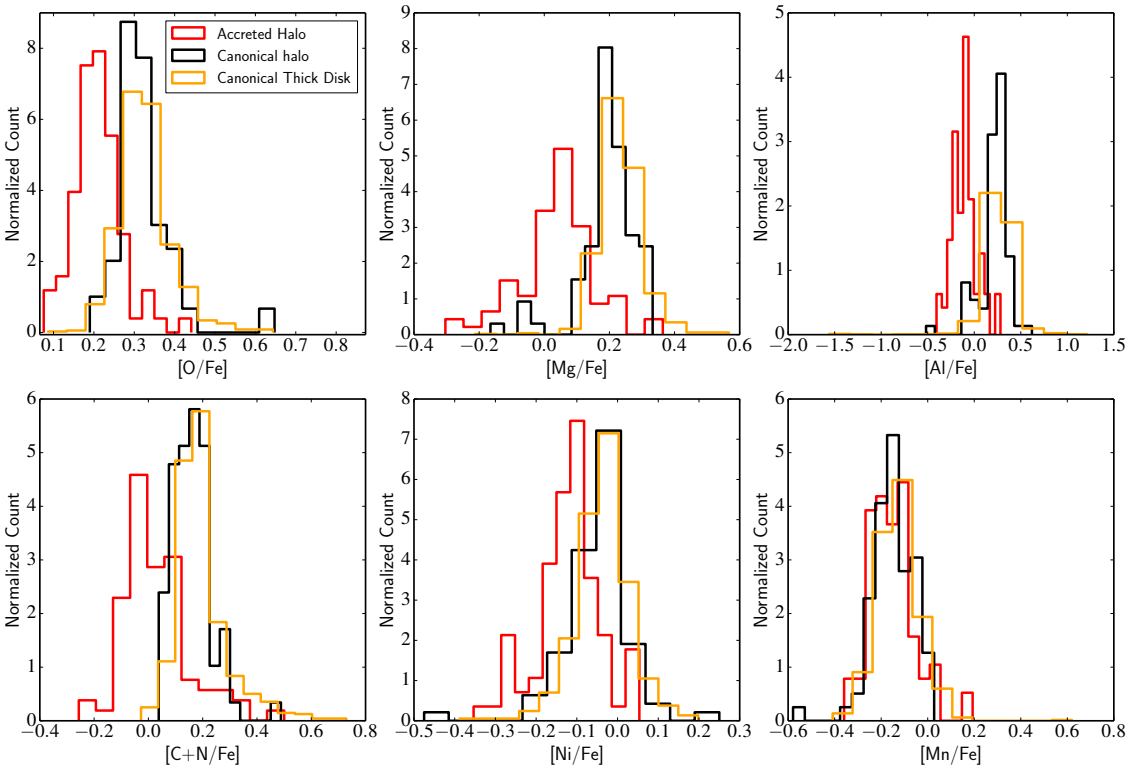

Figure 4.7 – The distribution of [O/Fe], [Mg/Fe], [Al/Fe], [C+N/Fe], [Ni/Fe], [Mn/Fe] abundance ratios for the accreted halo (red), canonical halo (black) and canonical thick disk sequence (orange). We find that in most elements (except Mn, Na) are systematically under abundant in the accreted halo sequence relative to the canonical halo sequence. The abundance dispersion in the accreted halo sequence is comparable or in most cases larger than the canonical halo sequence. Further Mn shows no chemical difference between the two sequences. In all chemical abundance ratios shown (and those not shown as well) the canonical thick disk and halo components overlap significantly.

(e.g. Mg, O, and S). To further illustrate the chemical distinction between the accreted halo and canonical halo sequences, in Figure 4.7 we plotted the chemical distribution of six key elements from all three elemental groups for the canonical halo (black line), accreted halo (red line) components.

In all chemical elemental abundance ratios shown in Figure 4.7 except [Mn/Fe] the *accreted halo is systematically under abundant compared to the canonical halo.* The lower [C+N/Fe] of the accreted halo indicates that the initial chemical composition of the gas that formed the α-poor stars were different from the α-rich providing further evidence that the α-poor stars are likely extragalactic in origin (e.g. Nissen et al., 2014). This is the first observation that [Al/Fe] is under abundant in the accreted halo population. This result is not surprising as Al is thought to be produced in SNII and correlated strongly to C+N. Therefore, if [C+N/Fe] is under abundant (see section 4.3.3 and Nissen et al., 2014) one would expect [Al/Fe] to also be under abundant. Furthermore, the dispersion of the accreted halo in all elemental ratios except Mn is larger than the canonical halo component. This may suggest several extragalactic systems being responsible for the production of the accreted halo component in contrast to the canonical halo, which is thought to form from one homogenous gas cloud. However, we remind the reader that the dispersion in each element is sensitive to the boundary that separates the canonical and accreted halo components. As such, we tested various boundaries between the canonical and accreted halo components to study how this would affect the dispersions and the separation of the two components. We shifted the line that separates the α-rich canonical and α-poor 'accreted' halos by at least $\pm$0.05 dex (twice the typical internal uncertainty in [α/Fe]). Lowering the boundary causes stars currently classified as accreted with moderate [α/Fe] to be reclassified as canonical halo. The overall result is a decrease in the dispersion of accreted halo in most elemental spaces and an increase in the dispersion in the elemental distributions for the canonical halo. Raising the boundary has the opposite effect. In both cases, the accreted halo is chemically distinct from the canonical halo in the elements listed above. If we were to not separate the halo into a 'canonical' and 'accreted' component at the onset, we would find a bimodal distribution in O, Mg, Al, C+N and Ni in the full halo sample consistent with two chemically distinct components.

As noted by Nissen & Schuster (2011) the [Mn/Fe] ratio is comparable between the α-poor and α-rich halo sequences. This is likely a result of the metallicity dependence on the SNIa yields. We also found that [K/Fe] and [V/Fe] ratios are comparable both in mean and dispersion between the accreted and canonical halos indicating that these elements do not give strong constraints to distinguish the canonical and accreted halo components. We recall that the [V/Fe] ratios have significantly larger scatter than expected from other literature (e.g. Fulbright, 2000; Battistini & Bensby, 2015) which may indicate this element is less reliable.

Additionally, increasing the kinematic GRV dispersion cut to 4σ reduces the contamination of the disk population in the halo stars however decreases the sample size significantly while reducing the kinematic GRV dispersion cut to 1σ increases the contamination from the α-poor disk population thereby broadening the chemical abundance ratio dispersions of the α-poor 'halo' sequence. In all cases in which we tested various GRV dispersion cuts, the canonical and accreted halo remain chemically distinct in the [C+N/Fe], [Al/Fe], [Ni/Fe] and the α-elements (particularly [O/Fe], [Mg/Fe], [S/Fe]).

Simulations of the Galactic halo (e.g. Bullock & Johnston, 2005; Zolotov et al., 2009; Cooper et al., 2010) have indicated that the halo may have been constructed primarily through a combination of dissipative collapse and accretion events of massive systems. The likely ac-

creted α-poor stars represent accretion from systems onto the halo and their [α/Fe] and chemical abundance distributions may be able to give insight to the mass of the systems that accreted. Furthermore, a careful study of the relative fraction of the accreted α-poor halo stars and the in situ α-rich halo stars will provide unique constraints on the relative importance of accretion events in the assembly of the Galactic halo. With the upcoming surveys it will be possible to build large samples of α-poor halo stars that will make these tests possible.

4.4.3 The undetermined group: thin disk at low metallicities?

The thin disk is thought to be rather metal-rich with [Fe/H] > -0.70 dex (e.g. Reddy et al., 2003; Fuhrmann, 2004). However, there has been some debate as to whether the thin disk actually extends to metallicities as low as [Fe/H] = –1.0 dex (e.g. Mishenina et al., 2004). Most recently Bensby, Feltzing & Oey (2014) used a sample of 714 F and G dwarf stars and found that the lower metallicity for the thin disk was [Fe/H] $\sim$ –0.70 dex. Their finding in combination with the extent of the accreted halo (e.g. Nissen & Schuster, 2010) is the reason our initial cut in [Fe/H] for our sample was at [Fe/H] = –0.70 dex separating the accreted halo from the canonical thin disk in the [α/Fe]-metallicity diagram. Upon separating our metal-poor sample into several subpopulations in section 4.2.2, we found that a non negligible amount of stars that are metal-poor and α-poor, yet the kinematics suggest they may be disk-like, which we called the undetermined subgroup (cyan diamonds).

In Figure 4.6, it is clear that the [C+N/Fe] and [Al/Fe] abundances of the undetermined subgroup at the high metallicity end (–0.83 $<$ [Fe/H] $<$ –0.70 dex) are, on average, consistent with the thin disk population at those metallicities while at lower metallicities ([Fe/H] $<$ – 0.90 dex) the undetermined population decreases in both [C+N/Fe] and [Al/Fe] and behaves like the accreted halo subgroup. For this reason, we changed the colour of the diamonds with metallicity [Fe/H] $>$ –0.83 dex to magenta in order to denote that these stars chemically resemble the canonical thin disk population. In Figure 4.8(a), we plot [Al/Fe] as a function of metallicity now with all α-rich stars as contours with the canonical thin disk (open magenta hexagons) and our candidate metal-poor thin disk (magenta diamonds). We leave the diamonds with metallicity [Fe/H] $<$ –0.83 dex as cyan because these stars are still undetermined although it is likely they are either accreted halo stars or miscategorized thick disk stars.

In the top panel Figure 4.8(b) we plot the GRV/cos(b) as a function of l and b as a function of l in the bottom panel for emphasizing the candidate metal-poor thin disk (magenta diamonds) and undetermined (cyan diamonds) subgroups relative to the canonical thin disk component (open magenta hexagons). We plot all α-rich stars (i.e. canonical thick disk and halo) as background orange contours, following our notation color for the thick disk, for comparison. We note the following: (1) the canonical thin disk at intermediate metallicities (open magenta hexagons) population is predominately found between $90 < l < 220$ deg and (2) the candidate metal-poor thin disk (magenta diamonds) are spatially and kinematically consistent with the canonical thin disk population. Specifically, the GRV dispersion of the candidate metal-poor thin disk at a constant l (i.e. magenta diamonds in Figure 4.8(b)) is very small and is thus consistent with thin disk. This suggests that the *canonical thin disk may extend to lower metallicities than found in recent studies* (e.g. Bensby, Feltzing & Oey, 2014). The lower metallicity extent compared to other studies (such as Bensby, Feltzing & Oey, 2014) could be a result of the fact that APOGEE has a large sampling of stars in the outer Galaxy, where the most metal-poor thin disk stars should exist. As noted in section 4.2.1, while the precision of the

metallicities are high, the accuracy or metallicity scale may not be well calibrated. Holtzman et al. (2015) used a sample of globular clusters and found that in this metallicity regime ([Fe/H] = –0.6 to –1.0 dex), [Fe/H] can be overestimated by as much as ~ 0.10 dex. This causes the metallicity extent of the thin disk to extend down to at least $\lesssim -0.83$ dex if we use the uncalibrated [Fe/H] or –0.95 dex if one calibrates the [Fe/H] scale using the globular clusters. We remind the reader we choose to use the uncalibrated [Fe/H] because the [X/Fe] trends match what is expected from literature while calibrating the [Fe/H] values has the effect of inflating the [X/Fe] (Holtzman et al., 2015). Given this uncertainty in the calibration, we plan to explore the metal-poor extent of the thin disk with other surveys, such as the Gaia-ESO survey (Gilmore et al., 2012), in order to investigate the absolute value of the metal-poor tail of the thin disk metallicity distribution.

Another interesting result to point out from Figure 4.8(b) is that our candidate metal-poor thin disk (magenta diamonds) and most of the intermediate metallicity stars of the canonical thin disk, are found at locations outside the solar circle ($90 < l < 270$ deg) while the more metal-rich canonical thin disk is seen at Galactic longitudes consistent with locations inside the solar circle indicative of a negative radial-metallicity gradient. Negative metallicity gradient are widely observed in the canonical thin disk both in small samples (e.g. Genovali et al., 2014) and large surveys (e.g. Cheng et al., 2012; Mikolaitis et al., 2014). Theoretically, the presence of a negative metallicity gradient in the canonical thin disk is evidence for an "inside out" formation scenario of the disk. Under this scenario, the oldest disk population is formed from the low angular momentum gas, which falls into the center of the halo and begins rapidly forming stars earlier compared to the outer disk. The rapid star formation leads to larger metallicities being produced in the central disk compared to the outer disk causing a negative metallicity gradient (e.g. Larson, 1976; Minchev, Chiappini & Martig, 2014). Our finding is thus suggestive of a negative radial metallicity gradient, which is consistent with the inside-out formation scenario.

4.5 Redefining the selection of Galactic components: a chemical tagging approach

The current method of decomposing the canonical Galactic component in the current scheme of chemokinematics (the use of both chemistry, e.g. [α/Fe] and metallicity) and kinematics (e.g. radial velocities, or U,V,W velocity vectors) has the disadvantage that it can be quite complex. The complexities lie in controlling the assignment of stars in the populations. For example, we saw in section 4.2.2 where we had to use both chemistry and kinematics just to separate out the Galactic components and even had an extra undetermined population that could not be categorized until after full chemical analysis. This caused each plot to contain many more symbols (and thus populations) than may be necessary. Furthermore, the assignment of populations on just kinematics (e.g. Bensby, Feltzing & Oey, 2014) or both chemistry and kinematics causes significant biases making it difficult to discern the chemical evolution of the Galaxy. This leads us to question: Is there a more simple approach? More specifically, can we just use chemistry to directly separate out the canonical Galactic components to then study the spatial and dynamical distributions?

In this section we attempt to answer this question by putting forward a chemical-only labelling approach to separate the Galactic components based on the above analysis. In section 4.3 and 4.4, we discussed that among the various elements studied here the canonical halo,

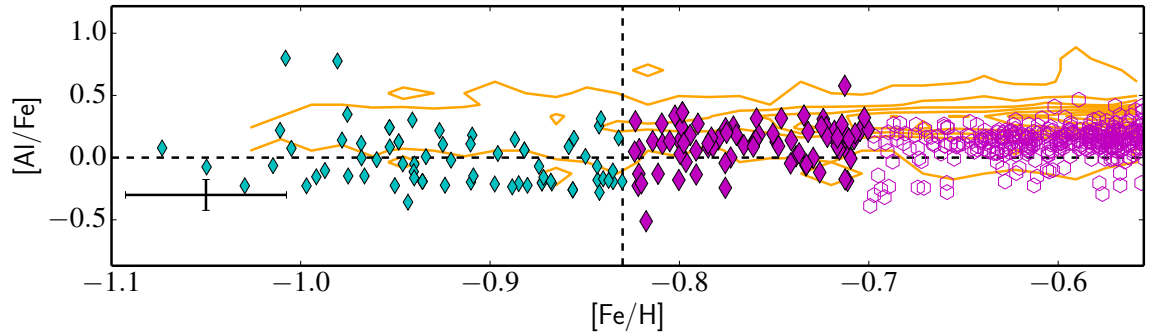

(a)

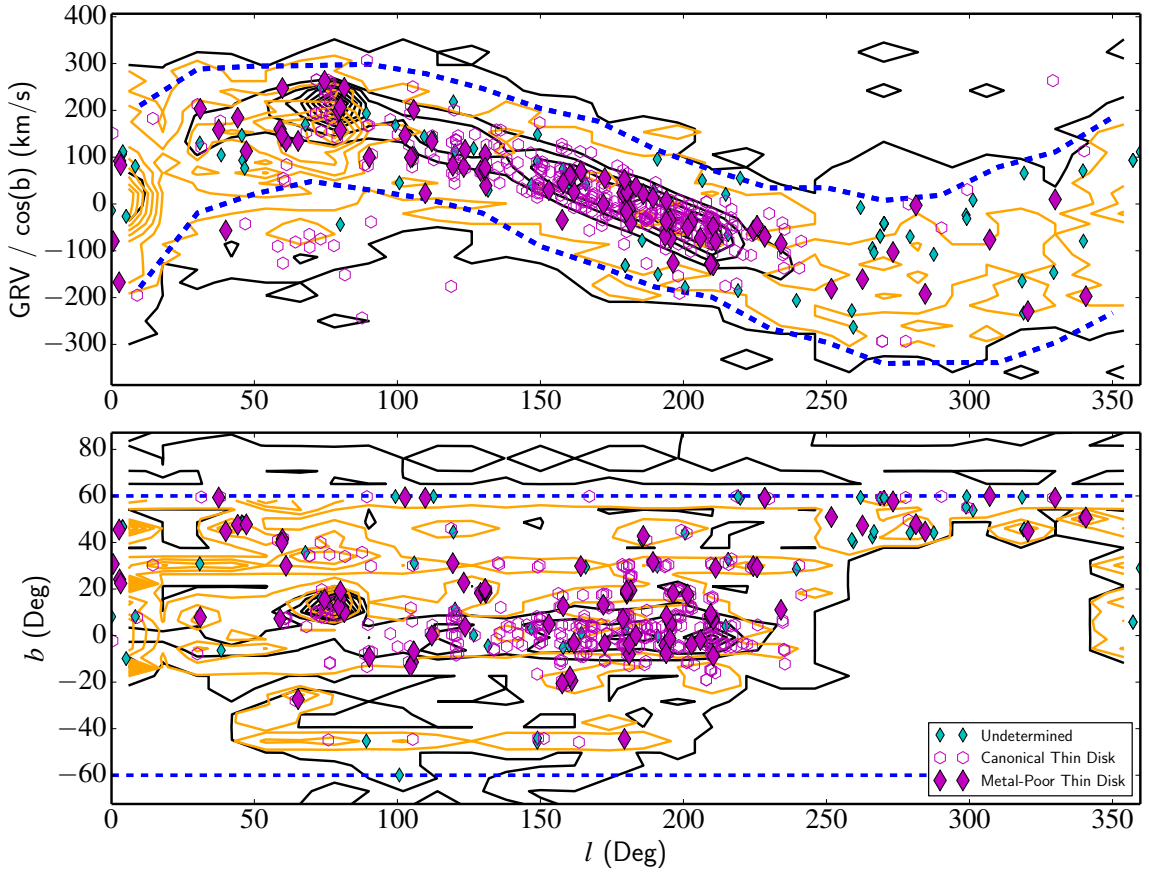

(b)

Figure 4.8 – (a) [Al/Fe] as a function of metallicity of the candidate metal-poor thin disk (magenta diamonds). All α-rich stars are shown as orange contours. The canonical thin disk sample is shown as open magenta hexagons for comparison. Dotted lines are placed at the metallicity cut [Fe/H] = –0.83 dex and a guiding line is placed at [Al/Fe] = 0 dex. (b) Upper panel: The GRV as a function of l for the candidate metal-poor thin disk. The full APOGEE sample that pass our quality cuts are shown as black contours. For consistency the blue dotted lines represent the initial kinematic selection. Lower Panel: The Galactic coordinates (l, b) of the various subgroups following the same symbols as the top panel. We found that the candidate metal-poor thin disk with metallicities down to $\sim$ –0.83 dex have kinematic-spatial coherence that is consistent with the canonical thin disk at these metallicities.

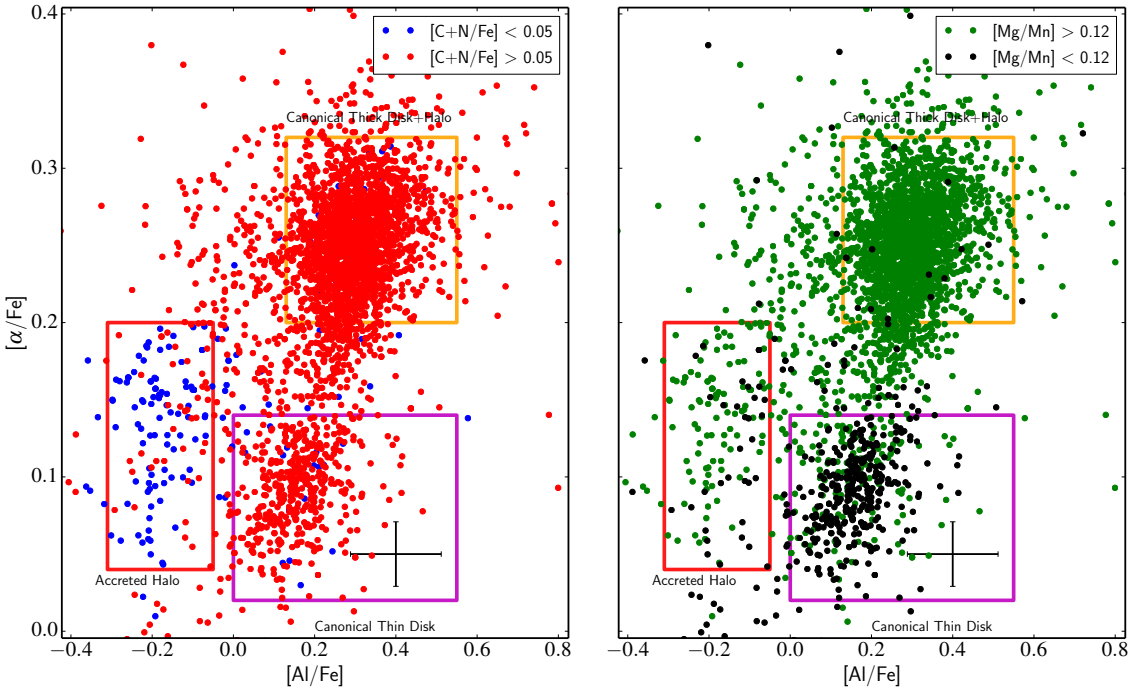

Figure 4.9 – Left Panel: The [α/Fe] abundance ratio as a function of [Al/Fe] for all intermediate metallicity stars with –1.20 $<$ [Fe/H] $<$ –0.55 dex coloured by [C+N/Fe] where red is [C+N/Fe] $>$ +0.05 dex and blue is [C+N/Fe] $<$ +0.05 dex. Right Panel: The same as the right panel but now colour coded by [Mg/Mn] where green is [Mg/Mn] $>$ +0.12 dex and black is [Mg/Mn] $<$ +0.12 dex. In both panels, the error bar represents the typical uncertainty in the abundance ratios. There are three clusters within the data. The canonical thick disk + canonical halo, canonical thin disk and accreted halo components which should fall within the orange, magenta and red selection boxes, respectively. Note with just these four chemical dimension each component is marked by a different colour (e.g. accreted halo it is blue indicating α-poor, Al-poor, and [Mg/Mn] is mixed while the canonical thin disk is α-poor, Al-rich and [Mg/Mn] is low) and thus will very strongly separate in these chemical spaces.

accreted halo and thin disk were able to be separated primarily in the α-elements (e.g. [α/Fe] Mg, or O), Al, C+N. In this way, we can use a combination of these elements relative to Fe (or even other Fe-peak elements such as Mn) to chemically separate the canonical thin disk, accreted halo and thick disk. We note from above that the canonical thick disk and halo are effectively chemically indistinguishable meaning they can, in principle, be treated as one population although they likely have an inhomogeneous kinematic and spatial distribution.

The [α/Fe] ratio is particularly important because it tracks the ratio of the elements produced in SNII and SNIa providing useful constraints on the formation timescale of the component. We note here that the abundance ratio [Mg, O/Mn] would actually be a better tracer of SNII/SNIa as Mg and O are the first elements to be affected as a result of SNII (e.g. Nomoto, Kobayashi & Tominaga, 2013) and Mn is produced at higher fractions compared to Fe in SNIa (e.g. Gratton, 1989). However, we choose to use [α/Fe] in part because it is more accessible in other non-APOGEE data compared to Mn as well as the fact that Mn is difficult to measure in optical spectra as several lines suffer from hyperfine structure splitting (Nissen et al., 2000; Jofré et al., 2015, e.g.). Al is important as it is produced via SNII and is sensitive to the initial C and N abundance, which in turn is produced by He burning or AGB evolution. For these reasons, in Figure 4.9 we show [α/Fe] as a function of [Al/Fe] in both panels. The data colored by their [C+N/Fe] in the left panel (red dots have [C+N/Fe] $>$ +0.05 dex while blue dots have [C+N/Fe] $<$ +0.05 dex) and [Mg/Mn] in the right panel (green dots have [Mg/Mn] $>$ +0.12 dex while black dots have [Mg/Mn] $<$ +0.12 dex). The data separates in three clusters in Figure 4.9. One being the thin disk stars with low [α/Fe], moderate [Al/Fe] and low [Mg/Mn] shown by a magenta selection box. The second is the thick disk+halo stars that have higher [α/Fe], higher [Al/Fe] and high [Mg/Mn] with an orange selection box. Lastly is the accreted halo stars that have low [α/Fe] with a larger spread than the thin disk, low [Al/Fe] and moderate to low [Mg/Mn] with a red selection box.

As a consistency check of the populations defined from the selection boxes in Figure 4.9, we looked at where they fall in the [α/Fe]-[Fe/H] plot (Figure 4.10(a)). In Figure 4.10(a) we see that we recover the same structure seen in Figure 4.2. The canonical halo and thick disk are not chemically distinct and represent the α-rich stars. The thin disk is α-poor and primarily at higher metallicities but extend to very low metallicities and the α-poor accreted halo is primarily found at low metallicities although extend to as high as –0.60 dex consistent with Nissen & Schuster (2010). The large gaps in the [α/Fe] in Figure 4.10(a) are artificial as they are a result of our selection boxes. We plan to explore a more sophisticated statistical approach, such as k-means (e.g. Hogg et al., 2016), to improve or abandon the selection boxes in favour of a probabilistic and clustering approach. Here we show that in a simple case of using [α/Fe], [Al/Fe], [C+N/Fe] and [Mg/Mn] we can indeed chemically tag the bulk of the Galactic components in a robust way.

This is confirmed when looking at the l-GRV space (Figure 4.10(b)). We use l-GRV space to determine if this purely chemical definition of the canonical Galactic components recover the kinematic structure we expect them to have. Like in Figure 4.3, the dotted blue line represents the sinusoidal pattern of stars following disk-like motion. The canonical thin disk (open magenta hexagons) not only have spatial-kinematic coherence indicating co-rotation with the disk, they are also located primarily outside of the solar circle. The accreted halo (red triangles) have hot kinematics although some are located inside a region of l-GRV space where they may be co-rotating with the disk (i.e. inside the blue dotted line in Figure 4.10(b)). Full 3D kinematics would be very helpful to validate these stars as accreted halo. In addition, the

accreted halo may extend to metallicities as high as [Fe/H] < -0.6 dex. The canonical thick disk + halo (orange stars) are dominated at these metallicities by the thick disk and thus by in large show a co-rotation with the disk. The GRV/cos(b) dispersion is much larger than the thin disk as expected. However, there are orange stars that reside quite far outside the disk-like patter (blue dotted line) which are the canonical halo stars. This test verifies that by *using the [α/Fe]-[Al/Fe] diagram in connection with [C+N/Fe] and [Mg/Mn] we can distinguish Galactic populations in a way that can be studied free of biases in the dynamical spaces.* This has the advantage to traditional methods that full 3D kinematics are not necessary (outside of validation) and one can break the degeneracies in the [α/Fe]-metallicity diagram (i.e. the initial undetermined group is now categorized, see Figure 4.10(a)). We also have less contamination in that we no longer have thin disk stars that have extreme velocities (i.e. the open magenta hexagons outside the dotted blue line in Figure 4.3). The population assignment also works just using the [α/Fe]-[Al/Fe] diagram alone rather than adding the addition [C+N/Fe] and [Mg/Mn] abundance ratios. The advantage to adding those ratios is to reduce contamination from the fringes of the thick disk and thin disk components. This is just a first step in showing that chemical-only approaches may be the way forward in decomposing the Galaxy especially with large chemical surveys either underway or planned for the near future. More work will be needed to move beyond the selection boxes we use here to more robustly quantify the discreetness between the components in these chemical spaces, which we plan to explore in a forthcoming paper.

4.6 Summary

We have studied the chemistry of a relatively large sample of intermediate metallicity ([Fe/H] $<$ –0.55 dex) giant stars using the APOGEE survey in order to explore the disk-halo transition though a chemical tagging approach. We selected a sample of $\sim$3200 intermediate metallicity stars using a set of quality control cuts described in section 4.2.1. We used the [α/Fe]-[Fe/H] diagram and the l-GRV diagram (e.g. Majewski et al., 2012; Sheffield et al., 2012) to split our sample into five subgroups: (1) canonical thin disk (open magenta hexagons), (2) canonical thick disk (orange stars), (3) canonical halo (black squares), (4) accreted halo (red triangles), (5) undetermined (cyan diamonds) as described in section 4.2.2. In section 4.3 we discussed the chemical abundance patterns of these four groups in α-elements (Mg, Ti, Si, Ca, O, S), Fe-peak elements (Mn, Ni), and odd, even, and light elements (C+N, Na, Al, K, V).

Our main results of this Galactic chemical evolution analysis can be summarized in the following points:

- The canonical halo and canonical thick disk are not chemically distinct in any of the elements studied. This is most evident in the abundance ratio distribution in the various elements shown in Figure 4.7 which indicates that the α-rich halo component (black line) and the α-rich disk component (orange line) overlap both in terms of mean and dispersions for both populations. This may suggest that the Galactic halo and thick disk are chemically formed from similar gas but one is pressure supported and the other is angular momentum support.

- We uncovered the largest sample of 'accreted' halo stars. We showed, for the first time, that accreted halo stars are under abundant in [S/Fe], which is unsurprising given its

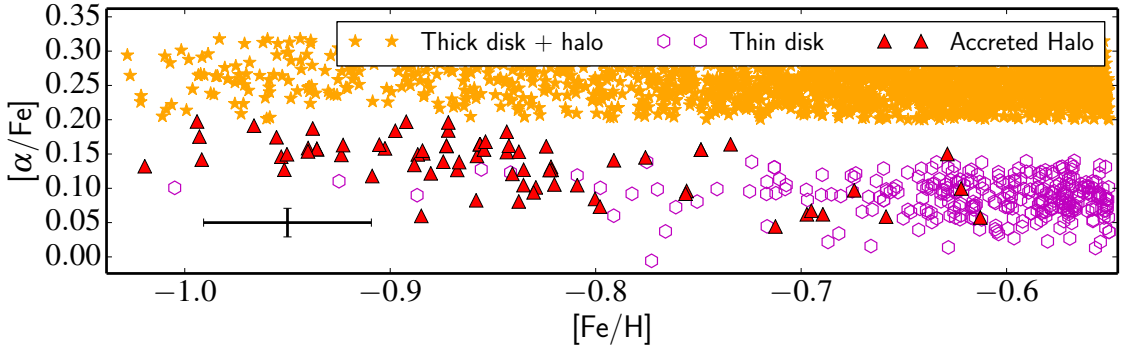

(a)

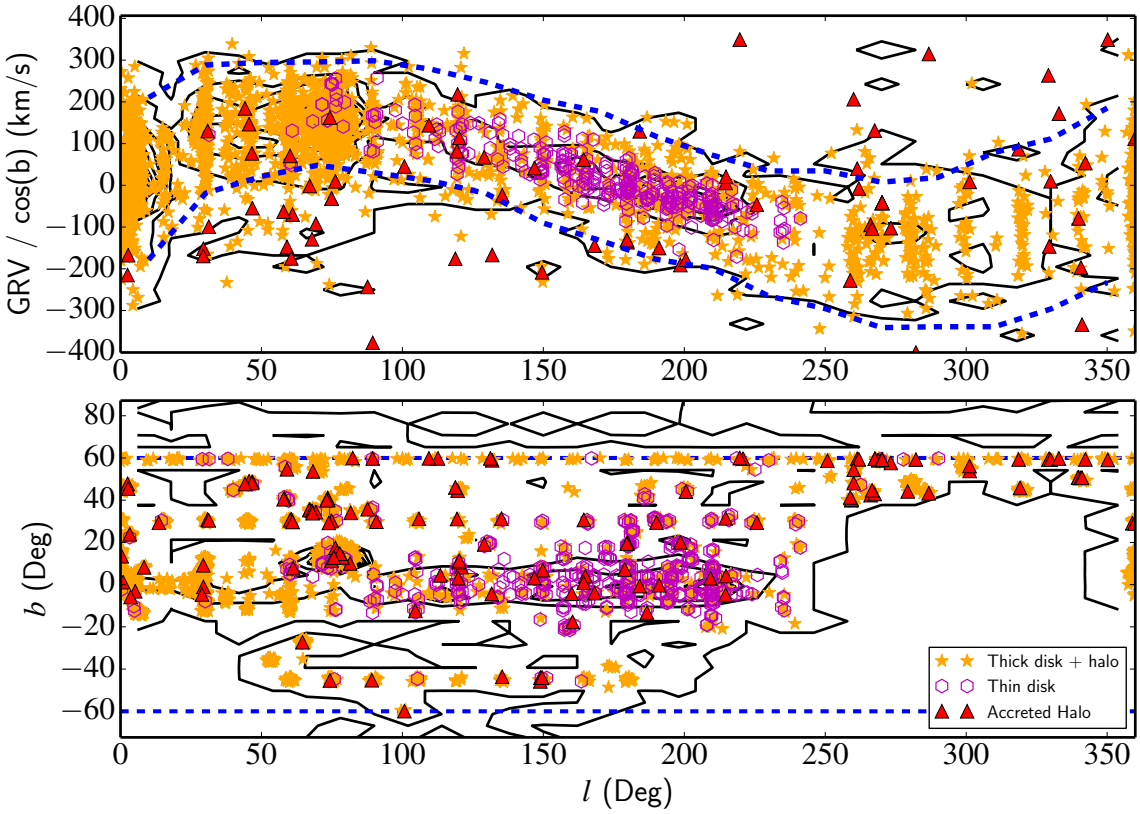

(b)

Figure 4.10 – (a) The [α/Fe] as a function of metallicity for the intermediate metallicity sample using only chemistry to separate the components. The canonical halo + thick disk stars (orange selection box of Figure 4.9) are shown as orange stars. The canonical thin disk (black dots in the magenta selection box of Figure 4.9) are shown as open magenta hexagons. The accreted halo (blue dots in the red selection box of Figure 4.9) are shown as red triangles. (b) Upper panel: The GRV as a function of l for the intermediate metallicity sample using only chemistry to separate the components with the same symbols as (a). For consistency the blue dotted lines represent the initial kinematic selection. Lower Panel: The Galactic coordinates (l, b) of the various subgroups.

status as an α-element. We have also showed that the accreted halo is under abundant in [Al/Fe] which is likely caused by the nuclear pathways in which Al is produced. The low abundances of [C+N/Fe] of accreted halo stars with respect to canonical stars imply that this gas had a slower chemical environment (Nissen et al., 2014). The Ni of the α-poor sequence is, on average, under abundant relative to the α-rich sequence consistent with previous studies. These results indicate that we have confirmed the existence of an α-poor halo sequence of stars that is chemically different from the stars formed in the rest of the halo with chemistry suggesting that these stars may born externally (e.g. Nissen & Schuster, 2010, 2011; Schuster et al., 2012; Ramírez, Meléndez & Chanamé, 2012; Hawkins et al., 2014).

- Upon closer investigation of the undetermined population, we have found evidence that the *thin disk extends down to very low metallicities ([Fe/H]* $\lesssim -0.83$ *dex)*. In Figure 4.8(b), we showed that the candidate metal-poor thin disk, which was the metal-rich end of the undetermined population, were consistent with the canonical thin disk at comparable metallicities both kinematically and spatially. This was the first indication that these stars may be among the lowest metallicity thin disk stars. However, this result will need to be confirmed within another survey with a more accurate metallicity scale. Spatially, the candidate metal-poor thin disk as well as the intermediate metallicity thin disk is located in the outer Galaxy compared to the more metal-rich thin disk component located in the inner Galaxy consistent with a negative metallicity gradient which is observed in the literature (e.g. Cheng et al., 2012).

- Finally, in section 4.5 we put forward a powerful chemically labeling approach to separate the chemically distinct canonical thin disk, thick disk+halo, and accreted halo components using the [α/Fe], [Al/Fe], [C+N/Fe], and [Mg/Mn] abundance ratios. For consistency in Figure 4.10(a) we plot our separated components on the standard [α/Fe]-metallicity plane. Finally, we verified this method by confirming that the kinematics of the resulting populations matched the expected distribution in l-GRV space (Figure 4.10(b)).

Ultimately the precise proper motions and distances from Gaia will allow us to study the full spatial position and dynamics of the stars from each of the components to compliment the chemical evolution analysis done here and help solidify the existence of the accreted halo and candidate metal-poor thin disk. Future surveys such as 4MOST (de Jong et al., 2012) and ongoing surveys such as the Gaia-ESO survey (Gilmore et al., 2012) and GALAH (De Silva et al., 2015) will be able to further study the chemical peculiarities of the accreted halo in a statistical way. With full space motions, positions and chemistry of a large sample of stars in hand, we may not only be able to study the accreted α-poor sequence but also confirm the existence of the very metal-poor thin disk and chemical continuity between the halo and thick disk.

5

Gaia FGK Benchmark Stars: New Candidates At Low-Metallicities

This chapter reproduces the paper: '*Gaia FGK benchmark stars: new candidates at low-metallicities*', **Hawkins, K.**, Jofré, P., Heiter, U, Soubiran, C., Blanco-Cuaresma, C., Casagrande, L., Gilmore, G., Lind, K., Magrini, L., Masseron, T., Pancino, E., Randich S., Worley, C. C., 2016a, A&A, accepted and in press.
The author's contribution to the chapter includes: determination of all $T_{\rm eff}$ for all candidate metal-poor benchmark stars using four separate angular diameter-photometric calibrations, analysis of the spectra with the iSpec node, and the production of the manuscript.

Abstract

We have entered an era of large spectroscopic surveys in which we can measure, through automated pipelines, the atmospheric parameters and chemical abundances for large numbers of stars. Calibrating these survey pipelines using a set of "benchmark stars" in order to evaluate the accuracy and precision of the provided parameters and abundances is of utmost importance. The recent proposed set of Gaia FGK benchmark stars of Heiter et al. (2015) has up to five metal-poor stars but no recommended stars within $-2.0 <$ [Fe/H]< -1.0 dex. However, this metallicity regime is critical to calibrate properly. In this chapter, we aim to add *candidate* Gaia benchmark stars inside of this metal-poor gap. We began with a sample of 21 metal-poor stars which was reduced to 10 stars by requiring accurate photometry and parallaxes, and high-resolution archival spectra. The procedure used to determine the stellar parameters was similar as in Heiter et al. (2015) and Jofré et al. (2014) for consistency. The difference was to homogeneously determine the angular diameter and effective temperature ($T_{\rm eff}$) of all of our stars using the Infrared Flux Method utilizing multi-band photometry. The surface gravity (log g) was determined through fitting stellar evolutionary tracks. The [Fe/H] was determined using four different spectroscopic methods fixing the $T_{\rm eff}$ and log g from the values determined

independent of spectroscopy. We discuss, star-by-star, the quality of each parameter including how it compares to literature, how it compares to a spectroscopic run where all parameters are free, and whether Fe I ionisation/excitation balance is achieved. From the 10 stars, we recommend a sample of five new metal-poor benchmark candidate stars which have consistent $T_{\rm eff}$, log g, and [Fe/H] determined through several means. These stars, which are within $-1.3 <$ [Fe/H] < -1.0, can be used for calibration/validation purpose of stellar parameter/abundance pipelines and should be of highest priority for future interferometric studies.

5.1 Introduction

Chemodynamical studies of our Galaxy are beginning to use large samples of stars embedded in multi-object spectroscopic surveys (e.g. Gaia-ESO, APOGEE, GALAH, and others). In particular, the recently launched Gaia satellite will undoubtedly revolutionise our understanding of the Milky Way with accurate parallaxes and proper motions, and accompanying spectral information for more than a billion stars. Combining data from the many multi-object spectroscopic surveys which are already underway, and the rich dataset from Gaia will be the way forward in order to disentangle the full chemo-dynamical history of our Galaxy. One example is the Gaia-ESO Public Spectroscopic Survey (GES, Gilmore et al., 2012; Randich, Gilmore & Gaia-ESO Consortium, 2013), which aims at providing atmospheric parameters and elemental abundances of more than 10^5 stars. Another example is the Australian GALAH survey (De Silva et al., 2015), which will undoubtedly contain large numbers of metal-poor stars, as well as the H-band APOGEE spectroscopic survey (Eisenstein et al., 2011) sampling giant stars in the Galaxy. In the future, even larger datasets will be produced, such as the southern 4MOST survey (de Jong et al., 2012) or its complimentary northern survey WEAVE (Dalton et al., 2014).

Our methods to do stellar spectroscopy, in particular, to determine the main atmospheric parameters including effective temperature ($T_{\rm eff}$), surface gravity (log g) and metallicity ([Fe/H]), have necessarily evolved towards a more automatic and efficient way. However, these methods need to be calibrated in order to judge their performance. This calibration can be properly done with a set of well-known stars, or *benchmark stars*. In addition, the multiple surveys need to be corrected for systematic offsets between them in order to compare results. This work is about the assessment of such stars.

Beside astrometry, Gaia will produce, for most stars, atmospheric parameters of stars through a pipeline named APSIS (Bailer-Jones et al., 2013). For the calibration of APSIS, we have, in previous reports on this subject, defined a set of stars that cover different parts on the Hertzsprung-Russell diagram (HRD) in the FGK spectral range (henceforth Paper I Heiter et al., 2015). We attempted to also cover a wide range in metallicities, such that these stars would represent a large portion of the Gaia observations. We have called this sample the Gaia FGK benchmark stars (GBS, Paper I). The $T_{\rm eff}$ and log g of the current set of GBS have been determined with fundamental relations, independently from spectroscopy, making use of the star's angular diameter ($\theta_{\rm LD}$) and bolometric flux ($F_{\rm bol}$) combined with its distance (Paper I). The metallicity is then determined by using a homogeneous library of spectra. That library is described in (Blanco-Cuaresma et al., 2014b, henceforth Paper II). This library is analysed to determine the metallicity based on the adopted values for $T_{\rm eff}$ and log g (Jofré et al., 2014, henceforth Paper III). High spectral resolution analyses not only yield atmospheric parameters

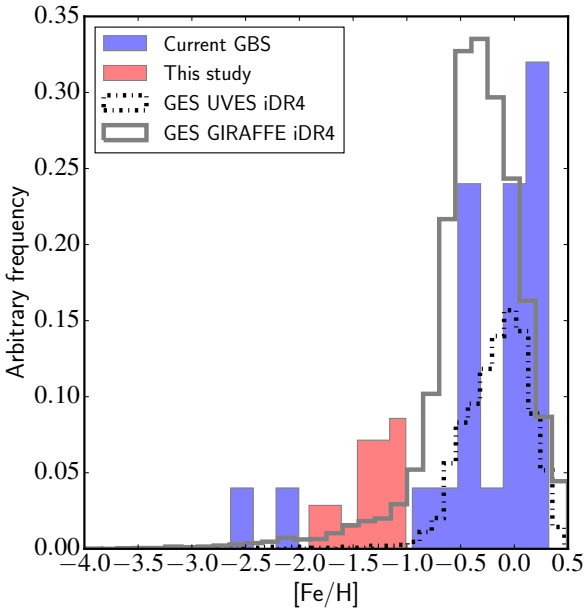

Figure 5.1 – The [Fe/H] distribution of the current GBS sample from Paper III (blue filled histogram) and the selected sample of metal-poor GBS candidates (red filled histogram). The GES iDR4 metallicity distribution from the UVES sample and GIRAFFE sample are shown as a black dash-dotted histogram and gray solid histogram, respectively.

but also individual abundances, thus the same library has been used to derive the abundance of 4 alpha elements and 6 iron-peak elements (Jofré et al., 2015, henceforth Paper IV).

These stars have been shown to be an excellent sample to calibrate the stellar parameter determination pipelines of the Gaia-ESO Survey (Smiljanic et al., 2014, Recio-Blanco et al. in prep) or other spectroscopic surveys and studies (e.g. Schönrich & Bergemann, 2014; De Pascale et al., 2014; Lemasle et al., 2014; De Silva et al., 2015; Boeche & Grebel, 2015). However, the calibrations are currently limited by less than a handful of metal-poor main-sequence stars in our initial GBS sample (e.g. see the calibration paper by Smiljanic et al., 2014). The reason is that metal-poor stars are normally further away and thus fainter, making it impossible to measure their $\theta_{\rm LD}$ accurately with current interferometric instruments except in very rare cases. The metallicity regime around [Fe/H] ~ -1.0 dex is particularly important because this represents the transition between several Galactic components (e.g. the overlap of the metal-weak thick disk, low- and high-α Galactic halos, Nissen & Schuster, 2010; Bensby, Feltzing & Oey, 2014; Hawkins et al., 2015a). Therefore, it is critical to calibrate this metallicity regime correctly.

Among the set of current GBS, nearly 20% (6 stars) have radius and bolometric flux estimated indirectly using photometric relations. At least one of the two current (recommended) metal-poor GBS have radius and bolometric flux estimated indirectly using photometric relations. In this chapter, we use similar and consistent relations to include more metal-poor stars in a homogeneous way. We do this because for many of these GBS candidates $\theta_{\rm LD}$ can not yet be reliably measured with interferometry. In particular, systematic effects might still be the major limitation at the sub-milliarcsec level (e.g. Casagrande et al., 2014).

In the current set of GBS there are a total of five metal-poor stars with [Fe/H] $<$ –1.0 dex (ψ Phe, HD122563, HD84937, HD140283, Gmb 1890). However among these five, three

have not been recommended for calibration or validation purposes in Paper I. HD140283 was not recommended because of the large uncertainties in the $T_{\rm eff}$ which is likely a result of a calibrated bolometric flux which had large systematic differences between the photometric and spectroscopic values. Gmb 1830 has a highly uncertain $T_{\rm eff}$ which could be due to calibration errors in the interferometry (Paper I) and thus it was not recommended. The measured angular diameter of Creevey et al. (2015) yields an effective temperature that is more than 400 K lower than the spectroscopic $T_{\rm eff}$. Additionally, the cool M giant star ψ Phe was not recommended, in part, because of an uncertain metallicity caused by the inability of the methods employed to properly deal with the molecular features which heavily crowd the spectrum.

This leaves only two metal-poor stars which have metallicities below –2.0 dex and effectively no stars with $-2.0 <$ [Fe/H] < -1.0 dex. We aim to provide a set of new GBS *candidate* stars inside of the metal-poor gap listed above. These new stars ultimately will allow the astronomical community and spectroscopic surveys to extend their calibrations based on the benchmark stars possibly reaching into the critical regime of $-1.3 <$ [Fe/H] < -1.0 dex. The metallicity distribution of the recommended set for calibration/validation purposes from Paper I (blue histogram) and the additional metal-poor candidate stars (red histogram) are shown in Figure 5.1. In the background of that figure is the metallicity distribution of the full recommended sample of stars from the GES iDR4 UVES (black dash-dotted histogram) and GIRAFFE (gray solid histogram) spectra (for more information on UVES see Dekker et al., 2000). A sizable fraction of the stars in the GES iDR4 are in the metal poor regime and thus a proper calibration through metal poor GBS is necessary. The recommended stellar parameters (and metallicity) of the GES iDR4 stars have been determined by spectral analysis of several methods (nodes) whose results have been homogenized and combined (details of this will be published in Hourihane et al. 2016 in prep).

In this fifth work of the series, we define a new set of GBS *candidate* stars inside of the metal-poor gap. We note that these candidates do not have $\theta_{\rm LD}$ measurements and should remain as candidates until an $\theta_{\rm LD}$ can be measured directly in the future. In addition, we aim to provide a set of metal-poor stars with predicted $\theta_{\rm LD}$ which can be used as the input for future interferometric studies.

As such, this chapter is organised in the following way: in section 5.2 we begin by selecting a sample of relatively bright metal-poor stars that have archival spectra. We then describe the several methods that we have used to determine the $T_{\rm eff}$ (section 5.3) and log g (section 5.4). Fixing these parameters, we determined the metallicity using methods consistent with Paper III, which we describe in section 5.5. In section 3.3 we present the results of the parameter analysis and discuss, star-by-star, the quality of the parameters and recommend a new set of metal-poor benchmark stars. We also compare our results with what is known about these stars in the literature. Finally, in section 5.7 we summarize our analysis and recommendations.

5.2 Sample

The initial target list was selected using the PASTEL database requiring the following: (1) $4500 < T_{\rm eff} < 6500$ K, (2) –2.0 < [Fe/H] < –1.0 dex, and (3) there were at least four $T_{\rm eff}$ and metallicity estimates in the literature, since 1990, with a standard deviation of less than 100 K and 0.1 dex, respectively. The third criterion was used filter out stars where there are obvious discrepancies in the stellar parameters or the star was ill-behaved in order to maximise

the chance that after our analysis, the stars will have metallicities and parameters in the regime of interest. These criteria result a total of 21 stars including Gbm1380 (HD103095). The metallicity distribution of these 21 stars can be found as the red histogram in Figure 5.1. We further required there to be known BVJHK photometry with defined uncertainties less than 0.15 mag in order to compute accurate photometric $T_{\rm eff}$. This criterion reduced the sample to 17 stars, removing BD+053640, HD199289, HD134440. We also required there to be a known, and non-negative, parallax with a relative uncertainty better than 50%. This criterion removed four stars (HD206739, HD204543, HD063791, HD083212). Finally, we required spectra in the ESO and NARVAL archives. This last criterion removed four stars (HD21581[1], HD023439A/B[2]). The stars BD+053640, HD206739, HD063791, and HD083212 also do not have high-resolution spectra in the ESO/NARVAL archives.

This reduced the sample to the final version of 10 selected stars. We note that after the above cuts, we have mostly selected stars with –1.3 $<$ [Fe/H]$<$ –1.0 dex, which is highly appropriate given that the interface of the thick disk, accreted halo, and possibly even the thin disk is within the regime (e.g. Hawkins et al., 2015a) and there is a lack of such stars in the current GBS. Throughout the rest of this chapter, we will consider and discuss only these 10 stars.

In Table 5.1, we present the basic collected information for the new candidates including the sky position (J2000 right ascension RA and declination DEC) and the mean and dispersion of the stellar parameters taken from PASTEL. Additionally, the photometric and parallax information can be found in Table 5.2. Their B- and V-band photometry were taken from the General Catalogue of Photometric Data (henceforth GCPD, Mermilliod, Mermilliod & Hauck, 1997). Where the B- and V-band photometry was not defined the in the GCPD catalogue the Simbad database was used. The $J_{\rm 2MASS}$ and $K_{\rm 2MASS}$ magnitudes are sourced from the 2MASS catalogue (Cutri et al., 2003). The adopted reddening values, E$(B-V)$ were taken from Meléndez et al. (2010), Casagrande et al. (2010), and Casagrande et al. (2011). The parallax for each star was adopted from the updated analysis of the Hipparcos catalogue (van Leeuwen, 2007). The tables have been separated by those stars which have been selected for further analysis and those which have not for clarity.

The final sample that we focus on in this chapter contains those 10 metal-poor stars, all covering the metallicity regime that we are most interested in, namely metal-poor ([Fe/H] $\sim$ –1.0 dex) stars with an emphasis on dwarf stars. More than half of these stars were suggested in Appendix B of Paper I. The analysis presented here is consistent with the previous papers in the series (Paper I, Paper II, Paper III) allowing the parameters of these metal-poor stars to be added to the GBS sample covering a wide and well sampled parameter space in the HRD.

As in Paper I-IV, we chose stars that have been widely studied in the past. Table 5.1 indicates there are between 4 – 35 studies for each star. However, as seen below, these studies are very different from each other (using different procedures to determine the stellar parameters) and thus the advantage of this work is to homogenise the stellar parameters with respect to Paper I-IV so that they can be ingested into the current GBS.

The parameters given in Table 5.1 have been determined through a variety of means. For example, the $T_{\rm eff}$ has been determined through both photometric (e.g. Alonso, Arribas & Martinez-Roger, 1996a; Nissen et al., 2002; Ramírez & Meléndez, 2005; Jonsell et al., 2005;

[1]This star now has spectra available in the ESO archive but was not public when the target selection for this project was completed

[2]This is a spectroscopic binary system in which neither component had an ESO/NARVAL spectrum.

Table 5.1 – General information on metal-poor benchmark candidates.

Star	RA (J2000)	DEC (J2000)	T_{eff} (K)	σT_{eff} (K)	N	log g (dex)	σlog g (dex)	N	[Fe/H] (dex)	σ[Fe/H] (dex)	N
Selected											
BD+264251	21:43:57.12	+27:23:24.00	5991	97	8	4.30	0.36	7	–1.27	0.08	7
HD102200	11:45:34.24	–46:03:46.39	6119	52	10	4.22	0.16	7	–1.22	0.06	7
HD106038	12:12:01.37	+13:15:40.62	6012	68	9	4.36	0.09	4	–1.31	0.04	4
HD126681	14:27:24.91	–18:24:40.44	5567	84	21	4.59	0.17	12	–1.18	0.09	12
HD175305	18:47:06.44	+74:43:31.45	5085	58	15	2.49	0.25	13	–1.43	0.07	14
HD196892	20:40:49.38	–18:47:33.28	5954	94	9	4.16	0.24	8	–1.03	0.08	9
HD201891	21:11:59.03	+17:43:39.89	5883	68	35	4.33	0.15	28	–1.05	0.08	28
HD218857	23:11:24.60	–16:15:04.02	5119	40	7	2.50	0.34	6	–1.91	0.09	7
HD241253	05:09:56.96	+05:33:26.75	5879	94	13	4.35	0.15	9	–1.06	0.06	9
HD298986	10:17:14.88	–52:29:18.71	6177	82	8	4.23	0.06	5	–1.33	0.04	5
Not Selected											
BD+053640	18:12:21.88	+05:24:04.41	5051	83	9	4.59	0.15	5	–1.20	0.10	5
HD021581	03:28:54.48	–00:25:03.11	4889	61	11	2.15	0.20	6	–1.67	0.08	7
HD023439A	03:47:02.12	+41:25:38.12	5059	73	13	4.51	0.11	13	–1.06	0.08	13
HD023439B	03:47:02.63	+41:25:42.56	4808	70	6	4.55	0.09	6	–1.04	0.09	6
HD063791	07:54:28.72	+62:08:10.76	4715	73	9	1.75	0.07	9	–1.68	0.08	9
HD083212	09:36:19.95	–20:53:14.75	4512	55	15	1.37	0.32	13	–1.46	0.06	13
HD103095	11:52:58.76	+37:43:07.23	5071	76	44	4.65	0.17	36	–1.34	0.10	38
HD134440	15:10:12.96	–16:27:46.51	4817	82	16	4.61	0.11	11	–1.44	0.08	11
HD199289	20:58:08.52	–48:12:13.45	5895	60	12	4.36	0.23	9	–1.01	0.06	10
HD204543	21:29:28.21	–03:30:55.37	4667	66	15	1.30	0.22	11	–1.80	0.10	12
HD206739	21:44:23.94	–11:46:22.84	4662	33	8	1.70	0.00	5	–1.58	0.02	5

NOTES: The stellar parameters for each star were compiled using the PASTEL database (Soubiran et al., 2010). The T_{eff}, σT_{eff}, log g, σlog g, [Fe/H], and σ[Fe/H] represent the mean and dispersion of the stellar parameters from N references in the PASTEL database.

Masana, Jordi & Ribas, 2006; Reddy, Lambert & Allende Prieto, 2006; González Hernández & Bonifacio, 2009; Casagrande et al., 2010, 2011; Ishigaki, Chiba & Aoki, 2012) and spectroscopic (e.g. Gratton, Carretta & Castelli, 1996; Nissen & Schuster, 1997; Gratton et al., 2000; Mishenina et al., 2000; Fulbright, 2000; Gratton et al., 2003; Sousa et al., 2011) means. In some cases the spectroscopic $T_{\rm eff}$ is determined by fitting the wing of the strong Balmer H features, usually Hα or Hβ (e.g. Axer, Fuhrmann & Gehren, 1994; Mashonkina & Gehren, 2000; Gehren et al., 2004). Since the distance is known, the log g is largely derived using the parallax (e.g. Gratton et al., 2000; Gehren et al., 2004; Jonsell et al., 2005). However, in some cases the Fe ionisation balance (Axer, Fuhrmann & Gehren, 1994; Fulbright, 2000; Sousa et al., 2011; Ishigaki, Chiba & Aoki, 2012) or Mg-triplet wing fitting (e.g. Mashonkina & Gehren, 2000) has been used. Metallicity is determined from the analysis of iron lines under 1D-LTE approximations in most of the works (e.g. Axer, Fuhrmann & Gehren, 1994; Fulbright, 2000; Jonsell et al., 2005; Valenti & Fischer, 2005; Sousa et al., 2011; Ishigaki, Chiba & Aoki, 2012). Extensive discussions of these works and our results are found in section 5.6.

5.3 Determination of Effective Temperature

$T_{\rm eff}$ was determined in two ways: (1) using $\theta_{\rm LD}$-photometric calibrations (van Belle, 1999; Kervella et al., 2004; Di Benedetto, 2005; Boyajian, van Belle & von Braun, 2014) and (2) using the IRFM (e.g. Blackwell & Shallis, 1977; Blackwell, Shallis & Selby, 1979; Blackwell, Petford & Shallis, 1980; Casagrande, Portinari & Flynn, 2006; Casagrande et al., 2010). The $T_{\rm eff}$ was determined by employing the Stefan-Boltzmann law. In section 5.3.1 we describe the first procedure and in section 5.3.2 we discuss the second procedure.

5.3.1 Deriving Temperature Using Angular Diameter-Photometric Relationships

To compute the $T_{\rm eff}$, we used Equation 1 of Paper I which relates the $T_{\rm eff}$ to the bolometric flux, $F_{\rm bol}$, and the $\theta_{\rm LD}$. We estimated the $F_{\rm bol}$ using the photometric relationship outlined in Equations 8 and 9 of Alonso, Arribas & Martinez-Roger (1995) which rely on the V and K photometry. We note that the photometric relationship to obtain the $F_{\rm bol}$ required that the K magnitude was in the Johnson rather than 2MASS bandpasses. Thus, we converted the 2MASS photometry (columns 7 and 9 in Table 2) bands into the Johnson system using the following relationship:

$$K_{\rm J} = K_{\rm 2MASS} - 0.1277(J-K)_{\rm 2MASS} + 0.0460, \tag{5.1}$$

where $K_{\rm J}$, $K_{\rm 2MASS}$ are the K-band magnitude in the Johnson and 2MASS systems, respectively. The 2MASS subscript refers to the 2MASS J, K, and (J-K), and the J subscript to Johnson system. This relationship was obtained by combining Equations 6, 7, 13, and 14 from Alonso, Arribas & Martinez-Roger (1994) and Equations 12 and 14 from Carpenter (2001)[3]. The uncertainty in $K_{\rm J}$ was determined by propagating the uncertainty in the $K_{\rm 2MASS}$

[3]We note that Equation 12 and 14 from Carpenter (2001) have been updated in 2003. These updates can be found at http://www.astro.caltech.edu/ jmc/2mass/v3/transformations/. The difference between the 2001 and 2003 values is negligible. For example, the mean difference in $K_{\rm J}$ is 0.005 mag leading to a change in $T_{\rm eff}$ on the order of less than 8 K.

Table 5.2 – Photometry and Parallax of Metal-Poor Benchmark Candidates.

Star	B (mag)	σB (mag)	V (mag)	σV (mag)	N	$J_{2\mathrm{MASS}}$ (mag)	σJ (mag)	$K_{2\mathrm{MASS}}$ (mag)	σK (mag)	π (mas)	$\sigma\pi$ (mas)	E$(B-V)$ (mag)
Selected												
BD+264251	10.52	0.03	10.05	0.03	2	8.98	0.02	8.64	0.02	9.03	1.68	0.007
HD102200	9.21	0.01	8.76	0.00	2	7.69	0.02	7.38	0.02	13.00	0.98	0.005
HD106038	10.63	0.01	10.16	0.01	9	9.11	0.03	8.76	0.02	9.98	1.57	0.003
HD126681	9.90	0.01	9.31	0.01	4	8.04	0.02	7.63	0.02	21.04	1.12	0.000
HD175305	7.93	0.02	7.17	0.01	6	5.61	0.02	5.06	0.02	6.39	0.36	0.000
HD196892	8.73	0.02	8.23	0.02	5	7.18	0.03	6.82	0.02	16.15	0.93	0.000
HD201891	7.89	0.01	7.38	0.02	10	6.25	0.02	5.93	0.02	29.10	0.64	0.000
HD218857	9.60	0.11	8.88	0.11	3	7.40	0.02	6.87	0.02	3.21	1.09	0.019
HD241253	10.24	0.00	9.72	0.00	2	8.64	0.03	8.29	0.02	8.66	1.77	0.001
HD298986	10.46	0.03	10.03	0.03	4	9.04	0.02	8.74	0.02	6.61	1.41	0.004
Not Selected												
BD+053640	11.16	...	10.43	...	0	8.85	0.04	8.34	0.04	15.58	1.82	...
HD021581	9.54	0.01	8.71	0.00	2	6.98	0.02	6.41	0.02	4.03	1.00	...
HD023439A	8.93	0.01	8.18	0.02	4	6.62	0.02	6.12	0.02	46.65	2.63	...
HD023439B	9.26	0.03	8.77	0.01	4	6.95	0.02	6.35	0.02	50.72	1.02	...
HD063791	8.81	0.02	7.90	0.01	0	6.05	0.04	5.43	0.02	1.07	0.73	...
HD083212	9.39	0.04	8.32	0.03	3	6.31	0.02	5.61	0.02	0.96	0.77	...
HD103095	7.19	0.02	6.44	0.02	2	4.94	0.20	4.37	0.03	109.99	0.41	...
HD134440	10.22	0.02	9.43	0.01	1	...	...	...	...	35.14	1.48	...
HD199289	8.82	...	8.30	...	1	7.18	0.02	6.84	0.02	18.95	0.76	...
HD204543	9.17	0.02	8.30	0.01	0	6.46	0.02	5.78	0.02	–0.13	1.08	...
HD206739	9.45	0.03	8.60	0.02	0	6.70	0.02	6.03	0.02	1.93	1.17	...

NOTES: The B and V magnitudes were sourced from the GCPD catalogue (Mermilliod, Mermilliod & Hauck, 1997) with N number of references. In cases where the B and V were not found in the GCPD catalogue, they were taken from the Simbad database. The $J_{2\mathrm{MASS}}$ and $K_{2\mathrm{MASS}}$ magnitudes are sourced from 2MASS (Cutri et al., 2003). All parallaxes were taken from a reanalysis of the Hipparcos catalogue (van Leeuwen, 2007). The adopted reddening values were taken from Meléndez et al. (2010), Casagrande et al. (2010), and Casagrande et al. (2011).

and $(J-K)_{\rm 2MASS}$. We note here that the photometry was corrected for reddening using the values in column 13 of Table 5.2. These corrections are very small and have the effect of changing the $\theta_{\rm LD}$ on the order of less than 1% and $T_{\rm eff}$ by less than 30 K when compared to the raw photometric values.

The $\theta_{\rm LD}$ was determined indirectly through photometric relationships. We have made use of four separate $\theta_{\rm LD}$-photometric relations in order to test the robustness of this procedure (van Belle, 1999; Kervella et al., 2004; Di Benedetto, 2005; Boyajian, van Belle & von Braun, 2014). The first set of calibrations used were taken from the work of van Belle (1999). We determined the angular diameter of all stars by taking the average of the $\theta_{\rm LD}$-$(B-V)$ relation (their Equation 2) and $\theta_{\rm LD}$-$(V-K)$ relation (their Equation 3). The second set of calibrations, which was used only for the dwarf stars, were taken from the photometric relationships of Kervella et al. (2004). Just as above, we averaged the $\theta_{\rm LD}$-$(B-V)$ relation (their Equation 22) and $\theta_{\rm LD}$-$(V-K)$ relation (their Equation 23). We note this procedure was used for the $\theta_{\rm LD}$ for the GBS HD22879 and ϵ For (Paper I). The third set of calibrations were from Di Benedetto (2005). We computed the $\theta_{\rm LD}$ of all stars using the $\theta_{\rm LD}$-$(B-V)$ relation (their Equations 1 and 2). The final set of calibrations used were from Boyajian, van Belle & von Braun (2014). We made use of their $\theta_{\rm LD}$-$(B-V)$ relation (their Equation 4) which is only applicable to the dwarf stars.

The results of the $\theta_{\rm LD}$ and $T_{\rm eff}$ computed using the various $\theta_{\rm LD}$-photometric calibrations above can be found in Figure 5.2. In top panel of Figure 5.2, we compare the $\theta_{\rm LD}$, in miliarcseconds (mas), of each star and relation used. We also plot the $\theta_{\rm LD}$ computed from the infrared flux method (hereafter IRFM, see section 5.3.2 and Casagrande, Portinari & Flynn, 2006; Casagrande et al., 2010, 2014, for more details). In the middle panel of Figure 5.2 we show the relative difference between the four $\theta_{\rm LD}$-photometric relations with that computed from the IRFM. In the bottom panel of Figure 5.2, we compare the $T_{\rm eff}$ derived from the different $\theta_{\rm LD}$-photometric calibrations and that computed from the IRFM. In most cases the $\theta_{\rm LD}$ from each of the photometric calibrations are consistent (within 1σ) with each other and the $\theta_{\rm LD}$ from the IRFM.

As noted by Paper I, we choose to use the (V-K)-$\theta_{\rm LD}$ relationships because they have the smallest dispersion in the fitted relationship (on the order of less than 1%) compared to other photometric colours. These equations are created by relating the $\theta_{\rm LD}$ of dwarf, subgiant, and giant stars determined via interferometry to their $(V-K)_{\rm J}$ colour and $K_{\rm J}$ magnitude (e.g. van Belle, 1999; Kervella et al., 2004; Di Benedetto, 2005; Boyajian, van Belle & von Braun, 2014). While it is likely that the brightest star (HD175305) may soon have direct $\theta_{\rm LD}$ measurements, most of these stars are dim, making direct interferometric $\theta_{\rm LD}$ measurements difficult with current instruments. Thus for the moment, we have the only option to rely on the photometric calibrations for $\theta_{\rm LD}$ and $F_{\rm bol}$.

It is important to note that recent studies (e.g. Creevey et al., 2012, 2015) have indicated the $\theta_{\rm LD}$ photometric relationship may underestimate the $\theta_{\rm LD}$ particularly at low metallicities. This is likely because the $\theta_{\rm LD}$-photometric relationship are often only constrained by less than a handful, around 2–3, metal-poor stars (e.g. see Figure 5 of Kervella et al., 2004). Since the $T_{\rm eff}$ is proportional to ${\theta_{\rm LD}}^{-0.5}$, underestimating the $\theta_{\rm LD}$ causes the $T_{\rm eff}$ to be overestimated. We also made use of the IRFM because it has the advantage of including not only information from V and K but also a broad range of photometry improving the $T_{\rm eff}$ estimate and predicted $\theta_{\rm LD}$ (see section 5.3.2).

We are also prompted to use the IRFM because there is a relatively large disagreement

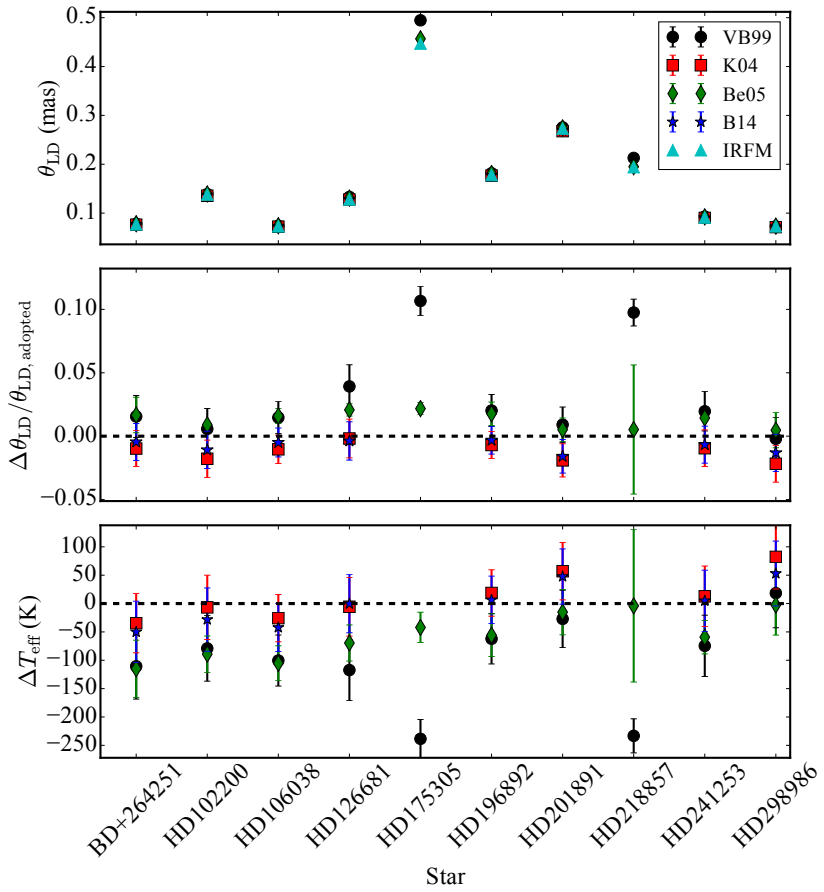

Figure 5.2 – Top Panel: The computed $\theta_{\rm LD}$ for each star from the four $\theta_{\rm LD}$-photometric relationships: (K04, Kervella et al., 2004) is represented by red squares, (VB99, van Belle, 1999) is represented by black circles, (Be05, Di Benedetto, 2005) is represented by green diamonds, (B14, Boyajian, van Belle & von Braun, 2014) is represented by blue stars. In addition, the infrared flux method (IRFM) is also displayed as (cyan triangles). Middle Panel: $\Delta\theta/\theta_{\rm adopted}$ for each star. Here $\Delta\theta_{\rm LD} = \theta_{\rm LD}$ - $\theta_{\rm LD,adopted}$. The adopted $\theta_{\rm LD}$ is that computed from the IRFM. Bottom Panel: Comparison of the $T_{\rm eff}$ for each star, computed from the $\theta_{\rm LD}$-photometric relationships, with the adopted value from the infrared flux method.

(on the order of 10% which causes differences in $T_{\rm eff}$ of more than 300 K) between the $\theta_{\rm LD}$ of the giant stars in our sample using the calibrations of van Belle (1999) and Di Benedetto (2005). The reason for this discrepancy is currently not clear. One explanation is that there are intrinsic errors in the procedures that were used to determine the fitted relations. For example, reddening was not taken into account when relating the photometric colours to $\theta_{\rm LD}$ in the work of van Belle (1999) which in part could cause discrepancies in their fitted relationships. In addition, it is important to note that a weakness of using these relations is that they do not include dependencies on [Fe/H]. As a result, many of these relations perform best around solar metallicity, by construction.

5.3.2 Infrared Flux Method

In addition to the $\theta_{\rm LD}$-photometric relationships used in the previous section, we also made use of the infrared flux method (IRFM). This is one of the least model-dependent techniques to determine effective temperatures in stars, and it was originally devised to obtain stellar angular diameters with an accuracy of a few percent (Blackwell & Shallis, 1977; Blackwell, Shallis & Selby, 1979; Blackwell, Petford & Shallis, 1980). Our analysis is based on the implementation described in Casagrande, Portinari & Flynn (2006); Casagrande et al. (2010).

The basic idea is to recover for each star its bolometric flux and infrared monochromatic flux, both measured on the Earth. Their ratio is then compared to that obtained from the two same quantities defined on a surface element of the star, i.e., the bolometric flux $\sigma T_{\rm eff}^4$ and the theoretical infrared monochromatic flux. The only unknown parameter in this comparison is $T_{\rm eff}$, which can be obtained (often with an iterative scheme, as described further below). For stars roughly earlier than M-type, the theoretical monochromatic flux is relatively easy to compute because the near infrared region is largely dominated by the continuum, with a nearly linear dependence on $T_{\rm eff}$ (Rayleigh-Jeans regime) and is largely unaffected by other stellar parameters such as metallicity and surface gravity. This minimizes any dependence on model atmospheres, and makes the IRFM complementary to most spectroscopic methods, where instead $T_{\rm eff}$ is often degenerate with gravity and metallicity. Once the bolometric flux and the effective temperature are known, the limb-darkened angular diameter is also trivially, and self-consistently, obtained from the IRFM. Since most of the times fluxes are derived from multi-band photometry, the problem is ultimately reduced to a derivation of fluxes in physical units, i.e., it depends on the photometric absolute calibration. Without exaggeration, this is the most critical point when implementing the IRFM, since it sets the zero-point of the $T_{\rm eff}$ scale. In our case, the absolute calibration has been anchored using solar twins, and the zero-point of the resulting effective temperature scale thoroughly tested (Casagrande et al., 2010, 2014; Datson, Flynn & Portinari, 2012, 2014).

For the sake of this work, the bolometric flux was recovered using multi-band photometry (Johnson-Cousins $BV(RI)_C$ and 2MASS ($J_{\rm 2MASS}$, $H_{\rm 2MASS}$, $K_{\rm 2MASS}$) and the flux outside of these bands estimated using theoretical model fluxes from Castelli & Kurucz (2004). For each star [Fe/H] and log g were fixed to the GBS recommended values. Whereas an iterative procedure was adopted in $T_{\rm eff}$, starting with an initial guess, and iterating the IRFM until convergence within 1 K was reached. Despite all candidate GBS being relatively nearby, some of them might be slightly affected by extinction. When available, we adopted the reddening values derived from interstellar Na I D lines (Meléndez et al., 2010) or from Casagrande et al. (2010) or Casagrande et al. (2011) for the remaining cases.

Ultimately, we adopted the $T_{\rm eff}$ computed from the IRFM, as opposed to the $\theta_{\rm LD}$-photometric calibrations, in large part because it provides a robust estimate of the $\theta_{\rm LD}$ for the two problematic giant stars making use of the available full broad band photometry rather than the $(V-K)$ colour. In addition, in this way we have $\theta_{\rm LD}$ and $T_{\rm eff}$ from both giant and dwarf stars that are computed using a homogenous framework. We note that for all dwarf stars, except for BD+264251, the IRFM temperature agrees very well with all four $\theta_{\rm LD}$-photometric relationships described in section 5.3.1 within the 1σ uncertainty. This is also the case for the giant stars when considering the calibration of Di Benedetto (2005) but not that of van Belle (1999). The top panel of Figure 5.3 shows the adopted $T_{\rm eff}$ from the IRFM with respect to literature values obtained from the PASTEL database. It indicates that the $T_{\rm eff}$ determined from the IRFM are systematically larger, by $\sim$60 K, compared to the mean $T_{\rm eff}$ from the PASTEL database. However typical uncertainties in $T_{\rm eff}$ are larger than this value. The reason for this minor discrepancy is unclear. The adopted $F_{\rm bol}$, $\theta_{\rm LD}$, and $T_{\rm eff}$and their uncertainties determined via the IRFM can be found in Table 5.3.

5.4 Determination of Surface Gravity

The surface gravity was determined using the same procedure as in Paper I. We briefly summarize this method below. The log g was determined using the adopted relationship g = GM / R^2 where G is Newton's gravitational constant, M is the mass of the star and R is its radius. The radius of the star was estimated using the adopted $\theta_{\rm LD}$ which is listed in column 1 of Table 5.3 and the parallax listed in column 11 of Table 5.2. The mass for each star was computed by fitting the stellar parameters to a set of stellar evolutionary tracks. In this case, those of Yonsei-Yale[4] were used (Y^2, Yi, Kim & Demarque, 2003; Demarque et al., 2004). The fitting procedure is described in Paper I. The luminosity was computed from the bolometric flux and parallax. The $T_{\rm eff}$ used was the value adopted from the IRFM. Additionally, the input metallicity was initially assumed to be the mean value from the PASTEL database. The log g does not change significantly when using the final metallicity values described in section 3.3. More details about the specific inputs to the Y^2 models, comparison of the masses determined from other stellar evolutionary tracks (e.g. Padova, Bertelli et al., 2008, 2009), and a comparison of the log g determined by this method and others can be found in sections 4 and 5 of Paper I. The middle panel of Figure 5.3 indicates that the log g values determined in the this way are consistent with the literature values from the PASTEL database. The grid of stellar models were interpolated with respect to mass and metallicity. The mass was then determined by minimizing the difference between the interpolated models and the position of the star on the HRD. The main source of uncertainty in the log g determined tends to be from the radius (and thus $\theta_{\rm LD}$) compared to the mass (see section 4.1 and Appendix A of Paper I).

Figure 5.4 shows the locations of all stars in the theoretical HRD, together with *Yonsei-Yale* evolutionary tracks for different metallicities. Most of the stars cluster around the tracks for 0.8 $M_{\odot}$, with two dwarfs and the most metal-poor giant at somewhat lower masses. The mass difference of successive tracks (0.05 $M_{\odot}$) corresponds to the typical uncertainty in mass.

[4]http://www.astro.yale.edu/demarque/yystar.html

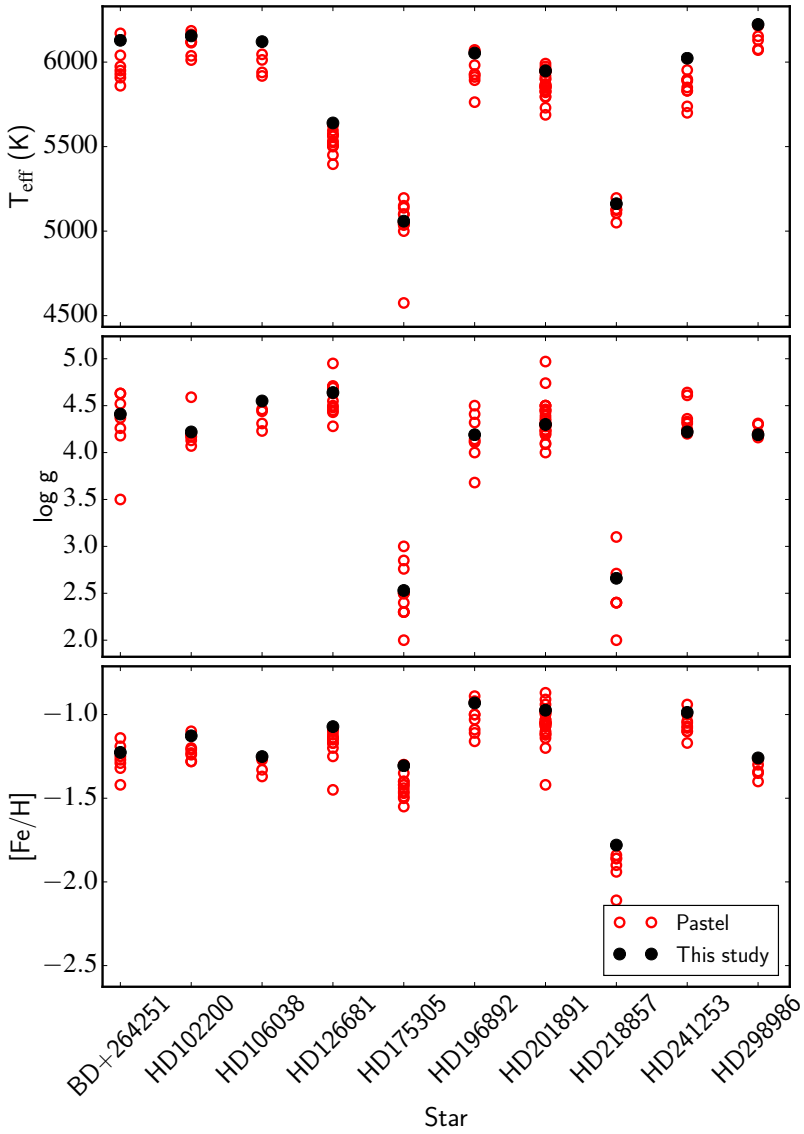

Figure 5.3 – The adopted T_{eff} (top panel), log g (middle panel), and [Fe/H] (bottom panel) of the metal-poor GBS candidate stars (black closed circles) compared with the values from the literature (open red circles) sourced from the PASTEL catalogue.

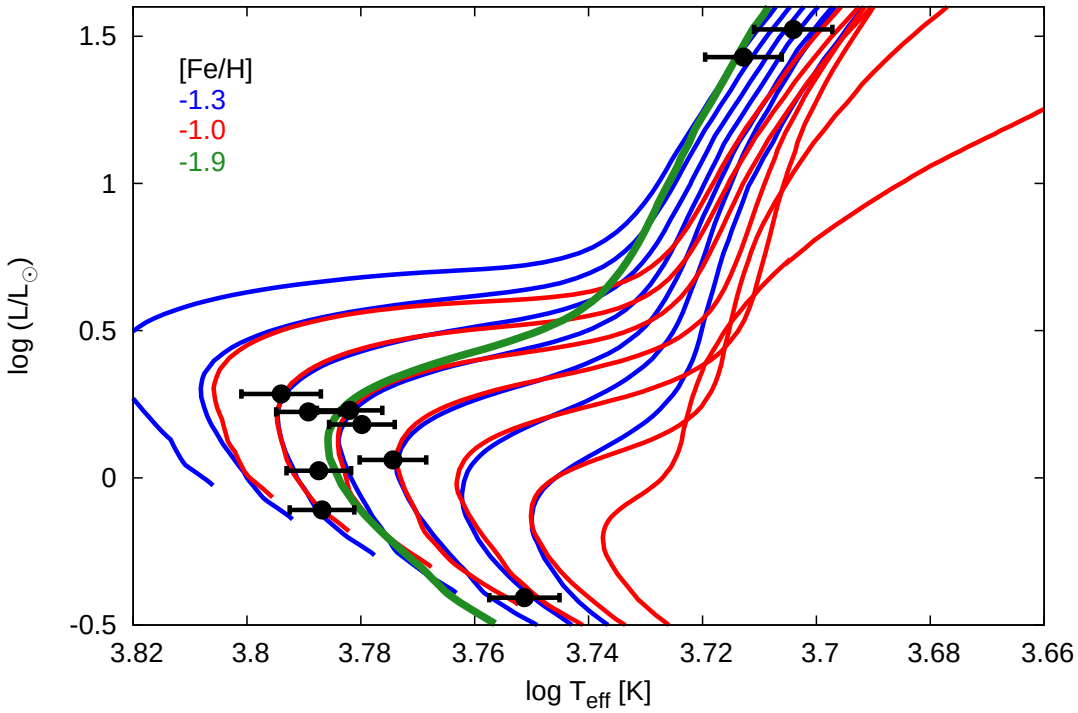

Figure 5.4 – HRD showing the stellar parameters of the metal-poor benchmark candidates (black circles with error bars) superimposed on *Yonsei-Yale* evolutionary tracks for [α/Fe]=+0.3, and [Fe/H]=-1.3 (blue lines) and [Fe/H]=-1.0 (red lines). Tracks are shown for masses increasing from 0.60 $M_\odot$ to the right to 0.90 $M_\odot$ to the left, in steps of 0.05 $M_\odot$. The green line shows a track for [Fe/H]=-1.9 and a mass of 0.70 $M_\odot$, corresponding to the properties of the giant star HD 218857.

Table 5.3 – Adopted parameters for metal-poor benchmark candidates.

Star	$\theta_{\rm LD}$ (mas)	$\sigma\theta_{\rm LD}$ (mas)	$\rm F_{bol}$ (10^{-11} Wm^{-2})	$\sigma \rm F_{bol}$ (10^{-11} Wm^{-2})	$\rm T_{eff}$ (K)	$\sigma \rm T_{eff}$ (K)	log g (dex)	σlog g (dex)	$v_{\rm mic}$ (km s^{-1})	$v \sin i$ (km s^{-1})	$\sigma v \sin i$ (km s^{-1})
*BD+264251	0.077	0.001	0.2759	0.0059	6129	80	4.41	0.16	1.40	2.81	2.10
HD102200	0.138	0.002	0.9062	0.0041	6155	80	4.22	0.07	1.43	1.90	4.59
HD106038	0.073	0.001	0.2477	0.0026	6121	80	4.55	0.14	1.39	0.00	0.00
*HD126681	0.128	0.002	0.5543	0.0050	5640	80	4.64	0.07	1.16	0.00	0.00
HD175305	0.447	0.006	4.3520	0.6752	5059	80	2.53	0.14	1.54	5.01	1.92
*HD196892	0.178	0.002	1.4130	0.0233	6053	80	4.19	0.06	1.36	0.00	0.00
HD201891	0.273	0.004	3.1154	0.0517	5948	80	4.30	0.04	1.29	2.93	5.31
*HD218857	0.194	0.003	0.8841	0.1625	5162	80	2.66	0.32	1.58	3.14	6.80
*HD241253	0.091	0.001	0.3642	0.0013	6023	80	4.22	0.18	1.34	1.89	4.50
HD298986	0.073	0.001	0.2691	0.0067	6223	100	4.19	0.19	1.48	4.07	5.98

NOTES: The $\theta_{\rm LD}$ were computed as a part of the IRFM. In addition, the $\rm T_{eff}$ and $\rm F_{bol}$ in this table represents the adopted $\rm T_{eff}$ and bolometric flux from the IRFM, respectively. We estimated v_{mic} using the GES relationship of Bergemann and Hill. The uncertainty in v_{mic} was conservatively assumed to be 0.20 km s^{-1} for all stars. Stars with an asterisk (*) in column 1 are currently not recommended (see section 5.6.1 for a star by star discussion on the recommendations.)

Table 5.4 – Spectra used for this study.

Star	I	Date_{obs}	SNR (pixel^{-1})	R_{in}	Program ID
BD+264251	U	2003-08-09	286	45254	71.B-0529(A)
HD102200	U	2001-03-06	160	51690	67.D-0086(A)
HD106038	U	2004-03-28	254	45254	072.B-0585(A)
HD126681	U	2000-04-09	240	51690	65.L-0507(A)
HD175305	N	2010-03-16	150	80000	...
HD196892	U	2005-10-15	268	45990	076.B-0055(A)
HD201891	U	2012-10-18	107	66320	090.B-0605(A)
HD218857	U	2001-10-09	102	56990	68.D-0546(A)
HD241253	U	2005-10-08	194	56990	076.B-0133(A)
HD298986	U	2000-04-09	173	51690	65.L-0507(A)

NOTES: The I, or instrument, is either the U580 setting for the UVES instrument on the Very Large Telescope (denoted by U) or the NARVAL instrument (denoted by N). We note that while the input resolution ($R_{\text{in}} = \lambda/\Delta\lambda$) varies depending on the instrument and setup, we convolved all spectra to a common value of R = 40000. In addition, all of the spectra have a spectral coverage of at least 4760 – 6840 Å.

5.5 Determination of Metallicity

To determine the metallicity of the candidates, we analysed their spectra. Because these stars were selected from the PASTEL database, they have been previously studied and thus their spectra can be found in archives (see Table 5.4). Nine stars have previously been observed in the U580 setup of the UVES instrument and the spectra were downloaded from the ESO archives[5]. Additionally, one star (HD175305) comes from the archive of the NARVAL spectrograph operated by the Télescope Bernard Lyot[6]. The spectra were prepared in the same way as Paper II: they were normalised, corrected by radial velocity and convolved to the lowest common resolution (R = 40000), in the same fashion as in the rest of the GBS. Note the resolution is lower in this case compared to our previous study because we could not find the whole data set with higher resolution. In all cases, the signal to noise ratio (SNR or S/N) of the spectra is better than 100 pixel^{-1}.

The analysis was done as in sections 4.1, 4.2, and 4.3 of Paper III, namely we used several codes. In addition, we used common input material (spectra, atomic data for the line list, Fe I, Fe II lines, etc.) and fixed the T_{eff} and log g to their adopted values determined in section 5.3 and 5.4, respectively. We made use of the 1D-LTE MARCS atmosphere models (Gustafsson et al., 2008b) and a common set of pre-defined iron lines, which were selected from the "golden lines" for metal-poor stars of Paper III. We considered the lines used for HD140283, HD122563, HD84937, HD22879 and Gmb 1830. Then, by visual inspection, we selected those lines that were visible in most of the new stars, obtaining a final list of 131 Fe I and Fe II lines (see Table 4 from Paper III for the input atomic data). Individual lines used for each star can be found in Tables A1-A10 of the online material. For clarity and reproducibility, in section 5.8, we outline

[5]http://archive.eso.org/cms.html

[6]http://tblegacy.bagn.obs-mip.fr/

the format of the online material.

In this work, we employed four methods, or nodes, to determine the metallicity. Two methods use the equivalent width (EW) technique which include: (1) Bologna – based on GALA developed by Mucciarelli et al. (2013) and (2) EPINARBO – based on FAMA developed by Magrini et al. (2013). Both of these methods measure the EWs of individual iron features using the DOOp code (Cantat-Gaudin et al., 2014) which is an automated wrapper for the DAOSPEC code (Stetson & Pancino, 2008). The other two methods use spectral synthesis including: (1) BACCHUS/ULB – developed by T. Masseron (Masseron, 2006) which made use of the Turbospectrum synthesis code (Alvarez & Plez, 1998; Plez, 2012) and (2) iSpec – developed by Blanco-Cuaresma et al. (2014a). For more details on these methods we refer the reader to section 4.3 of Paper III, section 3.3, Table 4 of Paper IV and the development papers cited above. The first three methods were also employed in our previous metallicity determination in Paper III, while all four methods were used to determine abundances of several elements for the GBS sample (Paper IV).

The initial metallicity for the analysis was considered to be $[\mathrm{Fe/H}] = -1.00$ dex for all stars. The macroturbulence parameter, v_{mac}, was determined simultaneously with the iron abundance, in the same way as in Paper III. The microturbulence parameter, v_{mic}, was set to the value determined by the GES v_{mic} relationship (e.g. Smiljanic et al., 2014, Paper III, Bergemann et al., in prep).

We conducted a total of eight runs which included: the "main run" fixing the T_{eff} and log g and v_{mic} to their adopted values and six "error" runs where these three fixed values were varied by their $\pm 1\sigma$ uncertainties listed in Table 5.3. This was done to evaluate the impact of the 1σ uncertainty in the adopted parameters on the [Fe/H]. In addition, each node solved for the stellar parameters independently using its own procedure, in what we define as the "free run" or eighth run. We note that in the free run we do not require the different nodes to use the same procedure (e.g. σ-clipping outlying Fe lines, tolerances of conversion, line selection etc.). This test was done primarily to see how each node performed when not using fixed T_{eff} and log g parameters. We emphasize that some of these nodes, particularly the EW nodes, often require a much larger number of lines for best performance. Thus, we remind the reader that the results of the free analysis simply allow us to quantify, in a different way, the benefit of fixing the T_{eff} and log g. We refer the reader to Paper III for a extensive discussion on this matter.

A node-to-node comparison of the [Fe/H] can be found in Figure 5.5, where we plot the metallicity of each star (including the results for the GBS in Paper III) obtained by each node relative to the mean literature value from PASTEL database. We also sort the stars on the x-axis towards increasing metallicity. The y-axis of the figure is the Δ[Fe/H]$_{\mathrm{lit}}$ (which is defined as [Fe/H]–[Fe/H]$_{\mathrm{lit}}$), where [Fe/H] is the metallicity of the star determined by a specific node and [Fe/H]$_{\mathrm{lit}}$ is the mean [Fe/H] from the PASTEL database. The name of the star is indicated on the bottom of the figure. We note that only 3 nodes (ULB, Bologna, and EPINARBO) of Paper III were included in this figure. These nodes are the same as in this work. Figure 5.5 indicates that the metallicities from the different nodes for the metal-poor candidates have a standard deviation of 0.028. In addition, the values generally agree well with the literature with a mean offset of +0.04 dex. This is consistent with the offset (+0.04 dex) and standard deviation (0.07 dex) of the FG dwarfs among the GBS (Paper III). The typical node-to-node scatter for the candidate stars are comparable to the GBS in the same T_{eff} regime. Again we note that the node abundances for each star were determined by averaging the abundances of each line.

NLTE-corrected metallicities for each star can be found in column 2 of Table 5.5. The

Table 5.5 – Adopted [Fe/H] for metal-poor benchmark candidates.

Star	[Fe/H]	σFeI	$\Delta(T_{eff})$	Δ(log g)	$\Delta(v_{mic})$	Δ(LTE)	$\Delta(ion)$	σFeII	N_{FeI}	N_{FeII}
*BD+264251	-1.225	0.066	0.087	0.019	0.019	0.030	-0.051	0.050	63	8
HD102200	-1.117	0.073	0.077	0.006	0.006	0.045	0.021	0.070	58	8
HD106038	-1.246	0.083	0.083	0.010	0.010	0.020	-0.026	0.055	66	7
*HD126681	-1.068	0.061	0.049	0.005	0.005	0.010	0.021	0.046	61	7
HD175305	-1.295	0.056	0.059	-0.010	-0.010	0.060	0.084	0.041	56	8
*HD196892	-0.929	0.054	0.054	0.006	0.006	0.039	0.026	0.052	68	8
HD201891	-0.970	0.056	0.063	-0.004	-0.004	0.030	0.068	0.021	68	8
*HD218857	-1.783	0.074	0.106	0.040	0.040	0.064	0.005	0.054	56	8
*HD241253	-0.993	0.065	0.090	0.005	0.005	0.030	0.096	0.028	66	7
HD298986	-1.257	0.074	0.087	0.015	0.015	0.052	0.040	0.048	66	6

NOTES: The [Fe/H] is the NLTE-corrected and is the recommended value for each star. The $\Delta(T_{eff})$ is the uncertainty in the [Fe/H] due to the uncertainty in T_{eff}, Δ(log g) is the uncertainty in the [Fe/H] due to the uncertainty in log g, and $\Delta(v_{mic})$ is the uncertainty in the [Fe/H] due to the uncertainty in v_{mic}. Δ(LTE) is the NLTE-corrected [Fe/H] minus the LTE [Fe/H]. $\Delta(ion)$ = [Fe I /H] – [Fe IIH]. The line-to-line dispersion of Fe I and Fe II are σFe II and σFe II, respectively. Finally N_{FeI} and N_{FeII} are the number of Fe I and Fe II lines used for the analysis, respectively. Stars with an asterisk (*) in column 1 are currently not recommended (see section 5.6.1 for a star-by-star discussion on the recommendations).

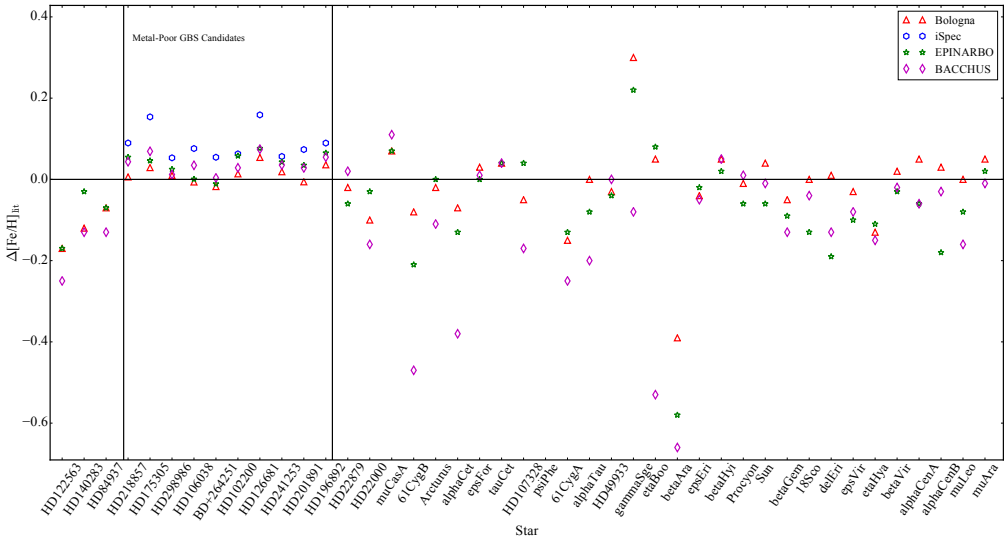

Figure 5.5 – The Δ[Fe/H]$_{\rm lit}$ = [Fe/H]- [Fe/H]$_{\rm lit}$ for each star and node for our GBS candidates and the current GBS stars ordered by metallicity. The node symbols are as follows: (1) iSpec is represented as a blue open hexagon, (2) BACCHUS/ULB is represented as a magenta open diamond, (3) EPINARBO is represented as a green open star, and (4) Bologna is represented as a red open triangle. We do not display the nodes that are used in Paper III and not this work. The typical dispersion between the methods is on the order of $\pm$0.03 dex while the typical offset between the literature and the each method is on the order of +0.04 dex.

uncertainty in [Fe/H] due to the uncertainty in T$_{\rm eff}$, log g, and $v_{\rm mic}$ can be found in columns 4, 5, and 6, respectively. The difference between the LTE and NLTE-corrected metallicity, Δ(LTE), and the difference between the mean Fe I and Fe II abundance, $\Delta(ion)$, is found in column 7 and 8 respectively. The line-to-line dispersion of Fe I , Fe II and the number of Fe I and Fe II lines used in the analysis are listed in columns 3, 10, 11, and 12, respectively. Table 5.5 indicates that the difference between Fe I and Fe II can be as high as 0.10 dex in the worst cases. The $\Delta(ion)$ values are smaller than for some of the GBS, e.g. HD 122563, where $\Delta(ion)_{\rm HD122563}$ = –0.19 dex (Paper III). We note here that HD 122563 is more metal-poor, with [Fe/H] = –2.64, than the stars we consider in this chapter. On the other hand the NLTE corrections, which are on the order of 0.05 dex, are similar to those of the current set of GBS.

We remind the reader that the final metallicity was computed as a mean of NLTE-corrected Fe lines. The NLTE corrections were computed in the same way as Paper III, namely by interpolating over a grid of NLTE corrections outlined in Lind, Bergemann & Asplund (2012). For this calculation, the adopted parameters were used. When the NLTE correction for a given line is not available the median of the NLTE corrections is assumed. This is both reasonable and reliable because the NLTE corrections per line are very similar for a single star (e.g. Bergemann et al., 2012). The NLTE correction range from +0.020 to +0.064 dex.

For each Fe I and Fe II line, run and star we have four measurements (one for each of the nodes) for the iron abundance, which can be found in the tables online. We note here that the EW measurements for the synthesis methods (ULB/BACCHUS, iSpec) are measured for completeness but are not used to measure the abundances. The Fe abundance for each of the selected "golden" lines, and its computed NLTE correction can also be found as part of the

online material. A description of this online material can be found in section 5.8.

5.6 Results and Discussion

In this section, we discuss, on a star-by-star basis the results of the stellar parameter analysis. We discuss the quality of each parameter for each star, separately. In addition, we describe the node-to-node variation in the stellar parameters. Finally, we compare the adopted stellar parameters with those determined spectroscopically.

As in Paper III and Paper IV, we selected only the lines that were sufficiently strong to have reliable abundances and sufficiently weak to not saturate, that is, line strength or reduced equivalent width (REW) was in the range of $-6.0 \leq$ REW ≤ -5.0 where REW = $\log(\mathrm{EW}/\lambda)$. For this selection, the adopted equivalent width (EW) was computed by averaging over the four measurements. Among the selected lines, we computed the mean of the four Fe abundance measurements and calculated its NLTE correction consistent with Paper III and references therein.

To help facilitate the discussion we plot the final NLTE-corrected abundances for each line and star in Figure 5.6 using different symbols for neutral and ionised lines. Each star is indicated in a different set of right-left panels. For reference, the star's name is listed in the right panel and its stellar parameters are indicated in the left panel. The left panels show the abundances as a function of REW while the right panels show the abundances as a function of excitation potential (EP). We performed linear fits to the neutral lines. The slope of the trend and its standard error are indicated at the top of each panel. A slope is considered to be significant if its absolute value is larger than the standard error. We also performed a linear fit to only high EP lines (with EP $\geq$ 2eV). We choose this cut because the low-excitation transitions are thought to experience significantly larger departures from 1D, LTE compared to higher excitation transitions (e.g. Bergemann et al., 2012). The red dashed lines correspond to the mean abundances determined from ionised lines.

In Figure 5.6, we find that three of the ten stars (HD126681, HD 218857, and HD 298986) have significant trends in REW and Fe abundance indicating an potential issue with their v_{mic}. Figure 5.6 also indicates that six of the ten stars have significant trends in the Fe abundance and EP whether using all of the Fe I lines or using just the high-EP lines as suggested by Bergemann et al. (2012).

The criteria for recommending a GBS candidate are as follows: (1) the T_{eff} derived from IRFM should be consistent with the θ_{LD}-photometric calibrations, (2) the T_{eff} determined via the IRFM and photometric calibrations should be consistent with the spectroscopic T_{eff} (i.e., the correlation between EP and Fe abundance should be null), (3) the log g determined via isochrone fitting (assuming the T_{eff} from IRFM) should be consistent with the spectroscopic log g (i.e., the mean abundance of Fe I should equal that of Fe II). Finally all stars where there is large discrepancies between the recommended parameters and PASTEL (i.e., differences in T_{eff} more than 500 K, log g larger than 0.5 dex, [Fe/H] larger than 0.5 dex) are flagged as suspicious.

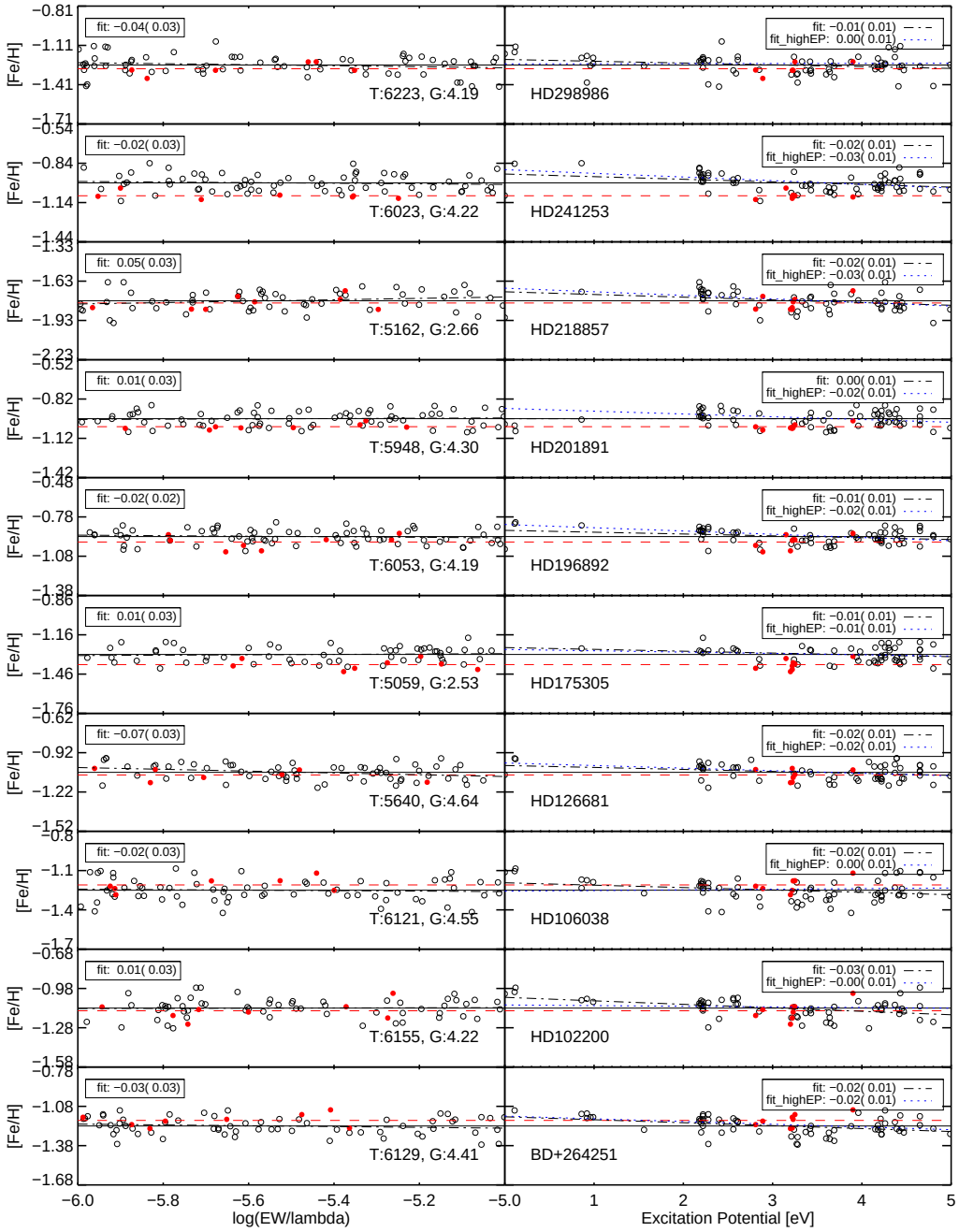

Figure 5.6 – Final iron abundances as a function of REW (left panels) and EP (right panels) for all stars analysed in this work. Open circles indicate neutral lines while filled red circles indicated ionised lines. A linear regression fit to the neutral lines is performed for all lines (indicated with a black dash-dotted line) and for high-EP lines (EP $\geq$ 2eV, indicated by a blue dotted line). The slope of the trend and its standard error are indicated at the top of each panel. A slope is considered to be significant if its absolute value is larger than the standard error. The effective temperature and surface gravity for each star is also indicated at the bottom of the left panels for reference. Dashed red line indicates the mean of the ionised lines.

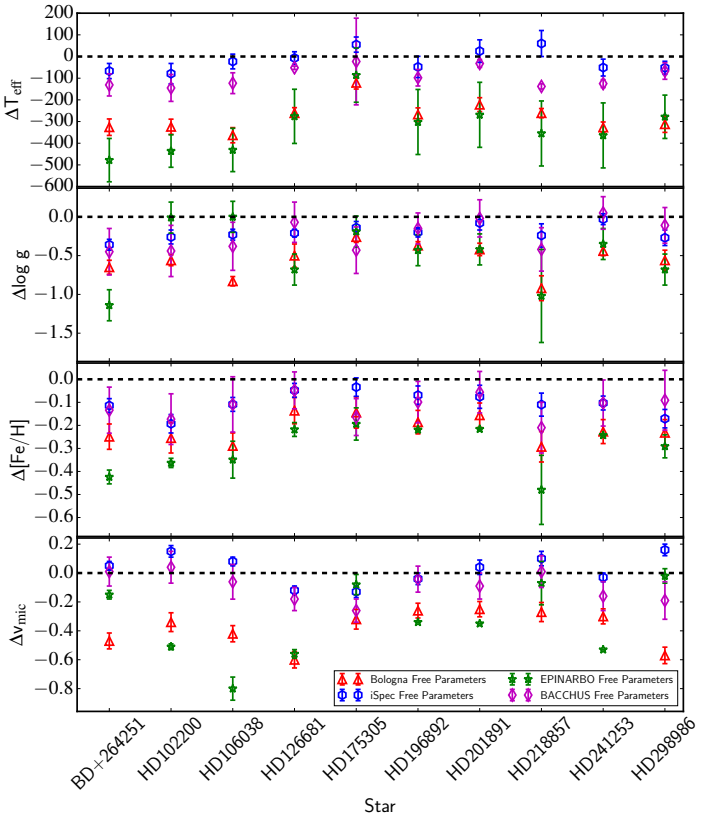

Figure 5.7 – The $\Delta T_{\rm eff}$, Δlog g, Δ[Fe/H], and $\Delta v_{\rm mic}$ computed from the free run (described in section 5.5) for each star from top to bottom, respectively. We note here that the Δ represents the difference of the node and adopted values for each parameter. For example, Δlog g = log $g_{\rm node}-$ log $g_{\rm adopted}$. The BACCHUS (ULB) method is denoted as the open magenta diamond, the iSpec method is denoted as the open blue hexagon, the EPINARBO method is denoted as a open green star and the Bologna method is denoted as an open red triangle.

5.6.1 Star-By-Star Discussion

In this subsection we discuss the results star-by-star. For this discussion, we remind the reader that the adopted $T_{\rm eff}$, determined via the IRFM, can be found in column 6 of Table 5.3. The adopted log g is determined though relating the $\theta_{\rm LD}$ and the mass. The mass is determined through isochrone fitting, using the Y^2 stellar evolutionary tracks, the adopted $T_{\rm eff}$ and the mean [Fe/H]. The recommended NLTE-corrected [Fe/H], derived using four spectroscopic methods and the adopted $T_{\rm eff}$ and log g, can be found in column 2 of Table 5.5.

We begin the discussion by comparing the adopted $T_{\rm eff}$ with that of the mean value from the PASTEL database and determined by the four $\theta_{\rm LD}$-photometric calibrations (van Belle, 1999; Kervella et al., 2004; Di Benedetto, 2005; Boyajian, van Belle & von Braun, 2014). In addition, we evaluate the spectroscopic validity of the $T_{\rm eff}$ by ensuring that the trend in the Fe abundance with EP is null. As a diagnostic, we compare the adopted $T_{\rm eff}$ and $T_{\rm eff}$ from the free run (described in section 5.5). We note here that the results of the free run indicate that the EW methods tend to systematically underestimate the $T_{\rm eff}$ and log g. A potential reason for this is that the EW methods are affected by the restriction of lines allowed to be used in this analysis while synthesis methods are less affected by this. In addition, there are stark differences in the EW and synthesis procedures (e.g. sigma-clipping, convergence threshold of the pipeline, etc.) that were not fixed during this test. We stress that this test is not attempting to quantify the performance of EW methods.

We then compare the adopted log g with those determined from various means in the literature and from the free stellar parameter run. We test its validity by confirming that the Fe I and Fe II abundance agree (ionisation balance). Next we compare the metallicity derived using the adopted $T_{\rm eff}$ and log g and that from the literature. The [Fe/H] from the literature in most cases assumes LTE while we tabulate the NLTE corrected metallicity. The NLTE correction listed in Table 5.5 is positive and thus may explain why in Figure 5.3 our final NLTE-corrected [Fe/H] (filled black circles) are a bit larger than the literature (open red circles). These NLTE correction are on the order of 0.05 dex. We note here that these corrections are treated as an uncertainty in our results.

We also inspect the trend between REW and Fe abundance as a way to access the quality of the $v_{\rm mic}$. As a general comment, the $T_{\rm eff}$ determined using indirect data in all stars is systematically higher than the mean $T_{\rm eff}$ from the PASTEL database (Figure 5.3) and determined spectroscopically (Figure 5.7). We compute the combined uncertainty in the [Fe/H] in the same way as Paper I (i.e., by quadratically summing all σ and Δ columns in Table 5.5). In addition, we remark as to whether the candidate can have direct $\theta_{\rm LD}$ measurements from current optical or near-infrared interferometers including the the VLT Interferometer or the CHARA array (for a detailed description of such facilities and their $\theta_{\rm LD}$ limitation see Dravins et al., 2012). Finally, using the above discussion we either recommend or not recommend the star as a new GBS candidate.

BD+264251

The adopted $T_{\rm eff}$ of this star is hotter than the mean literature value by 140 K (2%). It is most discrepant from the $T_{\rm eff}$ derived via $(B-V)$ photometry in the work of Mishenina et al. (2000). In addition, the adopted $T_{\rm eff}$ for this star is in fair agreement with the temperature derived from the various photometric calibration of angular diameter (van Belle, 1999; Kervella et al., 2004; Di Benedetto, 2005; Boyajian, van Belle & von Braun, 2014). The $T_{\rm eff}$ from the

free run output of this star is between 0.01% and 6% smaller than the adopted $T_{\rm eff}$ for the iSpec and EPINARBO nodes, respectively. The spectroscopic and adopted $T_{\rm eff}$ do not agree which is consistent with the significant trend in the Fe abundance as a function of EP (Fig 5.6). However, this trend can be resolved by varying the stellar parameters within the uncertainties. In particular, it may be resolved by reducing $v_{\rm mic}$ by 0.2 km s^{-1} (i.e., the assumed uncertainty in the $v_{\rm mic}$).

The adopted log g of this star is 0.1 dex (2%) larger than the mean value from the PASTEL database. The Fe I and Fe II lines agree to within 0.05 dex (Table 5.5). In addition, the most discrepant log g from the literature is from Mishenina et al. (2000). In this study the log g is derived from the ionisation balance however only making use of 20 Fe I and 5 Fe II lines. We not only make use of a method independent of spectroscopy for our adopted log g, we also find relatively good agreement between 63 Fe I and 8 Fe II lines.

The [Fe/H] derived from the spectrum assuming the adopted $T_{\rm eff}$ and log g is 0.05 dex (4%) larger than the mean value from the PASTEL database and from 0.10 – 0.40 dex (or 8–32%) larger than the free run output of the ULB/BACCHUS and EPINARBO nodes, respectively. The combined uncertainty in [Fe/H] is on the order of $\pm$0.15 dex. There is no significant correlation between Fe abundance with REW.

We do not recommend this star as a GBS candidate because of the discrepant photometry, ranging a total of 0.15 mag in V, which leads to relatively uncertain $T_{\rm eff}$. Additionally, the agreement between the $T_{\rm eff}$ from the $\theta_{\rm LD}$-photometric relationships and the IRFM is in worse agreement than all of the other candidates. This uncertainty in $T_{\rm eff}$ propagates to all other parameters. In addition, the predicted $\theta_{\rm LD}$ of this star is 0.07 mas and thus will be impossible to measure directly with the current state-of-the-art interferometers (with limits on the order of 0.1 mas with the Cherenkov Telescope Array) and possibly future intensity interferometers (e.g. Figure 1 of Dravins et al., 2012).

HD102200

The adopted $T_{\rm eff}$ of this star is in excellent agreement (less than 1%) with other spectroscopic and photometric studies (e.g. Mashonkina et al., 2003; Gehren et al., 2004; Jonsell et al., 2005; Sousa et al., 2011). It is also in good agreement with the $T_{\rm eff}$ derived from the various $\theta_{\rm LD}$-photometric calibrations. We note that the $T_{\rm eff}$ from the free run output of this star ranges between less than 0.1% and 6% from the adopted $T_{\rm eff}$ for the iSpec and EPINARBO nodes, respectively. Additionally, the adopted $T_{\rm eff}$ is consistent with the spectroscopic $T_{\rm eff}$. This is indicated by the null trend in the [Fe/H] abundance as a function of EP validating the adopted $T_{\rm eff}$.

The adopted log g of this star is in excellent agreement (less than 0.5%) with the mean value of studies collated in the PASTEL database. It is also in fair agreement with the free parameter run. The disagreement between the adopted value and the free parameter run ranges between 0.5 and 10% for the EPINARBO and Bologna methods, respectively. There is also very good agreement (within 0.02 dex) between mean Fe I abundance, determined from averaging 58 lines and, the average Fe II abundance, determined by averaging 8 Fe II lines. This indicates that the adopted log g is in good agreement with the spectroscopic log g.

The [Fe/H] derived from the spectrum assuming the adopted $T_{\rm eff}$ and log g is $\sim$ 0.10 dex (10%) larger than the mean literature value and 0.17 – 0.35 dex (15–30%) larger than the [Fe/H] determined in the free spectroscopic run with the ULB/BACCHUS and EPINARBO methods,

respectively (Figure 5.7). However, it is important to keep in mind that both the free run and the bulk of the literature assumes LTE. The NLTE correction for this star is on the order of +0.05 dex (see Table 5.5). The combined uncertainty in [Fe/H] is on the order of $\pm$0.13 dex. There is no significant correlation between Fe abundance with REW.

In light of good agreement between the adopted stellar parameters and the various literature sources, the spectroscopic validation, and the free run output, we recommend this star as a GBS candidate. In addition, its predicted $\theta_{\rm LD}$ is 0.14 mas (twice as large as BD+264251). However, due to its faintness (V=8.8) it would be very challenging to achieve a direct estimate of the $\theta_{\rm LD}$ of this star with current interferometers.

HD106038

The adopted $T_{\rm eff}$ of this star agrees well ($\sim$ 2%) with the mean value from the literature (Alonso, Arribas & Martinez-Roger, 1996a; Nissen & Schuster, 1997; Nissen et al., 2002; Ramírez & Meléndez, 2005; Gratton et al., 2003; Casagrande et al., 2011). The most discrepant $T_{\rm eff}$ from the literature is cooler than the adopted $T_{\rm eff}$ by $\sim$200 K determined via $(V-K)$-$T_{\rm eff}$ relations (Nissen et al., 2002). The adopted $T_{\rm eff}$ is also in good agreement with the derived from the photometric calibration of $\theta_{\rm LD}$ ($\sim$1%). Additionally, the $T_{\rm eff}$ from the free run output of this star ranges between less than 0.1% and 6% from adopted $T_{\rm eff}$ for the iSpec and EPINARBO nodes, respectively. The spectroscopic analysis showed that there is a null trend in the Fe abundance as a function EP. This indicates that the spectroscopic and adopted $T_{\rm eff}$ are consistent with one another.

The adopted log g of this star is in good agreement (4%) with the mean value from the literature. It is also in good agreement the values determined from the free parameter run (between 0.5 – 18% for the EPINARBO and Bologna methods, respectively). The Fe I and Fe II are consistent with each other within –0.026 dex which indicates that the adopted and spectroscopic log g are in agreement.

The [Fe/H] derived assuming the adopted $T_{\rm eff}$ and log g is $\sim$ 0.05 dex (4%) larger than the mean from literature and 0.08 – 0.28 dex (15–30%) larger than the [Fe/H] determined from the free run from the ULB and EPINARBO methods, respectively (Figure 5.7). In addition, the combined [Fe/H] uncertainty is on the order of 0.13 dex. Finally, There is no significant correlation between Fe abundance with REW.

We have shown that there is good agreement between the adopted stellar parameters and the various literature sources, the spectroscopic validation and the free run output. As a result we recommend this star as a GBS candidate. However, similar to BD+264251, this star has a predicted $\theta_{\rm LD}$ of 0.07 mas making it impossible to observe with current interferometers.

HD126681

The adopted $T_{\rm eff}$ is in excellent agreement ($\sim$ 1.2%) with the typical $T_{\rm eff}$ found in the literature (e.g. Tomkin et al., 1992; Blackwell & Lynas-Gray, 1998; Fulbright, 2000; Nissen et al., 2002; Gratton et al., 2003; Reddy, Lambert & Allende Prieto, 2006; Masana, Jordi & Ribas, 2006; Sousa et al., 2011). The most discrepant $T_{\rm eff}$ is from the work of Reddy, Lambert & Allende Prieto (2006). The authors determine the $T_{\rm eff}$ of their sample using Strömgen $(b-y)$ photometry (e.g. Alonso, Arribas & Martinez-Roger, 1996b). However, we note that at the $T_{\rm eff}$ of this star, the authors show (in their Figure 6) that the difference in $T_{\rm eff}$ determined by Strömgen $(b-y)$ photometry and $(V-K)$ photometry has a dispersion of at least 100 K. The adopted $T_{\rm eff}$ is

also consistent with those derived from the photometric calibrations of $\theta_{\rm LD}$ within 100 K. The $T_{\rm eff}$ from the free run output of this star ranges between less than 0.1% and 4% from adopted $T_{\rm eff}$ for the iSpec and EPINARBO nodes, respectively. However, there is a significant trend in the [Fe/H] abundance as a function of EP. This trend cannot be resolved by accounting for the uncertainties in the stellar parameters. This indicates that the adopted $T_{\rm eff}$ is not in good agreement with the spectroscopic $T_{\rm eff}$.

The adopted log g of this star is in good agreement with the mean value from the PASTEL database (4%). It is also in good agreement with the free run output (between 0.5 – 18% for the EPINARBO and Bologna methods, respectively). In addition, the mean abundance of Fe I (using 61 neutral lines) and Fe II (using 7 ionised lines) agrees within 0.021 dex.

The [Fe/H] derived from the spectrum assuming the adopted $T_{\rm eff}$ and log g (described in section 5.5) is $\sim$ 0.05 dex (4%) larger than the mean literature value and 0.08 – 0.28 dex (15–30%) larger than the [Fe/H] determined in the free parameter run by the ULB and EPINARBO methods, respectively (Figure 5.7). The NLTE corrections on the Fe abundance are on the order of +0.02 dex. The combined uncertainty in the [Fe/H] is on the order of 0.10 dex. We also found a significant correlation between Fe abundance with REW indicating that the $v_{\rm mic}$ may not be adequate.

We do not recommend this star as a GBS candidate because we cannot validate its $T_{\rm eff}$ using Fe I ionisation/excitation balance. In addition the $v_{\rm mic}$ must be changed in order to balance the correlation between Fe abundance and REW. The $\theta_{\rm LD}$ of this star is on the order of 0.10 mas which would make it out of reach for current interferometers.

HD175305

The adopted $T_{\rm eff}$ is in excellent agreement ($\sim$ 1%) with the mean literature value (e.g. Wallerstein et al., 1979; Alonso, Arribas & Martinez-Roger, 1996a; Nissen & Schuster, 1997; Fulbright, 2000; Burris et al., 2000; Ishigaki, Chiba & Aoki, 2012). While the most discrepant $T_{\rm eff}$ in the literature, from Fulbright (2000), is more than 400 K cooler than the adopted $T_{\rm eff}$, it is an outlier among many other studies. Disregarding this outlying study, the mean difference between the adopted $T_{\rm eff}$ and the literature is 20 K. The $\theta_{\rm LD}$ determined from the photometric calibration from van Belle (1999) is larger by nearly a factor of five compared to that of Di Benedetto (2005). This in turn causes the temperature to be discrepant by 250 K ($\sim$4.5%) between these calibrations. The adopted $T_{\rm eff}$ is consistent with Di Benedetto (2005). The discrepancy between these two $\theta_{\rm LD}$-photometric calibrations is in part what motivated using the IRFM as the adopted procedure. The adopted $T_{\rm eff}$ and the $T_{\rm eff}$ derived from the free run output agrees within 2%. There is a null trend in the [Fe/H] abundance as a function of EP indicating good agreement between the spectroscopic and adopted $T_{\rm eff}$.

The adopted log g of this star agrees within 1% of the mean value from the literature and those determined from the free spectroscopic run (less than 15%). While there is an offset of 0.08 dex between the abundance of Fe I, determined from 56 neutral Fe lines, and Fe II, determined from 8 ionised Fe lines, it can be resolved by taking into account the uncertainty in $T_{\rm eff}$ and log g.

The [Fe/H] derived from the spectrum assuming the adopted $T_{\rm eff}$ and log g is $\sim$ 0.05 dex (4%) larger than the mean from the PASTEL database and 0.08 – 0.28 dex (15–30%) larger than the [Fe/H] determined in the free spectroscopic run from the ULB and EPINARBO methods, respectively (Figure 5.7). The combined uncertainty in the [Fe/H] is on the order of 0.14 dex.

There is also a null correlation between the Fe abundance with REW.

Because of the good agreement (less than 2% in $T_{\rm eff}$, 18% in log g and less than 15% in [Fe/H]) between the various methods (i.e., the adopted, validation through Fe excitation/ionisation balance, free run output, and literature) of determining the stellar parameters, we recommend this star as a GBS candidate. In addition, the relatively large $\theta_{\rm LD}$ of this star (0.447 $\pm$ 0.006 mas), makes it possible to be observed in the near future with current interferometers.

HD196892

The adopted $T_{\rm eff}$ is in good agreement (less than 2%) with the mean literature value (e.g. Axer, Fuhrmann & Gehren, 1994; Jehin et al., 1999; Thévenin & Idiart, 1999; Gratton et al., 2003; Jonsell et al., 2005; Sousa et al., 2011). The most discrepant $T_{\rm eff}$ is from the work of Axer, Fuhrmann & Gehren (1994) where it is derived using Hα, Hβ,Hγ, and Hδ fitting. These authors note that there are likely systematic differences of their $T_{\rm eff}$ with photometric values from other studies (e.g. Fuhrmann, Axer & Gehren, 1994). This may, in part, explain the discrepancy. The $T_{\rm eff}$ derived from the various photometric calibrations of $\theta_{\rm LD}$ are consistent within 100 K of the adopted value. We note that the adopted $T_{\rm eff}$ and that from the free run output agree within 4%. There is a significant trend in the [Fe/H] abundance as a function of EP indicating that the spectroscopic and adopted $T_{\rm eff}$ disagree. This trend cannot be resolved accounting for the uncertainties in the parameters.

The adopted log g of this star is in excellent agreement (less than 1%) with the mean value from the PASTEL database. In addition, it is consistent with the free run. The mean Fe I abundance, derived using 68 neutral Fe lines is consistent (within 0.03 dex) of the Fe II abundance, derived from 8 ionised Fe lines. This indicates that the spectroscopic log g is consistent with the adopted value.

The [Fe/H] derived from the spectrum is $\sim$ 0.1 dex (10%) larger than the mean literature value and as much as 0.22 dex (25%) larger than the [Fe/H] determined from the free spectroscopic run (Figure 5.7). We remind the reader that this is not taking into account the NLTE correction which in this star is on the order of +0.04 dex. The combined [Fe/H] uncertainty is on the order of $\pm$0.08 dex. There is no significant correlation between REW and Fe abundance.

We do not recommend this star as a GBS candidate because of the statistically significant trend in Fe I abundance and EP. In particular, this trend cannot be resolved varying the parameters within their uncertainties. In addition, the $\theta_{\rm LD}$ of this star is on the order of 0.18 $\pm$ 0.002 mas making interferometric $\theta_{\rm LD}$ measurements very challenging.

HD201891

This star has an adopted temperature that is in good agreement ($\sim$1%) with the typical value from other studies (e.g. Edvardsson et al., 1993; Fuhrmann et al., 1997; Israelian, García López & Rebolo, 1998; Clementini et al., 1999; Thévenin & Idiart, 1999; Chen et al., 2000; Zhao & Gehren, 2000; Mishenina & Kovtyukh, 2001; Qui et al., 2002; Ramírez & Meléndez, 2005; Valenti & Fischer, 2005; Reddy & Lambert, 2008; Casagrande et al., 2011). In fact, of the 35 studies which are listed in the PASTEL database, only 7 have $T_{\rm eff}$ that differ by more than 100 K from our adopted value. The most discrepant $T_{\rm eff}$ is 260 K lower (Valenti & Fischer, 2005) than the adopted $T_{\rm eff}$. It is important to note that Valenti & Fischer (2005) determined the $T_{\rm eff}$ of this star using a spectral fitting procedure. In addition, the $T_{\rm eff}$ from Valenti & Fischer (2005) are well calibrated around solar $T_{\rm eff}$ and metallicity, but get increasingly worse at low

metallicities and high $T_{\rm eff}$ (e.g. see Fig 11, top panel of Casagrande et al., 2011). The 1D-LTE assumption under which the $T_{\rm eff}$ is determined through spectroscopy may also account, in part, for the discrepancy. The adopted $T_{\rm eff}$ is also in good agreement with the four $\theta_{\rm LD}$-photometric calibrations. The adopted $T_{\rm eff}$ and free run $T_{\rm eff}$ of this star are in fair agreement (within 4%). While HD201891 has a statistically significant correlation between Fe I abundance and EP, this correlation can effectively be resolved by varying the parameters within their uncertainty.

The adopted log g is in excellent agreement with the mean value from the literature. The log g is also consistent (between 0 – 10% level for the ULB and Bologna nodes, respectively) with the free run output. There is a slight discrepancy (at the 0.06 dex level) between the mean abundance neutral Fe (using 68 Fe I lines) and the mean abundance of ionised Fe (using 8 Fe II lines). This discrepancy can be reduced to $\sim$0.02 dex by varying the parameters within their uncertainties.

The derived [Fe/H] is 0.07 dex (8%) larger than the mean literature value and as much as 0.22 dex (23%) larger than the [Fe/H] from the free run output. The total NLTE correction is on the order of +0.03 dex. The combined uncertainty in [Fe/H] is $\pm$0.10 dex. We also find no significant correlation between REW and Fe abundance.

We recommend this star as a GBS candidate. While we noted a statistically significant correlation between the Fe I abundance and EP, this can be resolved by taking into account the uncertainties on the parameters. In addition the discrepancy between the neutral and ionised Fe lines is also reduced to an acceptable level by accounting for the uncertainties in the parameters. Finally HD201891 has a relatively high $\theta_{\rm LD}$, with $\theta_{\rm LD}$ = 0.273 $\pm$ 0.004, for a dwarf star and thus it may be possible with current interferometers to achieve an $\theta_{\rm LD}$ estimate for this star.

HD218857

The adopted $T_{\rm eff}$ is in excellent agreement (typically less than 1%) with the literature (Axer, Fuhrmann & Gehren, 1994; Pilachowski, Sneden & Kraft, 1996; Burris et al., 2000; Mishenina & Kovtyukh, 2001; Ishigaki, Chiba & Aoki, 2012). The $T_{\rm eff}$ derived from the photometric calibration on angular diameter from Di Benedetto (2005) is in excellent agreement with the adopted $T_{\rm eff}$. However, the photometric calibration of van Belle (1999), is $\sim$250 K lower than the adopted value. We note that the $T_{\rm eff}$ from the free run output of this star ranges between less than 0.1% and 8% from adopted $T_{\rm eff}$ for the iSpec and EPINARBO nodes, respectively. HD218857 also has a statistically significant correlation between Fe I abundance and EP lines considering both high EP and all EP Fe I lines indicating that the $T_{\rm eff}$ from spectroscopic techniques may be in tension with the values determined in section 5.3. This trend cannot be resolved by varying the stellar parameters within the uncertainty.

The adopted log g of this star is $\sim$0.1 dex (4%) larger than the typical value from the literature and as much as 1 dex larger (40%) than the value determined from the free run. However, the mean abundance of Fe I , determined using 56 Fe I lines, is within 0.01 dex of the mean abundance of Fe II determined using 8 Fe II lines.

The derived [Fe/H] is 0.13 dex (8%) larger than the mean literature value and as as much as 0.48 dex (27%) larger than the [Fe/H] determined in the free spectroscopic run. The typical NLTE Fe corrections for this star are on the order of +0.06 dex. The combined uncertainty in [Fe/H] is on the order of 0.16 dex. In addition, we find a significant correlation between REW and Fe abundance indicating a potential issue with the $v_{\rm mic}$.

We do not recommend this star as a GBS candidate because of the significant trend in

Fe I abundance and EP as well as the uncertain log g. This trend cannot be resolved through varying the $T_{\rm eff}$, log g, [Fe/H], and $v_{\rm mic}$ within their uncertainties). In addition, the typical uncertainties in the parameters (particularly the uncertainty in log g) of this star are quite large compared to the other stars. However, the star is rather faint (V=8.9) making interferometric $\theta_{\rm LD}$ measurements very challenging if not impossible.

HD241253

The adopted $T_{\rm eff}$ of this star is 150 K (3%) larger than the typical literature value (e.g. Axer, Fuhrmann & Gehren, 1994; di Benedetto, 1998; Prochaska et al., 2000; Nissen et al., 2002; Gehren et al., 2004; Mashonkina et al., 2003; Masana, Jordi & Ribas, 2006; Reddy, Lambert & Allende Prieto, 2006; Reddy & Lambert, 2008). The $T_{\rm eff}$ is most discrepant with the literature at the 350 K level (Reddy, Lambert & Allende Prieto, 2006). As we noted above these authors determine the $T_{\rm eff}$ of their sample using Strömgen $(b-y)$ photometry. Interestingly, these authors revise the $T_{\rm eff}$ of the star two years later (Reddy & Lambert, 2008) which makes it consistent with our adopted $T_{\rm eff}$. The $T_{\rm eff}$ determined using the $\theta_{\rm LD}$-photometric calibration are in good agreement with the adopted value (less than 2%). The $T_{\rm eff}$ from the free run output of this star is in moderate agreement with the adopted $T_{\rm eff}$ (within 7%). However, this star has a statistically significant correlation between Fe I abundance and EP lines considering both high EP and all EP Fe I lines. This correlation cannot be resolved by varying the stellar parameters within the uncertainty.

The adopted log g of this star is 0.14 dex (2%) less than the typical value from the literature and as much as 0.45 dex larger (10%) than the value determined from the free run. The mean Fe I abundance, derived using 66 neutral Fe lines does not agree well (at the 0.10 dex level) with the Fe II abundance, derived from 7 ionised Fe lines. This indicates that the spectroscopic log g is not consistent with the adopted value. This ionisation imbalance is not resolved taking into account the uncertainties in the parameters.

The [Fe/H] derived is 0.06 dex (6%) larger than the mean literature value and up to 0.24 dex (25%) larger than the [Fe/H] determined in the free spectroscopic run. The NLTE Fe corrections are on the order of +0.03 dex. There is no significant correlation between REW and Fe abundance.

We do not recommend this star as a GBS candidate because of the significant trend in Fe I abundance and EP as well as the disagreement between Fe I and Fe II. This trend cannot be resolved through varying the $T_{\rm eff}$, log g, [Fe/H], and $v_{\rm mic}$ within their uncertainties. In addition, we cannot achieve ionisation balance accounting for the uncertainties in the parameters. This star has a predicted $\theta_{\rm LD}$ that is 0.09 mas and thus is impossible to achieve with current interferometers.

HD298986

The adopted $T_{\rm eff}$ of this star is in excellent agreement ($\sim 1.5-1.7\%$) with typical values from other studies (e.g. Axer, Fuhrmann & Gehren, 1994; Nissen et al., 2002; Mashonkina et al., 2003; Masana, Jordi & Ribas, 2006; Casagrande et al., 2010, 2011). The adopted $T_{\rm eff}$ also agrees well with those derived from the $\theta_{\rm LD}$-photometric calibrations. We note that the $T_{\rm eff}$ from the free run output of this star agrees with the adopted $T_{\rm eff}$ within 5%. Additionally, the adopted $T_{\rm eff}$ is consistent with the spectroscopic $T_{\rm eff}$, as indicated by a null trend in the [Fe/H] abundance as a function of EP.

Table 5.6 – Summary of Star-by-Star Consistency Check.

Star	$T_{\rm eff}$	log g	[Fe/H]	$v_{\rm mic}$	$\theta_{\rm LD}$
*BD+264251	×	✓	✓	✓	I
HD102200	✓	✓	✓	✓	I
HD106038	✓	✓	✓	✓	I
*HD126681	×	✓	✓	×	I
HD175305	✓	✓	✓	✓	P
*HD196892	×	✓	✓	✓	I
HD201891	✓	✓	✓	✓	P
*HD218857	×	✓	✓	×	I
*HD241253	×	×	✓	✓	I
HD298986	✓	✓	✓	✓	I

NOTES: In this table the ✓ represents a star that has 'passed' (or × for 'failed') a consistency check for the $T_{\rm eff}$ (column 2), log g (column 3), [Fe/H] (column 4), and $v_{\rm mic}$(column 5) parameters. In addition, we remark whether the $\theta_{\rm LD}$ of the star is possible (P) or impossible (I) to directly measure with current (or near future) interferometers.

The adopted log g of this star is within 0.02 dex (less than 1%) of the typical value from the literature. The uncertainty in the log g is on the order of 0.19 dex. While this uncertainty is on the high end, it is not significantly larger than several current GBS including α Tau, α Cet, and γ Sge. However, these stars are very cool giants. It is also consistent with the spectroscopic value as indicated by the agreement, on the order of 0.03 dex, of mean abundance of ionised (6 lines) and neutral iron (66 lines).

The derived [Fe/H] agrees within 0.06 dex (5%) of the mean from the PASTEL database and can be as much as 0.29 dex (23%) larger than the [Fe/H] determined from the free run (Figure 5.7). The NLTE corrections for Fe are on the order of +0.05 dex. The combined uncertainty in the [Fe/H] is on the order of 0.13 dex. While we do find significant correlation between REW and Fe abundance, this is resolved by increasing the $v_{\rm mic}$ within its uncertainty.

Given the good agreement between the adopted values determined semi-independent of spectroscopy and other studies, as well as consistent with Fe I ionisation and excitation balance, we recommend this star as a GBS candidate. The predicted angular diameter of this star is 0.07 mas and is below the detection limit of current interferometers.

A summary of the consistency checks we have outlined above can be found for each star in Table 5.6.

5.6.2 Recommendations

From the above discussion, we recommend the following metal-poor stars as GBS candidates for calibration and validation purposes: HD102200, HD106038, HD175305, HD201891, and HD298986. A summary of the consistency checks and discussion can be found in Table 5.6. The other five stars do not pass the primary criteria for good GBS candidates. In most cases, these stars are not recommended due to not being able to validate (through Fe excitation balance) the $T_{\rm eff}$ of the star. The stars BD+264251, HD126681, HD196892, HD218857, HD241253 are denoted with an astrix in Table 5.3 and 5.5 to indicate that they are not recommended as GBS candidates.

5.7 Summary and Conclusions

In this chapter, we make an analysis of a sample of well-studied metal-poor stars in order to evaluate which of them can be included as *Gaia* benchmark stars. The GBS are a necessary set of calibrator stars that have already been invaluable in the era of large spectroscopic surveys. These surveys (e.g. Gaia-ESO, GALAH, and others) use them to calibrate their automated stellar parameter pipeline. As the astronomical community continues to lean towards even larger spectroscopic surveys (e.g. 4MOST and WEAVE) the need for improved samples of GBS will increase. Therefore, the aim of this chapter was to add stars to the metal-poor gap defined by $-2.0 <$ [Fe/H] < -1.0 dex. We initially began with 21 stars all within the desired metallicity range, however, only 10 stars remained for spectral analysis of which 5 were ultimately recommended for calibration purposes (details on their selection and all quality control cuts can be found in section 5.2). Six of the ten stars in our sample were initially suggested in Appendix B of Paper I. In this work we, performed an analysis on the stellar parameters that are consistent with the previous set of GBS.

We used up to four $\theta_{\rm LD}$-photometric calibrations to estimate the $\theta_{\rm LD}$ using the broad band photometry available for each star. The bolometric fluxes were computed also using photometric calibrations. This procedure has been also employed for 6 stars (20 %) in the current GBS (Paper I). These together were used to determine the $T_{\rm eff}$ of each star using the adopted Stefan-Boltzmann law. The $\theta_{\rm LD}$-photometric calibrations of the two giant stars in our sample produced results that disagreed at the 10% level (leading to a $T_{\rm eff}$ discrepancy of $\sim$300 K). As such, we also employed the IRFM to estimate the $T_{\rm eff}$. We found very good agreement of the $T_{\rm eff}$ between the IRFM and the four $\theta_{\rm LD}$-photometric calibrations. The log g for the stars was computed by fitting a stellar evolutionary track (from the Y^2 set).

The ESO and NARVAL archival spectra were then employed to derive the [Fe/H] for the stars. We processed (e.g. continuum normalised, convolved to common resolution of $R = 40000$, etc.) these spectra in the same way as described in Paper II. We used a set of 131 Fe I and Fe II lines from Paper III and four separate methods (nodes) to compute the [Fe/H]. There were 2 'equivalent width' nodes (EPINARBO and Bologna) and 2 spectral synthesis codes (BACCHUS and iSpec) that were used in Paper III and IV. We employed seven separate runs per node which consisted of: a main run where the $T_{\rm eff}$, log g, and $v_{\rm mic}$ were fixed to their adopted value determined from the procedures outlined in sections 5.3 and 5.4, and six 'error' runs which varied each of the three parameters by $\pm 1\sigma$ of their uncertainties. The 'error' runs were used to evaluate the impact of the uncertainties in the adopted derived stellar parameters on the [Fe/H] analysis.

The final combined metallicity was computed as the average of that from the four nodes. The metallicity-EP and metallicity-REW plots (shown in Figure 5.6) were used to validate the stellar parameters on the basis of the standard Fe I ionisation/excitation balance method. We also used Figure 5.6 in our discussion of the results and the star-by-star analysis noting the consistence of the adopted and spectroscopic parameters in section 5.6.1. We found that five of the ten stars (HD102200, HD106038, HD175305, HD201891, and HD298986) have stellar parameters which are consistent between the photometric methods and the spectroscopic analysis. In section 3.3, we evaluate the parameters in the context of the literature.

We present, in Table 5.5, the recommended parameters of the metal-poor GBS candidates and correspond to those which do not have an asterisk. The typical uncertainties in $T_{\rm eff}$, log g, and [Fe/H] are $\pm$80 K, $\pm$0.14 dex, and $\pm$0.13 dex, respectively. While these uncertainties

are marginally higher compared to the current set of FGK GBS, this is likely a result of not having a direct measurement of the $\theta_{\rm LD}$. We recommend all stars with large angular diameters (particularly HD175305, HD201891, and HD102200) be included in future interferometric $\theta_{\rm LD}$ studies. In fact, HD175305 and HD201891 can, in principle, be observed with current interferometers (Table 5.6) and a possible extension of this work is to obtain a direct $\theta_{\rm LD}$ measurement for these two stars. Direct measurement on the $\theta_{\rm LD}$ is what will be needed to improve their accuracy so that they can take their place among stars with the highest quality parameters to calibrate the next generation of surveys.

The recommended metal-poor candidates in this chapter are dominated by stars within the metallicity range of $-1.3 <$ [Fe/H] < -1.0 dex. This is a critical metallicity regime because it is the interface of several Galactic components, such as the thick disk, the accreted halo, the inner halo and potentially the metal-poor tail of the thin disk. Furthermore, there is a lack of recommended GBS at these metallicities. With this work, we have decreased the $\sim$1 dex metallicity gap by 30% and provided the astronomical community with these urgently needed calibration stars. Additionally, I have been working with a team of people across Europe to study the origin of the systematics in the stellar parameters and abundances from several nodes. This project is ongoing and will likely culminate in a paper in the next few months.

In addition, In Paper IV it was shown that a line-by-line differential approach, whereby the abundance of the star of interest is compared directly with the abundance of a reference star, to derive the metallicity yields more precise results. This could be done with Fe as well to improve the precision of the metallicity values. This was not done in the present work to remain consistent with Paper III which derived the metallicity in an absolute way. Redoing the metallicity analysis of all of the GBS in a differential framework will undoubtedly improve the precision of the derived metallicities and is planned in the near future. Therefore we stress that this work was a first step. We will soon have a new version of the PASTEL catalogue (Soubiran in prep) and more precise parallaxes from Gaia which will certainly significantly increase the number of of metal-poor candidate benchmark stars.

5.8 Description of Online Tables

For clarity and reproducibility of our analysis we are providing ten online tables. There is one table per star, each of which contains the information, on a line-by-line basis, to reproduce this work. These tables have the same format and structure. Table 5.7 displays the structure of the online tables which can be found in electronic format the CDS.

Table 5.7 – Online Table Format.

Column	Label	Unit
(1)	Element	
(2)	Absorption line wavelength	Å
(3)	Mean EW	mÅ
(4)	Mean Abundance (A)	dex
(5)	NLTE correction[a]	dex
(6)	EW (EPI)	mÅ
(7)	EW (BOL)	mÅ
(8)	EW (ULB)	mÅ
(9)	EW (iSpec)	mÅ
(10)	A(EPI)	dex
(11)	A(BOL)	dex
(12)	A(ULB)	dex
(13)	A(iSpec)	dex

NOTES: This table is only available in electronic form at CDS. For the EW and abundances, the node is noted in the parentheses. For example EW (EPI) denotes the EW measurement of a specific line from the EPINARBO node while A(BOL) is the log(abundance) of a specific line for the Bologna node. ([a]) In the online table, the lines with NLTE corrections of -0.000 are those that do not have corrections available. This is done for identification purposes. In these cases, the median of the NLTE corrections of the other lines is assumed.

6

An Accurate and Self-Consistent Chemical Abundance Catalogue for the APOGEE/Kepler Sample

This chapter reproduces the paper: *'An Accurate and Self-Consistent Chemical Abundance Catalogue for the APOGEE/Kepler Sample'*, **Hawkins, K.**, Masseron, T., Jofré, P., Gilmore, G., 2016b, Elsworth, Y., Hekker, S., A&A, submitted
The author's contribution to the chapter includes: obtaining the spectral data of the sample and clusters from the SDSS-III database, visual inspection and line selection for all 21 elements, all wrapping codes require to interact with the BACCHUS pipeline (written by T. Masseron), measurement of all stellar parameters and chemical abundances for all stars, and the production of the manuscript.

Abstract

THE APOGEE survey has obtained high-resolution infrared spectra of more than 100,000 stars. Deriving chemical abundances patterns of these stars is paramount to piecing together the structure of the Milky Way. While the derived chemical abundances have been shown to be precise for most stars, some calibration problems have been reported, in particular for more metal-poor stars. In this chapter, we aim to (1) re-determine the chemical abundances of the APOGEE+Kepler stellar sample (APOKASC) with an independent procedure, line list and line selection, and high-quality surface gravity information from asteroseismology, and (2) extend the abundance catalogue by including abundances that are not currently reported in the most recent APOGEE release (DR12). We fixed the T_{eff} and log g to those determined using spectrophotometric and asteroseismic techniques, respectively. We made use of the Brussels Automatic Stellar Parameter (BACCHUS) code to derive the metallicity and broadening parameters for the APOKASC sample. In addition, we derived differential abundances with respect to

Arcturus. We have validated the BACCHUS code on APOGEE data using several well-known stars, and stars from open and globular clusters. We also provide the abundances of C, N, O, Mg, Ca, Si, Ti, S, Al, Na, Ni, Mn, Fe, K, P, Cr, Co, Cu, Rb, Yb and V for every star, line, and show the impact of line selection on the final abundances. These include abundances of five new elements and improved abundances for Si, Ti, S, and V. In this chapter, we present an independent analysis of the APOKASC sample and provide abundances of up to 21 elements. This catalogue can be used not only to study chemical abundance patterns of the Galaxy but also to train data driven spectral approaches which can improve the abundance precision in a restricted dataset, but also full APOGEE sample.

6.1 Introduction

The Milky Way is a complex system and is known to host several structural components. Over the last few decades, it has been shown, with small-to-modest samples of local stars, that some of these components may be chemically distinct from one another (e.g. Edvardsson et al., 1993; Fuhrmann, 1998; Venn et al., 2004; Nissen & Schuster, 2010; Sheffield et al., 2012; Ramírez, Meléndez & Chanamé, 2012; Feltzing & Chiba, 2013; Bensby, Feltzing & Oey, 2014). The advent of large multi-object spectroscopic surveys, such as the Apache Point Observatory Galactic Evolution Experiment (henceforth APOGEE, Eisenstein et al., 2011; Majewski et al., 2015), the Gaia-ESO survey (henceforth GES, Gilmore et al., 2012), the Australian GALAH survey (De Silva et al., 2015), and others, have greatly supplemented and advanced these local samples. In particular, these aforementioned surveys are collecting large samples ($\sim 10^5$) of high-resolution (R = $\lambda/\Delta\lambda \sim$ 20,000 – 60,000) spectra which, with the help of automatic stellar parameters and abundance pipelines, have enable homogenous bulk Galactic chemical evolution studies (e.g. Nidever et al., 2014; Recio-Blanco et al., 2014; Mikolaitis et al., 2014; Masseron & Gilmore, 2015; Hawkins et al., 2015a).

The spectra from these surveys have been used to homogeneously derive the basic stellar parameters, effective temperature ($T_{\rm eff}$), surface gravity (log g), metallicity ([Fe/H]), and, in some cases, microturbulent velocity ($v_{\rm mic}$) for up to 100,000 stars. In addition, these surveys have produced up to 34 elemental abundances for a sizable fraction of the sampled stars. These parameters, and the chemical abundances in particular, are integral to study the nature and structure of our Galaxy as they provide useful 'tags' as to the environment the stars were born in (e.g. Freeman & Bland-Hawthorn, 2002; Hawkins et al., 2015a; Hogg et al., 2016).

In the context of chemical abundance patterns in the Milky Way, the SDSS-III/APOGEE project (Majewski et al., 2015) has been transformative because it not only surveys a large volume within the Galaxy, thanks to its targeting of giant stars, but it also has done high-resolution H-band spectroscopy and delivered stellar parameters and chemical abundance of up to 15 elements. This has made it possible to study the interfaces of Galactic components (e.g. Nidever et al., 2014; Hayden et al., 2015; Hawkins et al., 2015a; Masseron & Gilmore, 2015) and their ages (Martig et al., 2016). In particular, several interesting conclusions have been made using the APOGEE data including the confirmation of the existence of a chemically distinct accreted halo (e.g. Nissen & Schuster, 2010; Hawkins et al., 2014), evidence of a metal-poor thin disk (Hawkins et al., 2015a), differing star formation rates in the thin and thick disks across all metallicities (Masseron & Gilmore, 2015), a positively skewed metallicity distribution function in the outer galaxy indicating the importance of radial migration (Hayden

et al., 2015), and chemical tagging of phase-space substructures (Hogg et al., 2016). These conclusions require chemical abundances, and in particular the metallicity, to be at least precise if not accurate. However, in addition to there being known issues with the APOGEE DR12 [Fe/H] calibration worsening at lower metallicities, there are also large systematic zero-point offsets in some elements with respect to literature (Holtzman et al., 2015).

Thus, the primary aim of this work is to solve the metallicity calibration issue seen in APOGEE DR12 down to metallicities around –1.0 dex for a subsample of the data. We present in this chapter an independent analysis using APOGEE spectra of Kepler targets (henceforth, the APOKASC sample) with several improvements in the atomic and molecular input data, elemental line selection, and a line-by-line differential analysis. In addition, the log g for the subsample of interest are determined independent of spectroscopy, via asteroseismology (Hekker et al., 2013), and the $T_{\rm eff}$ is derived using the spectra but corrected using photometry. We used these to determine the remaining stellar parameters ([Fe/H], $v_{\rm mic}$) and chemical abundances of up to 20 elements including elements, such as Co, which are currently not provided by the APOGEE stellar parameter and chemical abundance pipeline (ASPCAP). The improved abundance ratios and determination of broadening parameters are crucial to extract further information about Galactic evolution from the APOGEE survey.

We organize this chapter in the following way: In section 6.2, we describe the APOGEE spectral data for the APOKASC sample and the Brussels Automatic Code for Characterising High accUracy Spectra (BACCHUS) pipeline which is used to derive the metallicity, broadening parameters, and chemical abundances. In that section, we also discuss the validation of the pipeline using a sample of Gaia benchmark stars and open and globular clusters. In section 6.3 we present the stellar parameters and chemical abundance for up to 21 elements for the APOKASC sample. We then discuss these results in the context of the literature and the APOGEE survey in section 6.4. Finally we summarize, conclude, and discuss future extensions to this project in section 6.5.

6.2 Data and Method

In section 6.2.1 we introduce the APOGEE survey and the properties of the spectral data. We then describe, in section 6.2.2, the BACCHUS pipeline which was used to derive the broadening parameters, metallicity, and chemical abundances. The validation of the pipeline using both benchmark stars and globular and open clusters is described in section 6.2.5.

6.2.1 Spectral Data

We have made use of a Kepler subsample of the twelfth data release (DR12) of the SDSS III-APOGEE survey (details of the APOGEE survey can be found in Eisenstein et al., 2011; Majewski et al., 2015). This subsample contains nearly 2000 stars. The APOGEE survey has collected a large number ($\sim 10^5$) of high-resolution (R$\sim$ 22,500) spectra. The spectra use for the APOGEE survey were taken using a fiber-fed infrared spectrograph which covers the H-band between 1.51 and 1.70 μm. The publicly available combined spectra[1] were used in this

[1]Details on the combined spectra and how to obtain the data can be found at `http://www.sdss.org/dr12/irspec/spectral_combination/` and `http://www.sdss.org/dr12/irspec/spectro_data/`, respectively.

survey. The spectra are characterized by a signal-to-noise ratio (SNR) which ranges from 70 to more than 800 pixel^{-1}. The typical SNR is around 200 pixel^{-1}. These spectra are the product of a combination of all of the visits that APOGEE has made to each star. The spectra have been radial velocity (RV) corrected and resampled to common wavelength sampling before being combined. A weighted combination of all of the spectra is then computed and is used in this work. These combined spectra have not been continuum normalized. That is accomplished by using the BACCHUS pipeline (see section 6.2.2 for more details).

The survey team has released stellar parameters ($T_{\rm eff}$, log g and [Fe/H]) and abundances for up to 15 chemical species (Holtzman et al., 2015; García Pérez et al., 2015). We refer the reader to the ASPCAP description paper by García Pérez et al. (2015) and its implementation for DR12 Holtzman et al. (2015) for more information. The stellar parameters have been derived by interpolating within a grid of synthetic spectra (see section 4.1 of Holtzman et al., 2015) using the FERRE code (Allende Prieto et al., 2006). However, the $v_{\rm mic}$ are fixed to a linear relationship with log g. This relationship was derived using a subset of stars within the APOGEE survey. Figure 2 of Holtzman et al. (2015) suggests that there is likely also a metallicity dependence as well. This may be a possible explanation, at least in part, for the metallicity calibration that is required to the ASPCAP values. To test this, we have solved the broadening parameters in this work.

6.2.2 The BACCHUS code

The BACCHUS code consists of three different modules that are designed to derive equivalent widths, stellar parameters, and abundances. Because we wanted to take full advantage of the asteroseismic data, we have fixed log g throughout the analysis process to those determined by Pinsonneault et al. (2014). The $T_{\rm eff}$ is also fixed and is selected to corrected ASPCAP $T_{\rm eff}$ from DR10 to be consistent with the asterosismic log g values. As a reminder, the $T_{\rm eff}$ were corrected by comparing the values determined from the ASPCAP pipeline and the value computed using the 2MASS $(J-K_s)$-$T_{\rm eff}$ relationship from González Hernández & Bonifacio (2009). The log g were taken from the asteroseismic scaling relations using the selected $T_{\rm eff}$ (see section4 and Equation 2 of Pinsonneault et al., 2014, for more details). The approach of fixing $T_{\rm eff}$ and log g to values determined independently of spectroscopy and deriving chemical abundances has been successfully applied to optical spectra with the BACCHUS code on the set of reference stars called Gaia benchmark stars, which are key calibrators of the Gaia-ESO survey (e.g. Jofré et al., 2014, 2015, Hawkins et al., submitted).

The current version of the BACCHUS code relies on the radiative transfer code Turbospectrum (Alvarez & Plez, 1998; Plez, 2012) and the MARCS model atmosphere grid (Gustafsson et al., 2008a). One particular asset of Turbospectrum is its ability to handle radiative transfer in spherical geometry, recommended when dealing with giants. With fixed $T_{\rm eff}$ and log g, the first step consists of determining the metallicity, the $v_{\rm mic}$ parameter, and the convolution parameter. The metallicity provided is the average abundance of selected Fe lines. The $v_{\rm mic}$ is obtained by minimising the trend of Fe abundances against their reduced equivalent width (REW). The convolution parameter stands for the total effect of the instrument resolution, the macroturbulence, and $v\sin i$ on the line broadening. However, given the quality of the data, we could not disentangle each of those effects. Furthermore, we note that the instrument resolution varies as a function of fiber position (Holtzman et al., 2015). Therefore, we derive one single global convolution value per spectrum, based on the average broadening of Fe lines. For this, we assume

a gaussian convolution profile. Once metallicity, microturbulence, and convolution parameters are determined, O, C, and N are derived. Indeed, the line opacities of those elements dominate the APOGEE spectra via the CO, OH, and CN molecules and thus must be taken into account when fitting any part of the spectrum. Once those elements are measured, the whole process is iterated until convergence.

For each element and each line, the abundance determination module then proceeds in the following way: (i) a spectrum synthesis, using the full set of (atomic and molecular) lines, is used to find the local continuum level via a linear fit, (ii) cosmic and telluric rejections are performed, (iii) the local S/N is estimated, (iv) a series of flux points contributing to a given absorption line is automatically selected, and (v) abundances are then derived by comparing the observed spectrum with a set of convolved synthetic spectra characterised by different abundances. Four different abundance determinations are used: (i) line-profile fitting, (ii) core line intensity comparison, (iii) global goodness-of-fit estimate (aka χ^2), and (iv) equivalent width comparison. Each diagnostic yields validation flags. Based on these flags, a decision tree then rejects the line or accepts it, keeping the best-fit abundance. We adopted the χ^2 diagnostic as the abundance because, by experience, it is the most robust. However, we store the information from the other diagnostics, including the standard deviation between all fourth methods (which we refer to as the method-to-method scatter), in order to aid in the line selection (see section 6.2.4).

6.2.3 Linelists

The linelists employed for the synthesis are the following: for atoms, the most recent release of VALD data (Ryabchikova et al., 2015) has been used has a basis. Hyperfine structure has been added for Co (Pickering, 1996), V (Unkel et al., 1989; Palmeri et al., 1995, 1997), and Mn (Blackwell-Whitehead et al., 2005) as well as isotopic shift information for Cu (Elbel & Fischer, 1961; Bergström, Peng & Persson, 1989; Bengtsson et al., 1990). Concerning molecular linelists, we include OH (Brooke et al., 2016), CN (Sneden et al., 2014), CO (Rothman et al., 2010), and their respective carbon isotopologs, as well as MgH (Yadin et al., 2012), NH (Brooke et al., 2016), CH (Masseron et al., 2014), C_2 (P. Quercy, private communication), SiO (Barton, Yurchenko & Tennyson, 2013), and CaH (Yadin et al., 2012). Note that, in contrast to Shetrone et al. (2015), we chose not to apply any empirical correction nor on line position, nor $\log gf$ or collisional broadening parameter on this linelist. As detailed in further sections, we rather make a careful line selection as well as providing abundances based on a line-by-line differential approach.

6.2.4 Line Selection

Although the pipeline has its own procedure to include or reject lines on a star-by-star basis, it is still important to select the lines beforehand because of the uncertainty related to the synthesis approach such as strong NLTE and/or 3D effects as well as line saturation. The initial line selection for iron was done by searching for all Fe lines with theoretical (i.e. synthetic) equivalent widths (EW) larger than 5 mÅ. These lines were then synthesized for the Sun and Arcturus using BACCHUS assuming the solar parameters $T_{\rm eff}$ = 5777 K, log g = 4.44 dex, [Fe/H] = 0.00 dex, and $v_{\rm mic}$ = 0.86 km s^{-1} and Arcturus stellar parameters of $T_{\rm eff}$ = 4286 K, log g = 1.64

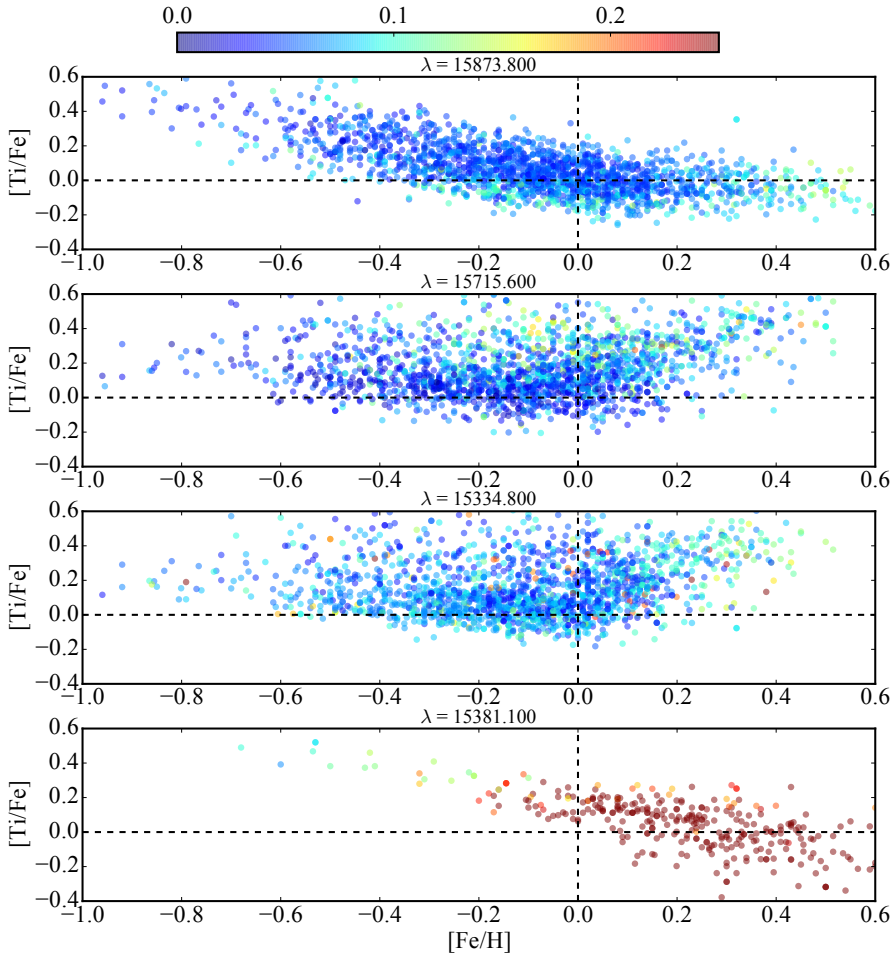

Figure 6.1 – The [Ti/Fe] as a function of metallicity for the full APOKASC sample for the 15873.8 Å, 15715.6 Å, 15334.8 Å, and 15381.1 Å lines from top to bottom, respectively. The stars are color-coded by the BACCHUS method-to-method dispersion, which is defined as the standard deviation of the abundance derived from the four procedures.

dex, [Fe/H] = –0.52 dex, and $v_{\rm mic}$ = 1.6 km s^{-1} . We note that we assume the solar chemical composition of Asplund, Grevesse & Sauval (2005). We then compared these synthesized Fe lines to a high-resolution infrared (R $\sim$ 100,000) Arcturus atlas (Hinkle & Wallace, 2005) and Solar atlas (Hinkle, Wallace & Livingston, 1995). The selected Fe lines were visually inspected to ensure that the spectral fit was adequate.

In addition, lines were rejected if they were found to have Fe abundances outside of $\pm$0.10 dex of the solar value ($\log(\epsilon_{\rm Fe})$ = 7.45). This was done to avoid selecting Fe lines where the fit was not good, or the atomic data was not adequate. In total, there are 20 Fe I lines that were selected for the determination of [Fe/H] and $v_{\rm mic}$, which was derived by forcing the correlation between the REW and [Fe/H] to be zero. Many of these lines were studied in the work of Smith et al. (2013), however, we included additional lines. The abundance of all selected Fe lines for every star in the APOKASC sample can be found in the provided online tables (see section 6.5 for more details).

The line selection for the other elements was done in a similar way as above. Lines for each element with theoretical equivalent widths (EW) larger than 5 mÅ in a synthetic Arcturus

spectrum were initially selected. Additionally, each line was also measured in every star in the APOKASC sample whether it was chosen for the final selection or not. Lines were first visually inspected for a good fit in the Sun and Arcturus. If the line was not well reproduced by the synthesis it was rejected. In addition, for most elements, lines were also rejected if they were flagged as problematic by the BACCHUS pipeline in a substantial fraction of the APOKASC sample. Finally, lines that were very discrepant to other selected lines were discarded.

In Figure 6.1, we present an example of a unique diagnostic diagram that has been used to aid the line selection. In the figure, we plot the [Ti/Fe] as a function of metallicity for 4 Ti lines (15873.8 Å, 15715.6 Å, 15334.8 Å, and 15381.1 Å lines from top to bottom, respectively) of the 31 lines initially selected for every star in the sample. Each circle represents a star and it is color-coded by the method-to-method scatter (described in Sect 6.2.2). Circles that are colored blue have low method-to-method scatter (i.e. all four procedures to measure abundance in BACCHUS agree well) and circles that are colored red have high method-to-method scatter (i.e. the methods disagree indicating the line fit may not be of good quality).

This diagram has been used to make careful line selection choices. For example, we have deselected the Ti line at 15381.1 Å for two reasons: (1) there is only a small subset (about 15%) of the data where this line is not flagged as a poor fit in the BACCHUS decision tree, and (2) in this small subset the method-to-method scatter is very large (as indicated by the red colored circles). Interestingly, the three lines that are left give vastly different [Ti/Fe]-[Fe/H] trends from each other. From the literature (e.g. Bensby, Feltzing & Oey, 2014) we know that [Ti/Fe] increases with decreasing metallicity at sub-solar metallicities and is roughly flat at super-solar metallicities. This is only the case for the Ti line at 15873.8 Å (top panel of Fig 6.1). So why are the other two lines (15715.6 Å and 15334.8 Å) so discrepant? This is likely due to NLTE or saturation effects as both lines are very strong. As such, these lines were rejected. This powerful diagnostic plot was constructed for every element to study the affect that different line selections would have on the chemical abundance patterns observed and was also used to aid the line selection process.

In addition to those diagnosis plots, we also systematically synthesised every element and line in Arcturus at high-resolution to compare with the Hinkle atlas. As an example, we show in Figure 6.2 the example of the two Al lines as used in the DR12 APOGEE release. It is striking that while the line at 16763 Å is well reproduced at high resolution, the 16719 Å line is poorly fit in the core. This is a strong indicator of NLTE effects occurring for that line. Therefore, despite the apparent good quality of the fit in the APOGEE spectrum, we reject the 16719 Å line and use only the 16763 Å line in this study. Beyond Ti and Al, the other element where we had strong indication of 3D and/or NLTE effects is S. Thus, we rejected the line at 15469.8 Å and selected only 15478.5 Å.

For all elements, the final line selection had, on average, between one and a five lines per element. Unlike for Fe, we did not ensure that the derived solar abundance of each element in each line were within 0.10 dex of the solar value. To get around this, we implemented a line-by-line differential analysis, with respect to Arcturus, in order to improve precision (e.g. see Jofré et al., 2015, for an extensive discussion on how differential analyses can improve precision). The abundances per line for every star can be found in the online tables.

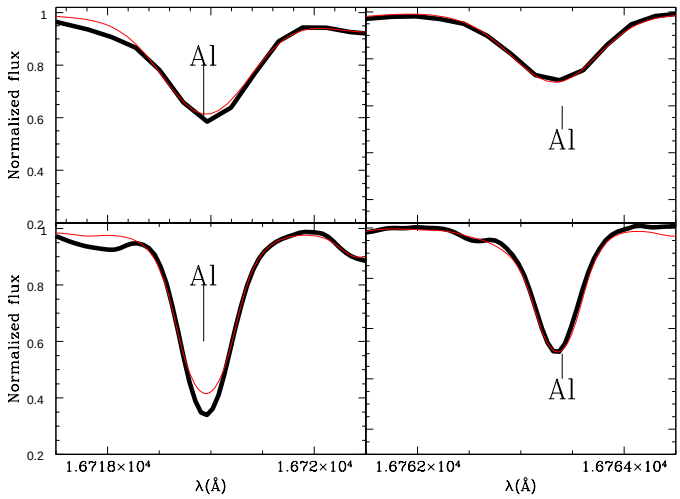

Figure 6.2 – Two Al lines in Arcturus high resolution spectrum (black thick) against synthesis (red thin). The upper panel shows the lines at the APOGEE resolution while bottom panel shows the line at high-resolution.

6.2.5 Validation

With the lines selection in place, we proceed to validate the procedure. We have done two sets of validation tests to quantify the performance of the BACCHUS pipeline, in particular on APOGEE data. The first test was done using the three *Gaia* benchmark stars the Sun, Arcturus, and μ Leo. These are well-studied stars which have T_{eff} and log g measured independently from spectroscopy. For more information on the absolute stellar parameters of the benchmark stars and the procedures used to determine them we refer the reader to the *Gaia* benchmark papers (Heiter et al., 2015; Jofré et al., 2014, 2015, Hawkins et al., submitted). This test is outlined in section 6.2.5

The second test made use of a sample of 119 stars in eight globular and open clusters. We compared the mean metallicity derived from BACCHUS with the literature values to infer its performance. This test is described in section 6.2.5

Benchmark Stars: The Sun, Arcturus, and μ Leo

One way to validate the pipeline is to determine how well it retrieves the stellar parameters of a set of well-known or benchmark stars. For this test we use three benchmark stars defined in a series of papers on the *Gaia* Benchmark star project (Heiter et al., 2015; Jofré et al., 2014, 2015, Hawkins et. al, submitted). The work of Heiter et al. (2015) discusses the T_{eff} and log g determination of the benchmark stars. The literature metallicity of the benchmark stars are sourced from Jofré et al. (2014).

The three benchmark stars that were chosen were the Sun, Arcturus, and μ Leo as these are the only benchmarks which have APOGEE spectra public. The Sun was chosen because it is our nearest star and the one with the highest quality parameters. However the Sun is a dwarf while the stars in the APOKASC sample are giants. Arcturus was chosen because it represents a red-giant star that was suggested by Jofré et al. (2015) for differential analysis. Finally, μ Leo

Table 6.1 – Benchmark Stars Stellar Parameters.

Star	T_{eff}[a] (K)	log g[a] (dex)	[Fe/H] (dex)	v_{mic} (km s^{-1})	$[Fe/H]^{b}_{lit}$ (dex)	$v_{mic}{}^{b}_{lit}$ (km s^{-1})
Sun	5777	4.44	–0.01	0.76	+0.03	1.2
Arcturus	4286	1.64	–0.54	1.21	–0.52	1.3
μ Leo	4474	2.51	+0.27	1.07	+0.25	1.1

NOTES: (^{a}) denotes parameters that have been taken from Heiter et al. (2015). (^{b}) denoted the [Fe/H] and v_{mic} are taken from Jofré et al. (2014).

was chosen because it is a metal-rich red-giant star. The other giant benchmark stars were not observed in DR12. The results from the benchmark validation analysis are summarized in Table 6.1.

We fixed T_{eff} and log g of the Sun to 5777 K and 4.44 dex, respectively and derived v_{mic} and [Fe/H] using the selected Fe lines (for a description of the line selection consult section 6.2.4) in order to test the validity of not only the line selection but also the BACCHUS procedure. Using these parameters we recovered a solar metallically of [Fe/H] = –0.01 dex $\pm$ 0.08 dex and a v_{mic} of 0.76 $\pm$ 0.07 km s^{-1} consistent with the literature (e.g. Jofré et al., 2014).

The T_{eff} and log g of Arcturus were set to 4286 K and 1.64 dex, respectively and the v_{mic} and [Fe/H] were derived. Using these parameters we recovered a metallically for Arcturus of [Fe/H] = –0.54 dex $\pm$ 0.09 dex and a v_{mic} of 1.21 $\pm$ 0.10 km s^{-1} . These values are in good agreement with the literature (e.g. Jofré et al., 2014).

In addition, we choose Arcturus as the reference star for the differential chemical abundance analysis that we implemented in section 6.3.3. This was done to improve the precision in the chemical abundances by effectively correcting systematics induced by the inaccuracies in the line list. The abundances that are derived for Arcturus using BACCHUS, found in Table 6.3, are generally in good agreement with the literature. There are some cases, Mn for example, which have up to a 0.20 dex offset in the abundance determined from BACCHUS and the literature. This is may result from inaccurate optical and/or infrared line lists or hyperfine structure effects.

The benchmark star μ Leo supplements Arcturus because of its relatively high metallicity ([Fe/H] = +0.25 $\pm$ 0.15 dex Jofré et al., 2014). We fixed the T_{eff} to 4474 K and the log g to 2.51 dex (e.g. Heiter et al., 2015). Using these parameters we performed the same procedure used for the APOKASC sample. The pipeline yielded a [Fe/H] = +0.27 dex and a v_{mic} = 1.07 $\pm$ 0.10 km s^{-1} . These values are consistent with the literature on this star (e.g. Jofré et al., 2014).

Figure 6.3 shows the difference of the derived metallicity from the BACCHUS pipeline and the literature metallicity as a function of the literature metallicity for the Sun, which shown as an orange star, Arcturus, which is shown as a red triangle, and μ Leo, which is shown as a magenta diamond. This figure indicates that the pipeline recovers the metallicity of these benchmark stars within 0.04 dex of their literature values.

Open and Globular Clusters

Globular and open clusters offer a great opportunity to quantify the validity of the BACCHUS pipeline which we use to derive the metallicity, chemical abundances, and broadening parameters for the APOKASC sample. For the sake of comparison with the DR12 of APOGEE, we

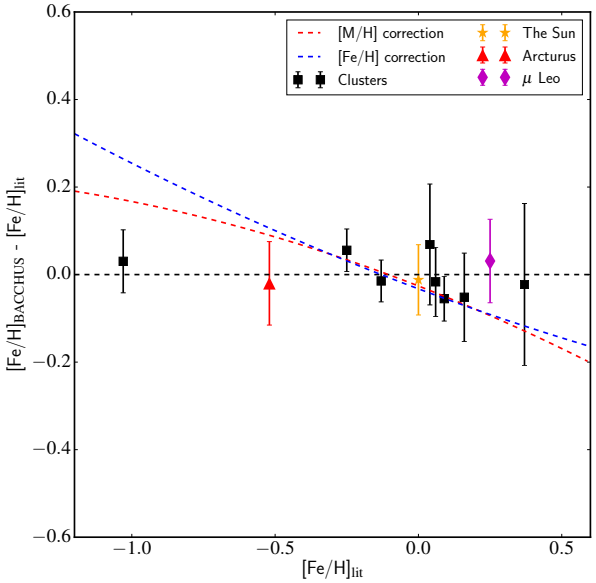

Figure 6.3 – The difference between the [Fe/H] derived of the eight clusters derived in this study with the literature value as a function of the literature [Fe/H]. In addition, the Sun and Arcturus are shown as an orange star and red triangle, respectively. The blue and red dotted lines represent the [M/H] and [Fe/H] corrections, respectively, that are derived in Holtzman et al. (2015) for comparison

have analyzed the spectra of 119 stars in eight globular and open clusters spanning the metallicity range +0.4 < [Fe/H] < –1.05. These clusters and their members were selected from Mészáros et al. (2013). We refer the reader to sections 2 and 3 of Mészáros et al. (2013) for a detailed discussion on cluster members, observations, data reduction, and the analysis of these stars with ASPCAP.

Since we fixed the T_{eff} and log g of the stars in the APOKASC sample, we also do the same for the cluster stars. In this way, we ensure that the pipeline treats these cluster stars in the same way as the APOKASC sample. Most of the cluster stars do not have seismic log g estimates and thus a caveat to this analysis is that we must assume the T_{eff} and log g of APOGEE DR12 which, at least for log g, is derived differently from the APOKASC sample. There are 28 stars in two metal-rich clusters (NGC6791 and NGC6819) which have publicly available seismic log g information in the APOKASC catalog. The mean metallicity of these two clusters are consistent when using both the seismic or corrected ASPCAP[2].

Table 6.2 contains the mean metallicity from the literature of the eight clusters that have been analyzed (e.g. Harris, 1996; Bragaglia et al., 2001; Carraro et al., 2006; Jacobson, Pilachowski & Friel, 2011). It also contains the mean metallicity we derive from BACCHUS for a certain number of stars within each cluster. It is important to keep in mind that while clusters are often cited as a great way to calibrate spectral pipelines, some clusters can have widely varied mean metallicities within the literature. For example, the work of Heiter et al. (2014) explored the status of the mean metallicity of many open clusters through the literature. They found that for at least three of the clusters analyzed in both APOGEE and this work, includ-

[2]We remind the reader that the ASPCAP log g values have been corrected using the APOKASC seismic information (see section 5.2 of Holtzman et al., 2015).

Table 6.2 – Calibration Clusters.

Cluster	$[Fe/H]_{Lit}$ dex	[Fe/H] dex	σ[Fe/H] dex	N	Reference
NGC6791	+0.37	+0.35	0.15	23	(1)
NGC6819	+0.16	+0.11	0.10	28	(2)
NGC7789	+0.09	+0.03	0.05	5	(3)
M67	+0.06	+0.04	0.08	23	(3)
NGC188	+0.04	+0.11	0.14	5	(3)
NGC2420	–0.13	–0.14	0.05	9	(3)
NGC2158	–0.24	–0.19	0.05	10	(3)
M107	–1.03	–1.01	0.07	16	(4)

NOTES: The literature mean metallicity, $[Fe/H]_{Lit}$, are sourced from the following: (1) Carraro et al. (2006), (2) Bragaglia et al. (2001), (3) Jacobson, Pilachowski & Friel (2011), and (4) 2010 version of Harris (1996). The [Fe/H] and σ[Fe/H] are the mean and star-to-star dispersion of each cluster, respectively.

ing NGC188, NGC2158, and NGC2420, the mean metallicity within the literature vary by as much as 0.20 dex between medium- and high-resolution studies. Specifically, NGC2158 has a metallicity of [Fe/H] = –0.03 in Jacobson, Friel & Pilachowski (2009) based on one star, yet a significantly lower metallicity of [Fe/H] = –0.28 dex in Jacobson, Pilachowski & Friel (2011) based on 15 stars. The discrepancy is attributed the choice of reddening E($B - V$) which in turn changes the T_{eff} and [Fe/H] of the stars in their sample. We choose to adopt the value from Jacobson, Pilachowski & Friel (2011) in part because it is based on a larger number of stars.

In addition to the benchmark stars, in Figure 6.3, we display the difference of the mean cluster metallicities found in this work and the literature value. We also plot the correction formulae that are derived for the [M/H] and [Fe/H] parameters based on these same clusters in Holtzman et al. (2015). This figure indicates that we adequately recover the mean literature metallicity of the eight clusters within the typical uncertainty of [Fe/H]. Figure 6.3 indicates that we do not need to apply a metallicity correction formula to force agreement with literature for metal-poor stars. The improvements we have implemented, namely a careful line selection and deriving the broadening parameters, might explain why APOGEE requires such a correction formula. In Sect 6.3.4, we derived the abundances of up to 21 elements for each cluster and use those results to provide additional tests of the abundance precision.

6.2.6 Differential Analysis

Unlike most large surveys, including APOGEE, we have implemented a line-by-line differential analysis with respect to a reference star. This procedure has been shown to be a way to improve abundance precision (and possibly accuracy) by accounting for systematics caused by inaccuracies in the line list and other effects (e.g. Bensby, Feltzing & Oey, 2014; Ramírez et al., 2014; Jofré et al., 2015). Under a differential approach we compare, line-by-line, the abundance of each star with that of the reference star. This leaves the derived abundances for each star relative to the reference star. To convert back to a solar normalised value we must assume an [X/H] value for the reference star. However, we note that the [X/H] value is just a

zero-point scaling factor but does not affect the overall abundance precision.

Arcturus is used as the reference star for differential analysis because the APOKASC sample are red-giant stars with metallicities around –0.10 dex not too dissimilar to Arcturus. In addition, it has measured chemical abundances from various sources in both the optical and infrared regimes. We derived the chemical abundances for a total of 21 chemical species.

Additionally, we have shown in section 6.2.5 that [Fe/H] values for the benchmark stars and clusters derived are well reproduced as a result of selecting lines which have good log gf values. We therefore do not apply a differential analysis on Fe. For the remaining elements, including C, N, O, Mg, Ca, Si, Ti, S, Al, Ni, Na, Mn, K, Cr, Co, Cu, and V, we have implemented a line-by-line differential analysis whereby we compare directly the abundances of each star with the values derived in Arcturus. The abundances are then solar-scaled using the adopted [X/H] abundances of these elements for Arcturus shown in the top part of Table 6.3. We note that we could not apply a differential analysis to P because there are very few phosphorus measurements in literature. Therefore, we have no independent way of checking that the absolute scale in our [P/Fe] diagrams are valid.

6.3 Results

In this section, we present the results of the analysis starting with the metallicity and $v_{\rm mic}$ parameters (section 6.3.1). We then present the results of the chemical abundance analysis for the APOKASC sample and turn to a discussion, on an element-by-element basis, of the quality of the measurements in section 6.3.3. Finally, in section 6.3.4 we describe the procedures that were used to estimate the precision in the chemical abundance ratios.

6.3.1 Metallicity

Figure 6.4 shows the difference in metallicity determined from BACCHUS and the global corrected [M/H] value from APOGEE as a function of APOGEE DR12 corrected [M/H], $T_{\rm eff}$, log g, and SNR from top to bottom, respectively. There is good agreement between the results from BACCHUS and that of the corrected [M/H] from ASPCAP for these stars. The typical difference between our [Fe/H] and the calibrated [M/H] from APOGEE is –0.03 dex with a dispersion of 0.08 dex (which is of the order of the line-to-line abundance dispersion for Fe). There does not seem to be a strong trend in the difference of the corrected [M/H] and the BACCHUS derived [Fe/H] as a function of $T_{\rm eff}$ and SNR. However, there is a weak but significant trend with metallicity and log g such that the BACCHUS metallicities are slightly lower than the corrected [M/H] for the high metallicity (and log g) end. As suggested in Figure 6.3, this could be a result of the calibration applied to the ASPCAP pipeline results.

6.3.2 Microturbulence

Smith et al. (2013) made use of 13 Fe I lines with a range of similar line strengths as this study. However, in this study we increase the number of lines from 13 to 20 in order to better quantify the correlation between abundance and REW to constrain $v_{\rm mic}$. This contrasts the procedures followed by APOGEE DR12.

Holtzman et al. (2015) derived $v_{\rm mic}$ for a subsample of the data and used that as a basis to construct an empirical relationship between log g and $v_{\rm mic}$ that they apply to the full sample

Table 6.3 – Arcturus Chemical Abundances.

Element	[X/H]	σ	N	Jofré[a]	Holtzman[b]	Smith[c]	Ramírez[d]	[X/Fe]	Adopted [X/H]
					Differential				
C	–0.41	0.08	4	...	–0.43	–0.43	–0.09	0.10	–0.41
N	–0.10	0.09	16	...	–0.52	–0.14	...	0.41	–0.14
O	–0.14	0.03	8	...	–0.32	–0.02	–0.02	0.37	–0.02
Mg	–0.09	0.06	6	–0.15	–0.40	–0.38	–0.15	0.42	–0.15
Ca	–0.44	0.05	3	–0.41	–0.51	–0.47	–0.41	0.07	–0.41
Si	–0.17	0.04	5	–0.25	–0.33	–0.39	–0.19	0.34	–0.25
Ti	–0.23	...	1	–0.31	–0.52	–0.31	–0.25	0.28	–0.12
S	–0.43	...	1	...	–0.41	...	...	0.08	–0.35
Al	0.00	...	1	...	–0.32	–0.21	–0.18	0.51	–0.18
Ni	–0.46	0.13	4	–0.49	–0.51	–0.46	–0.46	0.04	–0.49
Na	–0.38	0.10	1	...	–0.61	...	–0.41	0.13	–0.52
Mn	–0.51	0.01	2	–0.89	–0.59	–0.53	–0.73	0.00	–0.53
K	–0.34	...	1	...	–0.54	–0.29	–0.32	0.17	–0.32
Cr	–0.67	...	1	–0.58	–0.58	...	–0.57	–0.53	–0.58
Co	–0.78	...	1	–0.41	...	–0.42	–0.43	–0.27	–0.41
V	–0.45	...	1	–0.44	–0.77	–0.39	–0.32	0.06	–0.32
Cu	–0.89	...	1	...	...	–0.66	...	–0.37	–0.66
					Non-Differential				
Fe	–0.54	0.08	20	–0.52	–0.58	–0.47	–0.52	0.00	...
P	–0.22	...	1	...	...	...	...	0.29	...
Rb	...	...	1	...	...	...	...	...	...
Yb	...	...	1	...	...	...	...	...	...

NOTES: The chemical abundances derived for Arcturus from the BACCHUS pipeline with N lines are shown in Column 2 and 3, respectively. The literature abundances are taken from ([a]) Jofré et al. (2015), ([b]) Holtzman et al. (2015), ([c]) Smith et al. (2013) and ([d]) Ramírez & Allende Prieto (2011) and can be found in columns 4, 5, 6, and 7, respectively. The adopted [X/H] value for Arcturus for the elements used in the differential analysis are given in Column 10.

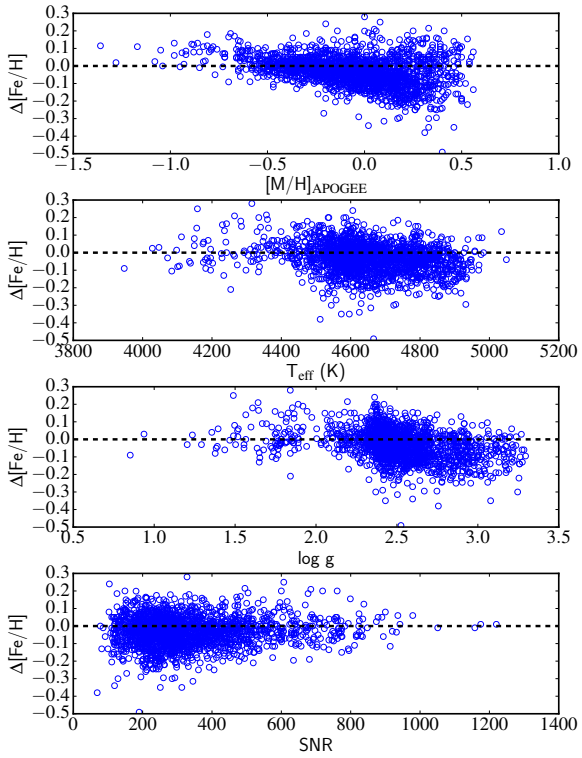

Figure 6.4 – The difference in the [Fe/H] derived from BACCHUS and the corrected [M/H] from APOGEE, Δ[Fe/H] = [Fe/H]$_{\rm BACCHUS}$ − [M/H]$_{\rm APOGEE}$, as a function of the APOGEE DR12 corrected global metallicity (denoted as [M/H]$_{\rm APOGEE}$), T$_{\rm eff}$, log g, and SNR for the APOKASC sample from top to bottom, respectively.

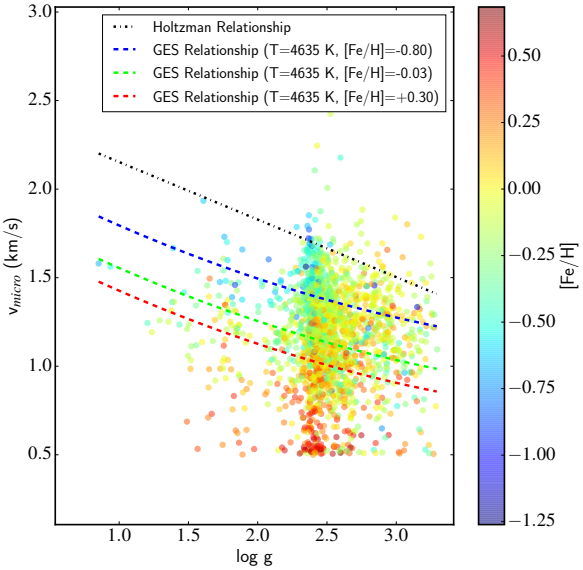

Figure 6.5 – The derived $v_{\rm mic}$ as a function of log g for the APOKASC sample. The color-code represents [Fe/H]. The black dot dashed line represents the $v_{\rm mic}$-log g relationship given in Equation 1 of Holtzman et al. (2015). The blue, lime and red dashed lines represent the $v_{\rm mic}$-log g relationship from the GES at a T$_{\rm eff}$= 4635 K (median T$_{\rm eff}$ of the sample), and [Fe/H]= –0.80, –0.03, +0.30 dex, respectively.

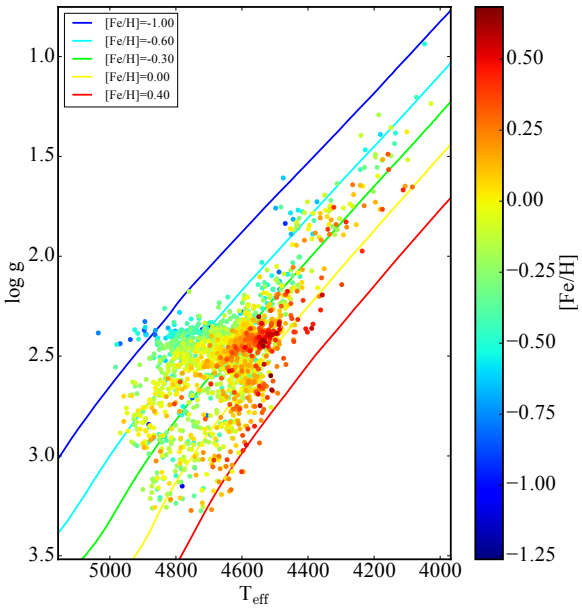

Figure 6.6 – log g as a function of T_{eff} for the APOKASC sample. Overlaid are five 5-Gyr Y^2 isochrones spanning in metallicity from –1.0 < [Fe/H] < +0.4 dex.

(see their section 4.2). However, Figure 2 of Holtzman et al. (2015) suggests that there is more than just a log g dependence for $v_{\rm mic}$. In addition to the line selection (see section 6.2.4), it is possible that one reason APOGEE DR12 overestimates [Fe/H] of stars at low metallicity is due to the discrepancy between the derived and assumed $v_{\rm mic}$ in this regime (Figure 2 of Holtzman et al., 2015). Indeed, this is why GES uses an empirical relation for $v_{\rm mic}$ that relates, in addition to log g, the T_{eff} and metallicity of the star (e.g. Smiljanic et al., 2014). In Figure 6.5, we show the derived $v_{\rm mic}$ of the APOKASC sample as a function of log g color-coded by [Fe/H]. We also show the empirical $v_{\rm mic}$-log g relationships from Holtzman et al. (2015) and the GES (Smiljanic et al., 2014). The $v_{\rm mic}$ determined from BACCHUS is offset with those adopted by APSCAP. It is also interesting to note that the GES relationship indicates that at the median T_{eff} of the sample (T_{eff}= 4635 K), the overall $v_{\rm mic}$ decreases with increasing metallicity which is exactly what is observed with the results from BACCHUS. The lowest metallicity stars have, on average, higher $v_{\rm mic}$. We note here that for a small number of stars ($\sim$4% of the sample) we flag as suspicious because they either have $v_{\rm mic}$ larger than 2.5 km s^{-1} or less than 0.60 km s^{-1} .

Another common way to assess parameters is to recover the expected trends in the HR diagram. Therefore, in Figure 6.6 we plot T_{eff} as a function of log g color-coded by metallicity. We have over laid tracks from the Yonsei-Yale[3] isochrones (Y^2, Yi, Kim & Demarque, 2003; Demarque et al., 2004). Figure 6.6 indicates that the stars follow the expected trend in T_{eff}-log g-[Fe/H] space and thus we conclude that no post-calibrations on the stellar parameters are needed

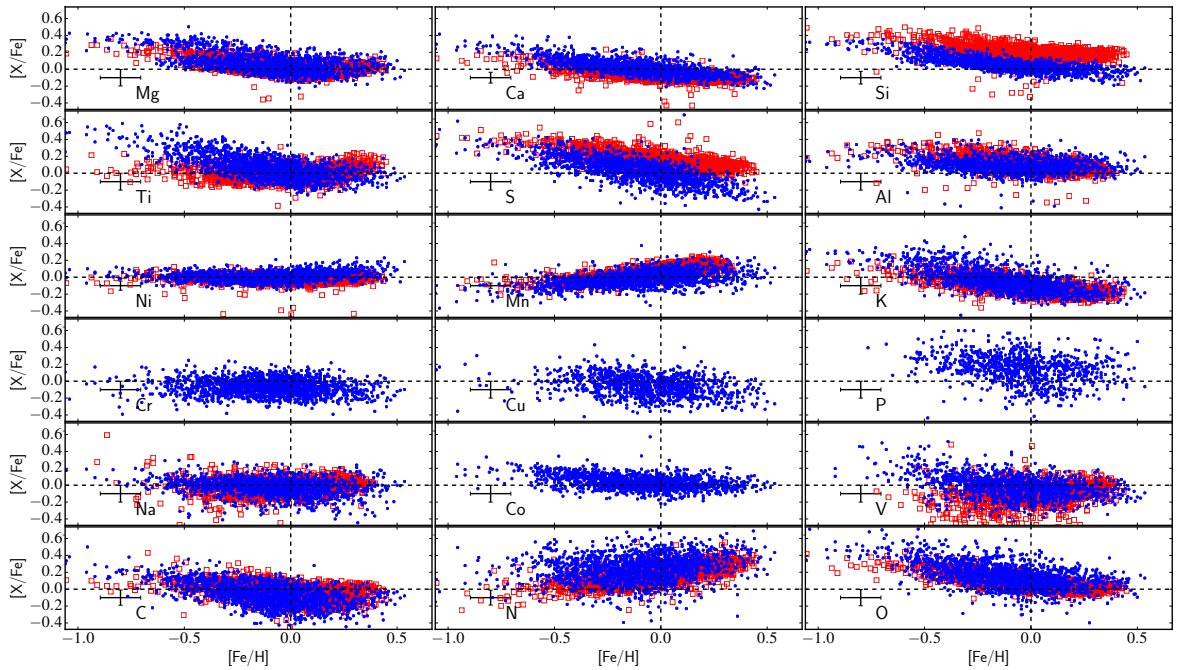

Figure 6.7 – The [X/Fe]-[Fe/H] diagram for each element for the APOKASC sample from the BACCHUS pipeline (blue points). We also plot the [X/Fe] derived from the ASPCAP (red open squares) for 18 elements. The error bars represents the median uncertainty in [Fe/H] and [X/Fe].

6.3.3 APOKASC Chemical Abundances

One of the primary advantages of large spectroscopic surveys, such as APOGEE, is that homogeneously derived chemical abundances can be determined for a large number of stars which enables bulk chemical abundance studies of the Milky Way. Thus one of the goals of this work is to provide updated chemical abundances, with minimal calibrations, for the nearly 2000 stars in the APOKASC catalogue. Now that the stellar parameters have been determined, we derived the abundances of up to 21 additional elements. These elements include Mg, Ca, Si, Ti, S, Al, Ni, Na, Mn, K, Cr, Co, Cu, P, Rb, Yb, and V. However, they do not include Fe, C, N, O which are determined along with the stellar parameters (see section 6.2.2 for more details).

In Figure 6.7, we present the [X/Fe]-[Fe/H] diagram for each element (including CNO) for the APOKASC sample derived from BACCHUS with the ASPCAP values in the background. We further remind the reader that all elements except P and Fe are derived using a line-by-line differential analysis and are solar scaled using the [X/H] values of Arcturus in Table 6.3. The other elements listed are solar scaled by using the solar abundances of Asplund, Grevesse & Sauval (2005). We do not display the results for Rb, Yb, and Cu, because, as it will be shown below, they only represent upper limits at this time.

The top five of panels from Figure 6.7 indicate that we recover the expected trends in the α-elements with respect to [Fe/H], namely that at low metallicity ([Fe/H] $<$ –0.80 dex) there is a plateau at high [Mg, Ti, Si, Ca, S/Fe] and at higher metallicities there is a decrease in those abundance ratios towards increasing metallicity. Furthermore, those panels indicate that

[3]http://www.astro.yale.edu/demarque/yystar.html

we reproduce the precision of the ASPCAP pipeline. However, there are minor differences in the range of certain abundance ratios comparing BACCHUS to ASPCAP. For example, while [Mg/Fe] shows very good agreement between the two pipelines, at lower metallicities the BACCHUS [Mg/Fe] plateaus at a higher value, near +0.40 dex, compared to ASPCAP.

We also found that the [Si/Fe] ratios derived with BACCHUS are on the order of 0.20 dex lower than the ASPCAP values. It is noted in the literature (Holtzman et al., 2015; Masseron & Gilmore, 2015; Hawkins et al., 2015a), that there are possible issues with the accuracy (i.e. zero-point) of ASPCAP abundances (particularly S, Si, and N). Additionally, the [Ti/Fe] panel indicates that the derived [Ti/Fe]-metallicity relationship from this study is similar to optical studies of nearby stars (e.g. Bensby, Feltzing & Oey, 2014). On the other hand, the ASPCAP abundance results show increasing [Ti/Fe] with increasing [Fe/H] inconsistent with the literature. This is, in large part, why Holtzman et al. (2015) flags Ti as unreliable. We have solved this with our line selection. It is clear in Figure 6.1 that the [Ti/Fe]-[Fe/H] pattern seen in APOGEE is found in the deselected lines at 15715.6 Å and 15334.8 Å.

The abundance ratios of [Ni/Fe], [Al/Fe], and [Mn/Fe] are in good agreement with the APOGEE DR12 results. However, there are some differences between DR12 and BACCHUS. In particular, the [Al/Fe] ratios derived in this study are smaller at low metallicity compared to DR12 at the 0.07 dex level. [Mn/Fe] abundance ratios from BACCHUS are lower by as much as $\sim$0.10 dex at high metallicity compared with APOGEE DR12 but the two are in excellent agreement at low metallicities.

Both the [K/Fe] and [Na/Fe] are in fair agreement with APOGEE DR12. At low metallicity, the [K/Fe] derived using the BACCHUS pipeline is larger by $\sim$0.10 dex compared to the values from APOGEE DR12. However, these values tend to agree at metallicities larger than –0.30 dex. The [V/Fe] shows an increasing trend with decreasing metallicity, in contrast to what is found in Holtzman et al. (2015). [V/Fe] is currently not recommended by APOGEE DR12 because it displays a large scatter. However, as we will show in section 6.4, we found that the [V/Fe]-[Fe/H] pattern found in this study is consistent with the literature. The [C/Fe] is in good agreement with the ASPCAP values but [N/Fe] derived in this study are $\sim$0.10 dex higher compared with ASPCAP. Similarly, the [O/Fe] is offset compared to APOGEE DR12 at low metallicity by +0.20 dex but becomes in good agreement at high metallicity.

Co and Cr are new elements not in the DR12 release, and we present in Figure 6.8 and Figure 6.9, the lines that have been used as they appear in Arcturus. Figure 6.8 indicates that they are both strong and only weakly blended. There is good agreements between the model and observed spectra at both high- and moderate-resolution. Figure 6.9 indicates that the Cr line is slightly blended, with CN, at bluer wavelengths. However, the synthesis fit is adequate at both resolution settings because of our good CN line list. We also note that the Cr line is in a region heavily blended by telluric features but these seem to be well subtracted in the ASPCAP reduction pipelines.

We have also attempted to measure an additional four new elements, namely Cu, Rb, Yb, and P, because they have detected lines in the Arcturus spectrum (Figure 6.10, 6.11, 6.12, and 6.13). However, those lines are weak and heavily blended and therefore the derived abundances strongly depends on the ability of properly reproducing the blend. At this time, we cannot guarantee the quality of the abundances for those elements. However, while Rb and Yb are extremely challenging, Cu and P both present two promising and strong lines. In section 6.4, we compare these results with literature.

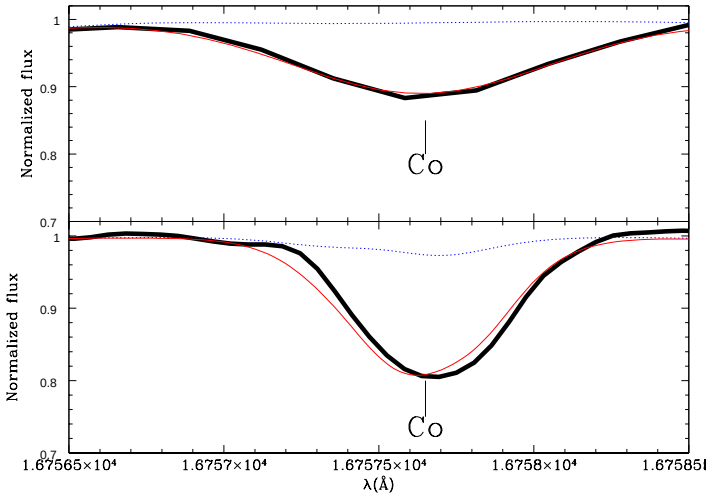

Figure 6.8 – Detection of a Co line in Arcturus. The thick black line is the observation, the thin red line is the synthesis with Co and the dotted blue line is the synthesis without the Co line. The upper panel shows the line at the APOGEE resolution while bottom panel shows the line at high-resolution.

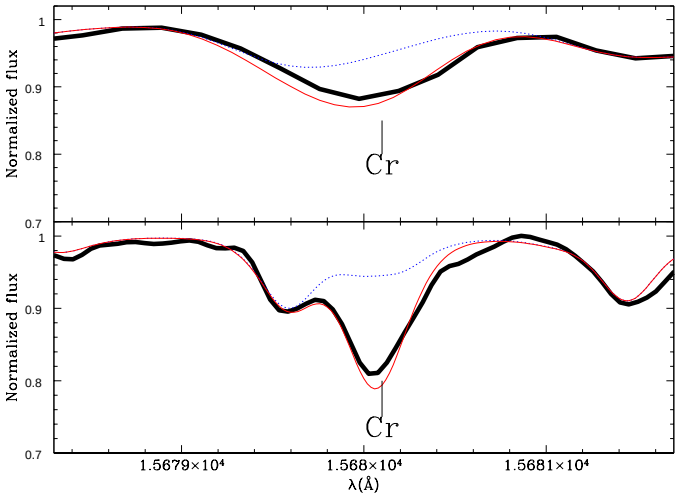

Figure 6.9 – As in Fig 6.8, this time showing for Cr detection.

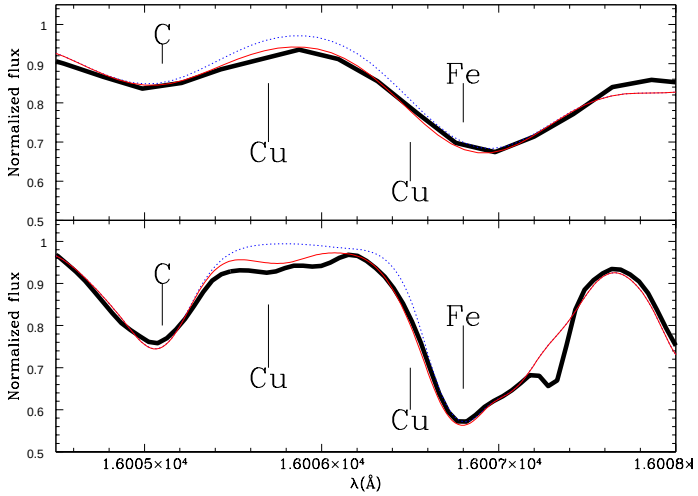

Figure 6.10 – Detection of two Cu lines. Line styles as in Fig 6.8.

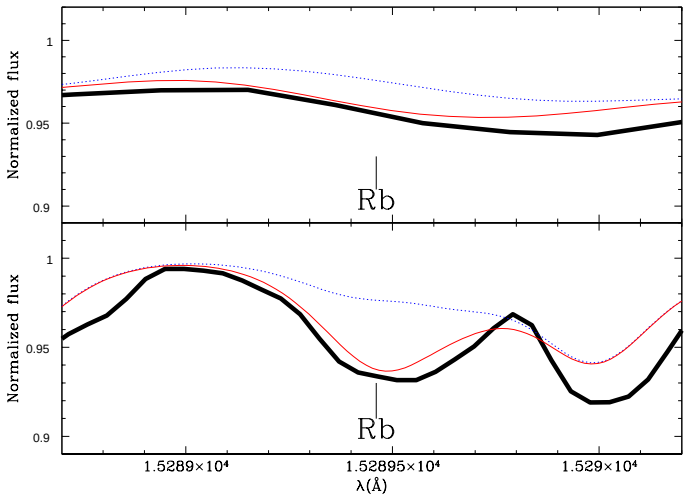

Figure 6.11 – Detection of a Rb line. Line styles as in Fig 6.8.

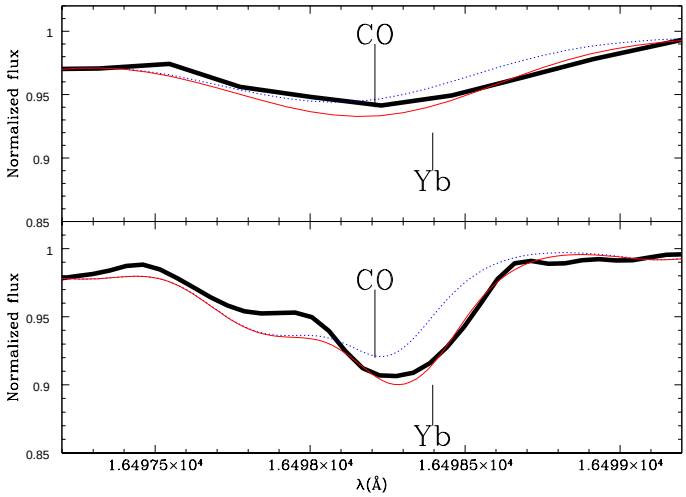

Figure 6.12 – Detection of a Yb line. Line styles as in Fig 6.8.

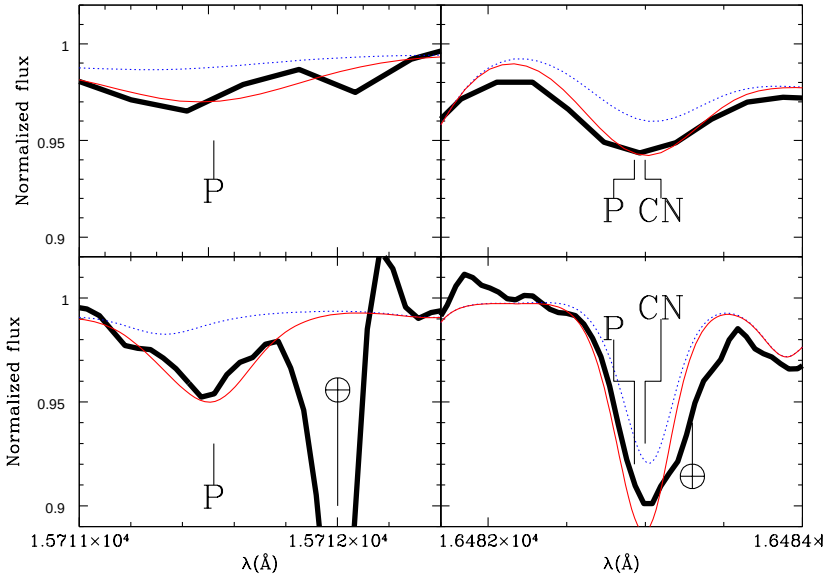

Figure 6.13 – Detection of two P lines. Line styles as in Fig 6.8. In both panels the ⊕ symbol represents a blend from a telluric feature.

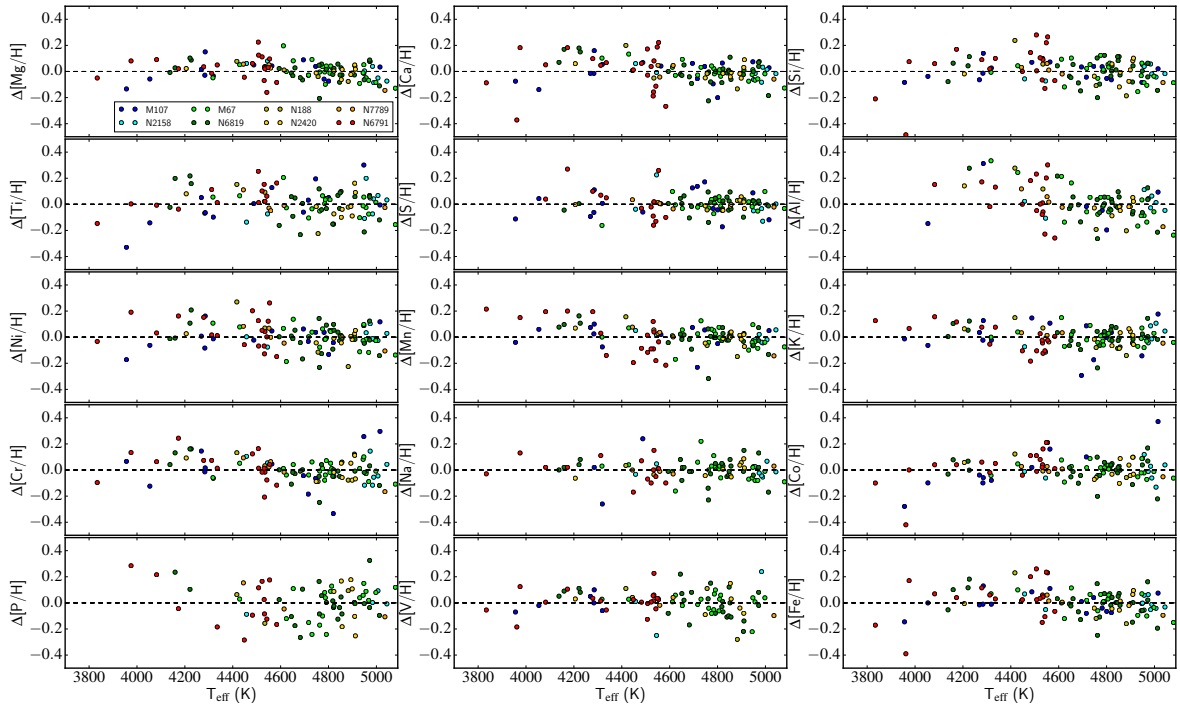

Figure 6.14 – The difference between the [X/H] for each star in a cluster and the cluster mean, Δ[X/H] = [X/H]$_{\rm star} - <$ [X/H]$_{\rm cluster}$ $>$, as a function of $T_{\rm eff}$ for every stars within each validation cluster. The color-coding indicates the cluster that the star belongs to (e.g. all blue points are from the metal-poor cluster M107).

6.3.4 Chemical Abundance Precision

Evaluating the precision of the chemical abundance can be done in several ways. One way is by deriving the star-to-star dispersion of the chemical abundances within a set of validation globular and open clusters. This works because clusters are thought to be chemically homogenous in many elements (e.g. Holtzman et al., 2015; Bovy, 2016). However, it is important to note that with anti-correlations, such as the Na-O or Mg-Al, specific elements (e.g. C, N, O, Mg, Al, Na) have been shown to be variant within clusters (e.g Gratton et al., 2001; Gratton, Carretta & Bragaglia, 2012, and references therein). However, we proceed under the assumption, for this test only, that globular and open cluster are chemically homogenous in all elements except CNO.

If this is the case, the precision with which one can measure chemical abundances can be assessed by deriving the star-to-star dispersion of each element within a cluster. In addition, the elemental abundances should not depend on a star's stellar parameters within the cluster. We have measured the abundances described in Sect 6.3.3, in all globular and open cluster used for validation in the same way as the APOKASC sample. We remind the reader that, unlike the APOKASC stars, these stars do not have astroseismic log g information and thus will likely have larger uncertainties in the log g and hence larger abundance uncertainties. In Figure 6.14 we show the difference of each star's [X/H] abundance ratio subtracted from the cluster's mean [X/H] ratio as a function of $T_{\rm eff}$. If the clusters were chemically homogenous and we could measure the abundances with infinite precision then each point in Figure 6.14 would have Δ[X/H] = 0. Thus the dispersion around zero yields an approximation of the total

Table 6.4 – Typical Abundance Uncertainties in Clusters and Sensitivity.

[X/H]	σ[X/H]$_{\rm clus}$	ΔT$_{\rm eff}$ ($\pm$80 K)	Δlog g ($\pm$0.02)	$\Delta v_{\rm mic}$ ($\pm$0.1 km s^{-1})	$\sigma_{\rm line}$
Mg	0.07	$\pm$0.05	$\pm$0.01	$\mp$0.01	0.04
Ca	0.09	$\pm$0.06	$\pm$0.03	$\mp$0.01	0.03
Si	0.10	$\pm$0.03	$\pm$0.01	$\mp$0.03	0.04
Ti	0.11	$\mp$0.07	$\pm$0.01	$\mp$0.02	...
S	0.07	$\mp$0.04	$\pm$0.01	$\mp$0.01	...
Al	0.15	$\pm$0.10	$\pm$0.02	$\pm$0.01	...
Ni	0.11	$\pm$0.05	$\pm$0.00	$\mp$0.01	0.03
Mn	0.09	$\pm$0.08	$\pm$0.00	$\mp$0.02	...
K	0.08	$\pm$0.10	$\pm$0.01	$\pm$0.01	...
Cr	0.10	$\pm$0.11	$\pm$0.01	$\mp$0.02	...
Na	0.09	$\pm$0.07	$\pm$0.02	$\mp$0.01	...
Co	0.09	$\pm$0.05	$\pm$0.00	$\mp$0.01	...
V	0.10	$\pm$0.10	$\pm$0.00	$\mp$0.01	...
Fe	0.08	$\pm$0.07	$\pm$0.02	$\mp$0.04	0.02
C	...	$\pm$0.03	$\pm$0.03	$\mp$0.03	0.04
N	...	$\pm$0.06	$\pm$0.01	$\mp$0.01	0.02
O	...	$\pm$0.10	$\pm$0.03	$\mp$0.04	0.04

NOTES: The typical star-to-star dispersion in [X/H] within the eight validation clusters is displayed for every element in column 2. Typical sensitivity of the abundance to uncertainties in the stellar parameters are computed by measuring the difference in [X/H] abundance due to changes of $\pm$80 K (column 3), $\pm$0.02 dex (column 4), and 0.10 km s^{-1} (column 5), in T$_{\rm eff}$, log g and $v_{\rm mic}$, respectively. This was done using three stars near the middle of the parameter space (i.e. T$_{\rm eff}$ $\sim$ 4700 K, log g $\sim$ 2.5, [Fe/H] $\sim$ –0.2). The standard error, $\sigma_{\rm line}$, of the mean abundance is displayed in column 6 for elements where there are more than two lines.

internal uncertainty in the abundances. In column 2 of Table 6.4, we show the typical star-to-star dispersion of [X/H] (around the mean value) within the validation clusters. These values are typically around $\sim$0.10 dex and are similar to the uncertainties reported by APOGEE.

We note that as in Holtzman et al. (2015), we could have chosen to internally calibrate the [X/H] abundances by fitting out any correlations between abundance and T$_{\rm eff}$. We have chosen not to do this because (1) we have only 119 stars which are dominated by 4600 $<$ T$_{\rm eff}$ $<$ 4800 K, thus we may not adequately sample the low temperature regime, (2) we do not have a good handle on the intrinsic abundance spreads within clusters particularly with the known anti-correlations, (3) the slope of the regression fit of Δ[X/H] and T$_{\rm eff}$ tends to vary significantly by removing just one cluster indicating that the calibration would not likely be robust.

Another way of evaluating the total internal uncertainty in the chemical abundances is to quantify the sensitivity in the abundance due to the uncertainties in the stellar parameters (T$_{\rm eff}$, log g, and $v_{\rm mic}$) and the mean abundance. We selected three stars for this analysis: (1) 2MASS J19070835+5016440 with T$_{\rm eff}$ = 4882 K, log g = 2.99 dex, [Fe/H] = –0.29 dex, (2) 2MASS J18583782+4822494 with T$_{\rm eff}$ = 4740 K, log g = 2.54 dex, [Fe/H] = –0.08 dex, and (3) 2MASS J19103742+4934534 with T$_{\rm eff}$ = 4689 K, log g = 2.39 dex, [Fe/H] = –0.08 dex. These stars are a good representation of the APOKASC sample and thus it is reasonable to assume that their

performance reflects the typical star analyzed in this study. For each of these stars we changed $T_{\rm eff}$ by $\pm$80 K, log g by $\pm$0.02 dex, which are the their typical uncertainties (Pinsonneault et al., 2014), and $v_{\rm mic}$ conservatively by $\pm$0.10 km s^{-1} . The abundance deviations due to the changes in the stellar parameters can be found in Table 6.4. The total internal uncertainty is then the abundance sensitivity to the stellar parameters added in quadrature with the standard error in the mean [X/H] abundance. We note that the uncertainty measured from the star-to-star dispersion of each element within the validation clusters, and the sensitivity of the stellar parameters are comparable.

6.4 Discussion

In this section, we discuss, element-by-element, how the results compare with a local sample of stars often observed using high-resolution optical spectra. For this, we refer the reader to Figure 6.15 which presents the [X/Fe] values derived in this study as a function of metallicity compared with several literature sources in the background. The literature data is taken from local samples of stars observed with high-resolution optical spectra. For most elements we draw from the work of Bensby, Feltzing & Oey (2014) and Battistini & Bensby (2015). However for [P/Fe] and [S/Fe] we take data from Caffau et al. (2011). Additionally, [K/Fe] and [C/Fe] data are sourced from Shimansky et al. (2003) and Nissen et al. (2014), respectively.

6.4.1 The α-elements: O, Mg, Si, S, Ca, and Ti

The α-elements are critical to understanding the star formation history of the Galaxy. This is because the ratio of α-elements to iron peak elements is linked to environment with which the population of stars of interest were born (e.g. Gilmore & Wyse, 1998; Matteucci & Recchi, 2001). The mean ratio of these elements, [α/Fe], has been show to be zero near solar metallicities. The [α/Fe] ratio tends to increase toward decreasing metallicity until [Fe/H] $\sim$–1.0 dex where it stabilizes around a plateau (e.g. Edvardsson et al., 1993; Reddy et al., 2003; Venn et al., 2004; Fuhrmann, 2004; Bensby, Feltzing & Oey, 2014). Structurally, the thin disk of the Galaxy is thought to be comprised of metal-rich stars with low [α/Fe], while the thick disk is thought to be more metal-poor with higher [α/Fe] compared to the thin disk.

In the top five panels of Figure 6.15, we observe the expected trend of increasing [Mg, Ca, Si, Ti, S, O/Fe] with decreasing metallicity. The abundance ratio of these elements are consistent with the literature. This is not the case for Ti, Si and S for ASPCAP. More specifically, at low metallicities, the plateau of [Mg, Ca, Si/Fe] derived in this work occurs at similar values as the literature. [S/Fe] is known, from the work of Caffau et al. (2011), to decrease to subsolar values at high metallicities ([Fe/H]$>$ 0.00 dex) which is recovered here but not in APOGEE. In addition, we improve the zero-point issue seen in APOGEE (e.g. [Si/Fe]) by the implementing the differential analysis.

Furthermore, we recover the expected [Ti/Fe]-[Fe/H] trend, albeit, with somewhat poorer precision compared to the high-resolution optical study of Bensby, Feltzing & Oey (2014). As mentioned before, this improvement is a result of the careful line selection. The lines which show [Ti/Fe]-[Fe/H] trends similar to APOGEE DR12 are those which are saturated or possibly strongly affected by NLTE (see section 6.2.4 for more details).

Interestingly, the [O/Fe] abundance ratio at super-solar metallicity has a slight discrepancy

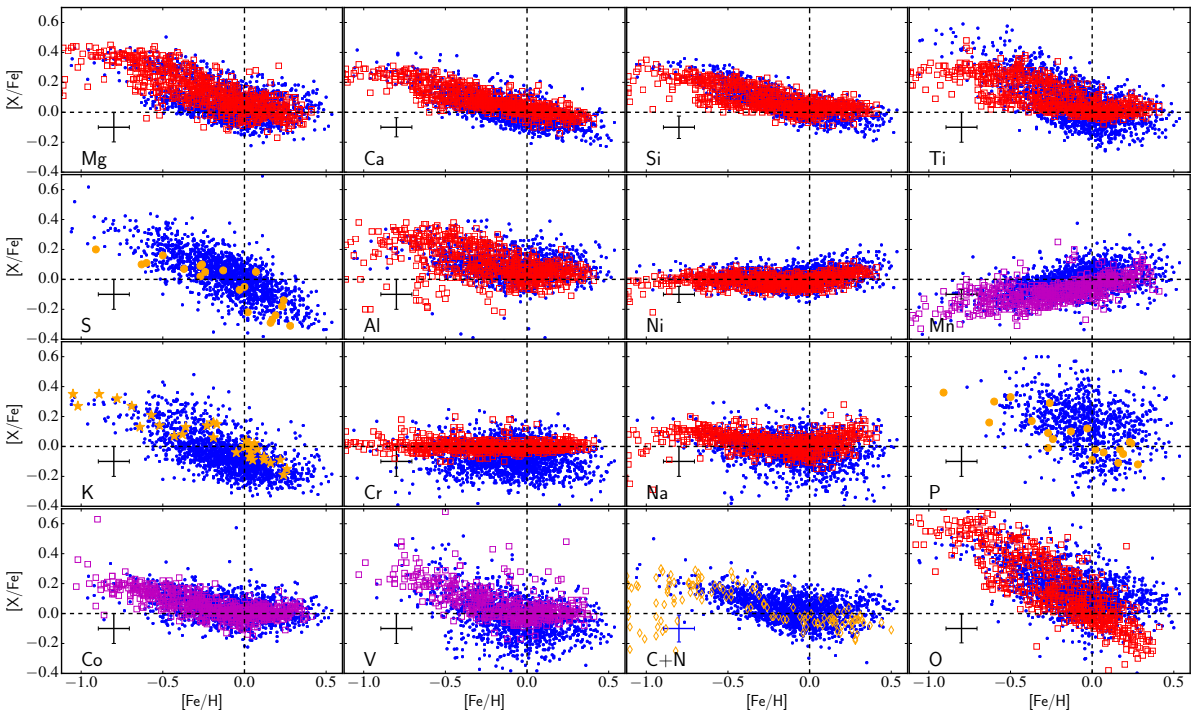

Figure 6.15 – The [X/Fe]-[Fe/H] diagram for each element for the APOKASC sample from the BACCHUS (blue points) and a local sample of dwarf stars observed in the optical from Bensby, Feltzing & Oey (2014) denoted by red open squares and Battistini & Bensby (2015) denoted as open magenta squares. In addition, the [P/Fe] and [S/Fe] are taken from Caffau et al. (2011) and are denoted as orange circle. The literature [K/Fe] are sourced from Shimansky et al. (2003) and are denoted as orange stars. The literature data for the [C+N/Fe] panel is the [C/Fe] data taken from Nissen et al. (2014) and is denoted as orange open diamonds. The error bars represents the median uncertainty in [Fe/H] and [X/Fe].

with Bensby, Feltzing & Oey (2014). The [O/Fe] derived both in this study, and in APOGEE DR12 shows a flat trend at super-solar metallicities. However, the [O/Fe] in Bensby, Feltzing & Oey (2014) shows a decreasing trend with increasing metallicity at [Fe/H] $>$ 0.00 dex. This could be a result of NLTE effects. As noted in Bensby, Feltzing & Lundström (2004), the downward trend in [O/Fe] with increasing metallicity at [Fe/H] $>$ 0.00 dex is seen for the forbidden [O I] line at 6363 Å, which is known not to be strongly affected by NLTE effects. However, if the [O/Fe] is computed from the oxygen triplet at $\sim$ 7774 Å, which is known to be strongly affected by NLTE, the trend at [Fe/H] $>$ 0.00 dex is significantly flatter, consistent with what we observe in Fig 6.15. This issue shows the power of doing Galactic archaeology combining different data set, as this allows us to take the best of each of them.

6.4.2 The Fe-peak elements: Mn, Ni, Co, Cr

The Fe-peak elements (Mn, Ni, Co, Cr) are produced and dispersed, in large quantities, in Type Ia supernovae similar to Fe but in contrast to the α-elements (e.g. Iwamoto et al., 1999). However, many Fe-peak elements are also produced in Type II supernovae (e.g. Kobayashi et al., 2006).Therefore, the evolution of these elements are thought to scale with Fe.

It is expected that [Mn/Fe] has a decreasing trend with decreasing metallicity. This trend is possibly a result of either a delay in the enrichment from Type Ia supernovae (e.g. Kobayashi & Nomoto, 2009) or metallicity dependent Mn yields from Type II supernovae (e.g. Feltzing, Fohlman & Bensby, 2007). The abundance determination of Mn is, however, complex due to hyperfine structure splitting. We have taken this into account in the line list. In addition, the [Mn/H] ratio of Arcturus, our reference star, ranges from –0.89 to –0.4 dex in the literature (e.g. Thevenin, 1998; Ramírez & Allende Prieto, 2011; Luck & Heiter, 2005; Smith et al., 2013; Jofré et al., 2015). Despite these complications, the expected behavior of [Mn/Fe] as a function of metallicity observed in Figure 6.15 matches a sample of local dwarf stars. However, there seems to be a very small offset, which causes our [Mn/Fe] to be too high on the 0.05 dex level compared to Battistini & Bensby (2015). This offset could easily be due to the choice of [Mn/H] adopted for Arcturus.

Ni and Cr track iron very well and thus are thought to vary essentially in lockstep with Fe. This was observed to be the case with the local sample of dwarf stars from Bensby, Feltzing & Oey (2014). The derived [Ni, Cr/Fe] have a near flat correlation with metallicity as seen in other studies. However, we note that the [Cr/Fe] derived in this study is significantly more dispersed compared to the results of Bensby, Feltzing & Oey (2014). In addition, [Ni/Fe] shows a slight upward trend with increasing metallicity at [Fe/H] $>$ 0.00 dex. This is also seen in the results of Bensby, Feltzing & Oey (2014).

Co is thought to be produced in both Type I and Type II supernovae (e.g. Kobayashi et al., 2006). Its correlation with metallicity is not exactly flat, which may be explained through supernovae yields of Co that are both mass and metallicity dependent. Additionally, Co is known to be affected by hyperfine structure effects, which are accounted for through the line list in the work. The [Co/Fe] in this study is in very good agreement with the local sample of dwarf stars from Battistini & Bensby (2015). In addition, this is an element ASPCAP currently does not provide.

6.4.3 The Odd-Z and Light Elements

C and N

Carbon and nitrogen have been shown to be very important elements in red-giants as they can be used to aid in age determination (e.g. Masseron & Gilmore, 2015). Carbon is made through several means but its production is thought to be dominated by He burning on the main sequence, Type II supernovae, and asymptotic giant branch (AGB) stars. In addition, C and N are affected by the dredge-up process, therefore, they do not stay constant over the lifetime of a star, unlike most elements (e.g. Iben, 1965). However, the combined ratio of [C+N/Fe] is thought to remain constant over the lifetime of the star (e.g. Masseron & Gilmore, 2015; Hawkins et al., 2015a). Therefore, in Figure 6.15, we use [C+N/Fe] as a proxy for [C/Fe]. We compared our results of the [C+N/Fe] with the [C/Fe] values from Nissen et al. (2014). There is very good agreement between the literature and the values derived from BACCHUS.

Odd-Z elements: Na, Al, K, V, P, Cu

Na and Al are odd-Z elements, which are produced in a variety of ways. Both are produced in carbon burning but Na is also produced in the NeNa cycle during H-shell burning and Al is also produced in the MgAl cycle (e.g. Nomoto, 1984; Nomoto et al., 1997; Iwamoto et al., 1999; Samland, 1998). Models predict that at [Fe/H] larger than –1.0 dex, [Na/Fe] and [Al/Fe] decrease with increasing metallicity. This has been shown in observations (e.g. Fulbright, 2000; Reddy et al., 2003; Bensby, Feltzing & Oey, 2014). Figure 6.15 indicates that [Na/Fe] decreases with increasing metallicity, albeit with relatively large scatter. This is likely due to somewhat poor fitting of Na lines in the spectral data. [Al/Fe] also shows a decreasing trend with increasing metallicity. Additionally, there is good agreement in the [Al/Fe] abundance ratio derived in this work and in APOGEE.

K is thought to be an odd-Z element formed in explosive oxygen burning during Type II supernovae (e.g. Samland, 1998). Although the yields are still rather uncertain, the models predict that [K/Fe] decreases with increasing metallicity (e.g. Samland, 1998; Nomoto, Kobayashi & Tominaga, 2013). Figure 6.15 indicates that the abundance ratio of [K/Fe] has a decreasing trend with increasing metallicity. This result is consistent with expectations from both models and observational data (e.g Shimansky et al., 2003).

V is an odd-Z element produced in a similar mechanism as K and also through neon burning (e.g. Samland, 1998). However, its yields are still uncertain. Models predict [V/Fe] to decrease with increasing metallicity at [Fe/H] $>$ –1.0 dex with values below zero. In Figure 6.15, we find that [V/Fe] shows the expected trends and is consistent with the literature (e.g. Battistini & Bensby, 2015), however its values are positive instead of negative as expected by the model. This suggest the need of improvement in supernovae yields.

P is an odd-Z element thought to be produced during carbon and/or neon burning which is then released in Type II supernovae (e.g. Woosley & Weaver, 1995; Samland, 1998; Caffau et al., 2013). Until recently, there have been very few studies of P because there are no P lines in the typical wavelength range in observed spectra of FGK-type stars in the optical. While theoretical models predict [P/Fe] to be negative and decreasing toward increasing metallicity above [Fe/H]= –1.0 dex (e.g. Kobayashi et al., 2006), the observations show mostly positive values for [P/Fe]. However, the observations from Caffau et al. (2011) do confirm that there is a decreasing trend of [P/Fe] with increasing metallicity. We found that [P/Fe] globally decreases

with increasing metallicity and is positive, consistent with the data from Caffau et al. (2011). However, we remind the reader that the P line used in this study is in a region heavily affected by telluric features, as seen in Figure 6.13, which may be the reason for the large scatter in [P/Fe].

Cu is an odd-Z element, which is likely produced in a variety of ways. It is thought that the primary source is through Type Ia supernovae but it is also produced in secondary phenomena in massive stars, or weak s-processes (e.g. Mishenina et al., 2002). Theoretically, it is expected that [Cu/Fe] shows a relatively flat trend with metallicity at [Fe/H] $>$ –1.0 dex and decreases with decreasing metallicity at [Fe/H] $<$ –1.0 dex (e.g. Kobayashi et al., 2006). In Figure 6.7 [Cu/Fe] shows a roughly flat trend with metallicity with large scatter. As noted in Figure 6.10, there are two heavily blended Cu lines which are detected. At least one line is blended with Fe and thus we cannot be sure that the flat trend with metallicity is astrophysical or due to the Fe blend. For this reason, and the significant scatter due to likely both telluric features and blending we caution on the accuracy of Cu but conclude that it is promising.

6.5 Summary

In this chapter, we have used an independent pipeline called BACCHUS described in Sect 6.2.2, an updated line list and a careful line selection to explore the chemical abundance patterns of the APOKASC sample. In particular, we have been focused on solving the metallicity calibration issues pointed out, particularly at low metallicity in Holtzman et al. (2015) and adding additional elements to the abundance catalogue. We have selected the APOKASC sample as a first subsample to study because of the very precise log g information that has been determined via astroseismology. As a result, we have fixed the $T_{\rm eff}$ and log g to those from Pinsonneault et al. (2014), which has typical uncertainties on the order of 80 K, and 0.014 dex. We determined the remaining stellar parameters, metallicity and broadening parameters and chemical abundances of up to 21 elements. The results of this analysis can be summarized in the following points:

1. In Sect 6.2.5 we have shown that with BACCHUS and APOGEE spectra, we can accurately recover the metallicity of the three benchmark stars, the Sun, Arcturus, and μ Leo, and 119 stars residing in eight globular and open clusters ranging in metallicity between –1.03 and +0.37 dex. This indicates that we do not need to calibrate the metallicity down to [Fe/H] = –1.0 dex. This is a significant improvement compared to the calibration required by APOGEE, which can be as large as 0.20 dex and can cause issues with [X/Fe] abundance ratios. We believe that this result was achieved through a careful line selection and solving for the broadening parameters (e.g. $v_{\rm mic}$). We recommend that surveys fixing the $v_{\rm mic}$ using a relationship with log g should also include [Fe/H] and $T_{\rm eff}$ effects on that relationship.

2. We have provided a self-consistent and accurate set of abundances for up to 21 elements including C, N, O, Mg, Ca, Si, Ti, S, Al, Na, Ni, Mn, Fe, K, P, Cr, Co, Cu, Rb, Yb and V which, can be used as a training set for other spectral analysis procedures. The [X/Fe] abundance ratios and line-by-line abundances of these elements can be found in the provided online tables. Among these elements, there are two (Co and Cr), which are new compared to APOGEE DR12 and accurate in this study. There are also four additional new elements (Rb, Yb, Cu, and P) provided, which we caution as they are either heavily blended or display large scatter, which may be due to telluric features.

3. We have shown the importance of line selection in chemical abundance analyses. In particular, through a careful line selection (i.e. deselecting saturated lines, or those, which are poorly reproduced in a high-resolution Solar and Arcturus spectrum) we have improved certain abundance ratios, e.g. [Ti/Fe], [V/Fe], which now follow the expected trends with metallicity found in the literature. We have presented a unique and powerful diagnostic diagram in section 6.2.4 which has allowed us to discuss the impact of line selection on the final abundances. Using these diagrams, we have been able to diagnose at least one reason why APOGEE DR12 [Ti/Fe] abundance ratios show inconsistent trends with metallicity compared to the other studies. We have illustrated in Figure 6.1 that the selection of different lines (Ti in that case) by surveys can completely change the chemical patterns seen in the Galaxy. Therefore, we urge that surveys consider publishing line-by-line abundances which may allow the impact of line selection to be fully studied.

With these new, self-consistent, and accurate abundances it is possible to study chemical abundance trends in the outer Galaxy where the Kepler field resides, which is something we plan to discuss in a forthcoming project. We also point out that these new abundances are derived for stars with very precise log g and $T_{\rm eff}$ which improves their overall accuracy. Additionally, the line-by-line differential analysis has helped correct some zero-point offsets (e.g. in Si, S, and N) which make these abundances a superior set to train machine-learning style parameter and abundances solvers such as *The Cannon* (Ness et al., 2015; Casey et al., 2016). Additionally, the abundances from this project have been provided to the astronomical community (see section 6.5) and have already been used in a project that I collaborated on, which showed that some of the high mass (i.e. young) stars with enhanced [α/Fe] may be be a result of mass-transfer binary systems (e.g. Jofre et al., 2016). Ultimately, the lessons learned in this study regarding solving for the broadening parameters, line selection, and line-by-line differential analysis can be incorporated in future APOGEE data releases and APOGEE2 when it comes online.

Appendix: Online Tables

We provide our results in four online tables found in electronic format at the CDS. The first online table, a sample of which can be found in Table 6.5, contains the absolute ($\log_\epsilon(X)$) abundances for every element and star on a line-by-line basis. We remind the reader that some of the $\log_\epsilon(X)$ values may be affected by improper line list data which is the motivation for the differential analysis. In addition, this table also contains the method-to-method scatter (see section 6.2.2 for more details), which can be used to generate the diagnostic line-by-line abundance plot found in Figure 6.1.

Table 6.6 contains a illustration of the recommended stellar parameters and chemical abundances for the APOKASC sample. The $T_{\rm eff}$, log g, and mass are taken from Pinsonneault et al. (2014). The convolution term (which includes information about the $v \sin i$, instrument broadening, and $v_{\rm mac}$, see section 6.2.2 for more details) and its uncertainty are also included in this table. The final abundances for C, N, O, Mg, Ca, Si, Ti, S, Al, Na, Ni, Mn, Fe, K, P, Cr, Co, Cu, and V as described in section 6.3.3 are provided with the formal uncertainties. The uncertainties provided in the table for the abundances are the standard error in the mean for elements which have more than 1 line and the method-to-method scatter in all other cases. To account for the full error budget, one should combine these in quadrature with the uncertainties in the

Table 6.5 – Line-by-line Abundances Online Table Format.

APOGEE ID	Element	λ (Å)	$\log_\epsilon(X)$	$\mathrm{elog}_\epsilon(X)$
J18582020+4824064	Al	16763.4	6.460	0.084
J18582020+4824064	P	15711.5	5.430	0.235
J18582020+4824064	S	15478.5	6.649	0.093
J18582020+4824064	K	15168.4	4.640	0.047
J18582020+4824064	Ca	16150.8	5.988	0.076
J18582020+4824064	Ca	16157.4	6.058	0.210
J18582020+4824064	Ti	15873.8	4.568	0.196
J18582020+4824064	V	15924.8	3.411	0.316
J18582020+4824064	Cr	15680.1	5.159	0.085
J18582020+4824064	Mn	15262.4	5.010	0.070
J18582020+4824064	Mn	15159.2	4.953	0.137
J18582020+4824064	Ni	15632.6	6.070	0.806
J18582020+4824064	Ni	16584.5	6.170	0.045
J18582020+4824064	Ni	16363.1	5.950	0.093
J18582020+4824064	Ni	15555.4	5.880	0.152
J18582020+4824064	Cu	16005.5	3.490	39.377
J18571019+4848067	Fe	15194.5	7.400	0.195
J18571019+4848067	Fe	15207.5	7.370	0.246
J18571019+4848067	Fe	15224.7	7.130	0.090
...	...	...	...	...

NOTES: This table contains the line-by-line abundance information for every stars in the APOKASC sample. This table is online-only. A portion is shown here to indicate form and content.

abundance caused by uncertainties in the stellar parameters (a typical values for these can be found in Table 6.4). Identical tables for cluster stars will also be electronically available.

Table 6.6 – Line Abundances Online Table Format.

APOGEE ID	KIC ID	Mass	T_{eff}(K)	log g	[Fe/H]	e[Fe/H]	convol	econvol	v_{mic}	ev_{mic}	[C/H]	e[C/H]	[N/H]	e[N/H]	[O/H]	e[O/H]	···
J18583782+4822494	10907196	1.500	4740	2.543	-0.26	0.11	13.546	0.049	1.720	0.007	-0.31	0.04	0.03	0.09	-0.16	0.06	···
J18582020+4824064	10962775	1.210	4736	2.444	-0.28	0.17	13.61	0.188	0.790	0.288	-0.31	0.09	-0.33	0.08	-0.49	0.20	···
J18571019+4848067	11177749	1.080	4644	2.427	-0.03	0.11	13.453	0.003	1.273	0.011	-0.28	0.13	0.15	0.08	0.13	0.20	···
J18584464+4857075	11231549	1.550	4541	2.371	-0.05	0.09	13.64	0.004	1.098	0.003	-0.12	0.09	0.12	0.10	0.04	0.13	···
J18582108+4901359	11284798	1.290	4283	1.854	0.22	0.14	13.265	0.505	0.622	0.015	0.12	0.21	0.41	0.12	0.44	0.09	···
J18583500+4906208	11337883	1.530	4802	3.076	-0.17	0.06	13.809	0.009	1.308	0.002	-0.13	0.04	-0.08	0.11	-0.03	0.08	···
J18590205+4853311	11178396	0.860	4824	2.359	-0.69	0.12	16.335	0.001	1.372	0.002	-0.55	0.09	-0.35	0.05	-0.33	0.13	···
J18581445+4901055	11284760	1.140	4658	2.433	-0.06	0.09	14.375	0.395	1.312	0.011	-0.12	0.17	-0.27	0.10	-0.21	0.06	···
J19010271+4837597	11072470	1.100	4558	2.403	0.16	0.16	13.095	0.054	1.251	0.007	0.17	0.16	0.28	0.11	0.28	0.08	···
J19004144+4836005	11072334	1.610	4716	2.794	0.05	0.10	13.283	0.072	1.277	0.015	-0.17	0.09	0.54	0.10	0.27	0.01	···
J19005385+4831394	11017831	1.020	4829	3.257	-0.17	0.10	12.464	0.021	1.300	0.008	-0.31	0.08	0.06	0.10	-0.08	0.09	···
J19005306+4856134	11232325	1.360	4588	2.672	0.14	0.11	13.126	0.141	1.195	0.032	-0.01	0.16	0.32	0.08	0.20	0.02	···
J19013400+4908307	11339000	1.330	4713	2.480	-0.03	0.10	13.588	0.033	1.171	0.036	-0.23	0.15	0.47	0.09	0.32	0.04	···
J19003958+4858122	11232225	1.300	4581	2.410	0.29	0.10	13.796	0.465	1.063	0.007	0.09	0.14	0.42	0.09	0.25	0.19	···
J19005590+4905481	11285650	1.250	4606	2.865	0.12	0.08	13.568	0.412	1.632	0.019	0.11	0.16	0.27	0.10	0.18	0.07	···
J19012632+4914106	11391750	1.260	4744	2.833	-0.19	0.08	13.354	0.017	1.029	0.015	-0.32	0.27	-0.03	0.08	-0.08	0.03	···
J19022554+4832549	11018481	1.240	4399	1.864	-0.02	0.12	13.003	0.003	0.955	0.001	-0.15	0.16	0.18	0.08	0.15	0.04	···
J19015877+4838074	11072852	1.410	4453	1.861	0.02	0.13	13.006	0.009	1.234	0.058	-0.27	0.14	0.45	0.06	0.19	0.22	···
J19032139+4847102	11126673	1.220	4602	2.630	-0.16	0.09	12.625	0.086	1.007	0.006	-0.03	0.08	0.21	0.10	-0.02	0.07	···
J19024750+4850053	11179815	1.250	4715	2.456	-0.15	0.08	13.081	0.181	1.253	0.005	-0.26	0.04	0.02	0.08	-0.02	0.05	···
J19025982+4834262	11018710	1.350	4561	2.618	0.12	0.10	12.592	0.359	1.070	0.01	0.05	0.04	0.40	0.08	0.19	0.19	···
J19032841+4845265	11126721	nan	4486	nan	nan	nan	nan	nan	nan	nan	nan	nan	nan	nan	nan	nan	···
J19041642+4850142	11180468	1.560	4617	2.598	0.30	0.12	12.912	0.132	0.821	0.063	-0.02	0.17	0.55	0.08	0.17	0.13	···
J19042303+4843556	11127105	1.030	4686	3.175	0.04	0.10	12.801	0.01	0.988	0.003	0.03	0.11	0.03	0.09	nan	nan	···
J19040509+4850191	11180378	0.960	4618	2.431	0.06	0.11	12.709	0.078	0.993	0.004	-0.03	0.01	0.18	0.07	0.13	0.02	···
J19053776+4843064	11127586	1.220	4782	2.795	-0.47	0.08	14.022	0.045	1.177	0.016	-0.55	0.13	-0.24	0.08	-0.25	0.11	···
J19042456+4907335	11340165	1.060	4725	2.417	-0.31	0.08	13.31	0.006	1.339	0.003	-0.34	0.02	-0.17	0.10	-0.14	0.05	···
J19052821+4848200	11180994	1.380	4617	2.730	0.01	0.09	13.635	0.016	1.252	0.007	-0.07	0.18	0.19	0.10	0.10	0.00	···
J19045132+4906064	11340377	0.910	4599	2.233	-0.30	0.09	12.991	0.04	1.041	0.073	-0.21	0.06	-0.20	0.12	-0.12	0.14	···
J19062780+4903417	11287844	1.680	4729	2.543	-0.11	0.09	13.564	0.34	0.968	0.009	-0.19	0.09	0.24	0.11	0.03	0.15	···
...	...	...	...	...	...	...	...	...	...	...	...	...	...	...	...	...	...

NOTES: This table contains the stellar parameters and abundance information for every star in the APOKASC sample. The T_{eff}, log g, and Mass are taken from Pinsonneault et al. (2014). The convolution parameter (which combines the $v \sin i$, instrument broadening and v_{mac}) and its uncertainty can be found in Columns 8 and 9, respectively. Only formal uncertainties are listed here. This table is online-only. A portion is shown here to indicate form and content.

7

Conclusions and Future Prospects

7.1 Summary

THIS Thesis has explored the dissection of our galaxy, the Milky Way, using several large spectroscopic surveys. It has focused on combining chemical, age, and kinematic information using these large surveys to further constrain our understanding of the formation and evolution of the Galaxy and its gross structural components. It has also developed spectroscopic techniques, calibration sets, and diagnostic tools which have been designed to improve large-scale spectroscopic surveys both present and future.

In particular, the main achievements of this Thesis are summarized as follows:

- I have developed a robust, semi-empirical spectral-index method, which was used to measure a star's [α/Fe] abundance ratio, with precision competitive to previous grid-matching techniques, from low-resolution SDSS spectra (Chapter 2). One of the advantages of this new method is that it is relatively insensitive to the stellar parameters of a star and is significantly faster than current techniques. Not only can this method be extended to find spectroscopically peculiar stars, but it can also be used to derive the abundance of other chemical species in low-resolution spectra.

- The spectral-index method was applied to a sample of SDSS spectra of halo field stars located near the MSTO and used to separate them into an α-rich and an α-poor group. This enabled us to measure the age-metallicity relation for the α-rich and α-poor halo field stars, separately, for a large sample of stars for the first time. This work indicated that the two are co-eval in the low metallicity regime (i.e., [Fe/H] $<$ –1.40 dex) but become bifurcated at higher metallicities where the α-poor group is systematically younger, by as much as 1 Gyr, compared to the α-rich group. The results of this work supports the idea that the Milky Way halo was formed long ago, that it has had a relatively quiet merger history for the last $\sim$8 Gyr, and that the α-rich population was likely formed in an environment with a high star formation rate compared to the α-poor group (Chapter 2).

- I have characterized local high-velocity stars using the RAVE survey. This work has shown that these stars are overwhelmingly metal-poor and enhanced in [α/Fe], consistent with the halo population. However, there are a non-negligible number of stars, on the order of a few percent, which show a chemical signature consistent with the Galactic disk yet kinematically halo. These stars represent evidence of stars that were ejected from the Galactic disk (Chapter 3).

- I have found evidence for late-type hypervelocity stars, which are in contrast to the known early B-type hypervelocity stars currently discussed in the literature (Chapter 3). The discovery and chemical abundance analysis of late-type hypervelocity stars is critical to understanding the physical processes that produces these stars with such extreme velocities. I recommended a systematic chemical abundance survey of all late-type hypervelocity stars, in the future, as a means to 'chemically' tag their origins.

- The Galactic thick disk and the 'in-situ' Galactic halo have been found to be chemically similar in at least 15 chemical abundances (Chapter 4). This indicates that these two components may have been formed from a common, chemically homogenous and well-mixed gas.

- Using APOGEE, I have confirmed the existence of a chemically distinct α-poor 'accreted' halo component, which was first suggested in Nissen & Schuster (2010). The work presented in this Thesis represents the largest sample of α-poor 'accreted' halo stars found to date surveying a relatively large volume.

- I suggested the use of a chemical-only approach (i.e., using abundance ratios such as [α/Fe], [Al/Fe], [C+N/Fe], and [Mg/Mn]) to dissect the gross components of the Galaxy (Chapter 4). This is in contrast to the kinematic-only approaches currently used and shown to be biased (e.g. Bensby, Feltzing & Oey, 2014).

- Using the APOGEE survey data, I uncovered evidence for a metal-poor thin disk component, which extends down to [Fe/H] < -0.83 dex and is primary located in the outer Galaxy (Chapter 4). The existence of a metal-poor thin disk indicates that it may have formed earlier than previously thought. However, the metallicity and chemical abundance scales within APOGEE are known to have issues. Thus, in the later chapters, I focused on two approaches to help resolve these issues.

- First, I constructed a new set of metal-poor Gaia FGK candidate Benchmark stars, which can be used for calibration purposes (Chapter 5). I undertook a detailed analysis, in collaboration with several nodes around Europe, to derive the stellar parameters ($T_{\rm eff}$, log g, [Fe/H]) of these candidate benchmark stars. The conclusion of that work led to set of five new metal-poor calibrator stars which are now being observed and used by the Gaia-ESO survey for calibration at metallicities around –1.0 dex. These metal-poor benchmark stars may be used to aid in reducing the metallicity calibrations issues seen in APOGEE and other surveys.

- Second, I used an independent stellar parameter and abundance pipeline (BACCHUS), along with infrared spectra from APOGEE stars that also have Kepler astroseismic data, to solve the metallicity calibrations issues that were found to exist within the survey.

The calibration issues were solved by accounting for the broadening parameters (e.g. $v_{\rm mic}$, $v\sin i$, and instrument broadening), fixing log g using astroseismology, an improved atomic line list and line selection among other advances compared to APOGEE.

- Finally, I developed an accurate and self-consistent chemical abundance catalogue for the APOKASC sample of up to 21 elements making use of the high-quality log g information from astroseismic data, a line-by-line differential approach (which helps improve accuracy and precision), and a careful line selection. The chemical abundance ratio of several elements including Ti, Si, S, and V with respect to iron were significantly improved in this catalogue by using a unique diagnostic diagram to explore the impact of line selection. Additionally, the abundance ratio of new elements (Co, Cr, P, Rb, and Yb) not provided in the current APOGEE release were explored. We have provided this catalogue to the astronomical community.

7.2 Future Prospects

7.2.1 Current Projects

With the (near) completion of the APOGEE survey, and GES, there has been a significant increase in the chemical abundance information compared to 2013, when I embarked on my decorate degree. This, along with the pending first data release from the Gaia mission in the summer of 2016, has made the short-term prospects of the field very exciting. With this wealth of data, there are many projects which can use chemistry, kinematics, and a mixture of the two as a means to further dissect the Galaxy.

For example, following the goal of outlined in Chapter 4, I have become interested in the degree to which the bulge/bar is chemically distinct from the Galactic disk. The Galactic bulge/bar sits at the very center of the galaxy (e.g., Figure 1.2). It has a very large range in metallicity, –3.00 $<$ [Fe/H] $<$ +0.60 dex, and [α/Fe], which ranges from 0.00 to +0.40 dex. Recent studies that have used large spectroscopic surveys, which have analyzed bulge stars, have shown that, from a chemical point-of-view, the bulge is not very different from the solar neighborhood (e.g. Meléndez et al., 2008; Bensby et al., 2010; Gonzalez et al., 2015; Ness & Freeman, 2015) when neglecting the outer disk population. However, this has not always been the case. Other authors (e.g. McWilliam & Rich, 1994; Hill et al., 2011; Johnson et al., 2011) have noted that the [α/Fe] of the bulge may be enhanced relative to the Galactic disk at the 0.10 to 0.20 dex level for a constant metallicity. This begs the question as to whether the bulge is chemically distinct or not from the disk population. It was pointed out by Barbuy et al. (2015), that at super solar metallicities, [Zn/Fe] of bulge stars decreases with increasing metallicity and can be as much as 0.40 dex lower than the [Zn/Fe] of the Galactic disk. This result not only indicated that the bulge maybe chemically distinct but also had implications for its formation. However, one of the primary drawbacks of this work is that it compared [Zn/Fe] measured in several studies without considering the systematics offsets between those studies, which may dilute the distinction.

Recently, with the successful completion of the APOGEE and RAVE surveys, which both sample red giant stars, it has been possible to further study the Galactic bulge. In particular, APOGEE has been a game-changer in studying the bulge because of its use of infrared stellar spectroscopy, which is able to penetrate the many magnitudes of dust extinction that blocks

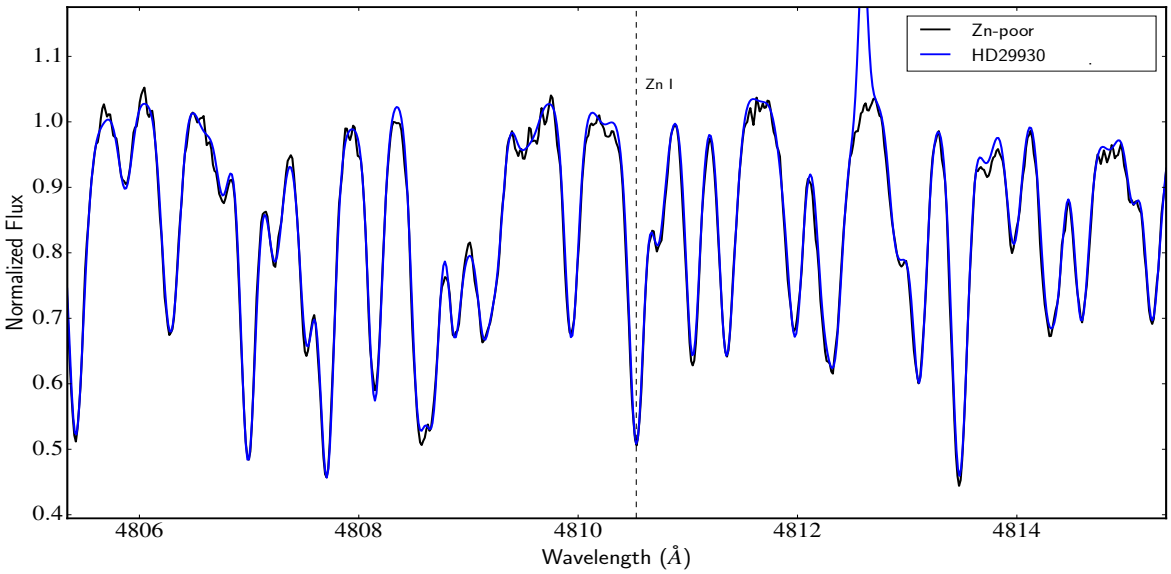

Figure 7.1 – A spectrum of a bulge star (black) taken by GES compared to a local disk star HD22930 (blue) taken from the ESO archive around the Zn I feature at 4810.5 Å (marked by a dashed line). It is clear that there is no systematic difference in the Zn I line of the disk and bulge star indicating the [Zn/Fe] abundance of these two stars are similar.

our view of the bulge. Additionally, GES has also observed bulge giant stars and analyzed them homogeneously compared to the Galactic disk. Therefore, there has been an explosion in studies of the Galactic bulge. This has motivated a project that I am leading, where I have used the high-resolution GES spectra of bulge stars to determine whether the bulge is chemically distinct from the disk using a homogeneously analyzed sample from the local disk and the bulge. Results indicate that there is *no chemical distinction* in [Zn/Fe] between the bulge and the local Galactic disk (Hawkins et al., in prep).

For example, Figure 7.1 shows a spectrum of a bulge red giant star in black and the local disk red giant star HD22930 in blue. HD22930 was chosen because its stellar parameters are, within the uncertainties, consistent with the bulge star (as indicated by the good agreement between the spectral features surrounding Zn in the two stars). If the bulge is under abundant in Zn, the Zn I feature at 4810.5 Å would be systematically weaker in bulge stars compared to disk stars of the same stellar parameters. However, Figure 7.1 illustrates that the Zn I line is equally strong between the two stars indicating that they have similar [Zn/Fe] values. While this is one example, I have found this to be the case in at least forty-two other disk-bulge comparison pairs. This is in tension with the results from Barbuy et al. (2015). However, it is important to point out that Barbuy et al. (2015) compares the [Zn/Fe] in bulge giants analyzed in their study to local disk dwarfs analyzed in other studies in the literature. Systematics in the [Zn/Fe] caused by the analysis procedures, and NLTE/3D effects may account for the discrepancy.

Additionally, I am in charge of the chemical analysis side of a project with G. Kordopatis, R. F. G. Wyse, and G. Ruchti, where we are studying metal-rich local giant stars to test whether they are enhanced relative to the local thin disk in the α-elements indicating they may have been born in the inner disk/Bulge region and radially migrated outward to the solar circle (see discussion in Kordopatis et al., 2015).

7.2.2 Long-Term Prospects

In 5 years time, Gaia will complete its mission and produce a catalogue of positions, proper motions, distances, radial velocities, and some chemical abundance information for nearly a billion stars. Combining this data with current (RAVE, GES, APOGEE, etc.) and future (e.g. 4MOST, WEAVE de Jong et al., 2012; Dalton et al., 2014) large spectroscopic surveys will provide even more chemical dimensions. These surveys have and will continue to use both high-, moderate- and low-resolution settings, each of which are useful for different things. Low-resolution data, like that of SDSS, Gaia BP/RP spectrometer, and the low-res mode of 4MOST, can provide useful RV, crude chemical information, and probe out to much larger volumes for a large number of stars with moderate exposure times, while the high-resolution data, such as the high-resolution mode of 4MOST, APOGEE(2), etc. can provide detailed and precise chemical abundance information for the most interesting but local targets.

The shear amount of data in the field of Galactic astronomy will be unprecedented. All of these future surveys will both test and allow detailed refinement of numerical galaxy formation models, particularly as stellar age data become available to complement the relative age and star formation rate information provided by element ratios, currently. In addition, there will certainly be opportunities within the data to search for rare stars (such as the high-velocity stars discussed in Chapter 3), and use kinematic and chemical information together to decompose the Galaxy (extending the procedures of Chapter 4). If history is any guide, there will undoubtedly be surprises lurking within the Gaia data which will keep astronomers busy for more than a few

decades to come.

The data can be used to address questions surrounding Galactic formation and structure as well as stellar evolution. A long-term project that I propose is to use the skills that I have learned during my Ph.D., including data mining, chemical abundance and spectroscopic analysis among others, to construct, for the first time, 3-dimension maps of the local Milky Way color-coded in chemistry space. Folding in the information on age will allow us to step through these chemical maps of the Galaxy in time opening a new field of Galactic astronomy: chemical cartography. In this new era, we will have the data to not only dissect the Milky Way, but also the knowledge put it back together again.

Bibliography

Abadi M. G., Navarro J. F., Steinmetz M., 2009, ApJLett, 691, L63

Adibekyan V. Z., Sousa S. G., Santos N. C., Delgado Mena E., González Hernández J. I., Israelian G., Mayor M., Khachatryan G., 2012, A&A, 545, A32

Ahn C. P. et al., 2012, ApJS, 203, 21

Allende Prieto C., Beers T. C., Wilhelm R., Newberg H. J., Rockosi C. M., Yanny B., Lee Y. S., 2006, ApJ, 636, 804

Allende Prieto C. et al., 2008, AJ, 136, 2070

Alonso A., Arribas S., Martinez-Roger C., 1994, A&AS, 107, 365

Alonso A., Arribas S., Martinez-Roger C., 1995, A&A, 297, 197

Alonso A., Arribas S., Martinez-Roger C., 1996a, A&AS, 117, 227

Alonso A., Arribas S., Martinez-Roger C., 1996b, A&A, 313, 873

Alvarez R., Plez B., 1998, A&A, 330, 1109

An D. et al., 2013, ApJ, 763, 65

Anguiano B. et al., 2014, in IAU Symposium, Vol. 298, IAU Symposium, Feltzing S., Zhao G., Walton N. A., Whitelock P., eds., pp. 322–325

Asplund M., Grevesse N., Sauval A. J., 2005, in Astronomical Society of the Pacific Conference Series, Vol. 336, Cosmic Abundances as Records of Stellar Evolution and Nucleosynthesis, Barnes III T. G., Bash F. N., eds., p. 25

Axer M., Fuhrmann K., Gehren T., 1994, A&A, 291, 895

Bailer-Jones C. A. L. et al., 2013, A&A, 559, A74

Barbuy B. et al., 2015, A&A, 580, A40

Barklem P. S., O'Mara B. J., 1998, MNRAS, 300, 863

Barton E. J., Yurchenko S. N., Tennyson J., 2013, MNRAS, 434, 1469

Battistini C., Bensby T., 2015, A&A, 577, A9

Beers T. C., Drilling J. S., Rossi S., Chiba M., Rhee J., Führmeister B., Norris J. E., von Hippel T., 2002, AJ, 124, 931

Belokurov V. et al., 2007, ApJ, 658, 337

Belokurov V. et al., 2006, ApJLett, 642, L137

Bengtsson J., Larsson J., Svanberg S., Wahlstrom C.-G., 1990, Phys. Rev. A, 41, 233

Bensby T., Alves-Brito A., Oey M. S., Yong D., Meléndez J., 2011, ApJLett, 735, L46

Bensby T. et al., 2010, A&A, 512, A41

Bensby T., Feltzing S., Lundström I., 2003, A&A, 410, 527

Bensby T., Feltzing S., Lundström I., 2004, A&A, 415, 155

Bensby T., Feltzing S., Lundström I., Ilyin I., 2005, A&A, 433, 185

Bensby T., Feltzing S., Oey M. S., 2014, A&A, 562, A71

Bergemann M., Lind K., Collet R., Magic Z., Asplund M., 2012, MNRAS, 427, 27

Bergström H., Peng W. X., Persson A., 1989, Zeitschrift fur Physik D Atoms Molecules Clus-

ters, 13, 203
Bertelli G., Girardi L., Marigo P., Nasi E., 2008, A&A, 484, 815
Bertelli G., Nasi E., Girardi L., Marigo P., 2009, A&A, 508, 355
Bilir S., Karaali S., Ak S., Önal Ö., Dağtekin N. D., Yontan T., Gilmore G., Seabroke G. M., 2012, MNRAS, 421, 3362
Binney J., 2013, NAR, 57, 29
Binney J. et al., 2014a, MNRAS, 437, 351
Binney J. et al., 2014b, MNRAS, 439, 1231
Binney J., Merrifield M., 1998, Galactic Astronomy. Princeton University Press
Blaauw A., 1961, Boletin de los Observatorios de Tonantzintla y Tacubaya, 15, 265
Blackwell D. E., Lynas-Gray A. E., 1998, A&AS, 129, 505
Blackwell D. E., Petford A. D., Shallis M. J., 1980, A&A, 82, 249
Blackwell D. E., Shallis M. J., 1977, MNRAS, 180, 177
Blackwell D. E., Shallis M. J., Selby M. J., 1979, MNRAS, 188, 847
Blackwell-Whitehead R. J., Pickering J. C., Pearse O., Nave G., 2005, ApJS, 157, 402
Blanco-Cuaresma S., Soubiran C., Heiter U., Jofré P., 2014a, A&A, 569, A111
Blanco-Cuaresma S., Soubiran C., Jofré P., Heiter U., 2014b, A&A, 566, A98, Paper II
Bodaghee A., Santos N. C., Israelian G., Mayor M., 2003, A&A, 404, 715
Boeche C. et al., 2013, A&A, 553, A19
Boeche C., Grebel E. K., 2015, ArXiv e-prints
Boeche C. et al., 2011, AJ, 142, 193
Boesgaard A. M., King J. R., Cody A. M., Stephens A., Deliyannis C. P., 2005, ApJ, 629, 832
Bovy J., 2016, ApJ, 817, 49
Bovy J., Rix H.-W., Hogg D. W., 2012, ApJ, 751, 131
Bovy J., Rix H.-W., Liu C., Hogg D. W., Beers T. C., Lee Y. S., 2012, ApJ, 753, 148
Boyajian T. S., van Belle G., von Braun K., 2014, AJ, 147, 47
Bragaglia A. et al., 2001, AJ, 121, 327
Bromley B. C., Kenyon S. J., Brown W. R., Geller M. J., 2009, ApJ, 706, 925
Brooke J. S. A., Bernath P. F., Western C. M., Sneden C., Afşar M., Li G., Gordon I. E., 2016, J. Quant. Spectrosc. Radiat. Transfer, 168, 142
Brown W. R., Geller M. J., Kenyon S. J., 2009, ApJ, 690, 1639
Brown W. R., Geller M. J., Kenyon S. J., 2012, ApJ, 751, 55
Brown W. R., Geller M. J., Kenyon S. J., 2014, ArXiv e-prints, arXiv:1401.7342
Bullock J. S., Johnston K. V., 2005, ApJ, 635, 931
Burris D. L., Pilachowski C. A., Armandroff T. E., Sneden C., Cowan J. J., Roe H., 2000, ApJ, 544, 302
Caffau E., Bonifacio P., Faraggiana R., Steffen M., 2011, A&A, 532, A98
Caffau E. et al., 2013, Astronomische Nachrichten, 334, 197
Cantat-Gaudin T. et al., 2014, A&A, 562, A10
Carollo D. et al., 2010, ApJ, 712, 692
Carollo D. et al., 2007, Nature, 450, 1020
Carpenter J. M., 2001, AJ, 121, 2851
Carraro G., Villanova S., Demarque P., McSwain M. V., Piotto G., Bedin L. R., 2006, ApJ, 643, 1151
Carretta E., Bragaglia A., Gratton R., Lucatello S., 2009, A&A, 505, 139
Casagrande L., Portinari L., Flynn C., 2006, MNRAS, 373, 13

Casagrande L. et al., 2014, MNRAS, 439, 2060
Casagrande L., Ramírez I., Meléndez J., Bessell M., Asplund M., 2010, A&A, 512, A54
Casagrande L., Schönrich R., Asplund M., Cassisi S., Ramírez I., Meléndez J., Bensby T., Feltzing S., 2011, A&A, 530, A138
Casey A. R., Hogg D. W., Ness M., Rix H.-W., Ho A. Q., Gilmore G., 2016, ArXiv e-prints
Castelli F., Kurucz R. L., 2004, ArXiv Astrophysics e-prints
Chen Y. Q., Nissen P. E., Zhao G., Zhang H. W., Benoni T., 2000, A&AS, 141, 491
Cheng J. Y. et al., 2012, ApJ, 746, 149
Chiba M., Beers T. C., 2000, AJ, 119, 2843
Clementini G., Gratton R. G., Carretta E., Sneden C., 1999, MNRAS, 302, 22
Coşkunoğlu B., Ak S., Bilir S., Karaali S., Önal Ö., Yaz E., Gilmore G., Seabroke G. M., 2012, MNRAS, 419, 2844
Cohen J. G., Meléndez J., 2005, AJ, 129, 303
Cooper A. P. et al., 2010, MNRAS, 406, 744
Creevey O. L. et al., 2015, A&A, 575, A26
Creevey O. L. et al., 2012, A&A, 545, A17
Cutri R. M. et al., 2003, VizieR Online Data Catalog, 2246, 0
Dalton G. et al., 2014, in Proc. SPIE, Vol. 9147, Ground-based and Airborne Instrumentation for Astronomy V, p. 91470L
Datson J., Flynn C., Portinari L., 2012, MNRAS, 426, 484
Datson J., Flynn C., Portinari L., 2014, MNRAS, 439, 1028
Davis M., Efstathiou G., Frenk C. S., White S. D. M., 1985, ApJ, 292, 371
de Jong R. S. et al., 2012, in Society of Photo-Optical Instrumentation Engineers (SPIE) Conference Series, Vol. 8446, Society of Photo-Optical Instrumentation Engineers (SPIE) Conference Series
De Pascale M., Worley C. C., de Laverny P., Recio-Blanco A., Hill V., Bijaoui A., 2014, ArXiv e-prints
De Silva G. M. et al., 2015, ArXiv e-prints
Dekker H., D'Odorico S., Kaufer A., Delabre B., Kotzlowski H., 2000, in Proc. SPIE, Vol. 4008, Optical and IR Telescope Instrumentation and Detectors, Iye M., Moorwood A. F., eds., pp. 534–545
Demarque P., Woo J.-H., Kim Y.-C., Yi S. K., 2004, ApJS, 155, 667
di Benedetto G. P., 1998, A&A, 339, 858
Di Benedetto G. P., 2005, MNRAS, 357, 174
Dotter A., Chaboyer B., Jevremović D., Kostov V., Baron E., Ferguson J. W., 2008, ApJS, 178, 89
Dravins D., LeBohec S., Jensen H., Nuñez P. D., 2012, NAR, 56, 143
Duchêne G., Kraus A., 2013, ARA&A, 51, 269
Edvardsson B., Andersen J., Gustafsson B., Lambert D. L., Nissen P. E., Tomkin J., 1993, A&A, 275, 101
Eggen O. J., Lynden-Bell D., Sandage A. R., 1962, ApJ, 136, 748
Eisenstein D. J. et al., 2011, AJ, 142, 72
Elbel M., Fischer W., 1961, Zeitschrift fur Physik, 165, 151
Feltzing S., Chiba M., 2013, NAR, 57, 80
Feltzing S., Fohlman M., Bensby T., 2007, A&A, 467, 665
Font A. S., Johnston K. V., Bullock J. S., Robertson B. E., 2006, ApJ, 638, 585

Font A. S., McCarthy I. G., Crain R. A., Theuns T., Schaye J., Wiersma R. P. C., Dalla Vecchia C., 2011, MNRAS, 416, 2802
Franchini M., Morossi C., Di Marcantonio P., Malagnini M. L., Chavez M., 2010, ApJ, 719, 240
Franchini M., Morossi C., Di Marcantonio P., Malagnini M. L., Chavez M., 2011, ApJ, 730, 117
Francis C., 2013, MNRAS, 436, 1343
Freeman K., Bland-Hawthorn J., 2002, ARA&A, 40, 487
Fuhrmann K., 1998, A&A, 338, 161
Fuhrmann K., 2004, Astronomische Nachrichten, 325, 3
Fuhrmann K., Axer M., Gehren T., 1994, A&A, 285, 585
Fuhrmann K., Pfeiffer M., Frank C., Reetz J., Gehren T., 1997, A&A, 323, 909
Fulbright J. P., 2000, AJ, 120, 1841
Fulbright J. P., 2002, AJ, 123, 404
García Pérez A. E. et al., 2015, ArXiv e-prints
Gehren T., Liang Y. C., Shi J. R., Zhang H. W., Zhao G., 2004, A&A, 413, 1045
Genovali K. et al., 2014, A&A, 566, A37
Gilmore G. et al., 2012, The Messenger, 147, 25
Gilmore G., Reid N., 1983, MNRAS, 202, 1025
Gilmore G., Wyse R. F. G., 1998, AJ, 116, 748
Gilmore G., Wyse R. F. G., Kuijken K., 1989, ARA&A, 27, 555
Gonzalez O. A. et al., 2015, A&A, 584, A46
González Hernández J. I., Bonifacio P., 2009, A&A, 497, 497
Gratton R. G., 1989, A&A, 208, 171
Gratton R. G. et al., 2001, A&A, 369, 87
Gratton R. G., Carretta E., Bragaglia A., 2012, A&A Rev., 20, 50
Gratton R. G., Carretta E., Castelli F., 1996, A&A, 314, 191
Gratton R. G., Carretta E., Desidera S., Lucatello S., Mazzei P., Barbieri M., 2003, A&A, 406, 131
Gratton R. G., Sneden C., Carretta E., Bragaglia A., 2000, A&A, 354, 169
Gustafsson B., Edvardsson B., Eriksson K., Jørgensen U. G., Nordlund Å., Plez B., 2008a, A&A, 486, 951
Gustafsson B., Edvardsson B., Eriksson K., Jørgensen U. G., Nordlund Å., Plez B., 2008b, A&A, 486, 951
Harris W. E., 1996, AJ, 112, 1487
Hawkins K., Jofré P., Gilmore G., Masseron T., 2014, MNRAS, 445, 2575
Hawkins K., Jofré P., Masseron T., Gilmore G., 2015a, MNRAS, 453, 758
Hawkins K. et al., 2015b, MNRAS, 447, 2046
Hayden M. R. et al., 2015, ApJ, 808, 132
Haywood M., Di Matteo P., Lehnert M. D., Katz D., Gómez A., 2013, A&A, 560, A109
Heber U., Edelmann H., Napiwotzki R., Altmann M., Scholz R.-D., 2008, A&A, 483, L21
Heiter U., Jofré P., Gustafsson B., Korn A. J., Soubiran C., Thévenin F., 2015, A&A, 582, A49, Paper I
Heiter U., Soubiran C., Netopil M., Paunzen E., 2014, A&A, 561, A93
Hekker S., Elsworth Y., Mosser B., Kallinger T., Basu S., Chaplin W. J., Stello D., 2013, A&A, 556, A59

Helmi A., 2008, A&A Rev., 15, 145
Hill V. et al., 2011, A&A, 534, A80
Hill V. et al., 2002, A&A, 387, 560
Hills J. G., 1988, Nature, 331, 687
Hinkle K., Wallace L., 2005, in Astronomical Society of the Pacific Conference Series, Vol. 336, Cosmic Abundances as Records of Stellar Evolution and Nucleosynthesis, Barnes III T. G., Bash F. N., eds., p. 321
Hinkle K. H., Wallace L., Livingston W., 1995, in Astronomical Society of the Pacific Conference Series, Vol. 81, Laboratory and Astronomical High Resolution Spectra, Sauval A. J., Blomme R., Grevesse N., eds., p. 66
Hogg D. W., Casey A. R., Ness M., Rix H.-W., Foreman-Mackey D., 2016, ArXiv e-prints
Holtzman J. A. et al., 2015, ArXiv e-prints
Humason M. L., Zwicky F., 1947, ApJ, 105, 85
Ibata R. A., Gilmore G., Irwin M. J., 1994, Nature, 370, 194
Iben, Jr. I., 1965, ApJ, 142, 1447
Ishigaki M. N., Aoki W., Chiba M., 2013, ApJ, 771, 67
Ishigaki M. N., Chiba M., Aoki W., 2012, ApJ, 753, 64
Isobe S., 1974, A&A, 36, 333
Israelian G., García López R. J., Rebolo R., 1998, ApJ, 507, 805
Ivezić Ž., Beers T. C., Jurić M., 2012, ARA&A, 50, 251
Ivezić Ž. et al., 2008, ApJ, 684, 287
Iwamoto K., Brachwitz F., Nomoto K., Kishimoto N., Umeda H., Hix W. R., Thielemann F.-K., 1999, ApJS, 125, 439
Jackson-Jones R. et al., 2014, A&A, 571, L5
Jacobson H. R., Friel E. D., Pilachowski C. A., 2009, AJ, 137, 4753
Jacobson H. R., Pilachowski C. A., Friel E. D., 2011, AJ, 142, 59
Jehin E., Magain P., Neuforge C., Noels A., Parmentier G., Thoul A. A., 1999, A&A, 341, 241
Jofré P. et al., 2015, A&A, 582, A81, Paper IV
Jofré P. et al., 2014, A&A, 564, A133, Paper III
Jofre P., Masseron T., Izzard R. G., Van Eck S., Hawkins K., Jorissen A., Gilmore G., Paladini C., 2016, ArXiv e-prints
Jofré P., Weiss A., 2011, A&A, 533, A59
Johnson C. I., Rich R. M., Fulbright J. P., Valenti E., McWilliam A., 2011, ApJ, 732, 108
Johnson D. R. H., Soderblom D. R., 1987, AJ, 93, 864
Johnston K. V., Sheffield A. A., Majewski S. R., Sharma S., Rocha-Pinto H. J., 2012, ApJ, 760, 95
Johnston K. V., Spergel D. N., Hernquist L., 1995, ApJ, 451, 598
Jonsell K., Edvardsson B., Gustafsson B., Magain P., Nissen P. E., Asplund M., 2005, A&A, 440, 321
Jönsson H., Ryde N., Nissen P. E., Collet R., Eriksson K., Asplund M., Gustafsson B., 2011, A&A, 530, A144
Jurić M. et al., 2008, ApJ, 673, 864
Kervella P., Thévenin F., Di Folco E., Ségransan D., 2004, A&A, 426, 297
Kim Y.-C., Demarque P., Yi S. K., Alexander D. R., 2002, ApJS, 143, 499
Klypin A., Kravtsov A. V., Valenzuela O., Prada F., 1999, ApJ, 522, 82
Kobayashi C., Nakasato N., 2011, ApJ, 729, 16

Kobayashi C., Nomoto K., 2009, ApJ, 707, 1466
Kobayashi C., Umeda H., Nomoto K., Tominaga N., Ohkubo T., 2006, ApJ, 653, 1145
Kollmeier J. A. et al., 2010, ApJ, 723, 812
Koposov S. E., Belokurov V., Torrealba G., Evans N. W., 2015, ApJ, 805, 130
Kordopatis G. et al., 2015, MNRAS, 447, 3526
Kordopatis G. et al., 2013a, AJ, 146, 134
Kordopatis G. et al., 2013b, MNRAS, 436, 3231
Kordopatis G. et al., 2013c, A&A, 555, A12
Kordopatis, G. R. C., 2014, ArXiv e-prints, arXiv:1410.4254
Kunder A. et al., 2015, ArXiv e-prints
Kupka F., Ryabchikova T. A., 1999, Publications de l'Observatoire Astronomique de Beograd, 65, 223
Larson R. B., 1976, MNRAS, 176, 31
Leaman R., VandenBerg D. A., Mendel J. T., 2013, MNRAS, 436, 122
Lee Y. S. et al., 2011, AJ, 141, 90
Lee Y. S. et al., 2008a, AJ, 136, 2022
Lee Y. S. et al., 2008b, AJ, 136, 2050
Lemasle B. et al., 2014, ArXiv e-prints
Letarte B. et al., 2010, A&A, 523, A17
Li Y., Luo A., Zhao G., Lu Y., Ren J., Zuo F., 2012, ApJLett, 744, L24
Lind K., Bergemann M., Asplund M., 2012, MNRAS, 427, 50
Löckmann U., Baumgardt H., 2008, MNRAS, 384, 323
Löckmann U., Baumgardt H., Kroupa P., 2008, ApJLett, 683, L151
Lu Y., Yu Q., Lin D. N. C., 2007, ApJLett, 666, L89
Luck R. E., Heiter U., 2005, AJ, 129, 1063
Magrini L. et al., 2013, A&A, 558, A38
Majewski S. R., 1993, ARA&A, 31, 575
Majewski S. R., Nidever D. L., Smith V. V., Damke G. J., Kunkel W. E., Patterson R. J., Bizyaev D., García Pérez A. E., 2012, ApJLett, 747, L37
Majewski S. R. et al., 2015, ArXiv e-prints
Marín-Franch A. et al., 2009, ApJ, 694, 1498
Martell S. L., Grebel E. K., 2010, A&A, 519, A14
Martig M. et al., 2016, MNRAS, 456, 3655
Masana E., Jordi C., Ribas I., 2006, A&A, 450, 735
Mashonkina L., Gehren T., 2000, A&A, 364, 249
Mashonkina L., Gehren T., Travaglio C., Borkova T., 2003, A&A, 397, 275
Masseron T., 2006, PhD thesis, Observatoire de Paris, France
Masseron T., Gilmore G., 2015, ArXiv e-prints
Masseron T. et al., 2014, A&A, 571, A47
Matijevič G. et al., 2012, ApJS, 200, 14
Matrozis E., Ryde N., Dupree A. K., 2013, A&A, 559, A115
Matteucci F., Recchi S., 2001, ApJ, 558, 351
McWilliam A., 1997, ARA&A, 35, 503
McWilliam A., Rich R. M., 1994, ApJS, 91, 749
Meléndez J. et al., 2008, A&A, 484, L21
Meléndez J., Casagrande L., Ramírez I., Asplund M., Schuster W. J., 2010, A&A, 515, L3

Mermilliod J.-C., Mermilliod M., Hauck B., 1997, A&AS, 124, 349
Mészáros S. et al., 2013, AJ, 146, 133
Mikolaitis Š. et al., 2014, A&A, 572, A33
Minchev I., Chiappini C., Martig M., 2014, A&A, 572, A92
Minchev I., Famaey B., Quillen A. C., Dehnen W., Martig M., Siebert A., 2012, A&A, 548, A127
Mishenina T. V., Korotin S. A., Klochkova V. G., Panchuk V. E., 2000, A&A, 353, 978
Mishenina T. V., Kovtyukh V. V., 2001, A&A, 370, 951
Mishenina T. V., Kovtyukh V. V., Soubiran C., Travaglio C., Busso M., 2002, A&A, 396, 189
Mishenina T. V., Soubiran C., Kovtyukh V. V., Korotin S. A., 2004, A&A, 418, 551
Moultaka J., Ilovaisky S. A., Prugniel P., Soubiran C., 2004, PASP, 116, 693
Mucciarelli A., Pancino E., Lovisi L., Ferraro F. R., Lapenna E., 2013, ApJ, 766, 78
Ness M., Freeman K., 2015, ArXiv e-prints
Ness M., Hogg D. W., Rix H.-W., Ho A. Y. Q., Zasowski G., 2015, ApJ, 808, 16
Nidever D. L. et al., 2014, ApJ, 796, 38
Nidever D. L., Majewski S. R., Muñoz R. R., Beaton R. L., Patterson R. J., Kunkel W. E., 2011, ApJLett, 733, L10
Nissen P. E., Akerman C., Asplund M., Fabbian D., Kerber F., Kaufl H. U., Pettini M., 2007, A&A, 469, 319
Nissen P. E., Chen Y. Q., Carigi L., Schuster W. J., Zhao G., 2014, A&A, 568, A25
Nissen P. E., Chen Y. Q., Schuster W. J., Zhao G., 2000, A&A, 353, 722
Nissen P. E., Primas F., Asplund M., Lambert D. L., 2002, A&A, 390, 235
Nissen P. E., Schuster W. J., 1997, A&A, 326, 751
Nissen P. E., Schuster W. J., 2010, A&A, 511, L10
Nissen P. E., Schuster W. J., 2011, A&A, 530, A15
Nissen P. E., Schuster W. J., 2012, A&A, 543, A28
Nomoto K., 1984, ApJ, 277, 791
Nomoto K., Iwamoto K., Nakasato N., Thielemann F.-K., Brachwitz F., Tsujimoto T., Kubo Y., Kishimoto N., 1997, Nuclear Physics A, 621, 467
Nomoto K., Kobayashi C., Tominaga N., 2013, ARA&A, 51, 457
Norris J., 1986, ApJS, 61, 667
Palladino L. E., Schlesinger K. J., Holley-Bockelmann K., Allende Prieto C., Beers T. C., Lee Y. S., Schneider D. P., 2014, ApJ, 780, 7
Palmeri P., Biemont E., Aboussaid A., Godefroid M., 1995, Journal of Physics B Atomic Molecular Physics, 28, 3741
Palmeri P., Biémont E., Quinet P., Dembczyński J., Szawiola G., Kurucz R. L., 1997, Phys. Scr, 55, 586
Pancino E., Carrera R., Rossetti E., Gallart C., 2010, A&A, 511, A56
Perryman M. A. C. et al., 2001, A&A, 369, 339
Pickering J. C., 1996, ApJS, 107, 811
Piffl T. et al., 2014, A&A, 562, A91
Piffl T., Williams M., Steinmetz M., 2011, A&A, 535, A70
Pilachowski C. A., Sneden C., Kraft R. P., 1996, AJ, 111, 1689
Pinsonneault M. H. et al., 2014, ApJS, 215, 19
Planck Collaboration et al., 2013, ArXiv e-prints
Plez B., 2012, Turbospectrum: Code for spectral synthesis. Astrophysics Source Code Library

Portegies Zwart S. F., 2000, ApJ, 544, 437
Portegies Zwart S. F., Baumgardt H., McMillan S. L. W., Makino J., Hut P., Ebisuzaki T., 2006, ApJ, 641, 319
Poveda A., Allen C., Hernández-Alcántara A., 2005, ApJLett, 627, L61
Poveda A., Ruiz J., Allen C., 1967, Boletin de los Observatorios Tonantzintla y Tacubaya, 4, 86
Prochaska J. X., Naumov S. O., Carney B. W., McWilliam A., Wolfe A. M., 2000, AJ, 120, 2513
Prugniel P., Soubiran C., 2001, A&A, 369, 1048
Przybilla N., Nieva M. F., Heber U., Firnstein M., Butler K., Napiwotzki R., Edelmann H., 2008, A&A, 480, L37
Purcell C. W., Bullock J. S., Kazantzidis S., 2010, MNRAS, 404, 1711
Qui H.-M., Zhao G., Takada-Hidai M., Chen Y.-Q., Takeda Y., Noguchi K., Sadakane K., Aoki W., 2002, PASJ, 54, 103
Ramírez I., Allende Prieto C., 2011, ApJ, 743, 135
Ramírez I., Meléndez J., 2005, ApJ, 626, 446
Ramírez I. et al., 2014, A&A, 572, A48
Ramírez I., Meléndez J., Chanamé J., 2012, ApJ, 757, 164
Randich S., Gilmore G., Gaia-ESO Consortium, 2013, The Messenger, 154, 47
Recio-Blanco A. et al., 2014, A&A, 567, A5
Reddy B. E., Lambert D. L., 2008, MNRAS, 391, 95
Reddy B. E., Lambert D. L., Allende Prieto C., 2006, MNRAS, 367, 1329
Reddy B. E., Tomkin J., Lambert D. L., Allende Prieto C., 2003, MNRAS, 340, 304
Rix H.-W., Bovy J., 2013, A&A Rev., 21, 61
Robertson B., Bullock J. S., Font A. S., Johnston K. V., Hernquist L., 2005, ApJ, 632, 872
Rogers B., Ferreras I., Peletier R., Silk J., 2010, MNRAS, 402, 447
Roman N. G., 1954, AJ, 59, 307
Rothman L. S. et al., 2010, J. Quant. Spectrosc. Radiat. Transfer, 111, 2139
Ruchti G. R. et al., 2010, ApJLett, 721, L92
Ryabchikova T., Piskunov N., Kurucz R. L., Stempels H. C., Heiter U., Pakhomov Y., Barklem P. S., 2015, Phys. Scr, 90, 054005
Ryan S. G., Smith I. M., 2003, MNRAS, 341, 199
Samland M., 1998, ApJ, 496, 155
Sanders J. L., Binney J., 2013, MNRAS, 433, 1813
Sanders J. L., Binney J., 2015, MNRAS, 449, 3479
Sbordone L., Bonifacio P., Buonanno R., Marconi G., Monaco L., Zaggia S., 2007, A&A, 465, 815
Schlesinger K. J. et al., 2012, ApJ, 761, 160
Schönrich R., 2012, MNRAS, 427, 274
Schönrich R., Asplund M., Casagrande L., 2011, MNRAS, 415, 3807
Schönrich R., Asplund M., Casagrande L., 2014, ApJ, 786, 7
Schönrich R., Bergemann M., 2014, MNRAS, 443, 698
Schuster W. J., Moitinho A., Márquez A., Parrao L., Covarrubias E., 2006, A&A, 445, 939
Schuster W. J., Moreno E., Nissen P. E., Pichardo B., 2012, A&A, 538, A21
Schuster W. J., Nissen P. E., 1988, A&AS, 73, 225
Searle L., Zinn R., 1978, ApJ, 225, 357

Sharma S., Bland-Hawthorn J., Johnston K. V., Binney J., 2011, ApJ, 730, 3
Sheffield A. A. et al., 2012, ApJ, 761, 161
Shetrone M. et al., 2015, ApJS, 221, 24
Shimansky V. V., Bikmaev I. F., Galeev A. I., Shimanskaya N. N., Ivanova D. V., Sakhibullin N. A., Musaev F. A., Galazutdinov G. A., 2003, Astronomy Reports, 47, 750
Siebert A. et al., 2011, AJ, 141, 187
Skuladottir A., Andrievsky S. M., Tolstoy E., Hill V., Salvadori S., Korotin S. A., Pettini M., 2015, ArXiv e-prints
Smiljanic R. et al., 2014, A&A, 570, A122
Smith M. C. et al., 2007, MNRAS, 379, 755
Smith V. V. et al., 2013, ApJ, 765, 16
Smolinski J. P. et al., 2011, AJ, 141, 89
Sneden C., Kraft R. P., Guhathakurta P., Peterson R. C., Fulbright J. P., 2004, AJ, 127, 2162
Sneden C., Lucatello S., Ram R. S., Brooke J. S. A., Bernath P., 2014, ApJS, 214, 26
Soderblom D. R., 2010, ARA&A, 48, 581
Soubiran C., Le Campion J.-F., Cayrel de Strobel G., Caillo A., 2010, A&A, 515, A111
Sousa S. G., Santos N. C., Israelian G., Lovis C., Mayor M., Silva P. B., Udry S., 2011, A&A, 526, A99
Spite M. et al., 2011, A&A, 528, A9
Steinmetz M. et al., 2006, AJ, 132, 1645
Stephens A., Boesgaard A. M., 2002, AJ, 123, 1647
Stetson P. B., Pancino E., 2008, PASP, 120, 1332
Tabur V., Kiss L. L., Bedding T. R., 2009, ApJLett, 703, L72
Takada-Hidai M., Takeda Y., 2012, in Astronomical Society of the Pacific Conference Series, Vol. 458, Galactic Archaeology: Near-Field Cosmology and the Formation of the Milky Way, Aoki W., Ishigaki M., Suda T., Tsujimoto T., Arimoto N., eds., p. 83
Thevenin F., 1998, VizieR Online Data Catalog, 3193
Thévenin F., Idiart T. P., 1999, ApJ, 521, 753
Thomas D., Maraston C., Bender R., 2003, MNRAS, 339, 897
Tillich A., Przybilla N., Scholz R.-D., Heber U., 2009, A&A, 507, L37
Tomkin J., Lemke M., Lambert D. L., Sneden C., 1992, AJ, 104, 1568
Unavane M., Wyse R. F. G., Gilmore G., 1996, MNRAS, 278, 727
Unkel P., Buch P., Dembczyński J., Ertmer W., Johann U., 1989, Zeitschrift fur Physik D Atoms Molecules Clusters, 11, 259
Valenti J. A., Fischer D. A., 2005, ApJS, 159, 141
van Belle G. T., 1999, PASP, 111, 1515
van Leeuwen F., 2007, A&A, 474, 653
Venn K. A., Irwin M., Shetrone M. D., Tout C. A., Hill V., Tolstoy E., 2004, AJ, 128, 1177
Vogelsberger M. et al., 2014, Nature, 509, 177
Walker I. R., Mihos J. C., Hernquist L., 1996, ApJ, 460, 121
Wallerstein G., Pilachowski C., Gerend D., Baird S., Canterna R., 1979, MNRAS, 186, 691
White S. D. M., Rees M. J., 1978, MNRAS, 183, 341
Woosley S. E., Weaver T. A., 1995, ApJS, 101, 181
Wyse R. F. G., 2008, in Astronomical Society of the Pacific Conference Series, Vol. 399, Panoramic Views of Galaxy Formation and Evolution, Kodama T., Yamada T., Aoki K., eds., p. 445

Wyse R. F. G., Gilmore G., 1988, AJ, 95, 1404
Yadin B., Veness T., Conti P., Hill C., Yurchenko S. N., Tennyson J., 2012, MNRAS, 425, 34
Yanny B. et al., 2009, AJ, 137, 4377
Yi S. K., Kim Y.-C., Demarque P., 2003, ApJS, 144, 259
York D. G. et al., 2000, AJ, 120, 1579
Yoshii Y., 1982, PASJ, 34, 365
Yoshii Y., Saio H., 1979, PASJ, 31, 339
Yu Q., Tremaine S., 2003, ApJ, 599, 1129
Zacharias N., Finch C. T., Girard T. M., Henden A., Bartlett J. L., Monet D. G., Zacharias M. I., 2013, AJ, 145, 44
Zhao G., Gehren T., 2000, A&A, 362, 1077
Zhong J. et al., 2014, ApJLett, 789, L2
Zolotov A., Willman B., Brooks A. M., Governato F., Brook C. B., Hogg D. W., Quinn T., Stinson G., 2009, ApJ, 702, 1058
Zolotov A., Willman B., Brooks A. M., Governato F., Hogg D. W., Shen S., Wadsley J., 2010, ApJ, 721, 738
Zwitter T. et al., 2008, AJ, 136, 421